Author: Brouwer, Margot
Title: Studying dark matter using weak gravitational lensing : from galaxies to the cosmic web
Date: 2017-12-20

Studying Dark Matter using Weak Gravitational Lensing

From Galaxies to the Cosmic Web

Proefschrift

ter verkrijging van
de graad van Doctor aan de Universiteit Leiden,
op gezag van Rector Magnificus prof. mr. C.J.J.M. Stolker,
volgens besluit van het College voor Promoties
te verdedigen op 20 december 2017
klokke 12:30 uur

door

Margot M. Brouwer
geboren te Amsterdam
in 1989

Promotiecommissie

Promotores:	Prof. dr. Koen Kuijken	(Universiteit Leiden)
	Prof. dr. Henk Hoekstra	
Overige leden:	Prof. dr. Huub Röttgering	
	Prof. dr. Joop Schaye	
	Prof. dr. Catherine Heymans	(University of Edinburgh)
	Prof. dr. Gianfranco Bertone	(Universiteit van Amsterdam)

ISBN: 978-94-6233-797-8

Dit proefschrift werd ondersteund door de Leidse Sterrewacht, de Leidse Faculteit voor Wis-en Natuurwetenschappen en de Leidse Universiteitsbibliotheek.

"When a man sits with a pretty girl for an hour, it seems like a minute. But let him sit on a hot stove for a minute and it's longer than any hour. That's relativity." – Albert Einstein

"The greatest good is the knowledge of the union which the mind has with the whole nature." – Baruch Spinoza

To Jasper, my brand new husband, who did not only show me the true meaning of relativity, but also helped me discover that the heavens can be found both above and inside.

Cover: Designed by Tineke Brouwer.

The background represents the cosmic structure of galaxies. Based on research by Coutinho et al. (2016) a set of 24,000 galaxies is connected to its closest neighbours, enabling a visualization (created by Kim Albrecht) of the cosmic web (see `http://cosmicweb.barabasilab.com`).

The looking glass on the back cover contains a Hubble Space Telescope composite image of dark matter (observed through weak gravitational lensing) in the galaxy cluster Cl 0024+17.

Credit: NASA, ESA, M.J. Jee and H. Ford (Johns Hopkins University)

Contents

1 Introduction

“A cosmic mystery of immense proportions, once seemingly on the verge of solution, has deepened and left astronomers and astrophysicists more baffled than ever. The crux of the riddle is that the vast majority of the mass of the universe seems to be missing. Or, more accurately, it is invisible to the most powerful telescopes on earth or in the heavens, which simply cannot detect all the mass that ought to exist in even nearby galaxies.” – William J. Broad, New York Times (September 11, 1984).

In these three sentences, New York Times reporter William Broad describes what is still one of the biggest mysteries in modern cosmology. Over the past decades, astronomers have found evidence that all known types of matter - stars, planets, gas, dust and even exotic objects like black holes and neutrino’s - only constitute $\sim 20\%$ of all mass in the universe. The other 80% is thought to consist of a hypothetical and invisible substance called dark matter. So far, however, all evidence is based exclusively on its gravitational interaction, either trough the dynamics of normal visible (often called ‘baryonic’) matter, or through the deflection of light in curved spacetime. This latter approach, called gravitational lensing, is a unique way to probe the distribution of dark matter without making any assumptions on its dynamical state (such as virial equilibrium in clusters), and on scales larger than the extent of baryons (e.g. outside the visible disks of galaxies). With this thesis, I hope to increase our knowledge of the distribution and behaviour of dark matter using weak gravitational lensing. On scales ranging from individual galaxies to groups, and even to large-scale structure, I study the link between baryonic and dark matter with the ultimate goal of gleaning some insight into its possible nature.

1.1 Dark Matter

1.1.1 Discovery and evidence

The first evidence of Dark Matter (DM) was found by Zwicky (1933), who used the virial theorem to study dynamics of galaxies in the Coma cluster. He found that the mass density of the cluster must be at least 400 times larger than expected from its luminous contents, and suggested 'Dunkle Materie' as a possible cause. At this time, he used this term to indicate *baryonic* DM, such as cold non-radiating gas, planets or compact objects. His findings were substantiated by Kahn and Woltjer (1959) who studied the dynamics of the Local Group. More than 20 years later Rubin (1983), who studied the spectra of galactic optical disks and found their rotation curves flattened, brought DM to a wider attention. By that time Freeman (1970) had already found the flattening of rotation curves in the disks of spiral and $\mathrm{S0}$ galaxies, and Bosma (1981) at scales far beyond the disks (using hydrogen profiles). All their research combined showed that, on scales ranging from individual galaxies to clusters, the gravitational potential found by applying Newtonian dynamics was too deep to be generated by the observed luminous matter. This 'excess gravity' was expected to arise from the DM coined by Zwicky, either in the form of baryonic or non-baryonic particles.

Some astrophysicists posed an alternative explanation to this problem: that the Newtonian laws of gravity are not accurate at these large scales. This could be solved by an adjustment of the laws of gravity, such as implemented by Milgrom (1983) who conceived Modified Newtonian Dynamics (MoND). Based on empirical evidence from galactic rotation curves, MoND adjusts Newton's second law of motion, $F = m\,a$, which relates the force F on a mass m to its acceleration a. Below a certain critical acceleration a_0 the Newtonian force F_N is adjusted as follows: $F_\mathrm{N} = m\,a_\mathrm{N} = m\,a^2/a_0$, which reproduces the observed flattening of the rotation curves. The necessary value of a_0 to describe these observations turns out to lie close to $c\,H_0$, where c is the speed of light and H_0 the present expansion rate of the universe. However, MoND's prediction for the mass of clusters, based on their visible baryonic content, is still too low without invoking some form of DM (Aguirre et al. 2001), such as massive neutrinos (Sanders 2003; Pointecouteau and Silk 2005).

During and after the conception of MoND, the COBE (Mather 1982) and WMAP (Spergel et al. 2003) missions produced accurate temperature maps of the Cosmic Microwave Background (CMB) radiation: the photons that were released during the era of recombination, ~ 380.000 years after the Big Bang. The spectrum of the observed temperature fluctuations revealed the acoustic oscillations present in the primordial plasma, caused by the interplay between light, mass and the expansion of the universe. As a non-relativistic theory, MoND could not explain the structure of the CMB. A relativistic generalization of MoND named TeVeS was created by Bekenstein (2004), but it is disputed whether a TeVeS model, even with the inclusion of massive neutrinos, can reproduce the observed structure formation and CMB power spectrum (Skordis et al. 2006; Xu et al. 2015).

So far, the theoretical framework that explains these observations best is the ΛCDM model. In this model, the majority of the energy density in the universe (68.5% as measured by Planck XIII 2016) consists of a cosmological constant Λ, which causes the Universe to expand at an accelerating rate. Only 4.9% of the energy density consists of normal baryonic matter. The remaining 26.6% of the universe's energy density constitutes the discussed 'missing mass', which consists of cold DM particles. Here 'cold' means that the DM was non-relativistic when it decoupled from baryonic matter. This is necessary since relativistic DM would have washed away the density fluctuations existing in the early universe, which originated from primordial quantum fluctuations. This would be inconsistent with our current observations, since these initial density variations accreted mass to form the Large Scale Structure (LSS) observed by galaxy redshift surveys today. Independent evidence that these DM particles cannot have a baryonic origin can be obtained from the abundances of primordial light elements (Deuterium, Lithium and several Helium isotopes), which were created during the first few minutes after the Big Bang (Alpher et al. 1948). The reconstruction of this period of 'Big Bang Nucleosynthesis', based on the principles of nuclear physics, shows that the baryon density is $\sim 5\%$ of the universe's total energy density (Pettini and Bowen 2001). This shows again that the baryonic density is much smaller than the total energy and matter density inferred from CMB observations.

But the most striking indication that DM might have a particle nature (as opposed to a modification of gravity) comes from weak gravitational lensing. The study by Clowe et al. (2006) of the Bullet Cluster, an ongoing merger of two colliding galaxy clusters, reveals that the major component of the gravitational potential resides at a different location than the major component of the baryonic mass (see Figure 1.1). The latter consists of hot gas, and is observed through its X-ray emission, while the former component is observed through the gravitational distortion of light from background galaxies. This famous example shows that weak gravitational

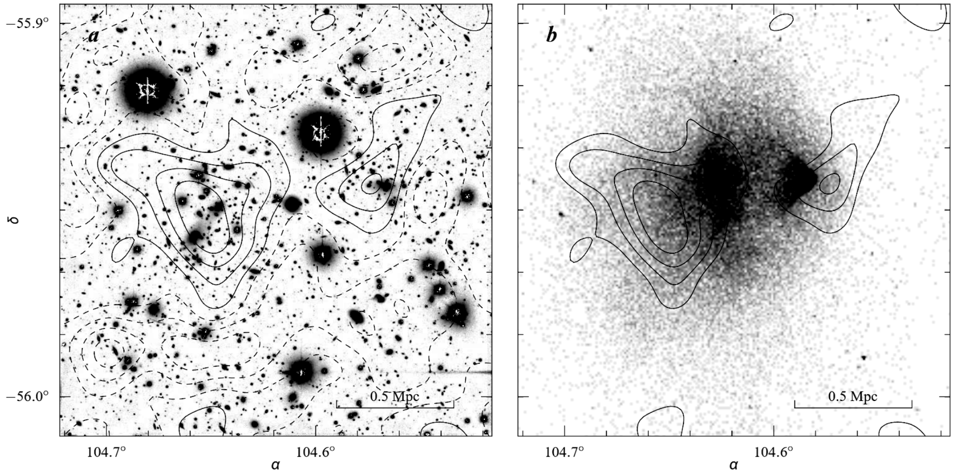

Figure 1.1: (a) An optical image of the galaxies in cluster 1E0657-56, or 'the Bullet Cluster', overlayed with the mass contours measured through weak gravitational lensing. The mass peak of the right subcluster (the 'bullet') approximately coincides with its galaxy concentration. This suggests that, like the galaxies, DM is collisionless. (b) An X-ray image of the Bullet Cluster, overlayed with the same mass contours. The X-ray is emitted by hot cluster gas, which constitutes the main baryonic mass component. The main dark and baryonic mass distributions do not coincide, suggesting that DM can exist separately from baryonic matter. Originally published in Markevitch et al. (2006).

lensing is a unique probe of the distribution of DM, independent of its dynamical state. It allows us to obtain a deeper understanding of its behaviour and relation to baryonic matter, which can ultimately lead us closer to the discovery of its fundamental nature.

1.1.2 Cosmic structure

The relation between dark and baryonic matter, which is one of the main themes of this thesis, can be studied on a wide range of scales: from individual galaxies to small groups, large clusters, and even to largest known structure in the universe: the 'cosmic web'. The exact nature of the relation between dark and baryonic matter at each scale, depends on how these structures formed. The first seeds of cosmic structure were established during the epoch of inflation: a period that took place $\sim 10^{-36}$ to 10^{-32} seconds after the Big Bang, in which space expanded exponentially (Guth 1981; Sato 1981). The 'inflaton field', which theoretically caused this exponential expansion, contained microscopic quantum fluctuations that were subsequently magnified to cosmic sizes. After ‘re-heating’, the decay of the inflaton field into matter and radiation, these macroscopic fluctuations remained as overdensities. The period of superluminal expansion also explains why our current universe appears homogeneous, isotropic, flat, and devoid of relic exotic particles (such as magnetic monopoles).

The thermalization of the universe is followed by the radiation-dominated era, where most of the energy density was contained by photons. During this epoch, the gravitational growth of structure was impeded by the rapid expansion of the universe. But while space continued to expand, the energy density of radiation diluted faster than that of matter, due to the redshifting of the photons. Around $47,000$ years after the Big Bang, the energy density in radiation and matter had equalized, marking the beginning of the matter-dominated era. At the start of this era, baryonic matter was still ionized due to the high temperatures (> 3000 Kelvin), and could not collapse due too radiation pressure. DM, however, which is not affected by radiation pressure, could now start to gravitationally collapse. Structure formation models pose that the primordial density perturbations grew into a network of roughly spherical DM halos (Peebles and Yu 1970). This early formation of structure, where density contrasts are still small, can be analytically described using the ‘linear power spectrum’.

Only after $\sim 380,000$ years the universe had cooled enough to allow for the recombination of electrons and protons into neutral hydrogen, which disconnected the baryonic matter from the photon pressure. The photons that escaped during recombination are currently observed as the CMB. In the ΛCDM paradigm, the total mass of the baryonic matter component is sub-dominant to that of DM (less than $\sim 1/5$ its mass), causing its spatial structure to broadly follow that of the DM through gravitational attraction. A galaxy forms when baryonic matter is pulled into the potential well of a DM halo, and cools at its centre (Blumenthal et al. 1984). Since baryonic matter can lose potential energy through radiative cooling (whereas DM cannot) the galaxies thus formed have a radius ~ 100 times smaller than that of the DM halo, which can only collapse through virialization.

As the density contrast of DM increases through further gravitational collapse, later stages of structure formation become impossible to describe analytically. Computational N-body simulations that incorporate Newtonian gravity are currently the most convenient method of studying structure formation at later times. The ΛCDM model constitutes the basis for extensive N-body simulations (containing $\sim 10^9$ particles), such as the Millennium Simulation (Springel et al. 2005b) and the EAGLE project (Schaye et al. 2015), which provide excellent predictions for LSS formation. These simulations show a hierarchical clustering of DM halos, forming combined structures from small groups to big clusters. On the largest scales, they exhibit a web-like structure formed by filaments and sheets of DM. At the intersection of these structures, the DM halos coalesce into giant superclusters, while in between there exist immense underdense regions named voids.

As the DM structure evolves the baryonic matter, consisting primarily of galaxies and gas, follows. On the level of a single galaxy inhabiting a DM halo, we observe mergers that increase both the halo and galaxy mass (White and Frenk 1991). If the local number density of halos (within a few Mpc range) is high, the increased merger rate is expected to boost the average galaxy and halo mass (Bardeen et al. 1986; Cole and Kaiser 1989). On even larger scales we observe that, through gravitational attraction, the cosmic DM web acts as a skeleton to the baryonic matter, which primarily consists of gas clouds, galaxies, clusters and superclusters (Bond et al. 1986). The reflection of the cosmic DM web in the large-scale distribution of galaxies can be observed by large scale redshift surveys, such as the 2dF Galaxy Redshift Survey (2dFGRS, Colless et al. 2001) and the Sloan Digital Sky Survey (SDSS, Abazajian et al. 2009). If and how this LSS affects galaxies and halos is still subject to debate (Hahn et al. 2009; Ludlow and Porciani 2011; Alonso et al. 2015), but so far no observational evidence for such effects has been found (Darvish et al. 2014; Alpaslan et al. 2015; Eardley et al. 2015).

Over the course of this thesis, we study the relation between galaxies and halos on the scale of individual galaxies and galaxy groups, we try to measure the effect of the local and large scale (cosmic web) density distribution on galaxies and haloes, and we measure the interplay between galactic and DM structures at the scale of the cosmic web. All observations of the aforementioned DM distributions are based on the weak gravitational lensing method.

1.2 Weak gravitational lensing

1.2.1 The weak lensing method

In Einstein's theory of General Relativity (GR), gravitational force is equivalent to the curvature of space-time. Based on this theory, he could calculate the deflection of light that travels through a part of space-time which is curved by a specific mass. Most famously, he predicted this deflection for the light of distant stars by the Sun, which was measured by Sir Arthur Eddington in 1919. The observation of stars close to the sun (in projection) could only be performed during a total eclipse, which required an expedition to the African island of Principé. Eddington confirmed Einstein's prediction, which provided both the theory of GR and themselves with instant credibility and fame.

This deflection of light by gravity is called 'gravitational lensing', and has become a widely used method to measure mass distributions in the universe. In this thesis, we use gravitational lensing to measure the total (baryonic + dark) mass distribution around galaxies, galaxy groups and larger structures. This is done specifically through 'weak gravitational lensing' (WL) of the light from background galaxies. When both the foreground lenses and the background sources are galaxies, this method is called 'galaxy-galaxy lensing' (for a more elaborate discussion, see e.g. Bartelmann and Schneider 2001; Schneider et al. 2006).

The fundamental principle behind lensing is illustrated in Fig. 1.2, where the light from one background source is deflected by a foreground point mass which acts as a gravitational lens. Because the angular diameter distances D_{l} and D_{s} to the lens and the source are very large compared to the width of the lens along the 'line of sight' (LOS), we can apply the 'thin lens approximation'. Instead of taking the full curved path of the light ray into account we can assume that the light is instantaneously deflected at the lens plane, where it passes the centre of the lens at a projected radial distance R. In GR, the deflection angle $\hat{\alpha}$ of the light ray is related to the mass M of the lens as:

$$\hat{\alpha} = \frac{4GM}{c^2 R}\,, \tag{1.1}$$

where c denotes the speed of light and G the gravitational constant. Also, the true position of the source with respect to the LOS, $\eta = \beta\, D_{\mathrm{s}}$, is related to its apparent position $R = \theta\, D_{\mathrm{l}}$ as:

$$\eta = \frac{D_{\mathrm{s}}}{D_{\mathrm{l}}} R - D_{\mathrm{ls}} \hat{\alpha}\,. \tag{1.2}$$

This can be rewritten as the 'lens equation':

$$\beta = \theta - \frac{D_{\mathrm{ls}}}{D_{\mathrm{s}}} \hat{\alpha} \equiv \theta - \alpha, \tag{1.3}$$

where α is the 'reduced deflection angle', scaled by the distance D_{ls} between the lens and the source.

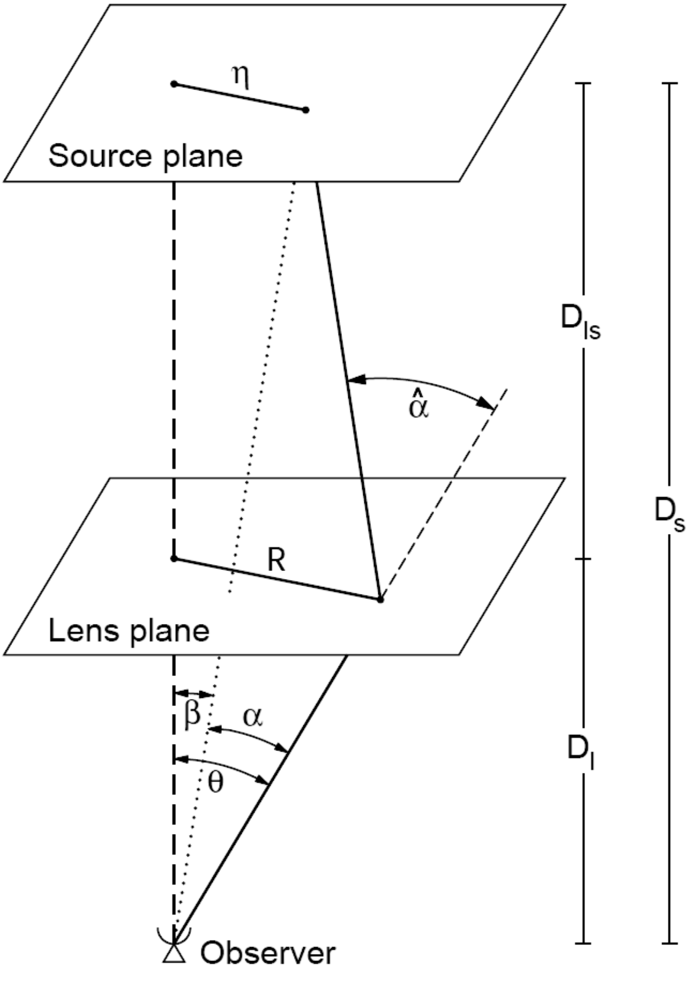

Figure 1.2: A schematic view of gravitational lensing. The dashed line shows the 'line of sight' (LOS), which goes from the observer through the center of the lens to the source plane. At projected distance η from the LOS, a source emits a light ray which is deflected at an angle $\hat{\alpha}$. This means it is now observed at a projected distance R from the center of the lens, instead of its true position. For an extended source, this results in a tangential shape distortion with respect to the lens center. This distortion, called shear, is a probe of the surface density distribution $\Sigma(R)$ of the lens. Originally published in Bartelmann & Schneider (2001).

Instead of a point mass, we can also consider a density distribution $\rho(R, z, \varphi)$. This distribution is represented in cylindrical coordinates, where z is the LOS direction and φ the angle with respect to the lens centre (in the lens plane). If we assume an azimuthally symmetric mass distribution we can integrate over φ, such that the density only depends on R and z. We can now represent the mass M from Eq. 1.1 as:

$$M = \int \rho(R, z, \varphi)\, R\, \mathrm{d}R\, \mathrm{d}z\, \mathrm{d}\varphi \; = 2\pi \int \rho(R, z)\, R\, \mathrm{d}R\, \mathrm{d}z\,. \tag{1.4}$$

However, the gravitational lensing method only provides information on the density integrated along the LOS, which is defined as the projected surface mass density:

$$\Sigma(R) = \int \rho(R, z)\, \mathrm{d}z\,. \tag{1.5}$$

We combine Eq. 1.4 and 1.5 to express the reduced deflection angle from Eq. 1.3 in terms of the surface density:

$$\begin{aligned} \alpha = \hat{\alpha}\,\frac{D_{\mathrm{ls}}}{D_{\mathrm{s}}} = \frac{4G}{c^2 R}\frac{D_{\mathrm{ls}}}{D_{\mathrm{s}}}\, 2\pi \int \Sigma(R)\, R\, \mathrm{d}R \; = \\ \frac{2}{D_{\mathrm{l}} R} \int \frac{4\pi G}{c^2} \frac{D_{\mathrm{l}}\, D_{\mathrm{ls}}}{D_{\mathrm{s}}}\, \Sigma(R)\, R\, \mathrm{d}R \; \equiv \; \frac{2}{D_{\mathrm{l}} R} \int \frac{\Sigma(R)}{\Sigma_{\mathrm{crit}}}\, R\, \mathrm{d}R\,. \end{aligned} \tag{1.6}$$

Here Σ_{crit} is the critical density surface mass density:

$$\Sigma_{\mathrm{crit}} = \frac{c^2}{4\pi G} \frac{D_{\mathrm{s}}}{D_{\mathrm{l}}\, D_{\mathrm{ls}}}\,, \tag{1.7}$$

which is the inverse of the lensing efficiency: a geometrical factor that determines the strength of the lensing effect based on the distances between the lens, the source and the observer. Defining the dimensionless surface mass density $\kappa(R) \equiv \Sigma(R)/\Sigma_{\mathrm{crit}}$ and remembering that $R = \theta\, D_{\mathrm{l}}$, the lens equation (Eq. 1.3) now becomes:

$$\beta(\theta) = \theta(1 - \alpha(\theta)/\theta) = \theta(1 - \langle\kappa\rangle) \tag{1.8}$$

where $\langle\kappa\rangle$ is the average dimensionless surface density inside radius R (or angle θ):

$$\langle\kappa(R)\rangle = \frac{2}{\theta\, D_{\mathrm{l}} R} \int \frac{\Sigma(R)}{\Sigma_{\mathrm{crit}}}\, R\, \mathrm{d}R = \frac{2}{\theta^2} \int \kappa(\theta)\, \theta\, \mathrm{d}\theta = \frac{\alpha(\theta)}{\theta}\,. \tag{1.9}$$

In this thesis the lensed sources are galaxies, which have extended 2D images. As can already be seen from Eq. 1.1, the amount of deflection depends on the distance vector $\vec{R}$ to the lens. When lensing affects an extended source, this causes a differential distortion of the image. The intrinsic surface brightness distribution $I_{\mathrm{int}}(\vec{\beta})$ (in the source plane) is mapped to the observed distribution $I_{\mathrm{obs}}(\vec{\theta})$ (in the lens plane) through the 2D coordinate transformation $\vec{\beta}(\vec{\theta})$:

$$I_{\mathrm{obs}}(\vec{\theta}) = I_{\mathrm{int}}[\vec{\beta}(\vec{\theta})] \tag{1.10}$$

In the case of our work, the size of the background sources is negligible compared to the angular scale on which the mass density of the lens changes. This means that the coordinate transformation can be linearised as follows:

$$\vec{\beta}(\vec{\theta}) = \vec{\beta}_0 + \frac{\delta\vec{\beta}}{\delta\vec{\theta}}(\vec{\theta} - \vec{\theta}_0)\,, \tag{1.11}$$

where β_0 and θ_0 are corresponding points in the source and lens plain respectively. The image distortion $\delta\vec{\beta}/\delta\vec{\theta}$ can be derived by applying the Jacobian to β (from Eq. 1.8) as follows:

$$\frac{\delta\vec{\beta}}{\delta\vec{\theta}} = \frac{\delta([1-\langle\kappa\rangle]\vec{\theta})}{\delta\vec{\theta}} = (1-\langle\kappa\rangle)\begin{bmatrix}1 & 0\\ 0 & 1\end{bmatrix} - \frac{\delta\langle\kappa\rangle}{\delta\theta}\begin{bmatrix}\theta_1^2 & \theta_1\theta_2\\ \theta_1\theta_2 & \theta_2^2\end{bmatrix}/|\theta|\,, \tag{1.12}$$

where θ_1 and θ_2 are the two components of the location vector $\vec{\theta}$ of the source with respect to the equatorial coordinate system. Since we are considering an azymuthally symmetric lens, it is convenient to express this location in terms of its angle ϕ with respect to the centre of the lens: $\vec{\theta} = |\theta|(\cos(\phi)\,,\,\sin(\phi))$. Furthermore, the derivative of $\langle\kappa(\theta)\rangle$ can be solved using the third term of Eq. 1.9, which yields:

$$\frac{\delta\langle\kappa\rangle}{\delta\theta} = \frac{-2}{\theta}\left(\frac{2}{\theta^2}\int\kappa\,\theta\,\mathrm{d}\theta\right) + \frac{2}{\theta^2}\kappa\,\theta = \frac{2}{\theta}(\kappa - \langle\kappa\rangle)\,. \tag{1.13}$$

Using Eq. 1.13 and the definition of $\vec{\theta}$ to re-write Eq. 1.12 gives:

$$\frac{\delta\vec{\beta}}{\delta\vec{\theta}} = [1-\kappa+(\kappa-\langle\kappa\rangle)]\begin{bmatrix}1 & 0\\ 0 & 1\end{bmatrix} - (\kappa-\langle\kappa\rangle)\begin{bmatrix}2\cos^2(\phi) & 2\cos(\phi)\sin(\phi)\\ 2\cos(\phi)\sin(\phi) & 2\sin^2(\phi)\end{bmatrix} =$$

$$(1-\kappa)\begin{bmatrix}1 & 0\\ 0 & 1\end{bmatrix} + (\kappa-\langle\kappa\rangle)\begin{bmatrix}\cos(2\phi) & \sin(2\phi)\\ \sin(2\phi) & -\cos(2\phi)\end{bmatrix}\,. \tag{1.14}$$

Based on this equation we can define the 'tangential shear' γ_t, which is the distortion of the source (called 'shear') tangential to the direction of the lens' centre:

$$\gamma_\mathrm{t} = \langle\kappa\rangle - \kappa = -\gamma_1 \cos(2\phi) - \gamma_2 \sin(2\phi) = -\Re(\gamma\, e^{-2i\phi}) \,, \tag{1.15}$$

where γ_1 and γ_2 are the components of the shear with respect to the equatorial coordinate frame, and:

$$\gamma = |\gamma| e^{2i\phi} = \gamma_1 + i\,\gamma_2 \,. \tag{1.16}$$

In the case of WL studies the surface density is much smaller than Σ_crit, and the convergence $\kappa = \Sigma/\Sigma_\mathrm{crit} \ll 1$ in Eq. 1.14 is often ignored. Consequently, γ_t is the primary measure for the shape distortion used to estimate the gravitational lensing effect. At an angle of 45° with respect to γ_t we find the 'cross shear' γ_x, which is analogously defined as:

$$\gamma_\mathrm{x} = -\Im(\gamma\, e^{-2i\phi}) = \gamma_1 \sin(2\phi) - \gamma_2 \cos(2\phi) \,. \tag{1.17}$$

Because γ_x is not affected by lensing, it is very useful as a null test.

Using Eq. 1.15 the tangential shear $\gamma_\mathrm{t}(R)$ can be related to the Excess Surface Density (ESD) $\Delta\Sigma(R)$, which is defined as the surface mass density $\Sigma(R)$ at projected radial distance R from the lens centre, subtracted from the average density $\langle\Sigma(<R)\rangle$ within that radius:

$$\gamma_\mathrm{t}(R)\Sigma_\mathrm{crit} = [\langle\kappa(<R)\rangle - \kappa(R)]\Sigma_\mathrm{crit} = \langle\Sigma(<R)\rangle - \Sigma(R) \equiv \Delta\Sigma(R) \,. \tag{1.18}$$

To measure the tangential shear we observe the ellipticity ϵ of the background galaxies, which can be expressed in terms of the source's axis ratio b/a:

$$\epsilon = \frac{1 - b/a}{1 + b/a} e^{2i\phi} \,, \tag{1.19}$$

or as a two-component vector: $\vec{\epsilon} = |\epsilon|(\cos(2\phi)\,,\, \sin(2\phi))$. In reality, the observed ellipticity ϵ_obs of each source is a combination of both the shear γ and the intrinsic ellipticity ϵ_int of the galaxy. The unknown intrinsic ellipticities of galaxies are a limitation to all WL measurements, referred to as 'shape noise'. Although the amount of shape noise does not vary significantly between source populations with different properties (Leauthaud et al. 2007), it can depend on the shape measurement method. Therefore, the amount of shape noise is always carefully measured and propagated in the lensing errors. Compared to this noise, the shape distortion from lensing is so weak ($\sim 1\%$ of the intrinsic galaxy ellipticity) that it can only be measured statistically. This is achieved by accurately measuring the shapes of thousands of background galaxies in the field around a foreground mass distribution. In this way, we can measure the average shear by assuming that the intrinsic shapes are randomly oriented ($\langle\epsilon_{\rm int}\rangle = 0$), such that:

$$\langle\epsilon_{\rm obs}\rangle = \langle\epsilon_{\rm int} + \gamma\rangle = \langle\gamma\rangle\,. \tag{1.20}$$

By azimuthally averaging the sources' tangential shear components, the radial mass distribution of the lens can be reconstructed. To improve the signal-to-noise (S/N) even further, the radial lensing profile is averaged ('stacked') for large samples (hundreds to thousands) of lenses, often selected according to their observable properties. Combining the tangential shear for all lens-source pairs of a lens sample, binned in circular apertures of increasing radial distance R, results in the average shear profile $\langle\gamma_{\rm t}\rangle(R)$ of a lens sample. Using the distances to the lenses and sources, this quantity can in turn be translated to the ESD profile $\Delta\Sigma(R)$ of a lens sample.

1.2.2 The galaxy-galaxy lensing pipeline

The galaxy-galaxy lensing (GGL) software pipeline translates the measured distances and ellipticities of background galaxies (sources) from the Kilo-Degree Survey (KiDS, de Jong et al. 2013) into gravitational lensing profiles around foreground galaxies, groups or other mass distributions (lenses). This pipeline is used to perform the lensing measurements at the basis of the four chapters in this thesis (among other publications), and has the ability to calculate:

- the tangential and cross shear $\gamma_{\rm t}$ and $\gamma_{\rm x}$, as a function of the projected radial separation θ from the lens centre.
- the Excess Surface Density (ESD) as a function of the projected physical distance R from the lens centre.
- the additive and multiplicative bias correction of the lensing signal.
- the standard variance error on the lensing signal, based on the number and reliability of the source ellipticities.
- the analytical covariance matrix and errors, which are based on the contribution of each individual background source to the lensing signal and take into account the covariance related to sources that contribute to the profiles of multiple lenses.

- the bootstrap covariance matrix and errors, which are based on bootstrapping 1×1 deg survey tiles and take into account the contributions from sample variance and cosmic variance.

The pipeline can be operated through a user-friendly interface that allows users to specify the parameters of the lensing measurement: the type of lensing measurement, the type of error estimate, the values and unit of the radial bins around the lens, the values of the cosmological parameters, and the redshift range of the sources. The interface accepts any lens catalogue as input, and allows the user to select the lenses used for the analysis based on their measured observables. The lenses can be subjected to individual cuts and/or split into any number of bins. In case of the latter, the analytical and bootstrap covariance matrix will provide the covariance between the bins in observable, in addition to the covariance between the radial bins. One can also supply individual weights to scale the contribution of each lens to the signal, which will be taken into account into the calculation of the covariance matrix and the multiplicative bias correction.

After I created the first version of the pipeline for application to the KiDS DR2 data (KiDS, de Jong et al. 2015), the pipeline has been greatly improved and adjusted for the arrival of the KiDS DR3 data (de Jong et al. 2017) by Andrej Dvornik. Cristóbal Sifón has extended the pipeline with a module that allows the user to easily fit DM halo models to the output lensing profiles. The halo model framework is based on work by Marcello Cacciato, as applied in e.g. Cacciato et al. (2013). The most up-to-date version of the GGL pipeline is available for download through Github (`https://github.com/KiDS-WL/KiDS-GGL`).

1.3 Outline

This thesis describes our studies into the behaviour and distribution of DM through WL with KiDS. The studied structures (lenses) are mainly observed using the spectroscopic Galaxy And Mass Assembly survey (GAMA, Driver et al. 2011). The following subsections describe the contents of the individual chapters.

1.3.1 KiDS+GAMA: properties of galaxy groups

Chapter 2 contains the first WL study with the KiDS and GAMA surveys. This effort was made possible by the combined work of many contributors from both collaborations. My personal contribution was the construction and description of the GGL pipeline (see Sect. 1.2.2). This pipeline forms the basis of multiple KiDS-GAMA GGL papers, four of which are described below:

In Viola et al. (2015) we used gravitational lensing to study 'rich' galaxy groups (with 5 or more members). The groups, that have masses between $10^{13} < M < 10^{14.5}\,h^{-1}\mathrm{M}_{\odot}$, represent the most common galaxy environment in the universe. They were detected in the spectroscopic GAMA survey, and defined using a Friend-of-Friend algorithm that was calibrated using simulations. We split the ~ 1400 groups into bins based on their observable properties, and measured the ESD profile of each sub-sample. Interpreting the ESD profiles using a halo model framework allowed us to measure the group halo mass as a function of luminosity, velocity dispersion, (apparent) number of members, and fraction of group light in the central galaxy. Comparing this last relation to predictions from the Cosmo-OverWhelmingly Large Simulations (Cosmo-OWLS), we ruled out galaxy formation models without AGN feedback.

Sifón et al. (2015) used galaxy-galaxy lensing to study galaxies that are satellites in the aforementioned groups. Their main goal was to constrain the effect of 'halo stripping', the tidal removal of mass from satellite haloes by the halo of their host group. They separated the sample of $\sim 10,000$ satellites into three bins as a function of their projected distance to the group central, and measured the ESD of each subsample. Using the halo model framework, they measured the satellite halo mass as a function of its distance to the central, which is an estimator of the time since infall. They found no significant change in the stellar-to-halo mass relation of the satellites, which would signify halo stripping.

The goal of van Uitert et al. (2016) was to study the stellar-to-halo mass relation of galaxies, and whether it depends on group environment. By simultaneously fitting a halo model to the lensing profiles and the stellar mass function of galaxies, they obtained significantly better constraints. They found no large differences between the stellar-to-halo mass relation of all galaxies and those in rich groups, suggesting that the dependence on group environment is weak. For satellites, they found weak evidence of an increase in the halo mass fraction with stellar mass, which would imply halo stripping. However, impurities in the satellite sample could also cause this observation.

Dvornik et al. (2017) searched for signatures of 'halo assembly bias': the dependence of the distribution of DM haloes on any property besides their mass, such as formation time. They selected galaxy groups with different radial distributions of the satellite galaxies, which is a proxy for formation time. After measuring the ESD profiles of galaxy groups with 4 or more members, they measured their masses using the halo model framework. Using this method, they found no evidence of halo assembly bias on group scales.

Of these papers, I have included Viola et al. (2015) as a chapter in this thesis. The reason for including this paper specifically is that it was the very first KiDS-GAMA GGL paper, and that I was among the lead authors.

1.3.2 Galaxy halo masses in cosmic environments

In **Chapter 3**, which is based on Brouwer et al. (2016), we used the GGL pipeline and halo model framework to study the DM haloes of GAMA galaxies as a function of their large-scale environment. This environment consists of the cosmic web, a large network of mass structures that may influence the formation and evolution of DM haloes and the galaxies they host. The cosmic environments in our study were defined by Eardley et al. (2015) through a tidal tensor prescription, which finds the number of dimensions in which a volume is collapsing. Based on this number, the entire GAMA survey is divided into voids, sheets, filaments and clusters (called 'knots'). We measured the lensing profiles of the galaxies in these four environments and, through the halo model framework, modelled the contribution of central and satellite galaxies of groups, and the '2-halo' term caused by neighbouring groups. By correcting for the galaxies' stellar mass and 'local density' (the galaxy density within $4\,h^{-1}\mathrm{Mpc}$), we aimed to find the dependence of halo mass on the cosmic environments alone. Although the measured lensing signal was very sensitive to the local density through the amplitude of the 2-halo term, we found no direct dependence of the galaxy halo mass on local density or cosmic environment.

1.3.3 A weak lensing study of troughs

In **Chapter 4** we aimed to study the structure of the cosmic web itself, by measuring the lensing profiles of projected underdensities (troughs) and overdensities (ridges) in the KiDS galaxy number density distribution. Based on the definition of Gruen et al. (2016), we defined troughs with a projected radius $\theta_{\mathrm{A}} = \{5, 10, 15, 20\}$ arcmin. Through the amplitude A of the lensing profiles of troughs/ridges as a function of their galaxy number density, we explored the connection between their baryonic and total mass. We found that the skewness of the galaxy density distribution, which reveals non-linearities caused by the formation of cosmic structure, is reflected in the distribution of the total (baryonic + DM) mass distribution measured by lensing. The measured signal-to-noise (S/N) of the trough/ridge profiles as a function of galaxy number density allowed us to optimally stack their lensing signal, obtaining trough detections with a significance of $|S/N| = \{17.12, 14.77, 9.96, 7.55\}$. By splitting a volume limited galaxy sample into two redshift slices between $0.1 < z < 0.3$, we attempted to measure redshift evolution of troughs/ridges. The troughs were selected to have equal *comoving* lengths and radii at the different redshifts, to correct for the expansion of the universe. We found that, at these relatively low redshifts, there is no significant evolution. However, the MICE-GC mock catalogues to which we compared all our results, predict that at higher redshifts ($z \sim 0.6$) both troughs and ridges will exhibit signatures of structure evolution.

1.3.4 Lensing test of Verlinde's emergent gravity

Chapter 5, which is based on Brouwer et al. (2017), describes the first test of Emergent Gravity (EG, Verlinde 2017) through WL. The observable prediction of this theory, which proposes an alternative explanation to the excess gravity attributed to DM, is currently limited to the gravitational potential around spherically symmetric, static and isolated baryonic density distributions. We used the GAMA survey to find a sample of $33,613$ central galaxies that contain no other centrals within the projected radial distance range of our WL measurement: $0.03 < R < 3\,h_{70}^{-1}\mathrm{Mpc}$. Using the measured stellar masses of these galaxies we modelled their radial baryonic mass distributions, both as a simple point source and as an extended distribution that takes into account stars, cold gas, hot gas and satellites. For both models we predicted the lensing profiles in the EG framework, assuming that light is bent by a gravitational potential as in GR, and the background cosmology behaves like ΛCDM with a constant Hubble parameter. For the point mass model, this prediction is very similar to that from MoND (Milgrom 2013). We compared this prediction, which is fully determined by the baryonic mass distribution, to the WL profiles of isolated centrals in four different stellar mass bins. We found that the EG theory predicts our measurements equally well as an NFW profile with the halo mass as a free parameter, especially if we take these free parameters into account. After the publication of our research, several follow-up papers appeared that attempted to test the EG prediction on different scales. Ettori et al. (2017), who used X-ray data, weak lensing and galaxy dynamics to study the mass distributions of two galaxy clusters, found that EG reproduced the DM distribution needed to maintain the gas in pressure equilibrium beyond 1 Mpc from the cluster core, with a remarkable good match at radius $r \approx R_{500}$, but that it showed significant discrepancies (a factor 2–3) in the innermost 200 kpc. Lelli et al. (2017) studied the radial acceleration of disk galaxies, and found that EG was only consistent with the observed Radial Acceleration Relation for very low stellar mass-to-light ratios. Hees et al. (2017) showed that EG's predictions for the perihelion advancement of Solar System planets were discrepant with the data by seven orders of magnitude, although it can be disputed if this system can be considered static and isolated. Also in general these requirements of sphericity, staticity and isolation greatly inhibit the applicability of the EG prediction to cosmological observations and simulations. All in all, the theoretical framework of EG still has a long way to go before it can be considered as a viable competitor to the current ΛCDM model.

2 KiDS+GAMA: properties of galaxy groups

Based on: “Dark matter halo properties of GAMA galaxy groups from 100 square degrees of KiDS weak lensing data”
Authors: Massimo Viola, Marcello Cacciato, Margot M. Brouwer, Konrad Kuijken, Henk Hoekstra, Peder Norberg, Aaron S. G. Robotham, Edo van Uitert, Mehmed Alpaslan, Ivan K. Baldry, Ami Choi, Jelte T. A. de Jong, Simon P. Driver, Thomas Erben, Aniello Grado, Alister W. Graham, Catherine Heymans, Hendrik Hildebrandt, Anthony M. Hopkins, Nancy Irisarri, Benjamin Joachimi, Jon Loveday, Lance Miller, Reiko Nakajima, Peter Schneider, Cristóbal Sifón, Gijs Verdoes Kleijn
Published in: Monthly Notices of the Royal Astronomical Society, Volume 452, Issue 4, p.3529-3550

Abstract:
The Kilo-Degree Survey (KiDS) is an optical wide-field survey designed to map the matter distribution in the Universe using weak gravitational lensing. In this paper, we use these data to measure the density profiles and masses of a sample of ~ 1400 spectroscopically identified galaxy groups and clusters from the Galaxy And Mass Assembly (GAMA) survey. We detect a highly significant signal (signal-to-noise-ratio ~ 120), allowing us to study the properties of dark matter haloes over one and a half order of magnitude in mass, from $M \sim 10^{13} - 10^{14.5}\, h^{-1}\mathrm{M}_{\odot}$. We interpret the results for various subsamples of groups using a halo model framework which accounts for the mis-centring of the Brightest Cluster Galaxy (used as the tracer of the group centre) with respect to the centre of the group's dark matter halo. We find that the density profiles of the haloes are well described by an NFW profile with concentrations that agree with predictions from numerical simulations. In addition, we constrain scaling relations between the mass and a number of observable group properties. We find that the mass scales with the total r-band luminosity as a power-law with slope 1.16 ± 0.13 (1-sigma) and with the group velocity dispersion as a power-law with slope 1.89 ± 0.27 (1-sigma). Finally, we demonstrate the potential of weak lensing studies of groups to discriminate between models of baryonic feedback at group scales by comparing our results with the predictions from the Cosmo-OverWhelmingly Large Simulations (Cosmo-OWLS) project, ruling out models without AGN feedback.

2.1 Introduction

Galaxy groups are the most common structures in the Universe, thus representing the typical environment in which galaxies are found. In fact, most galaxies are either part of a group or have been part of a group at a certain point in time (Eke et al. 2004). However, group properties are not as well studied compared to those of more massive clusters of galaxies, or individual galaxies. This is because groups are difficult to identify due to the small number of (bright) members. Identifying groups requires a sufficiently deep[1] spectroscopic survey with good spatial coverage, that is near 100% complete. Even if a sample of groups is constructed, the typically small number of members per group prevents reliable direct dynamical mass estimates (Carlberg et al. 2001; Robotham et al. 2011). It is pos-

---

[1] Fainter than the characteristic galaxy luminosity L^* where the power-law form of the luminosity function cuts off

sible to derive ensemble averaged properties (e.g., More et al. 2009a), but the interpretation ultimately relies on either a careful comparison to numerical simulations or an assumption of an underlying analytical model (e.g., More et al. 2011) .

For clusters of galaxies, the temperature and luminosity of the hot X-ray emitting intracluster medium can be used to estimate masses under the assumption of hydrostatic equilibrium. Simulations (e.g., Rasia et al. 2006; Nagai et al. 2007) and observations (e.g., Mahdavi et al. 2013) indicate that the hydrostatic masses are biased somewhat low, due to bulk motions and non-thermal pressure support, but correlate well with the mass. In principle, it is possible to apply this technique to galaxy groups; however, this is observationally expensive given their faintness in X-rays, and consequently samples are generally small (e.g., Sun et al. 2009; Eckmiller et al. 2011; Kettula et al. 2013; Finoguenov et al. 2015; Pearson et al. 2015) and typically limited to the more massive systems.

Furthermore, given their lower masses and the corresponding lower gravitational binding energy, baryonic processes, such as feedback from star formation and active galactic nuclei (AGN) are expected to affect groups more than clusters (e.g., McCarthy et al. 2010; Le Brun et al. 2014). This may lead to increased biases in the hydrostatic mass estimates. The mass distribution in galaxy groups is also important for predictions of the observed matter power spectrum, and recent studies have highlighted that baryonic processes can lead to significant biases in cosmological parameter constraints from cosmic shear studies if left unaccounted for (e.g., van Daalen et al. 2011; Semboloni et al. 2011, 2013).

The group environment also plays an important role in determining the observed properties of galaxies. For example, there is increasing evidence that star formation quenching happens in galaxy groups (Robotham et al. 2013; Wetzel et al. 2014), due to ram pressure stripping, mergers, or AGN jets in the centre of the halo (Dubois et al. 2013). The properties of galaxies and groups of galaxies correlate with properties of their host dark matter halo (Vale and Ostriker 2004; Moster et al. 2010; Behroozi et al. 2010; Moster et al. 2013), and the details of those correlations depend on the baryonic processes taking place inside the haloes (Le Brun et al. 2014). Hence, characterisation of these correlations is crucial to understand the effects of environment on galaxy evolution.

The study of galaxy groups is thus of great interest, but constraining models of galaxy evolution using galaxy groups requires both reliable and complete group catalogues over a relatively large part of the sky and unbiased measurements of their dark matter halo properties. In the past decade, several large galaxy surveys have become available, and significant effort has been made to reliably identify bound structures and study their properties (Eke et al. 2004; Gerke et al. 2005; Berlind et al. 2006; Brough et al. 2006; Knobel et al. 2009). In this paper, we use the group catalogue presented in Robotham et al. (2011) (hereafter R11) based on the three equatorial fields of the spectroscopic Galaxy And Mass Assembly survey (herafter GAMA, Driver et al. 2011). For the reasons outlined above, determining group masses using "traditional" techniques is difficult. Fortunately, weak gravitational lensing provides a direct way to probe the mass distribution of galaxy groups (e.g., Hoekstra et al. 2001; Parker et al. 2005; Leauthaud et al. 2010). It uses the tiny coherent distortions in the shapes of background galaxies caused by the deflection of light rays from foreground objects, in our case galaxy groups (e.g., Bartelmann and Schneider 2001). Those distortions are directly proportional to the tidal field of the gravitational potential of the foreground lenses, hence allowing us to infer the properties of their dark matter haloes without assumptions about their dynamical status. The typical distortion in the shape of a background object caused by foreground galaxies is much smaller than its intrinsic ellipticity, preventing a precise mass determination for individual groups. Instead, we can only infer the ensemble averaged properties by averaging the shapes of many background galaxies around many foreground lenses, under the assumption that galaxies are randomly oriented in the Universe.

The measurement of the lensing signal involves accurate shape estimates, which in turn require deep, high quality imaging data. The shape measurements presented in this paper are obtained from the ongoing Kilo-Degree Survey (KiDS; de Jong et al. 2015). KiDS is an optical imaging survey with the OmegaCAM wide-field imager (Kuijken 2011) on the VLT Survey Telescope (Capaccioli and Schipani 2011; de Jong et al. 2013) that will eventually cover 1500 square degrees of the sky in 4 bands ($ugri$). Crucially, the survey region of GAMA fully overlaps with KiDS. The depth of the KiDS data and its exquisite image quality are ideal to use weak gravitational lensing as a technique to measure halo properties of the GAMA groups, such as their masses. This is the main focus of this paper, one of a set of articles about the gravitational lensing analysis of the first and second KiDS data releases (de Jong et al. 2015). Companion papers will present a detailed analysis of the properties of galaxies as a function of environment (van Uitert et al. 2016), the properties of satellite galaxies in groups (Sifón et al. 2015), as well as a technical description of the lensing and photometric redshift measurements (Kuijken et al. 2015, K15 hereafter).

In the last decade, weak gravitational lensing analyses of large optical surveys have become a standard tool to measure average properties of dark matter haloes (Brainerd et al. 1996; Fischer et al. 2000; Hoekstra 2004; Sheldon et al. 2004; Parker et al. 2005; Heymans et al. 2006a; Mandelbaum et al. 2006a; Johnston et al. 2007; Sheldon et al. 2009; van Uitert et al. 2011; Leauthaud et al. 2012b; Choi et al. 2012; Velander et al. 2014; Coupon et al. 2015; Hudson et al. 2015). However, the interpretation of the stacked lensing signal of haloes with different properties is not trivial. Haloes with different masses are stacked together, and a simple fit of the signal using some function describing an average halo profile, like a Navarro-Frenk-White profile (Navarro et al. 1995, hereafter NFW) , can provide biased measurements. A natural framework to describe the statistical weak lensing signal is the so-called halo model (Cooray and Sheth 2002; van den Bosch et al. 2013). It provides a statistical description of the way observable galaxy properties correlate with the mass of dark matter haloes taking into account the halo mass function, the halo abundance and their large scale bias.

The outline of this paper is as follows. In Section 2.2, we summarise the basics of weak lensing theory. We describe the data used in this work in Section 2.3, and we summarise the halo model framework in Section 2.4. In Section 2.5, we present our lensing measurements of the GAMA galaxy groups, and in Section 2.6, we derive scaling relations between lensing masses and optical properties of the groups. We conclude in Section 2.7.

The relevant cosmological parameters entering in the calculation of distances and in the halo model are taken from the Planck best fit cosmology (Planck Collaboration et al. 2013): $\Omega_{\rm m} = 0.315$, $\Omega_{\Lambda} = 0.685$, $\sigma_8 = 0.829$, $n_{\rm s} = 0.9603$ and $\Omega_{\rm b} h^2 = 0.02205$. Throughout the paper we use M_{200} as a measure for the masses of the groups as defined by 200 times the mean density (and corresponding radius, noted as R_{200}).

2.2 Statistical weak gravitational lensing

Gravitational lensing refers to the deflection of light rays from distant objects due to the presence of matter along the line-of-sight. Overdense regions imprint coherent tangential distortions (shear) in the shape of background objects (hereafter sources). Galaxies form and reside in dark matter haloes, and as such, they are biased tracers of overdense regions in the Universe. For this reason, one expects to find non-vanishing shear profiles around galaxies, with the strength of this signal being stronger for groups of galaxies as they inhabit more massive haloes. This effect is stronger in the proximity of the centre of the overdensity and becomes weaker at larger distances.

Unfortunately, the coherent distortion induced by the host halo of a single galaxy (or group of galaxies) is too weak to be detected. We therefore rely on a statistical approach in which many galaxies or groups that share similar observational properties are stacked together. Average halo properties (e.g. masses, density profiles) are then inferred from the resulting high signal-to noise shear measurements. This technique is commonly referred to as 'galaxy-galaxy lensing', and it has become a standard approach for measuring masses of galaxies in a statistical sense.

Given its statistical nature, galaxy-galaxy lensing can be viewed as a measurement of the cross-correlation of some baryonic tracer $\delta_{\rm g}$ and the matter density field $\delta_{\rm m}$:

$$\xi_{\rm gm}(\mathbf{r}) = \langle \delta_{\rm g}(\mathbf{x})\delta_{\rm m}(\mathbf{x}+\mathbf{r})\rangle_{\mathbf{x}}\,, \tag{2.1}$$

where $\mathbf{r}$ is the three-dimensional comoving separation. The Equation above can be related to the projected matter surface density around galaxies via the Abel integral:

$$\Sigma(R) = \bar{\rho}_{\rm m} \int_0^{\pi_{\rm s}} [1 + \xi_{\rm gm}(\sqrt{R^2 + \Pi^2})]\, {\rm d}\Pi\,, \tag{2.2}$$

where R is the co-moving projected separation from the galaxy, $\pi_{\rm s}$ the position of the source galaxy, $\bar{\rho}_{\rm m}$ is the mean density of the Universe and Π is the line-of-sight separation.[2] Being sensitive to the density *contrast*, the shear is actually a measure of the excess surface density (ESD hereafter):

$$\Delta\Sigma(R) = \bar{\Sigma}(\leqslant R) - \Sigma(R)\,, \tag{2.3}$$

where $\bar{\Sigma}(\leqslant R)$ just follows from $\Sigma(R)$ via

$$\bar{\Sigma}(\leqslant R) = \frac{2}{R^2}\int_0^R \Sigma(R')\, R'\, {\rm d}R'\,. \tag{2.4}$$

The ESD can finally be related to the tangential shear distortion $\gamma_{\rm t}$ of background objects, which is the main lensing observable:

$$\Delta\Sigma(R) = \gamma_{\rm t}(R)\Sigma_{\rm cr}\,, \tag{2.5}$$

---

[2] Here and throughout the paper we assume spherical symmetry. This assumption is justified in the context of this work since we measure the lensing signal from a stack of many different haloes with different shapes, which washes out any potential halo triaxiality.

where

$$\Sigma_{\mathrm{cr}} = \frac{c^2}{4\pi G} \frac{D(z_{\mathrm{s}})}{D(z_{\mathrm{l}})D(z_{\mathrm{l}}, z_{\mathrm{s}})}, \tag{2.6}$$

is a geometrical factor accounting for the lensing efficiency. In the previous equation, $D(z_l)$ is the angular diameter distance to the lens, $D(z_l, z_s)$ the angular diameter distance between the lens and the source and $D(z_s)$ the angular diameter distance to the source.

In the limit of a single galaxy embedded in a halo of mass M, one can see that Equation 2.1 further simplifies because $\xi_{\mathrm{gm}}(\mathbf{r})$ becomes the normalised matter overdensity profile around the centre of the galaxy. The stacking procedure builds upon this limiting case by performing a weighted average of such profiles accounting for the contribution from different haloes. This is best formulated in the context of the halo model of structure formation (see e.g. Cooray and Sheth 2002, van den Bosch et al. 2013), and for this reason, we will embed the whole analysis in this framework (see Section 2.4). In Section 2.3.3, we describe how the ESD profile is measured.

2.3 DATA

The data used in this paper are obtained from two surveys: the Kilo-Degree Survey (KiDS) and the Galaxy And Mass Assembly survey (GAMA). KiDS is an ongoing ESO optical imaging survey with the OmegaCAM wide-field imager on the VLT Survey Telescope (de Jong et al. 2013). When completed, it will cover two patches of the sky in four bands (u, g, r, i), one in the Northern galactic cap and one in the South, adding up to a total area of 1500 square degrees overlapping with the 2 degree Field Galaxy Redshift survey (2dFGRS herafter, Colless et al. 2001). With rest-frame magnitude limits (5σ in a 2" aperture) of 24.3, 25.1, 24.9, and 23.8 in the u, g, r, and i bands, respectively, and better than 0.8 arcsec seeing in the r-band, KiDS was designed to create a combined data set that included good weak lensing shape measurements and good photometric redhifts. This enables a wide range of science including cosmic shear 'tomography', galaxy-galaxy lensing and other weak lensing studies.

In this paper, we present initial weak lensing results based on observations of 100 KiDS tiles, which have been covered in all four optical bands and released to ESO as part of the first and second 'KiDS-DR1/2' data releases to the ESO community, as described in de Jong et al. (2015). The effective area after removing masks and overlaps between tiles is 68.5 square

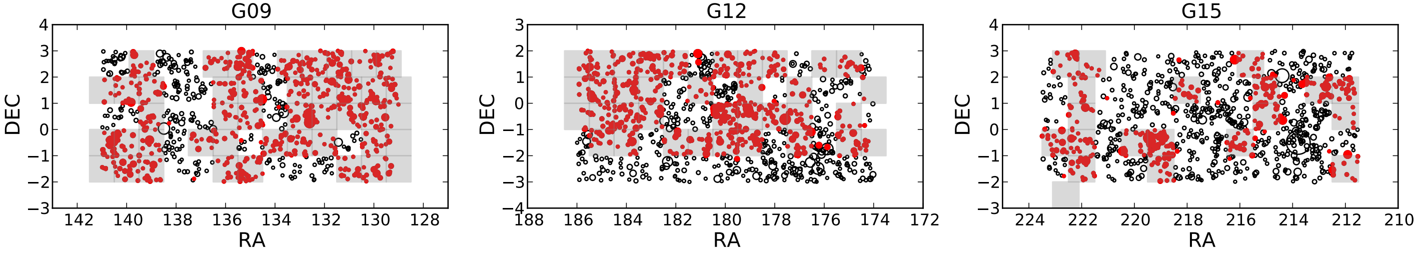

Figure 2.1: KiDS-ESO-DR1/2 coverage of the three equatorial GAMA fields (G09, G12, G15). Each grey box corresponds to a single KiDS tile of 1 square degree. The black circles represent groups with $\mathrm{N_{fof}} \geqslant 5$ in the $\mathrm{G^3Cv7}$ catalogue (R11). The size of the dots is proportional to the group apparent richness. The filled red circles indicate the groups used in this analysis. These are all groups either inside a KiDS field or whose centre is separated less than 2 $h^{-1}\mathrm{Mpc}$ from the centre of the closest KiDS field.

Table 2.1: Summary of the area overlap of KiDS-DR1/2 in the three GAMA fields and the number of groups with at least 5 members used in this analysis. In parenthesis we quote the effective area, accounting for masks, used in this work.

GAMA field	KiDS-DR1/2 overlap (deg^2)	Number of groups
G09	44.0 (28.5)	596
G12	36.0 (25.0)	509
G15	20.0 (15.0)	308

degrees[3].

In the equatorial region, the KiDS footprint overlaps with the footprint of the GAMA spectroscopic survey (Baldry et al. 2010; Robotham et al. 2010; Driver et al. 2011; Liske et al. 2015), carried out using the AAOmega multi-object spectrograph on the Anglo-Australian Telescope (AAT). The GAMA survey is highly complete down to petrosian r-band magnitude 19.8 [4], and it covers ~ 180 square degrees in the equatorial region, which allows for the identification of a large number of galaxy groups.

Figure 2.1 shows the KiDS-DR1/2 coverage of the G09, G12 and G15 GAMA fields. We also show the spatial distribution of the galaxy groups in the three GAMA fields (open black circles) and the selection of groups entering in this analysis (red closed circles).

Table 2.1 lists the overlap between KiDS-DR1/2 and GAMA and the total number of groups used in this analysis. Figure 2.2 shows the redshift distribution of the GAMA groups used in this work and of the KiDS source galaxies, computed as a weighted sum of the posterior photometric redshift distribution as provided by BPZ (Benítez 2000). The weight comes from the *lens*fit code, which is used to measure the shape of the objects (Miller et al. 2007) (see Sec. 2.3.2). The median redshift of the GAMA groups is z=0.2, while the weighted median redshift of KiDS is 0.53. The multiple peaks in the redshift distribution of the KiDS sources result from degeneracies in the photometric redshift solution. This is dicussed further in K15. The different redshift distributions of the two surveys are ideal for a weak lensing study of the GAMA groups using the KiDS galaxies as background sources.

---

[3] A further 48 tiles from the KiDS-DR1/2, mostly in KiDS-South, were not used in this analysis since they do not overlap with GAMA.

[4] The petrosian apparent magnitudes are measured from SDSS-DR7 and they include extinction corrections (Schlegel maps)

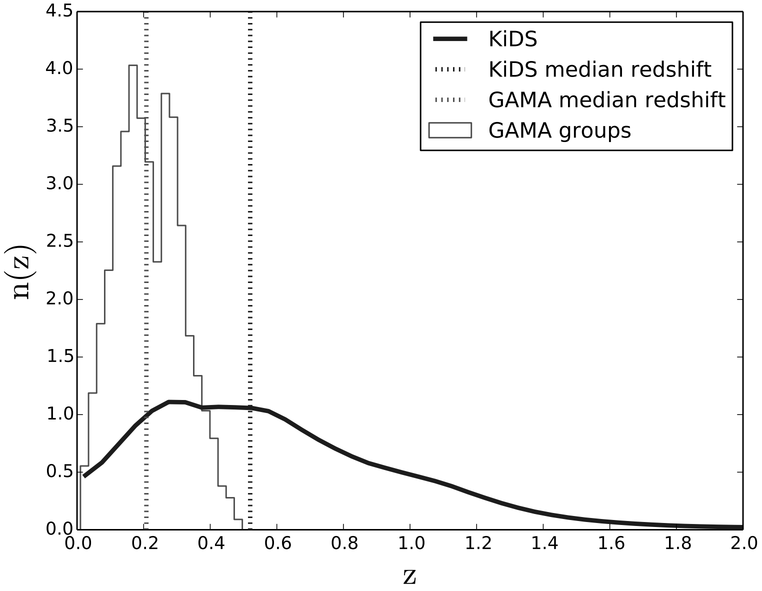

Figure 2.2: Redshift distribution of the GAMA groups used in this analysis (thin histogram) and the KiDS galaxies (thick line). In the case of the GAMA groups, we use the spectroscopic redshift of the groups with at least 5 members (R11), while for the KiDS galaxies the redshift distribution is computed as a weighted sum of the posterior photometric redshift distribution as provided by BPZ (Benítez 2000). The weight comes from *lens*fit, used to measure the shape of the objects (Miller et al. 2007). The two vertical lines show the median of the redshift distribution of the GAMA groups and of the KiDS sources. The two peaks in the redshift distribution of the GAMA groups are physical (and not caused by incompleteness), due to the clustering of galaxies in the GAMA equatorial fields.

2.3.1 Lenses: GAMA Groups

One of the main products of the GAMA survey is a group catalogue, G^3C (R11), of which we use the internal version 7. It consists of 23,838 galaxy groups identified in the GAMA equatorial regions (G09, G12, G15), with over 70,000 group members. It has been constructed employing spatial and spectroscopic redshift information (Baldry et al. 2014) of all the galaxies targeted by GAMA in the three equatorial regions. The groups are found using a friends-of-friends algorithm, which links galaxies based on their projected and line-of-sight proximity. The choice of the linking length has been optimally calibrated using mock data (R11, Merson et al. 2013) based on the Millennium simulation[5] (Springel et al. 2005b) and a semi-analytical galaxy formation model (Bower et al. 2006). Running the final group selection algorithm on the mock catalogues shows that groups with at least 5 GAMA galaxies are less affected by interlopers and have sufficient members for a velocity dispersion estimate (R11). For this reason we use only such groups in our analysis. This choice leaves us with 1413 groups, in KiDS-DR1/2, 11% of the full GAMA group catalogue.

Figure 2.3 shows the distribution of the total group r-band luminosity as a function of the redshift of the group, the group apparent richness, which is the number of members brighter that $r = 19.8$, and the group velocity dispersion corrected for velocity uncertainty, for this subsample. These group r-band luminosity values are calculated by summing the r-band luminosity of all galaxies belonging to a group and targeted by GAMA and they also include an estimate of the contribution from faint galaxies below the GAMA flux limit, as discussed in R11. This correction is typically very small, a few percent at low redshift and a factor of a few at $z \sim 0.5$ since most of the luminosity comes from galaxies around $\mathrm{M}^{\star} - 5\log h \sim -20.44$ (Loveday et al. 2012, 2015), and most of the groups are sampled well below $\mathrm{M}^{\star}$. Note that all absolute magnitudes and luminosities used in the paper are k-corrected and evolution corrected at redshift $z = 0$ (R11). The global k-correction used by R11 is compatible with the median k-correction of the full GAMA (McNaught-Roberts et al. 2014, Fig.1 in the paper).

All the stellar masses used in this work are taken from Taylor et al. (2011a), who fitted Bruzual and Charlot (2003) synthetic stellar spectra to the broadband SDSS photometry assuming a Chabrier (2003) IMF and a Calzetti et al. (2000) dust law.

2.3.2 Sources: KiDS galaxies

We measure the gravitational lensing effect induced by the GAMA groups using galaxy images from KiDS. We refer to K15 for a detailed description of the pipelines used to measure shapes and photometric redshifts for those objects. We briefly summarise here the aspects of the data processing most relevant for this analysis.

Shape measurements

All of our lensing measurements are derived from the r-band exposures in KiDS. This is the band with the highest image quality of the survey, as the

---

[5] $(\Omega_m, \Omega_b, \Omega_\Lambda, h, \sigma_8, n_s)$=$(0.25, 0.045, 0.75, 0.73, 0.9, 1.0)$

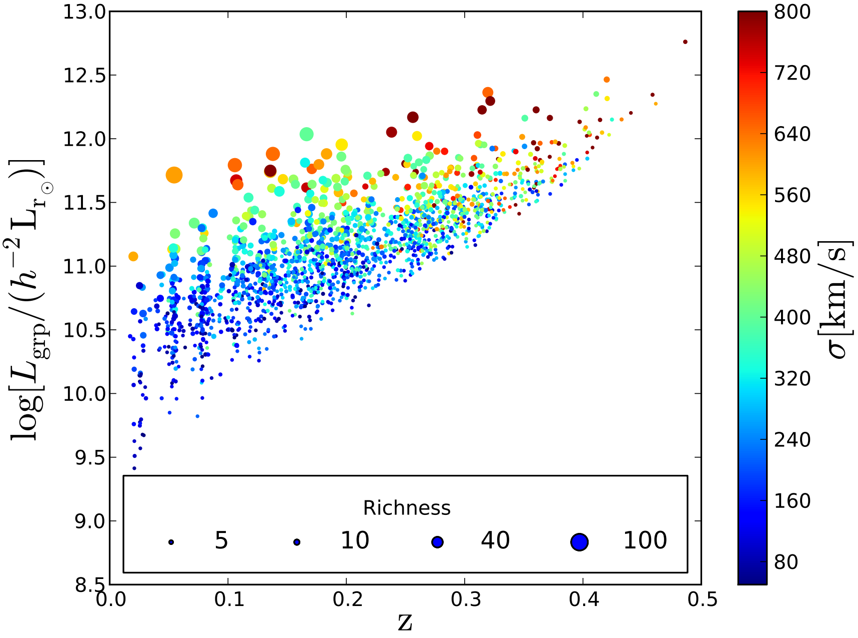

Figure 2.3: Total group r-band luminosity as a function of the redshift of the group. The size of the points is proportional to the group apparent richness and the colour of the points indicates the group velocity dispersion corrected for velocity uncertainty. The shape of the distribution is typical of a flux limited survey.

queue-scheduling at the telescope ensures that observations in this filter are taken in the best seeing conditions. The images are processed with the THELI pipeline, which has been optimized for lensing applications (Erben et al. 2013), and ellipticities for the galaxies are derived using the *lens*fit code (Miller et al. 2007; Kitching et al. 2008; Miller et al. 2013a). *lens*fit takes full account of the point-spread function in the individual (dithered) exposures and prior knowledge of the ellipticity and size distributions of faint galaxies, returning an ellipticity estimate for each galaxy as well as an inverse variance weight that is related to the uncertainty of the measurement.

The average number density of galaxies with *lens*fit weight w larger than 0, and satisfying the photometric redshift cuts described in the next section, is 8.88 per square arcmin, corresponding to an effective number density:

$$n_{\rm eff} = \frac{\sigma^2_{\epsilon^{\rm s}}}{A} \sum_i w_i \, , \tag{2.7}$$

of 4.48 galaxies per square arcmin, where A is the survey area and $\sigma^2_{\epsilon^{\rm s}} = 0.065$ is the intrinsic ellipticity variance. This is a measurement of the statistical power of the weak lensing data (see Chang et al. (2013) and K15 for more details).

It is well known that shape measurements for galaxies with low signal-to-noise ratio and small sizes tend to be biased (e.g., Melchior and Viola 2012; Refregier et al. 2012; Miller et al. 2013a; Viola et al. 2014). This 'noise-bias' stems from the non-linear transformations of the image pixels involved in the derivation of galaxy image shapes. It has the form of a multiplicative bias, and a calibration of the shape measurements is typically required in order to get an unbiased shear estimator. In this paper, we use the same calibration that was determined in Miller et al. (2013a). This calibration depends on the signal-to-noise and the size of the objects and needs to be applied, in an average sense, to the recovered shear field. In addition to this multiplicative bias, shape measurements can also be affected by an additive bias caused by a non-perfect PSF deconvolution, centroid bias and pixel level detector effects. This bias can be empirically quantified and corrected for directly from the data, using the residual average ellipticity over the survey area. More detail on these ~ 10 per cent bias corrections can be found in K15.

The analysis presented in this paper has been applied to four different ellipticity catalogues. Three of these catalogues were generated by rescaling all the ellipticity measurements by some factors unknown to the team and chosen by a colleague, Matthias Bartelmann[6], external to the collaboration. The amplitude of the rescaling has been chosen such that the cosmological parameters derived from a cosmic shear analysis using the four blind catalogues would not differ more than 10-σ, where sigma is the error from the Planck cosmological papers. We refer to this procedure as *blinding*, and we have used it to mitigate confirmation bias in our data analysis. The authors asked our external to *unblind* the true shear catalogues only just before paper submission. The authors were not allowed to change any of the results after the unblinding, without documenting those changes. Whilst the shear was blind, we did not blind measurements of group properties, such as their luminosity, or measurements of the source photometric redshifts.

---

[6] bartelmann@uni-heidelberg.de

Photometric redshift measurements

The observable lensing distortion depends on the distances to the lens and source (Equation 2.6). Redshifts to the lenses are known from the GAMA spectroscopy, but for the sources we need to resort to photometric redshifts derived from the KiDS-ESO-DR1/2 ugri images in the ESO data release. Processing and calibration of these images is done using the Astro-WISE environment (McFarland et al. 2013), and flux and colour measurements use the 'Gaussian Aperture and Photometry' (GAaP) technique designed to correct aperture photometry for seeing differences (Kuijken 2008). These colours form the basis of the photometric redshift estimates, obtained with BPZ (Benítez 2000; Hildebrandt et al. 2012). After extensive tests, we reject galaxies whose photometric redshift posterior distribution $p(z)$ peaks outside the range [0.005,1.2] (see K15). In what follows the $p(z)$ for each source is used in the calculation of distances, and in particular in the calculation of the critical surface density (see Equation 2.6). Kuijken et al. (2015) show that if the peak of each source's $p(z)$ had been used as the estimate of the redshift, the average value of $\Sigma_{\rm cr}$ and hence the average ESD would have been underestimated by $\sim$ 10 %.

2.3.3 Measurement of the stacked excess surface density profile

The shape measurement algorithm used in this work, *lens*fit, provides measurements of the galaxy ellipticities (ϵ_1, ϵ_2) with respect to an equatorial coordinate system.

For each source-lens pair we compute the tangential $\epsilon_{\rm t}$ and cross component $\epsilon_{\rm x}$ of the source's ellipticity around the position of the lens,

$$\begin{pmatrix}\epsilon_{\rm t}\\ \epsilon_{\rm x}\end{pmatrix} = \begin{pmatrix}-\cos(2\phi) & -\sin(2\phi)\\ \sin(2\phi) & -\cos(2\phi)\end{pmatrix}\begin{pmatrix}\epsilon_1\\ \epsilon_2\end{pmatrix}, \tag{2.8}$$

where ϕ is the position angle of the source with respect to the lens. The average of the tangential ellipticity of a large number of galaxies in the same area of the sky is an unbiased estimate of the shear. On the other hand, the average of the cross ellipticity over many sources should average to zero. For this reason, the cross ellipticity is commonly used as an estimator of possible systematics in the measurements. Each lens-source pair is then assigned a weight

$$\tilde{w}_{\rm ls} = w_{\rm s}\tilde{\Sigma}_{\rm cr}^{-2}, \tag{2.9}$$

which is the product of the *lens*fit weight w_s assigned to the given source ellipticity, and a geometric term $\tilde{\Sigma}_{\rm cr}$ which downweights lens-source pairs that are close in redshift and therefore less sensitive to lensing. We compute the 'effective critical surface density' for each pair from the spectroscopic redshift of the lens z_l and the full posterior redshift distribution of the source, $p(z_s)$:

$$\tilde{\Sigma}_{\rm cr}^{-1} = \frac{4\pi G}{c^2} \int_{z_l}^{\infty} \frac{D_l(z_l) D_{ls}(z_l, z_s)}{D_s(z_s)} p(z_s) {\rm d}z_s \, . \tag{2.10}$$

Finally, following Equation 2.5, we compute the ESD in bins of projected distance R to the lenses:

$$\Delta\Sigma(R) = \left(\frac{\sum_{ls} \tilde{w}_{ls} \epsilon_{\rm t} \tilde{\Sigma}_{\rm cr}}{\sum_{ls} \tilde{w}_{ls}} \right) \frac{1}{1 + K(R)} \, , \tag{2.11}$$

where the sum is over all source-lens pairs in the distance bin, and

$$K(R) = \frac{\sum_{ls} \tilde{w}_{ls} m_s}{\sum_{ls} \tilde{w}_{ls}} \, , \tag{2.12}$$

is an average correction to the ESD profile that has to be applied to correct for the multiplicative noise bias m in the *lens*fit shear estimates. Typically, the value of the $K(R)$ correction is around 0.1, largely independent of the scale at which it is computed.

Figure 2.4 shows the stacked ESD profile for all groups either inside a KiDS field or whose centre is separated by less than 2 $h^{-1}\mathrm{Mpc}$ from the centre of the closest KiDS field. It shows a highly significant detection of the lensing signal (signal-to-noise ratio $\sim$ 120). We note that the signal-to-noise is very poor at scales smaller than $20\,h^{-1}\mathrm{kpc}$. This is due to the fact that many objects close to the group centres are blended, and *lens*fit assigns them a vanishing weight. We exclude those scales from any further analysis presented in this paper.

For reference, we also show the best fit singular isothermal sphere (SIS) and NFW models to the stacked ESD signal. In the case of the NFW model, the halo concentration is fixed using the Duffy et al. (2008) mass-concentration relation. Neither of the two single-parameter models provides a good fit to the data ($\chi^2_{\rm red} > 2.5$), highlighting how a more complex modelling of the signal is required (see Section 2.4).

Figure 2.4 also includes two tests for residual systematic errors in the data: the cross-component of the signal and the signal measured around random points in the KiDS tiles. On scales larger than $2\,h^{-1}\mathrm{Mpc}$, small but significant deviations are evident. We believe that one possible origin of

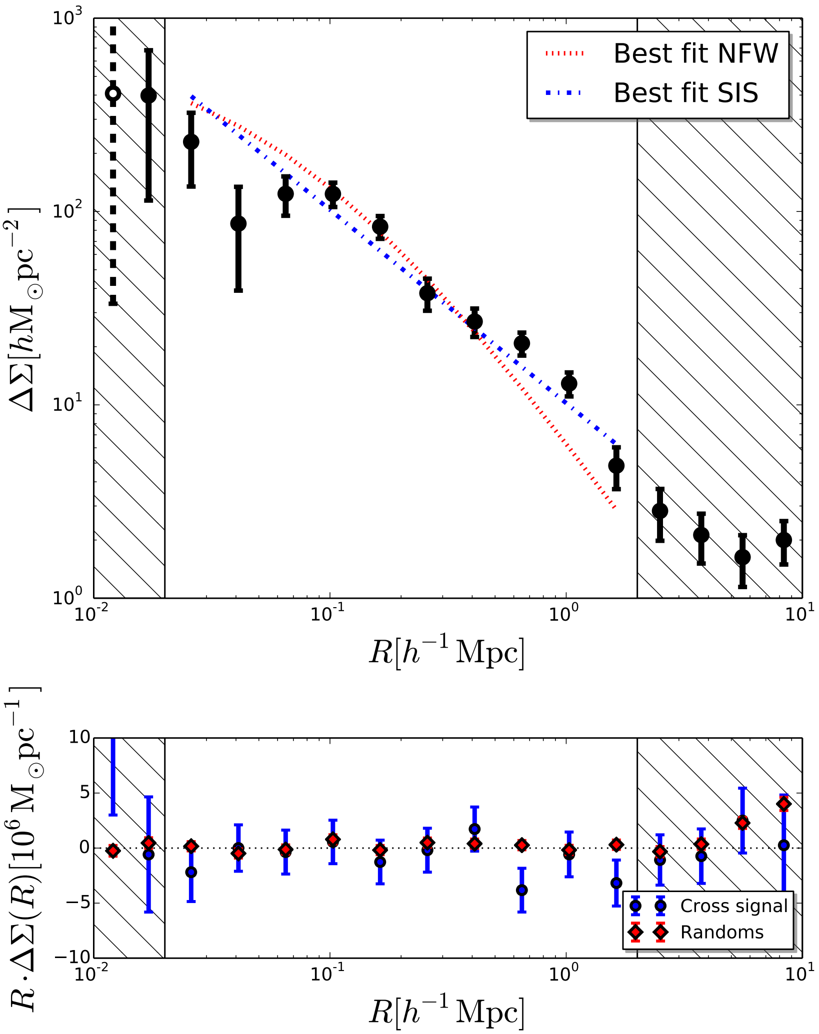

Figure 2.4: *Top panel:* ESD profile measured from a stack of all GAMA groups with at least 5 members (black points). Here, we choose the Brightest Cluster Galaxy as the group centre. The open white circle with dashed error bars indicates a negative $\Delta\Sigma$. The dotted red line and the dash-dotted blue line show the best fits to the data of NFW (Navarro et al. 1995) and singular isothermal sphere profiles, respectively. Neither of the single-parameter models provides a good fit to the data, highlighting that complex modelling of the signal is required. *Bottom panel:* ESD profile, multiplied by R to enhance features at large radii, measured from the cross-component of the ellipticities for these same groups (blue points) and measured around random points using the same redshift distribution of the groups (red points). We only use measurements at scales outside the dashed areas for the rest of the paper.

the non-vanishing signal around random points at these scales is due to the incomplete azimuthal average of galaxy ellipticities, but we cannot exclude some large scale systematics in the shear data. The current patchy coverage of lensing data complicates a detailed analysis and here we simply note that the effect is small (less than 10 percent of the signal at $2\,h^{-1}\mathrm{Mpc}$) and exclude data on scales larger than $2\,h^{-1}\mathrm{Mpc}$. Future analyses based on more uniform coverage of the GAMA area from the KiDS survey will need to address these potential issues.

To summarise, in the rest of the paper we will use only projected distances in the range $(0.02-2)\,h^{-1}\mathrm{Mpc}$. Both the cross-component of the shear and the signal around random points are consistent with a null-detection over these scales.

2.3.4 Statistical error estimate

In a stacking analysis with many foreground lenses, the ellipticity of any source galaxy can contribute to the $\Delta\Sigma_i$ estimate in multiple radial bins i of different lenses. We summarize here how we compute the resulting covariances between the ESD estimates $\Delta\Sigma_i$ from the data.

We start from Equation 2.11, which gives the expression for $\Delta\Sigma_i$. For simplicity, we drop in what follows the noise bias correction factor $1+K(R)$ as it can be considered to have been absorbed in the effective critical density $\tilde{\Sigma}_{\mathrm{cr}}$.

We first rearrange the sum in Equation 2.11 to separate the contributions from each source s, by summing first over all lenses l that project within the radial bin i from source s; for each source s we denote this set of lenses as i_s. We can then rewrite Equation 2.11 as

$$\Delta\Sigma_i = \frac{\sum_s w_s \left(\epsilon_{1s} C_{si} + \epsilon_{2s} S_{si}\right)}{\sum_s w_s Z_{si}}\,, \tag{2.13}$$

where C, S and Z are sums over the lenses

$$C_{si} = \sum_{l \in i_s} -\tilde{\Sigma}^{-1}_{\mathrm{cr},ls} \cos(2\phi_{ls})\,, \tag{2.14}$$

$$S_{si} = \sum_{l \in i_s} -\tilde{\Sigma}^{-1}_{\mathrm{cr,ls}} \sin(2\phi_{ls})\,, \tag{2.15}$$

and

$$Z_{si} = \sum_{l \in i_s} \tilde{\Sigma}^{-2}_{\mathrm{cr},ls}\,. \tag{2.16}$$

Since each ϵ_{ks} is an independent estimate of the shear field, where k=1,2, the ESD covariance between radial bins i and j can then be easily written as:

$$\mathbf{Cov}_{ij} = \frac{\sum_s \sigma_\epsilon^2 w_s^2 \left(C_{si}C_{sj} + S_{si}S_{sj}\right)}{(\sum_s w_s Z_{si})(\sum_s w_s Z_{sj})}\,, \tag{2.17}$$

where $\sigma_\epsilon^2 = 0.078$ is the ellipticity dispersion weighted with the *lens*fit weight, for one component of the ellipticity. We compute this number from the whole KiDS-ESO-DR1/2 area.

Equation (2.17) can be generalised to also compute the covariance between the ESD estimates for two different lens samples m and n:

$$\mathbf{Cov}_{mnij} = \frac{\sum_s \sigma_\epsilon^2 w_s^2 \left(C_{si,m}C_{sj,n} + S_{si,m}S_{sj,n}\right)}{(\sum_s w_s Z_{si,m})(\sum_s w_s Z_{sj,n})}\,, \tag{2.18}$$

by restricting the sums for the C, S and Z terms to lenses in the relevant samples.

We test the accuracy of the above calculation, which doesn't account for cosmic variance, against the covariance matrix obtained via a bootstrapping technique. Specifically, we bootstrap the signal measured in each of the 1-square degree KiDS tiles. We limit the comparison to the case in which all groups are stacked together[7] and compute the signal in 10 logarithmically spaced radial bins between $20\,h^{-1}$kpc and $2\,h^{-1}$Mpc. This leads to an ESD covariance matrix with 55 independent entries, which can be constrained by the 100 KiDS tiles used in this analysis. The corresponding matrix is shown in Figure 2.5 together with the correlation matrix obtained from Equation 2.17. The small but significant correlation between the largest-radial bins is a consequence of the survey edges. We further show the diagonal errors obtained with the two methods, labelled Analytical and Bootstrap. Based on the work by Norberg et al. (2009), we might expect that the bootstrapping technique leads to somewhat larger error bars, although on larger scales this trend may be counteracted to some degree by the limited independence of our bootstrap regions. However, the conclusions of Norberg et al. (2009) are based on an analysis of galaxy clustering, and a quantitative translation of their results to our galaxy-galaxy lensing measurements is not easy and beyond the scope of this work. The difference between the error estimates using these two independent methods is at most 10% at scales larger than 300 h^{-1}kpc.

---

[7] If the signal is split further into several bins according to some property of the group, we expect the relative contribution from cosmic variance compared to the contribution from shape noise to be even lower.

Based on the results of this test, we consider the covariance matrix estimated from Equation 2.17 to be a fair estimation of the true covariance in the data, and we use it throughout the paper. In our likelihood analyses of various models for the data (see next section), we account for the covariance between the radial bins as well as between the different lens samples used to compute the stacked signal. We note that future analyses with greater statistical power, for example those based on the full KiDS and GAMA overlap, and studies focusing on larger scales than those considered in this analysis, will need to properly evaluate the full covariance matrix that incorporates the cosmic variance contribution that is negligible in this work.

2.4 Halo model

In this Section, we describe the halo model (e.g. Seljak 2000; Cooray and Sheth 2002), which we use to provide a physical interpretation of our data. We closely follow the methodology introduced in van den Bosch et al. (2013) and successfully applied to SDSS galaxy-galaxy lensing data in Cacciato et al. (2013).

This model provides the ideal framework to describe the statistical weak lensing signal around galaxy groups. It is based on two main assumptions:

1. a statistical description of dark matter halo properties (i.e. their average density profile, their abundance and their large scale bias);
2. a statistical description of the way galaxies with different observable properties populate dark matter haloes.

As weak gravitational lensing is sensitive to the mass distribution projected along the line-of-sight, the quantity of interest is the ESD profile, defined in Equation 2.3, which is related to the galaxy-matter cross correlation via Equation 2.2. Under the assumption that each galaxy group resides in a dark matter halo, its average $\Delta\Sigma(R, z)$ profile can be computed using a statistical description of how galaxies are distributed over dark matter haloes of different mass and how these haloes cluster. Specifically, it is fairly straightforward to obtain the two-point correlation function, $\xi_{\rm gm}(r, z)$, by Fourier transforming the galaxy-dark matter power-spectrum, $P_{\rm gm}(k, z)$, i.e.

$$\xi_{\rm gm}(r, z) = \frac{1}{2\pi^2} \int_0^\infty P_{\rm gm}(k, z) \frac{\sin(kr)}{kr}\, k^2 \, {\rm d}k \,, \tag{2.19}$$

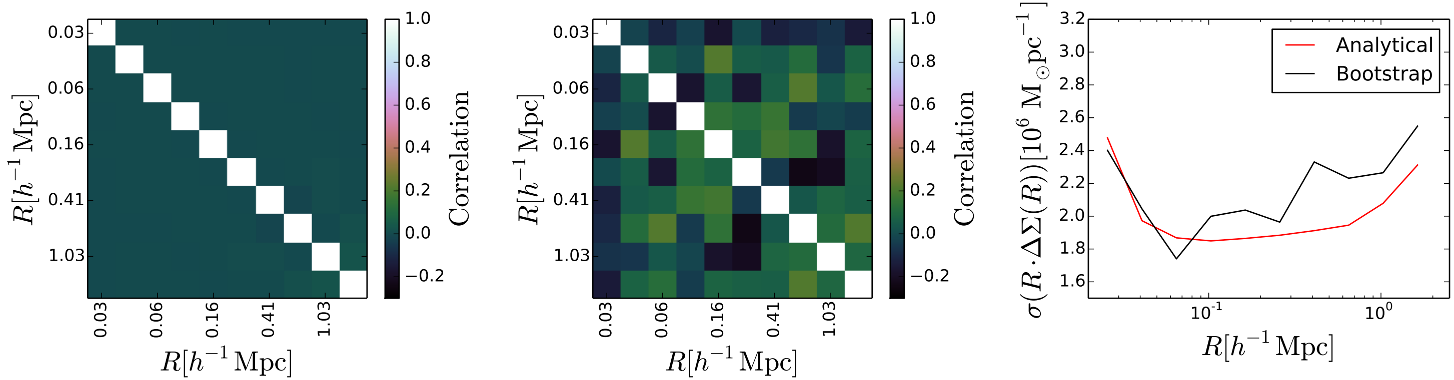

Figure 2.5: *Left panel:* ESD correlation matrix between different radial bins estimated from the data. This matrix accounts for shape noise and the effect of the mask and is computed as described in Section 2.3.4. *Middle panel:* ESD correlation matrix between different radial bins estimated using a bootstrap technique. It accounts for cosmic variance as well as shape noise. *Right panel:* Comparison of the square root of the diagonal elements of the two covariance matrices as a function of distance from the group centre (here the BCG). Note the lower noise in the left-hand panel and the small but significant correlation between the largest-radial bins, which is a consequence of the many survey edges.

with k the wavenumber, and the subscript ‘g’ and ‘m’ standing for ‘galaxy’ and ‘matter’.

In what follows, we will use the fact that, in Fourier space, the matter density profile of a halo of mass M at a redshift z can be described as $M\,\tilde{u}_{\rm h}(k|M,z)$, where $M \equiv 4\pi(200\bar{\rho})R_{200}^3/3$, and $\tilde{u}_{\rm h}(k|M)$ is the Fourier transform of the normalized *dark* matter density profile of a halo of mass M[8] We do not explicitly model the baryonic matter density profile (Fedeli 2014) because, on the scales of interest, its effect on the lensing signal can be approximated as that of a point mass (see Section 2.4.1). Because the lensing signal is measured by stacking galaxy groups with observable property $\mathcal{O}_{\rm grp}$, on scales smaller than the typical extent of a group, we have $P_{\rm gm}(k,z) = P^{\rm 1h}_{\rm grp\,m}(k,z)$, where

$$P^{\rm 1h}_{\rm grp\,m}(k,z) = \int \mathcal{P}(M|\mathcal{O}_{\rm grp})\,\mathcal{H}_{\rm m}(k,M,z)\,{\rm d}M\,, \tag{2.20}$$

and

$$\mathcal{H}_{\rm m}(k,M,z) \;\equiv\; \frac{M}{\bar{\rho}_{\rm m}}\,\tilde{u}_{\rm h}(k|M,z)\,, \tag{2.21}$$

with $\bar{\rho}_{\rm m}$ the co-moving matter density of the Universe. Throughout the paper, the subscript ‘grp’ stands for ‘galaxy group’.

The function $\mathcal{P}(M|\mathcal{O}_{\rm grp})$ is the probability that a group with observable property $\mathcal{O}_{\rm grp}$ resides in a halo of mass M. It reflects the halo occupation statistics and it can be written as:

$$\mathcal{P}(M|\mathcal{O}_{\rm grp}){\rm d}M = \mathcal{H}_{\rm grp}(M,z)\,n_{\rm h}(M,z)\,{\rm d}M\,. \tag{2.22}$$

Here, we have used

$$\mathcal{H}_{\rm grp}(M,z) \;\equiv\; \frac{\langle N\rangle_{\mathcal{O}_{\rm grp}}(M)}{\bar{n}_{\rm grp}(\mathcal{O}_{\rm grp},z)}\,, \tag{2.23}$$

where, $\langle N\rangle_{\mathcal{O}_{\rm grp}}(M)$ is the average number of groups with observable property $\mathcal{O}_{\rm grp}$ that reside in a halo of mass M.

Note that $n_{\rm h}(M,z)$ is the halo mass function (i.e. the number density of haloes as a function of their mass) and we use the analytical function suggested in Tinker et al. (2008) as a fit to a numerical N-body simulation.

---

[8] We use M_{200} masses for the groups throughout this paper, i.e. as defined by 200 times the mean density (and corresponding radius, noted as R_{200}).

Furthermore, the comoving number density of groups, $\bar{n}_{\rm grp}$, with the given observable property is defined as

$$\bar{n}_{\rm grp}(\mathcal{O}_{\rm grp}, z) = \int \langle N \rangle_{\mathcal{O}_{\rm grp}}(M)\, n_{\rm h}(M, z)\, {\rm d}M \, . \qquad (2.24)$$

Note that in the expressions above we have assumed that we can correctly identify the centre of the galaxy group halo (e.g., from the position of the galaxy identified as the central in the GAMA group catalogue). In Section 2.4.1, we generalize this expression to allow for possible *mis-centring* of the central galaxy.

Galaxy groups are not isolated, and on scales larger than the typical extent of a group, one expects a non-vanishing contribution to the power spectrum due to the presence of other haloes surrounding the group. This term is usually referred to as the two-halo term (as opposed to the one-halo term described in Equation 2.20). One thus has:

$$P_{\rm gm}(k) = P^{\rm 1h}_{\rm grp\, m}(k) + P^{\rm 2h}_{\rm grp\, m}(k) \, . \qquad (2.25)$$

These terms can be written in compact form as

$$P^{\rm 1h}_{\rm grp\, m}(k, z) = \int \mathcal{H}_{\rm grp}(k, M, z)\, \mathcal{H}_{\rm m}(k, M, z)\, n_{\rm h}(M, z)\, {\rm d}M, \qquad (2.26)$$

$$\begin{aligned} P^{\rm 2h}_{\rm grp\, m}(k, z) = & \int {\rm d}M_1\, \mathcal{H}_{\rm grp}(k, M_1, z)\, n_{\rm h}(M_1, z) \\ & \int {\rm d}M_2\, \mathcal{H}_{\rm m}(k, M_2, z)\, n_{\rm h}(M_2, z)\, Q(k|M_1, M_2, z) \, . \end{aligned} \qquad (2.27)$$

The quantity $Q(k|M_1, M_2, z)$ describes the power spectrum of haloes of mass M_1 and M_2. In its simplest implementation[9], used throughout this paper, $Q(k|M_1, M_2, z) \equiv b_{\rm h}(M_1, z) b_{\rm h}(M_2, z) P^{\rm lin}(k, z)$, where $b_{\rm h}(M, z)$ is the halo bias function and $P^{\rm lin}(k, z)$ is the linear matter-matter power spectrum. We note that, in the literature, there exist various fitting functions to describe the mass dependence of the halo bias (see for example Sheth et al. 2001; Sheth and Tormen 1999; Tinker et al. 2010). These functions may exhibit differences of up to $\sim 10\%$ (e.g. Murray et al. 2013). However, a few points are worth a comment.

---

[9] See, for example, van den Bosch et al. (2013) for a more refined description of this term.

First, the use of the fitting function from Tinker et al. (2010) is motivated by the use of a halo mass function calibrated over the same numerical simulation. Second, the halo bias function enters in the galaxy-matter power spectrum only through the two-halo term and as part of an integral. Thus, especially because we will fit the ESD profiles only up to $R = 2\,h^{-1}$Mpc, the uncertainty related to the halo bias function is much smaller than the statistical error associated to the observed signal.

2.4.1 Model specifics

The halo occupation statistics of galaxy groups are defined via the function $\langle N\rangle_{\mathcal{O}_{\rm grp}}(M)$, the average number of groups (with a given observable property $\mathcal{O}_{\rm grp}$, such as a luminosity bin) as a function of halo mass M. Since the occupation function of groups as a function of halo mass, $N_{\rm grp}(M)$, is either zero or unity, one has that $\langle N\rangle_{\mathcal{O}_{\rm grp}}(M)$ is by construction confined between zero and unity. We model $\langle N\rangle_{\mathcal{O}_{\rm grp}}(M)$ as a log-normal characterized by a mean, $\log[\tilde{M}/(\,h^{-1}{\rm M}_{\odot})]$, and a scatter $\sigma_{\log\tilde{M}}$:

$$\langle N\rangle_{\mathcal{O}_{\rm grp}}(M) \propto \frac{1}{\sqrt{2\pi}\,\sigma_{\log\tilde{M}}} \exp\left[-\frac{(\log M - \log\tilde{M})^2}{2\sigma^2_{\log\tilde{M}}}\right]. \tag{2.28}$$

We caution the reader against over-interpreting the physical meaning of this scatter; this number mainly serves the purpose of assigning a distribution of masses around a mean value.

Ideally, for each stack of the group ESD (in bins of group luminosity or total stellar mass) we wish to determine both these parameters, but to keep the number of fitting parameters low we assume here that $\sigma_{\log\tilde{M}}$ is constant from bin to bin, with a flat prior $0.05 \leqslant \sigma_{\log\tilde{M}} \leqslant 1.5$. This prior does not have any statistical effect on the results and it only serves the purpose of avoiding numerical inaccuracies. There is evidence for an increase in this parameter with central galaxy luminosity or stellar mass, (e.g. More et al. 2009a,b, 2011), but these increases are mild, and satellite kinematics (e.g. More et al. 2011) support the assumption that $\sigma_{\log\tilde{M}}$ is roughly constant on massive group scales (i.e. $\log[M/(\,h^{-1}{\rm M}_{\odot})] > 13.0$). We have verified that our assumption has no impact on our results in terms of either accuracy or precision by allowing $\sigma_{\log\tilde{M}}$ to be different in each observable bin.

For each given bin in an observable group property, one can define an effective mean halo mass, $\langle M \rangle$, as

$$\begin{aligned}\langle M \rangle_{\mathcal{O}_{\rm grp}} &\equiv \int \mathcal{P}(M|\mathcal{O}_{\rm grp})\, M \,{\rm d}M \\ &= \frac{\int \langle N \rangle_{\mathcal{O}_{\rm grp}}(M)\, n_h(M,\bar{z}) M {\rm d}M}{\bar{n}_{\rm grp}(\mathcal{O}_{\rm grp},\bar{z})}\,, \end{aligned} \qquad (2.29)$$

where $\bar{z}$ is the mean redshift of the groups in the bin under consideration, and we have made use of Equation (2.22) and (2.24). The effective mean halo mass, $\langle M \rangle_{\mathcal{O}_{\rm grp}}$, is therefore obtained as a weighted average where the weight is the multiplication of the halo occupation statistics and the halo mass function.

The dark matter density profile of a halo of mass M, $\rho_{\rm m}(r|M)$, is assumed to follow a NFW functional form:

$$\rho_{\rm m}(r|M) = \frac{\overline{\delta}\,\overline{\rho}}{(r/r_s)(1+r/r_s)^2}\,, \qquad (2.30)$$

where r_s is the scale radius and $\overline{\delta}$ is a dimensionless amplitude which can be expressed in terms of the halo concentration parameter $c_{\rm m} \equiv R_{200}/r_s$ as

$$\overline{\delta} = \frac{200}{3}\,\frac{c_{\rm m}^3}{\ln(1+c_{\rm m}) - c_{\rm m}/(1+c_{\rm m})}\,, \qquad (2.31)$$

where the concentration parameter, $c_{\rm m}$, scales with halo mass. Different studies in the literature have proposed somewhat different fitting functions (e.g. Bullock et al. 2001; Eke et al. 2001; Macciò et al. 2008; Duffy et al. 2008; Klypin et al. 2011; Prada et al. 2012; Dutton and Macciò 2014) to describe the relation $c_{\rm m}(M,z)$. Overall, these studies are in broad agreement but unfortunately have not converged to a robust unique prediction. Given that those fitting functions have been calibrated using numerical simulations with very different configurations (most notably different mass resolutions and cosmologies), it remains unclear how to properly account for the above mentioned discrepancies. As these fitting functions all predict a weak mass dependence, we decide to adopt an effective concentration-halo mass relation that has the mass and redshift dependence proposed in Duffy et al. (2008) but with a rescalable normalization:

$$\begin{aligned} c_{\rm m}^{\rm eff}(M_{200},z) &= f_{\rm c} \times c_{\rm m}^{\rm Duffy}(M_{200},z) \\ &= f_{\rm c} \times 10.14 \left(\tfrac{M_{200}}{2\times10^{12}}\right)^{-0.081} (1+z)^{-1.01} \quad . \end{aligned} \qquad (2.32)$$

Note that at $z = 0.25$, one has $c_{\mathrm{m}}^{\mathrm{Duffy}} \approx 5$ for halo masses with $\log[M/(h^{-1}\mathrm{M}_{\odot})] \approx 14.3$. We leave f_{c} free to vary within a flat uninformative prior $0.2 \leqslant f_{\mathrm{c}} \leqslant 5$.

The innermost part of a halo is arguably the site where a 'central' galaxy resides. The baryons that constitute the galaxy may be distributed according to different profiles depending on the physical state (for example, exponential discs for stars and β-profiles for hot gas, see Fedeli 2014). The lensing signal due to these different configurations could in principle be modelled to a certain level of sophistication (see Kobayashi et al. 2015). However, at the smallest scales of interest here[10], those distributions might as well be accounted for by simply assuming a point mass, M_{P}. In the interest of simplicity, we assume that the stellar mass of the brightest cluster galaxy ($M_{\star}^{\mathrm{BCG}}$; Taylor et al. 2011a) is a reliable proxy for the amount of mass in the innermost part of the halo. Specifically, we assume that

$$M_{\mathrm{P}} = A_{\mathrm{P}} M_{\star}^{\mathrm{BCG}} \,, \tag{2.33}$$

where A_{P} is a free parameter, within a flat prior between 0.5 and 5.

The adopted definition of centre may well differ from the true minimum of the gravitational potential well. Such a mis-centring of the 'central' galaxy is in fact seen in galaxy groups (see e.g. Skibba and Macciò 2011 and references therein). George et al. (2012) offer further independent support of such a mis-centring, finding that massive central galaxies trace the centre of mass to less than 75 kpc/h.

We model this mis-centring in a statistical manner (see also Oguri and Takada 2011, Miyatake et al. 2013, More et al. 2014 and references therein). Specifically, we assume that the degree of mis-centring of the groups in three dimensions, $\Delta(M, z)$, is proportional to the halo scale radius r_s, a function of halo mass and redshift, and parametrize the probability that a 'central' galaxy is mis-centred as p_{off}. This gives

$$\mathcal{H}_{\mathrm{grp}}(k, M, \bar{z}) = \frac{\langle N \rangle_{\mathcal{O}_{\mathrm{grp}}}(M)}{\bar{n}_{\mathrm{grp}}(\bar{z})} \left(1 - p_{\mathrm{off}} + p_{\mathrm{off}} \times \mathrm{e}^{[-0.5 k^2 (r_s \mathcal{R}_{\mathrm{off}})^2]}\right) . \tag{2.34}$$

Setting either p_{off} or $\mathcal{R}_{\mathrm{off}}$ to zero implies that there is *de facto* no offset. We treat the two as free parameters in Section 2.5. The parameter p_{off}, being a probability, is bound between zero and unity. We apply a flat uniform prior to $\mathcal{R}_{\mathrm{off}} \in [0, 1.5]$. We note that this prior is very conservative, as according

---

[10] We fit the data in the range $0.02 < R/(h^{-1}\mathrm{Mpc}) < 2.0$

to George et al. (2012) and Skibba and Macciò (2011) the mis-centring is expected to be smaller than the scale radius of a group, for which $\mathcal{R}_{\mathrm{off}} = 1$.

In summary, the model parameter vector, is defined as $\lambda = (\log\widetilde{M}_i, \sigma_{\log\widetilde{M}}, f_{\mathrm{c}}, A_{\mathrm{P}}, p_{\mathrm{off}}, \mathcal{D}\mathrm{off})$ where $i = 1 ... N_{\mathrm{bins}}$. Throughout the paper, we bin group observable properties in 6 bins. This leads to a 11 parameter model. We use Bayesian inference techniques to determine the posterior probability distribution $P(\lambda|\mathcal{D})$ of the model parameters given the data, $\mathcal{D}$. According to Bayes' theorem,

$$P(\lambda|\mathcal{D}) \propto P(\mathcal{D}|\lambda)\, P(\lambda) \propto \exp\left[\frac{-\chi^2(\lambda)}{2}\right] P(\lambda)\,, \tag{2.35}$$

where $P(\mathrm{D}|\lambda)$ is the likelihood of the data given the model parameters, assumed to be Gaussian, and $P(\lambda)$ is the prior probability of these parameters. Here,

$$\chi^2(\lambda) = [\widetilde{\Delta\Sigma}_{k,j} - \Delta\Sigma_{k,j}]^T (\mathbf{C}^{-1})_{kk',jj'} [\widetilde{\Delta\Sigma}_{k',j'} - \Delta\Sigma_{k',j'}]\,, \tag{2.36}$$

where $\Delta\Sigma_{k,j}$ is the j'th radial bin of the observed stacked ESD for the groups in bin k, and $\widetilde{\Delta\Sigma}_{k,j}$ is the corresponding model prediction. **C** is the full covariance matrix for the measurements, computed as detailed in Section 2.3.4.

We sample the posterior distribution of our model parameters given the data using a Markov Chain Monte-Carlo (MCMC). In particular, we use[11] a proposal distribution that is a multi-variate Gaussian whose covariance is computed via a Fisher analysis run during the burn-in phase of the chain, set to 5000 model evaluations.

2.5 Density profile of galaxy groups

We measure the ESD signal around each GAMA group with at least 5 members in 10 logarithmically-spaced radial bins in the range 20 h^{-1}kpc to 2 h^{-1}Mpc. We first assign errors to those measurements by propagating the shape noise on the tangential shear measurement in each radial bin. We divide the groups into 6 bins according to a given observable property, such as their velocity dispersion, total r-band luminosity, apparent richness or r-band luminosity fraction of the BCG. Bin limits are chosen to make the

---

[11] A python implementation of this sampling method is available via the MontePython code thanks to the contribution by Surhud More.

signal-to-noise of the ESD roughly the same in each bin. Once the bin limits are defined, we compute the data covariance between radial bins and between group bins as outlined in Section 2.3.4. We summarise the bin-limits, the number of groups in each bin, the mean redshift of the bin and the mean stellar mass of the BCG in Table 2.2 for the four observables considered in this work.

The typical signal-to-noise ratio in each of the 6 luminosity bins is of order $\sim 20-25$. This is comparable to the signal-to-noise ratio reported by Sheldon et al. (2009) for a weak lensing analysis of $\sim 130\,000$ MaxBCG clusters using SDSS imaging, once we restrict the comparison to a similar luminosity range.

We jointly fit the signal in the 6 bins using the halo model described in Section 2.4. Since GAMA is a flux limited survey, the redshift distributions of the groups in the six luminosity bins are different, as shown in Figure 2.6. When we fit the halo model to the data, we calculate the power spectra and mass function (Equations 2.20-2.27) using the median of the redshift distribution in each bin.

For each observable property, we run 5 independent chains with different initial conditions. We evaluate the convergence of the MCMC by means of a Gelman Rubin test (Gelman and Rubin 1992), and we impose $\mathrm{R} < 1.03$, where the R-metric is defined as the ratio of the variance of a parameter in the single chains to the variance of that parameter in an "*über-chain*", obtained by combining 5 chains.

2.5.1 Matter density profiles of group-scale haloes

We first test whether the ESD measurements themselves support the halo model assumption that the group density profile can be described in terms of a mis-centred NFW profile with a contribution from a point-mass at small scales, and what constraints can be put on the model parameters. In the interest of being concise, we only present the results derived by binning the groups according to their total r-band luminosity (see Section 2.3), as statistically equivalent results are obtained when the groups are binned according to their velocity dispersion, apparent richness or r-band luminosity fraction of the BCG. The binning by other observables will become important in the study of scaling relation presented in Section 2.6.

One needs to define the centre of the halo before stacking the ESD profiles of the groups. Following R11, we have three choices for the group centre: the centre of light (`Cen`), the Brightest Cluster Galaxy (`BCG`) and the brightest galaxy left after iteratively removing the most distant galaxies

Table 2.2: Summary of the bin limits used to compute the stacked ESD signal, the number of groups in each bin, the mean redshift of the groups in each bin and the mean stellar mass of the BCG.

`Observable`	`Bin limits`	`Number of lenses`	`Mean redshift`	$\log(\langle M_\star^{BCG}[h^{-2}\mathrm{M}_\odot]\rangle)$
$\log[\mathrm{L}_{\mathrm{grp}}/(h^{-2}\mathrm{L}_\odot)]$	$(9.4, 10.9, 11.1, 11.3, 11.5, 11.7, 12.7)$	$(540, 259, 178, 233, 142, 66)$	$(0.13, 0.20, 0.23, 0.26, 0.30, 0.35)$	$(11.00, 11.23, 11.29, 11.37, 11.47, 11.70)$
$\sigma/(\mathrm{s}^{-1}\mathrm{km})$	$(0, 225, 325, 375, 466, 610, 1500)$	$(501, 359, 124, 198, 147, 89)$	$(0.15, 0.19, 0.21, 0.23, 0.26, 0.31)$	$(11.05, 11.20, 11.30, 11.36, 11.41, 11.64)$
$\mathrm{N}_{\mathrm{fof}}$	$(5, 6, 7, 8, 11, 19, 73)$	$(481, 261, 170, 239, 181, 86)$	$(0.21, 0.21, 0.21, 0.19, 0.18, 0.16)$	$(11.17, 11.23, 11.29, 11.29, 11.35, 11.45)$
$\mathrm{L}_{\mathrm{BCG}}/\mathrm{L}_{\mathrm{grp}}$	$(1.0, 0.35, 0.25, 0.18, 0.13, 0.08, 0)$	$(346, 252, 296, 227, 200, 97)$	$(0.10, 0.16, 0.20, 0.25, 0.29, 0.34)$	$(11.16, 11.19, 11.22, 11.29, 11.36, 11.53)$

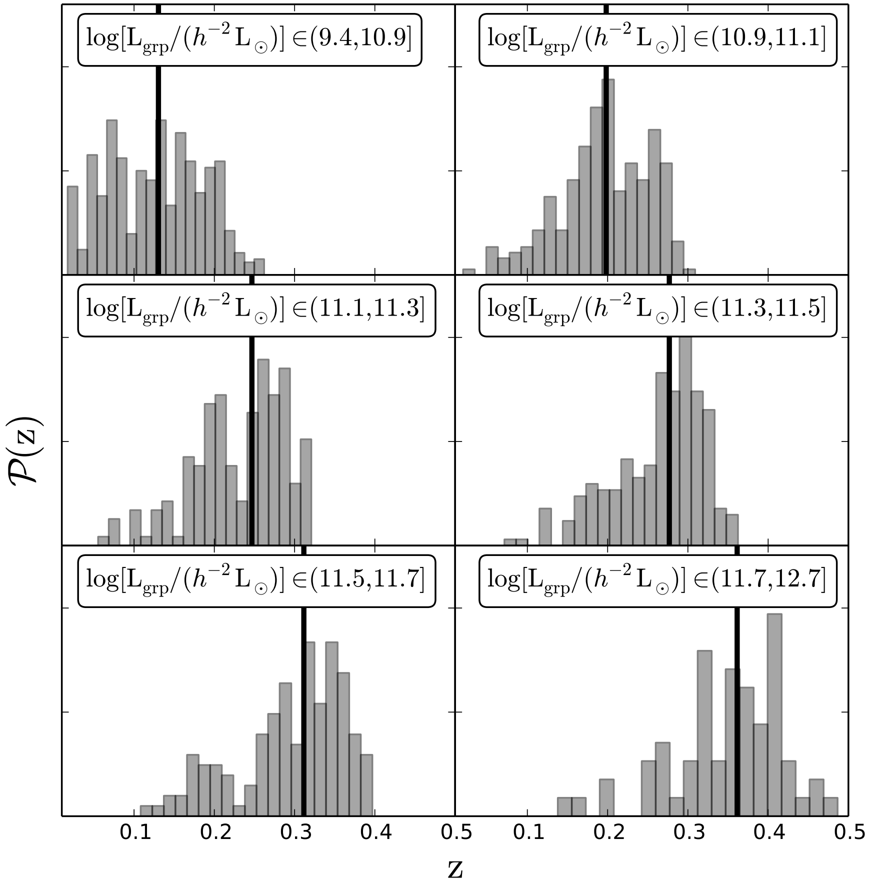

Figure 2.6: Redshift distributions of the GAMA groups used in this paper in the six r-band luminosity bins. The group luminosity increases from left to right and from top to bottom. The solid vertical black lines indicate the median of the distributions.

from the group centre of light (`IterCen`). Throughout the paper, unless stated otherwise, we use the `BCG` as the definition of the centre, as it is a common choice in the literature. We investigate the effect of using the other two definitions of the group centre in Section 2.5.1 and in Appendix A.

Figure 2.7 shows the stacked ESD profiles (green points with error bars) for the 6 bins in total r-band luminosity. Note that the error bars are the square root of the diagonal elements of the full covariance matrix, and we use dashed bars in the case of negative values of the ESD. The ESD profiles have high signal-to-noise throughout the range in total luminosity and in spatial scales. Red lines indicate the best-fit model, whereas orange and yellow bands indicate the 68 and 95% confidence interval. The model describes the data well with a reduced $\chi^2_{\mathrm{red}} = 1.10$, 49 d.o.f, over the full scale range, for all the luminosity bins. This justifies our assumption that the ESD profile can be accurately modelled as a weighted stack of mis-centred NFW density profiles with a contribution from a point mass at the centre.

The main results of this analysis can be summarised as follows (68% percent confidence limits quoted throughout):

- For each r-band luminosity bin, we derive the probability that a group with that luminosity resides in a halo of mass M (see Equation 2.22). We show the median of the probability distribution for the 6 bins in Figure 2.8. We constrain the scatter in the mass at a fixed total r-band luminosity to be $\sigma_{\log\tilde{\mathrm{M}}} = 0.74^{+0.09}_{-0.16}$. This sets the width of the log-normal distribution describing the halo occupation statistics. We remind the reader that $\sigma_{\log\tilde{\mathrm{M}}}$ is the width of the distribution in halo masses at given total luminosity of the groups and it is *not* the scatter in luminosity (or stellar mass) at a fixed halo mass that is often quoted in the literature and that one would expect to be considerably smaller (e.g. Yang et al. 2009; Cacciato et al. 2009; More et al. 2011; Leauthaud et al. 2012b). This hampers the possibility of a one-to-one comparison with most studies in the literature. However, we note that van den Bosch et al. (2007) and More et al. (2011) reported values of the scatter in halo mass at fixed luminosity that are as high as 0.7 at the bright end. Furthermore, More et al. (2015) reported a value of $0.79^{+0.41}_{-0.39}$ for the width of the low mass end distribution of the halo occupation statistics of massive CMASS galaxies. Given the non-negligible differences between the actual role of this parameter in all these studies, we find this level of agreement satisfactory.

- For each luminosity bin, a mean halo mass is inferred with a typical uncertainty on the mean of $\sim$ 0.12 dex.

- The relative normalisation of the concentration-halo mass relation (see Equation 2.32) is constrained to be $f_{\mathrm{c}} = 0.84^{+0.42}_{-0.23}$, in agreement with the nominal value based on Duffy et al. (2008).

- The probability of having an off-centred BCG is $\mathrm{p}_{\mathrm{off}} < 0.97$ (2-sigma upper limit), whereas the average amount of mis-centring in terms of the halo scale radius, $\mathcal{R}_{\mathrm{off}}$, is unconstrained within the prior.

- The amount of mass at the centre of the stack which contributes as a

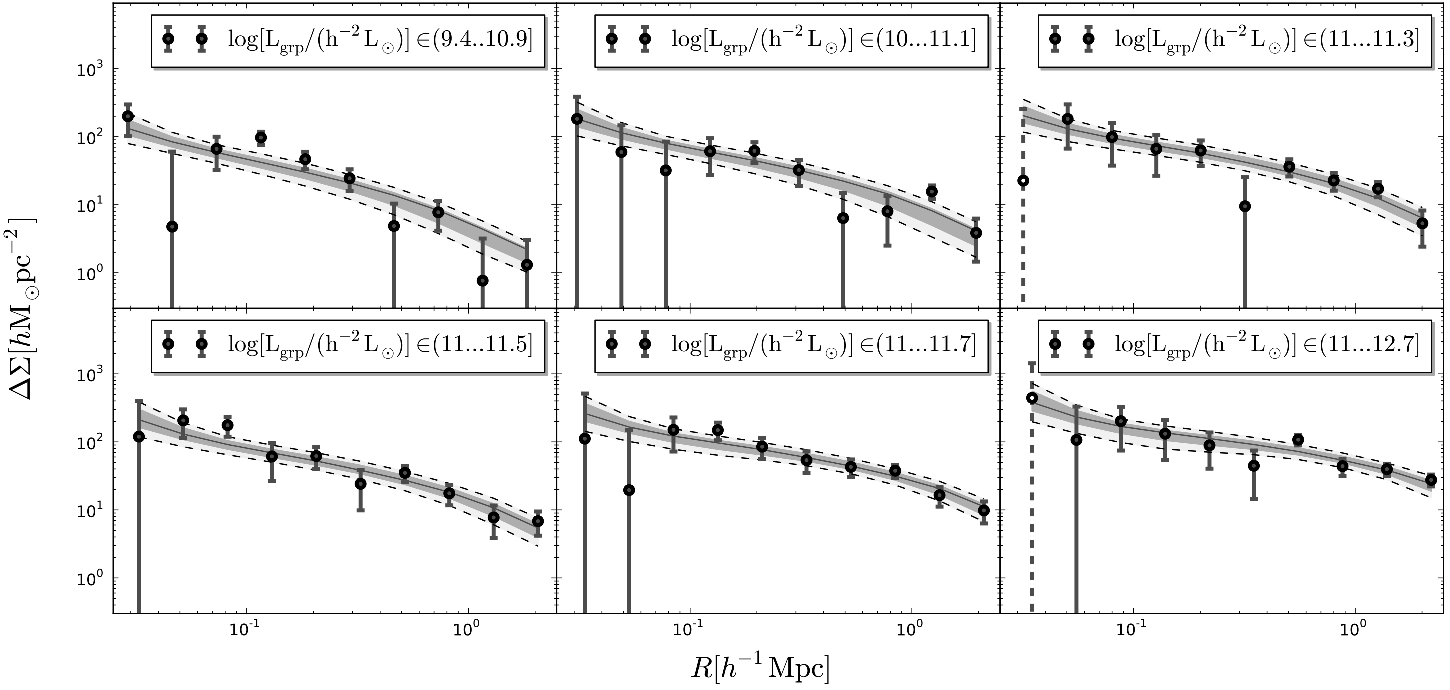

Figure 2.7: Stacked ESD profile measured around the groups BCG of the 6 group luminosity bins as a function of distance from the group centre. The group r-band luminosity increases from left to right and from top to bottom. The stacking of the signal has been done using only groups with $\mathrm{N}_{\mathrm{fof}} \geqslant 5$. The error bars on the stacked signal are computed as detailed in section 2.3.4 and we use dashed bars in the case of negative values of the ESD. The grey bands represent the 68 and 95 percentile of the model around the median, while the dark line shows the best fit model.

point mass to the ESD profiles is constrained to be $M_{\rm PM} = {\rm A}_{\rm PM} \langle M_\star^{BCG} \rangle = 2.06^{+1.19}_{-0.99} \langle M_\star^{BCG} \rangle$.

Figure 2.9 shows the posterior distributions of the halo model parameters and their mutual degeneracies. Table 2.3 and 2.4 list the median values of the parameters of interest with errors derived from the 16th and 84th percentiles of the posterior distribution. We discuss the constraints on the model parameters in further detail in the remainder of this section.

Masses of dark matter haloes

The dark matter halo masses of the galaxy groups that host the stacked galaxy groups analysed in this work span one and a half orders of magnitude with $M \in [10^{13}..10^{14.5}]\, h^{-1}{\rm M}_\odot$. Since our ESD profiles extend to large radii, our $2\, h^{-1}{\rm Mpc}$ cut-off is larger than R_{200} over this full mass range, these mass measurements are robust and direct as they do not require any extrapolation. The uncertainties on the masses are obtained after marginalising over the other model parameters. Typically these errors are 15% larger than what would be derived by fitting an NFW profile to the same data, ignoring the scatter in mass inside each luminosity bins. Note that a simple NFW fit to the data in the 6 luminosity bins, with fixed concentration (Duffy et al. 2008) would also lead to a bias in the inferred masses of approximately 25%.

The inferred halo masses in each luminosity bin are slightly correlated due to the assumption that the scatter in halo mass is constant in different bins of total luminosity. We compute the correlation between the inferred halo masses from their posterior distribution, and we show the results in Figure 2.10. Overall, the correlation is at most 20%, and this is accounted for when deriving scaling relations (see Section 2.6).

Concentration and mis-centring

The shape of the ESD profile at scales smaller than $\sim 200\, h^{-1}{\rm kpc}$ contains information on the concentration of the halo and on the mis-centring of the BCG with respect to the true halo centre. However, the relative normalisation of the concentration-halo mass relation, $f_{\rm c}$, and the two mis-centring parameters, ${\rm p}_{\rm off}$ and $\mathcal{R}_{\rm off}$ are degenerate with each other. A small value of $f_{\rm c}$ has a similar effect on the stacked ESD as a large offset: both flatten the profile. To further illustrate this degeneracy, we show in Figure 2.11 the 2D posterior distribution of the average projected offset (${\rm p}_{\rm off} \times \mathcal{R}_{\rm off}$) and

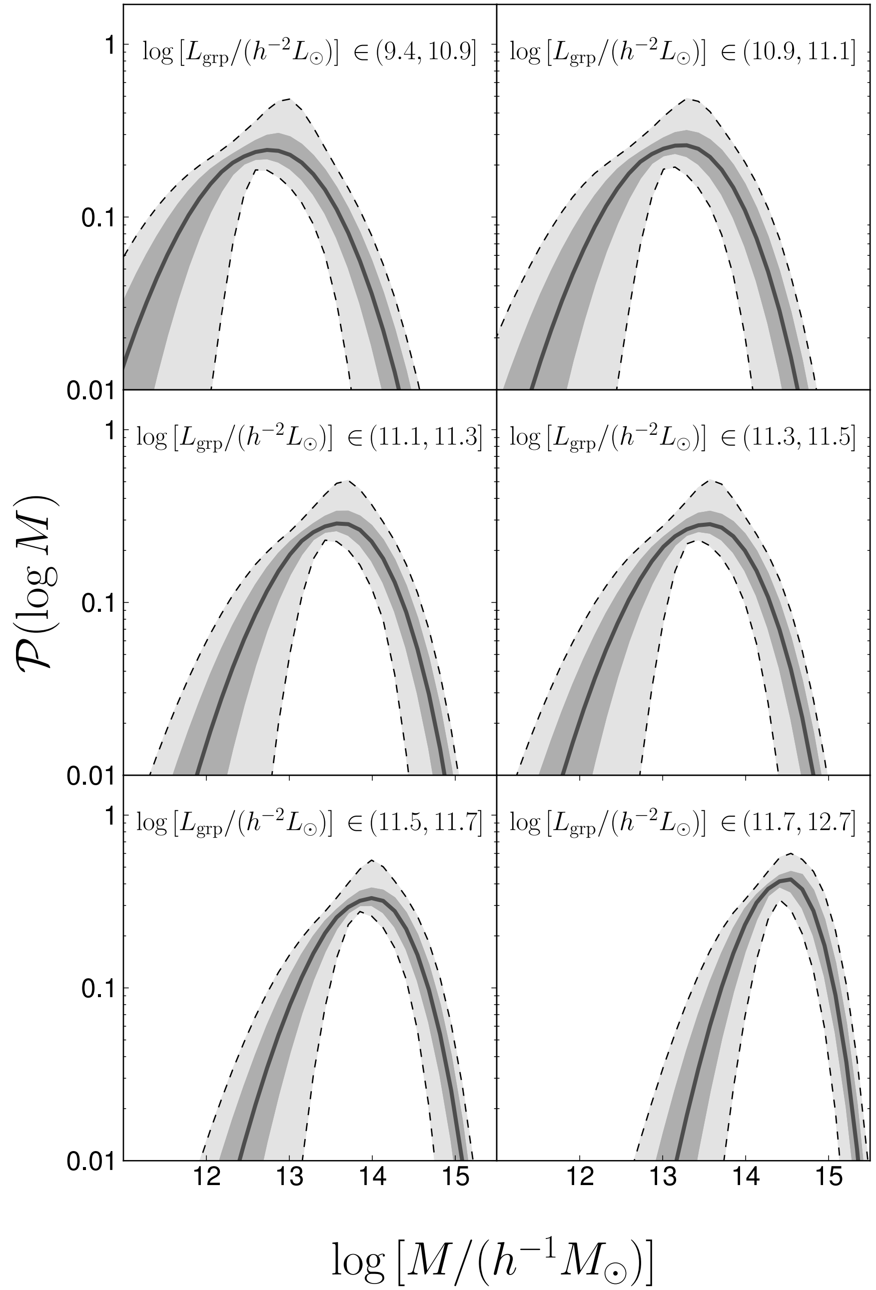

Figure 2.8: Probability that a group with a given r-band luminosity resides in a halo of mass M. The lines show the median distribution, while the grey contours show the 68 and 95 percentile around the median.

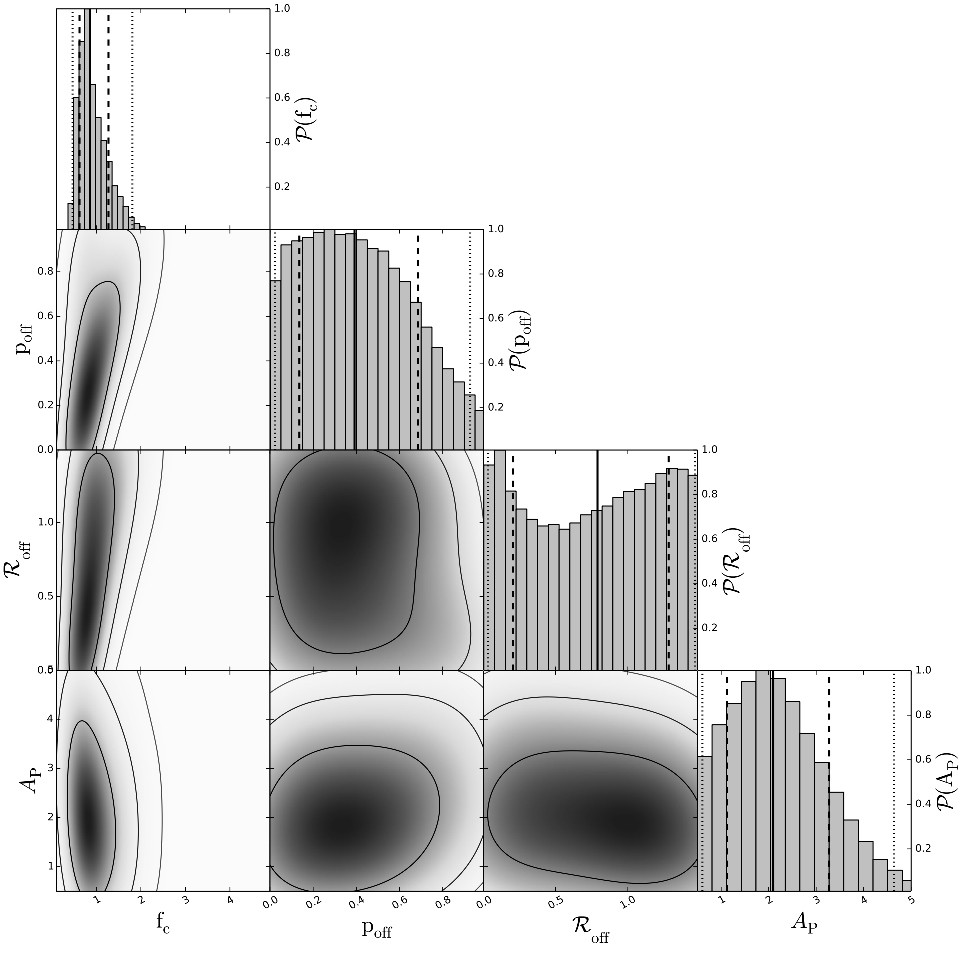

Figure 2.9: Posterior distribution of the normalisation of the mass-concentration relation f_c, of the mis-centring parameters $\mathrm{p_{off}}$ and $\mathcal{R}_{\mathrm{off}}$ and of the amplitude of the point mass $\mathrm{A_P}$. The contours indicate the 1, 2, 3 sigma confidence regions. The dashed vertical lines and the dotted vertical lines correspond respectively to the 1 and 2 sigma marginalised confidence limits. These are the constraints from a joint halo model fit of the ESD signal in the 6 luminosity bins using `BCG` as the group centre. The range in each panels reflect the priors used for the different parameters.

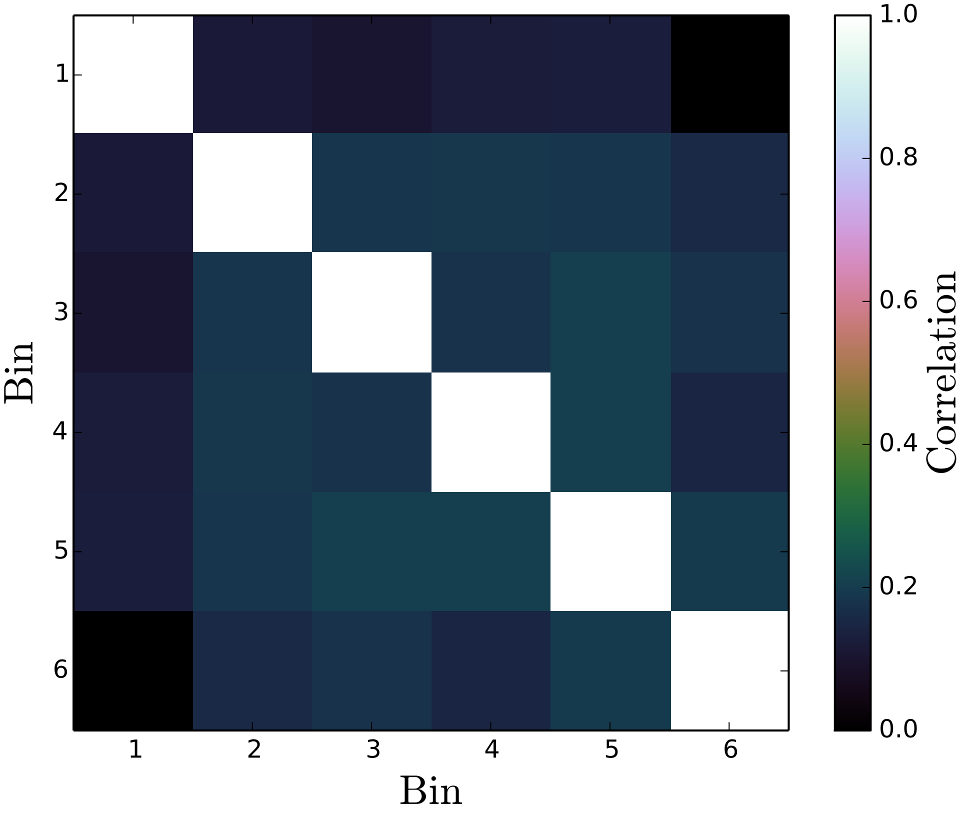

Figure 2.10: Correlation matrix between the mean halo masses derived in the six r-band luminosity bins from the halo model fit. The reason for the correlation is the assumption of a constant scatter as a function of group luminosity in the halo occupation distribution.

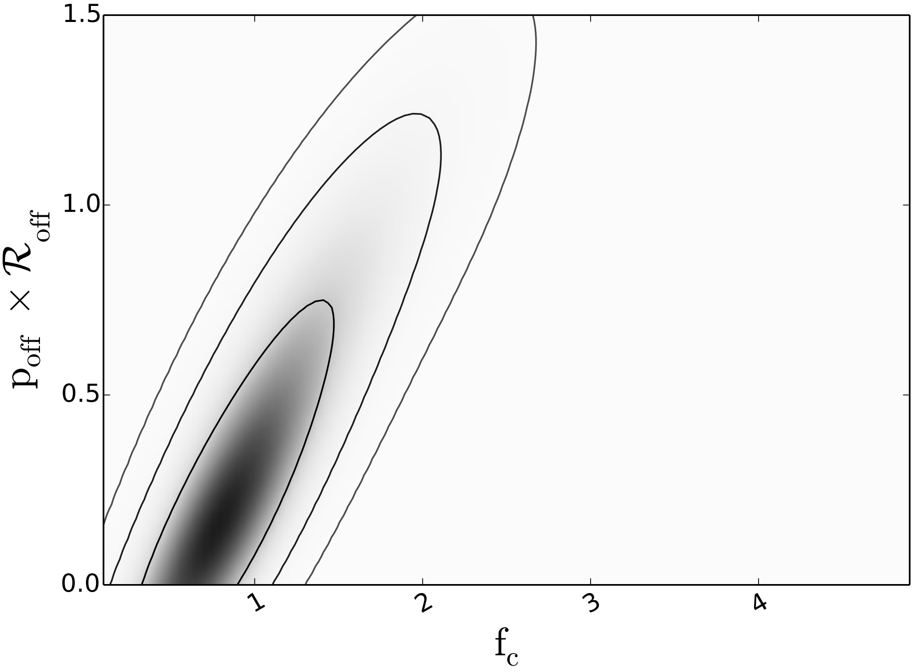

Figure 2.11: 2D posterior distribution of the average projected offset ($\mathrm{p_{off}} \times \mathcal{R}_{\mathrm{off}}$) and the normalisation of the concentration-halo mass relation f_{c}. The contours indicate the 68%, 95% and 99% confidence region.

the normalisation of the concentration-halo mass relation. It is clear how a vanishing offset would require a low value of the concentration.

The derived constraints on the average projected BCG offset are quite loose: $\mathrm{p_{off}} \times \mathcal{R}_{\mathrm{off}} < 1.10\,\mathrm{r_s}$ (2-sigma). Hence one might argue in favour of a simpler model or a model with a less informative prior on $\mathcal{R}_{\mathrm{off}}$. We address both aspects in the following ways. First, we run a version of the halo model on the same 6 luminosity bins in which we assume no mis-centring (i.e. we assume that the BCG is always at the centre of the dark matter halo). We find a similar value of the reduced chi-squared ($\chi^2_{\mathrm{red}} = 1.04$, 51 d.o.f.), comparable values for the 6 masses (always within one sigma) but tighter constraints for the relative normalisation of the concentration-halo mass relation, $f_{\mathrm{c}} = 0.59^{+0.13}_{-0.11}$. This is perhaps not entirely surprising given that in this case f_{c} is not degenerate with any other model parameter. Second, we relax the prior for $\mathcal{R}_{\mathrm{off}}$ from $0 \leq \mathcal{R}_{\mathrm{off}} \leq 1.5$ to $0 \leq \mathcal{R}_{\mathrm{off}} \leq 5$. Also in this case, we find statistically equivalent halo masses and similar constraints on

$\mathrm{p_{off}}$, $\mathcal{R}_{\mathrm{off}}$, and f_{c} as in the fiducial case. We summarise the results of these tests in Figure 2.12. We conclude that the fact that the reduced χ^2 values for the three model-configurations are very similar and always larger than unity suggests that the 11-parameter model is not too complex given the signal-to-noise of the data. Ignoring the mis-centring in the model lowers the relative normalisation of the concentration-halo mass relation to a 3-sigma deviation from the nominal value of Duffy et al. (2008). However, we caution the reader against over-interpreting this result as our test shows that this is probably driven by the very strong prior on the location of the BCGs rather than actually being a physical property of the stacked haloes.

Lower values of the normalisation of the concentration-halo mass relation from weak lensing analysis have been previously reported. For example, Mandelbaum et al. (2008) studied a sample of LRGs and MaxBCG clusters from SDSS and reported a 2-sigma deviation of the normalisation of the mass-concentration relation with respect to the simulation predictions. In this case, the lenses were assumed to be the true centre of the dark matter halo, and the analysis limited to scales larger than 0.5 $h^{-1}\mathrm{Mpc}$ to limit the impact of mis-centring. From a weak lensing and clustering analysis of SDSS-III CMASS galaxies, Miyatake et al. (2013) also found a lower normalisation if mis-centring of the lenses is not included in the model but report agreement with the theoretical predictions once the mis-centring is included. A similar conclusion was derived by van Uitert et al. (2015) from a lensing analysis of LOWZ and CMASS LRGs from the Baryon Oscillation Spectroscopic Survey (BOSS) SDSS-DR10 using imaging data from the second Red-sequence Cluster Survey (RCS2). In an analysis of the CFHT Stripe 82 Survey for haloes of masses around $10^{14}\mathrm{M}_{\odot}$, Shan et al. (2015) also reported a nominal value of the normalisation of the concentration-halo mass relation lower than the Duffy et al. (2008) prediction, but the discrepancy between observations and predictions from numerical simulations was not statistically significant.

Possible explanations for a lower normalisation of the concentration-halo mass relation might include halo-triaxiality, which we do not account for in our model, substructures inside the main halo (Giocoli et al. 2012), galaxy formation related processes which can make halo density profiles shallower by expelling baryons into the outer region of the halo (Sales et al. 2010, van Daalen et al. 2011) and the assumed cosmological model. In fact, the value of the concentration at a given redshift, as a measure of the formation time of haloes, depends on the background cosmology. To address this last point, we run the halo model assuming two alternative cosmologies:

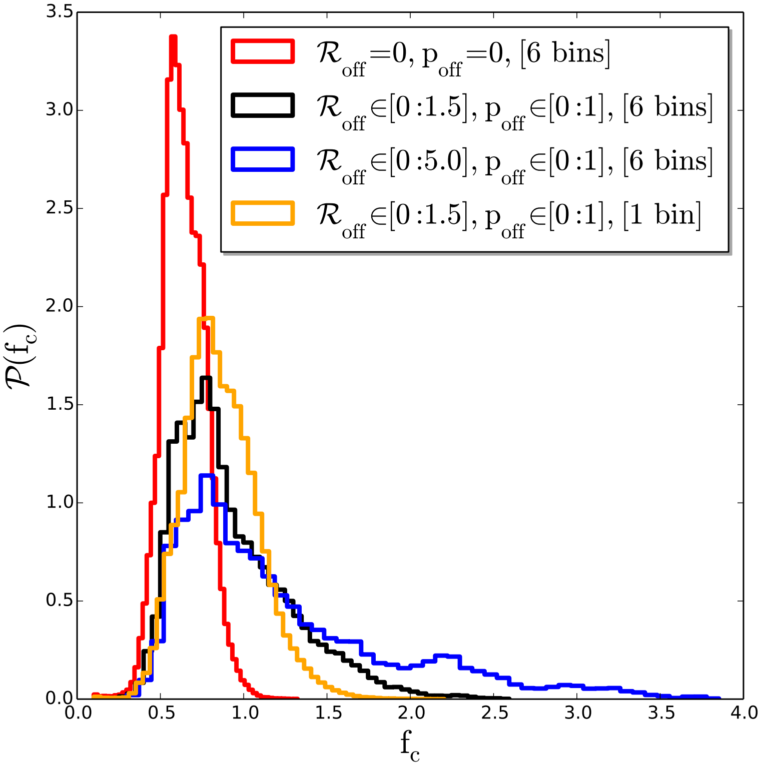

Figure 2.12: Posterior distribution for the normalisation of the mass-concentration relation (Duffy et al. 2008) after marginalising over the other model parameters. We show here the effect of changing the prior in the mis-centring parameters: $\mathcal{R}_{\rm off} = 0$ (red line), $\mathcal{R}_{\rm off} \in [0..1.5]r_s$ (black line) and $\mathcal{R}_{\rm off} \in [0..5]r_s$ (blue line). As a reference, the orange line shows the posterior distribution for f_c in the case of a global stack of all groups. This has to be compared with the black line, where the constraints were derived from a joint fit of the stacked ESD in 6 luminosity bins.

a slight deviation from the nominal Planck result $(\Omega_m, \sigma_8, h, n_s, \Omega_b h^2) = (0.302, 0.818, 0.68, 0.9686, 0.02197)$ (Spergel et al. 2015), and the best fit result of a clustering and lensing analysis on SDSS data $(\Omega_m, \sigma_8, h, n_s, \Omega_b h^2) = (0.278, 0.763, 0.739, 0.978, 0.02279)$ (Cacciato et al. 2013), which we regard as an extreme change in light of the recent Planck results. We do not find any difference in the posterior distributions of any model parameters, in particular on $f_{\rm c}$. We hence conclude that our results are not affected by the assumed cosmology.

Point mass: the innermost part of the halo

Measurements of the ESD profile at scales smaller than $\sim 50\ h^{-1}{\rm kpc}$ constrain the amount of mass at the centre of the halo. We model this as a simple point mass. The measured amplitude of the point mass is not degenerate with any of the other halo model parameters, demonstrating that, given the quality of the data, the details of the distribution of the baryons at the very centre of the haloes are not relevant to infer global properties of the dark matter halo, such as their masses or concentrations.

Other definitions of the group centre

Finally, we repeat the analysis using two alternative definitions of the group centre in the GAMA catalogue: the centre of light (`Cen`) and the brighter galaxy left after iteratively removing the most distant galaxy from the group centre of light (`IterCen`). We present the results in Appendix A, Table 2.3 and 2.4. We do not find any significant difference in the ESD profile when using `IterCen` instead of the `BCG`. However, the profile is very different when we use `Cen`. In this case, we find tight constraints on the probability of the centre of light of not being the centre of the dark matter halo with $\rm p_{off} \geqslant 0.67$ at 2-sigma and we find that on average the amount of mis-centring of the centre of light with respect to the minimum of the halo potential well is $\mathcal{R}_{\rm off} = 1.00^{+0.37}_{-0.51}$. The constraints on the halo masses in the 6 luminosity bins, as well as the constraints on $\sigma_{\rm log\tilde{M}}$, $f_{\rm c}$, and $\rm A_P$, are however consistent within 1-sigma with those calculated using the BCG position.

In summary, our results highlight the importance of a proper model for the mis-centring in the analysis of the ESD signal from groups or clusters of galaxies. Neglecting it could lead to biases in the derived parameters, particularly the normalisation of the concentration-mass relation.

Table 2.3: Constraints on the average halo mass in each r-band luminosity bin using the three definitions of halo centre. We quote here the median of the mass posterior distribution, marginalised over the other halo model parameters, and the errors are the 16th and 84th percentile of the distribution. All of the constraints derived using the three different proxies for the halo centre agree within 1-sigma.

`Centre`	$\log[\mathrm{M}_{200}^{(1)}/(\mathrm{h}^{-1}\mathrm{M}_{\odot})]$	$\log[\mathrm{M}_{200}^{(2)}/(\mathrm{h}^{-1}\mathrm{M}_{\odot})]$	$\log[\mathrm{M}_{200}^{(3)}/(\mathrm{h}^{-1}\mathrm{M}_{\odot})]$	$\log[\mathrm{M}_{200}^{(4)}/(\mathrm{h}^{-1}\mathrm{M}_{\odot})]$	$\log[\mathrm{M}_{200}^{(5)}/(\mathrm{h}^{-1}\mathrm{M}_{\odot})]$	$\log[\mathrm{M}_{200}^{(6)}/(\mathrm{h}^{-1}\mathrm{M}_{\odot})]$
`BCG`	$13.15^{+0.13}_{-0.15}$	$13.52^{+0.13}_{-0.15}$	$13.83^{+0.11}_{-0.12}$	$13.76^{+0.10}_{-0.12}$	$14.13^{+0.09}_{-0.10}$	$14.55^{+0.10}_{-0.10}$
`IterCen`	$13.21^{+0.12}_{-0.13}$	$13.45^{+0.13}_{-0.16}$	$13.76^{+0.11}_{-0.13}$	$13.77^{+0.10}_{-0.11}$	$14.16^{+0.08}_{-0.09}$	$14.53^{+0.09}_{-0.09}$
`Cen`	$13.00^{+0.17}_{-0.23}$	$13.64^{+0.12}_{-0.16}$	$13.92^{+0.10}_{-0.12}$	$13.85^{+0.10}_{-0.12}$	$14.18^{+0.09}_{-0.10}$	$14.64^{+0.10}_{-0.10}$

Table 2.4: Constraints on the halo model parameters using the three definitions of halo centre. For each of the parameters, we quote the median of the posterior distribution, marginalised over the other parameters, while the errors are the 16th and 84th percentile of the distribution. All the constraints derived using the three different proxies for the halo centre agree within 1-sigma.

`Centre`	$\sigma_{\log[\tilde{\mathrm{M}}]}$	f_{c}	$\mathrm{p_{off}}$	$\mathcal{R}_{\mathrm{off}}$	$\mathrm{A_P}$
`BCG`	$0.74^{+0.09}_{-0.16}$	$0.84^{+0.42}_{-0.23}$	$0.38^{+0.30}_{-0.27}$	$0.79^{+0.52}_{-0.62}$	$2.06^{+1.19}_{-0.99}$
`IterCen`	$0.74^{+0.10}_{-0.16}$	$0.94^{+0.43}_{-0.23}$	$0.37^{+0.27}_{-0.26}$	$0.87^{+0.46}_{-0.65}$	$1.76^{+1.12}_{-0.87}$
`Cen`	$0.67^{+0.10}_{-0.17}$	$1.10^{+0.32}_{-0.46}$	$0.98^{+0.02}_{-0.09}$	$1.00^{+0.37}_{-0.51}$	$0.91^{+0.63}_{-0.33}$

2.6 Scaling relations

In the last Section of this paper, we investigate the correlations between the halo masses derived using weak gravitational lensing and optical properties of galaxy groups measured from SDSS images and the GAMA catalogue R11. There are two main reasons to study these scaling relations: i) to understand which physical processes take place inside galaxy groups and their impact on galaxy formation; ii) to constrain a mean relation, as well as the scatter, between some observable property of the groups and their halo mass for use in cosmological analyses that rely on the halo mass function.

2.6.1 The relation between halo mass and group r-band luminosity

We first investigate the scaling relation between the total halo mass and the total r-band luminosity of the groups. As described in the previous section, we bin the groups according to their total r-band luminosity (see Table 2.2), fit a halo model to the stacked ESDs, and record the halo mass posteriors for each bin. We show the results, halo mass a function of group luminosity, in the left panel of Figure 2.13.

We fit a power-law relation between the halo mass and the total r-band luminosity of the group:

$$\frac{\mathrm{M}_{200}}{10^{14}\,h^{-1}\mathrm{M}_{\odot}} = (0.95 \pm 0.14)\left(\frac{\mathrm{L}_{\mathrm{grp}}}{10^{11.5}h^{-2}\mathrm{L}_{\odot}}\right)^{(1.16\pm0.13)} . \qquad (2.37)$$

The linear regression is performed in the log-basis, since the errors on the masses are log-normal distributed, by minimizing the offset of the mass measurements from the power-law relation. We explicitly account for the correlation between halo masses (see Section 2.5). The red line in Figure

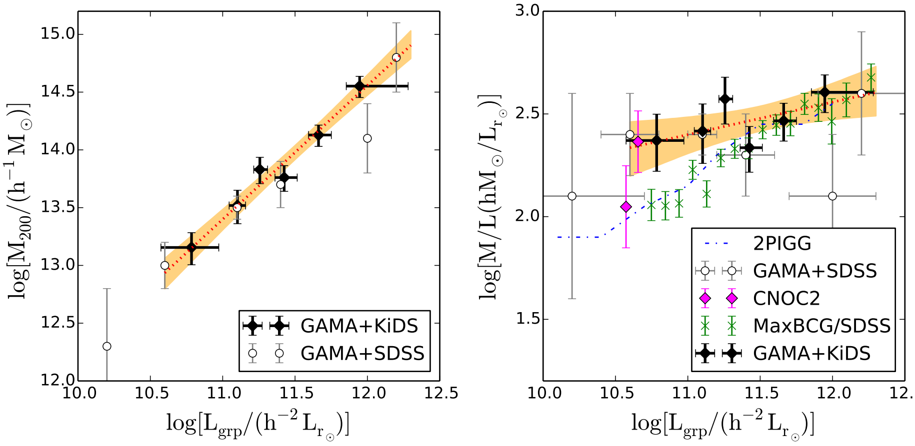

Figure 2.13: *Left panel:* Halo mass as a function of the total group r-band luminosity. The solid black points show the halo masses derived in this work from a halo model fit to the stacked ESD profile of groups with at least 5 members brighter than the GAMA magnitude limit. The vertical error bars indicate the 1-sigma uncertainty on the average halo mass after marginalising over the other halo model parameters, while the horizontal error bars indicate the 16th and 84th percentile of the luminosity distribution in each bin. The red line shows the best fit power-law to the data points, while our estimate of the 1-sigma dispersion around this relation is shown as the orange area (see text). The open black circles show the halo masses derived from a lensing analysis of GAMA groups using SDSS galaxies as background sources (Han et al. 2014). *Right panel:* Derived mass-to-light ratio as a function of the group total luminosity from this work (black points), from the GAMA+SDSS analysis (open black circles), from the analysis of the CNOC2 group sample (Parker et al. 2005) (magenta diamonds) and from a lensing analysis of 130000 groups from the MaxBCG catalogue using SDSS imaging (Sheldon et al. 2009, (green crosses)). In blue we show the median relation derived using the 2PIGG catalogue (Eke et al. 2004). The red lines and the orange area correspond to those of the left panel.

2.13 shows the best-fit relation. Our estimate of the 1-sigma dispersion around this relation is shown as the orange band and is derived from the joint posterior distributions for the halo masses from 5 independent MCMCs. We jointly extract 10^5 random values of the masses in each of the 6 r-band luminosity bins (in order to preserve the correlation between the masses), and we fit a linear relation to each log-mass vector as a function of the logarithm of the r-band luminosity. Finally, we compute the 16th and 84th percentiles of the best fit models in the different r-band luminosity bins. The average logarithmic scatter in halo mass at fixed r-band luminosity is $\sigma_{\log \langle \mathrm{M}_{200} \rangle} = 0.17$

In the left panel of Figure 2.13, we also compare our results to a previous weak lensing analysis of the same group catalogue (open black points) that used SDSS galaxies as background sources (Han et al. 2014). That analysis included all groups with $\mathrm{N_{fof}} \geqslant 3$ and fitted a single maximum likelihood mass to all the galaxies within a number of r-band luminosity bins. The agreement between the two analyses is remarkable given the different quality of data and the different techniques used to infer the halo masses. Nevertheless, we stress that the current analysis based on the first KiDS data not only yields some of the tightest lensing constraints on group masses to date but also does this whilst marginalising over halo model parameters not considered in the previous work.

Mock simulations suggest that the GAMA group catalogue is significantly contaminated by chance projections for groups with 2 and 3 members and marginally contaminated for groups with 4 members. Thus, while the only way to obtain constraints on low-luminosity systems ($\mathrm{L_{grp}} \lesssim 10^{10.5}$ $L_{\odot}h^{-2}$) is to include such sparse groups in the analysis, the impurity of the selection makes any results on the average mass of such groups unreliable and difficult to quantify (most likely underestimated). Our lowest-luminosity bin may suffer from a bias due to this same richness criterion if, as seems plausible, the poorer groups that are not included at a given luminosity have systematically lower masses.

According to our current understanding of galaxy formation, one would expect the slope of the mass-luminosity relation to change towards the low-mass end, for haloes of about $10^{12} - 10^{13} M_{\odot}h^{-1}$. This is mostly due to star formation being most efficient in haloes of $\sim 10^{12}h^{-1}M_{\odot}$ (see for example Behroozi et al. 2013 and references therein), implying the dominant feedback process is mass ejection from supernovae (see e.g. Dekel and Silk 1986). However, we are only able to probe the mass-luminosity relation for haloes more massive than about $10^{13}M_{\odot}h^{-1}$. In the regime modeled here, the relation is well fitted by a single power-law.

The right panel of Figure 2.13 shows the relation between halo mass and total r-band luminosity in terms of the mass-to-light ratio. The mass-to-light ratio is relatively constant with total group r-band luminosity, with a slight increase of less than 0.1 dex from the lowest to the highest luminosity bin. The scatter around this ratio is as large as 0.2 dex. Ideally, one would like to compare this result with previous results from the literature. Unfortunately, different authors use different definitions of halo masses, group luminosities are often measured in different bands, and group selection functions might differ due to different survey depths or different algorithms used to identify groups. This might easily lead to different scaling relations, and we would like to highlight to the reader that a face-value comparison might be misleading. Despite these uncertainties, we qualitatively compare our results with previous measurements in what follows.

One of the first analyses of a large sample of groups was based on the 2dFGRS, using a percolation technique to identify groups while also allowing dynamical mass measurements (Eke et al. 2004). The group luminosity was measured both in b_J and r_F-band. We show this result as the blue line in the right panel of Figure 2.13. We find a qualitatively similar trend of the mass-to-light ratio as a function of the total group r-band luminosity for $L_{\rm grp} > 10^{11} L_{r_\odot} h^{-2}$. However, our data do not support the steep increase of the mass-to-light ratio in the range $10^{10} L_{r_\odot} h^{-2} < L_{\rm grp} < 10^{11} L_{r_\odot} h^{-2}$ reported by Eke et al. (2004).

Han et al. (2014) carried out a detailed comparison between their results (which are in agreement with the one presented in this work) and the results from Eke et al. (2004), concluding that the steep increase in the mass-to-light ratio observed in the 2dFGRS sample could be mostly explained by the different depth between 2dFGRS and GAMA (2 magnitudes deeper). We stress again here that our first data point might be affected by the apparent richness selection we applied on the group catalogue. If we exclude this data point, the agreement with Eke et al. (2004) is fairly reasonable.

We also compare our results with a lensing analysis of MaxBCG clusters (Koester et al. 2007) using SDSS imaging (Sheldon et al. 2009). We show their result as the green points in Figure 2.13. In this case the groups/clusters were binned according to their total luminosity and the masses were measured by first inverting the ESD signal to 3D density and mass profiles and then by inferring the mass inside R_{200}. Also in this case we find a reasonable agreement once we exclude our first data point, which, as discussed, might be affected by the apparent richness selection we applied to the group catalogue.

Finally Parker et al. (2005) considered a sample of 116 groups from the CNOC2 survey (Yee et al. 1998). The halo masses were measured by fitting a SIS profile to the stacked ESD signal measured using weak gravitational lensing. In this case, the luminosity was measured in B-band. Given the small sample of groups, only two measurements were possible at quite low group luminosity. We show their results as the magenta points in Figure 2.13. Following Jee et al. (2014), we applied a 0.8 multiplicative correction to the B-band mass-to-light ratio in order to have an estimate for the mass-to-light ratio in r-band.

Only the mass-to-light ratio measurement in the high luminosity bin of the CNOC2 analysis, which corresponds to our low luminosity bin, can be directly compared to our analysis, given the luminosity range we probe. We find a good agreement.

2.6.2 The relation between halo mass and velocity dispersion

Next, we focus on the scaling relation between the total halo mass and the group velocity dispersion. Again, we bin the groups in 6 bins according to their velocity dispersion, with the boundaries chosen so that the signal-to-noise ratios of the stacked ESD profiles are equal (see Table 2.2). The halo masses in each bin are then found by a joint halo model fit to the ESD profile in each velocity dispersion bin. Figure 2.14 shows the corresponding results. The GAMA groups span an order of magnitude in velocity dispersion, but most of the constraining power for the scaling relation comes from groups with $\sigma \sim 500\mathrm{km\,s}^{-1}$. This is expected given that the cut imposed on group apparent richness excludes the low mass systems from this analysis, and that the survey volume is relatively small, and hence our sample does not contain many very massive galaxy clusters. As in the case of binning by luminosity, we believe that the apparent richness cut imposed on the GAMA group catalogue will have a non-neglible effect on the measurement of the average halo mass in the first velocity dispersion bin $\sigma < 200\,\mathrm{km\,s}^{-1}$.

At low velocity dispersion, we compare our results with those from the CNOC2 survey (Carlberg et al. 2001), for which the mass measurements are derived from the dynamical properties of the groups. In Figure 2.14 we show the average CNOC2 mass measurements in 3 velocity dispersion bins; the error bars are the 1-sigma scatter between measurements in each bin.

At high velocity dispersion, we compare our results to the analysis of the HeCS sample (Rines et al. 2013), where masses are measured using a redshift-space caustic technique. The mean redshift of the HeCS clusters is similar to that of the GAMA groups. As for the CNOC2 sample, we binned the HeCS clusters according to their velocity dispersion, and we calculated the median mass and the 1-sigma dispersion in each bin. Both the CNOC2 and the HeCS sample agree well with the mass-velocity dispersion relation we derived using galaxy groups from GAMA.

We fit a power-law between the halo mass and the group velocity dispersion (using the same procedure outlined in the previous section) and we

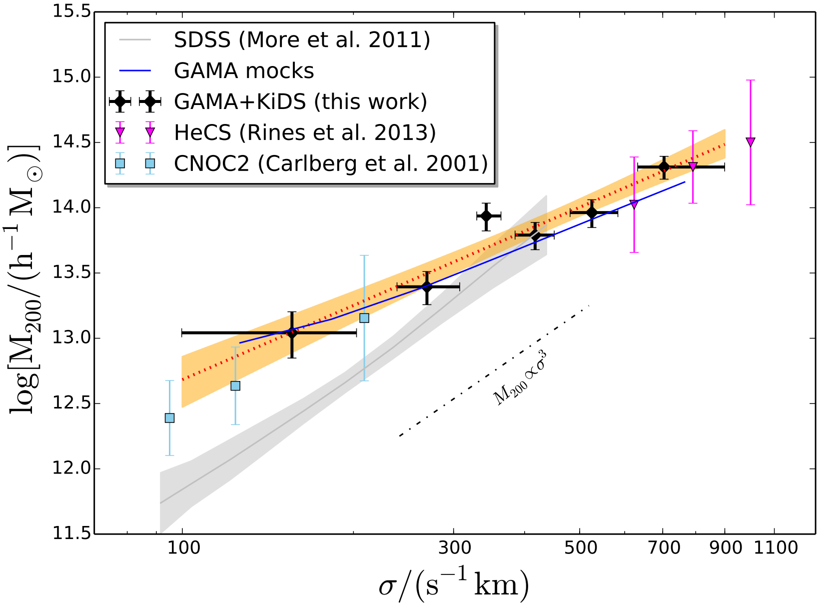

Figure 2.14: Halo mass as a function of the group velocity dispersion. The black points show the halo masses derived in this work from a halo model fit to the stacked ESD profile of groups with at least 5 members brighter than the GAMA magnitude limits. The red line shows the best fit power-law to the data points and the orange area indicates our estimate of the 1-sigma dispersion around this relation. The cyan points show the results from the CNOC2 survey (Carlberg et al. 2001), while the magenta points show the results from the HeCS sample of clusters (Rines et al. 2013). The grey band shows the mass-velocity dispersion relation obtained from measurements of satellite kinematics in SDSS (More et al. 2011). Finally, the blue line shows the relation calculated from the GAMA mocks using the same selection function applied to the data.

constrain this relation to be:

$$\left(\frac{M_{200}}{10^{14}\,h^{-1}\mathrm{M}_\odot}\right) = (1.00 \pm 0.15)\left(\frac{\sigma}{500\mathrm{s}^{-1}\mathrm{km}}\right)^{(1.89\pm0.27)} . \qquad (2.38)$$

We find that the average scatter in the halo mass-velocity dispersion relation is $\sigma_{\log\langle \mathrm{M}_{200}\rangle} = 0.20$.

We do not see any indication of a change in the slope over almost two order of magnitude in mass, from massive clusters to small groups. However, the slope we find is significantly shallower than what would be expected from a virial scaling relation ($M \propto \sigma^3$) as is seen in dissipationless numerical simulation (Evrard et al. 2008). A very similar result ($M \propto \sigma^{2.09\pm0.34}$) was found by a previous weak lensing analysis of the same group catalogue using SDSS galaxies as background sources (Han et al. 2014).

There are at least two possible explanations for this effect:

- Hydrodynamical simulations have shown that galaxies trace shallower mass-velocity dispersion relations (slope lower than 3) than dark matter particles (Munari et al. 2013). This is due to dynamical friction and tidal disruption, acting on substructures and galaxies, but not on dark matter particles. The typical effect measured in simulations is of order 10%, which is too small to explain the value of the power-law slope we measure when comparing with the virial expectation.

- The apparent richness cut we imposed to the group catalogue, the GAMA selection function and the limited cosmological volume we probe might introduce selection biases on our mass measurements. In particular the apparent richness cut might introduce a positive bias for mass-measurements in the lowest velocity dispersion bin, and the small volume used in this work might introduce negative biases in the highest velocity dispersion bins. The combination of these two effects would result in a shallower mass-velocity dispersion relation.

To investigate the second hypothesis further we compare our inferred scaling relation with one measured from the dark matter only mock GAMA catalogue (Robotham et al. 2011; Merson et al. 2013) applying the same apparent richness cut. In the GAMA mocks the velocity dispersion is measured using the underlying/true dark matter haloes while the stored mass of the haloes (DHalo mass) are computed as the sum of the masses of their component subhaloes (Jiang et al. 2014). For the purpose of the comparison we convert them into M_{200} (McNaught-Roberts in prep.). We show the results as the blue line in Figure 2.14. We find a good agreement with the scaling relation measured from the data, supporting the hypothesis that the shallower scaling relation we measure is mostly caused by selection effects. However we cannot exclude at this stage that part of the reason for the shallower mass-velocity dispersion relation might be dynamical processes acting on the galaxies in the groups.

A detailed investigation will be presented in a forthcoming paper (Robotham et al. in prep.) in the context of finding optimal dynamical mass estimates using weak lensing measurements of the group masses.

Finally, we compare our results with measurements of the mass-velocity dispersion relation obtained from measurements of satellite kinematics in SDSS (More et al. 2011). In this case, we extrapolate the mass-velocity dispersion relation from measurements of the stellar mass - halo mass and stellar mass - velocity dispersion relations which are provided in that paper. Note that these two relations have not been derived independently from each other. We find a good agreement with our results for $\sigma > 300 \mathrm{km\,s^{-1}}$. For lower mass haloes, we have already discussed the potential selection effect due to the apparent richness cut that affects our first data point. However, we also note that there is some tension between the CNOC2 results (Carlberg et al. 2001) and the SDSS satellite kinematics results. In general, velocity dispersion and mass measurements are more difficult for low mass groups than for massive systems because of the smaller number of members and more severe selection effects.

2.6.3 The relation between halo mass and r-band luminosity fraction of the BCG

Feedback from supernovae (Dekel and Silk 1986) and AGNs (Springel et al. 2005a) have been proposed in the past decade as a possible solution for reducing the star formation efficiency in hydrodynamical simulations (e.g. Sijacki et al. 2007, Fabjan et al. 2010, McCarthy et al. 2010, Booth and Schaye 2013, Vogelsberger et al. 2014, Schaye et al. 2015 and references therein). It is important to test the hypothesis of feedback and to constrain its efficiency by comparing complementary predictions of hydrodynamical simulations with observations. Motivated by the work of Le Brun et al. (2014), we focus here on the relation between the r-band luminosity fraction of the BCG, defined as $\mathrm{L_{BCG}/L_{grp}}$, and the group halo masses calculated in this work by binning the groups according to $\mathrm{L_{BCG}/L_{grp}}$ (see Table 2.2). The r-band luminosity of the BCG is calculated from the $\mathrm{r_{AB}}$ petrosian magnitude from the GAMA catalogue. We apply a k-correction and evolution correction to the magnitude following R11:

$$(k+e)(z) = \sum_{i=0}^{4} a_i (z-0.2)^i - 1.75z\,, \tag{2.39}$$

with $a_i = [0.2085, 1.0226, 0.5237, 3.5902, 2.3843]$. We note that the original correction presented in Equation 8 in R11 presents an error in the sign of the last term in the above equation. Figure 2.15 shows the halo masses obtained for groups stacked according to $\mathrm{L_{BCG}/L_{grp}}$ as a function of $\mathrm{L_{BCG}/L_{grp}}$.

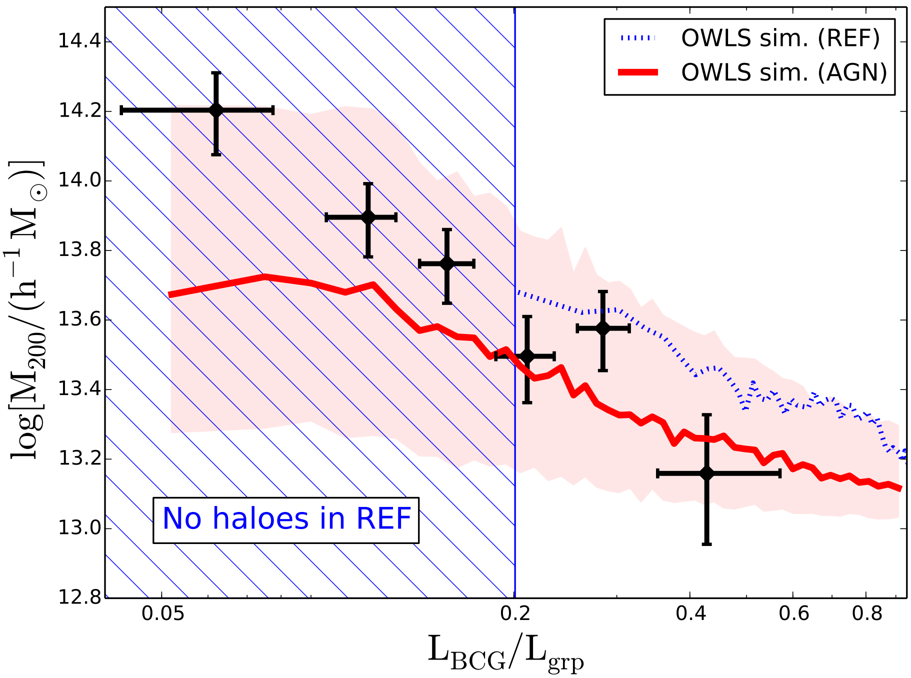

Figure 2.15: Group masses as a function of the r-band luminosity fraction of the BCG. The solid black points show the halo masses derived in this work from a halo model fit to the stacked ESD profile of groups with at least 5 members brighter than the GAMA magnitude limit. The solid red and the dashed blue lines are predictions from the Cosmo-OWLS simulation at the median redshift of the GAMA groups for a run including AGN feedback and a reference run without AGN feedback (Le Brun et al. 2014). The luminosities measured in the simulation are $(k + e)$ corrected to redshift 0 using the same functional form (Equation 2.39) applied to the data. The red area encompasses the 16th and 84th percentile of the mass distribution in each luminosity fraction bin for the AGN simulation. The shaded blue area indicates the range in $L_{\rm BCG}/L_{\rm grp}$ in which there are no haloes in the REF simulation.

There is a clear trend of group masses with the r-band luminosity fraction of the BCG. This trend has been previously observed at group scales by Rasmussen and Ponman (2009) and at cluster scales by Lin and Mohr (2004). The explanation is that the growth of the BCG is modest compared with the growth of the entire group.

Since the luminosity of the BCG is proportional to its stellar mass content and the group luminosity is an increasing function of the total halo mass, one can compare the results reported in this paper with studies of the stellar-to-halo mass ratio (SHMR) as a function of halo mass (e.g. George et al. 2011; Leauthaud et al. 2012a; van der Burg et al. 2014; Coupon et al. 2015). There is a clear consensus on the decline of the SHMR with halo mass, which is a different manifestation of the trend dispayed in Figure 2.15 where we report the halo mass as a function of the r-band luminosity fraction of the BCG. In particular, for central galaxies, it has been shown (Behroozi et al. 2013; Coupon et al. 2015) that halos of $\sim 2 \times 10^{14}\, h^{-1}\mathrm{M}_{\odot}$ have a SHMR about an order of magnitude lower than that of halos of $\sim 10^{13}\, h^{-1}\mathrm{M}_{\odot}$, again in qualitative agreement with the result shown in Figure 2.15. The steep decline of the relation between the group mass and the r-band luminosity fraction is a consequence of star formation becoming less efficient in more massive halos. Several mechanisms, beyond AGN feedback, have been invoked to explain this phenomenon such as halo mass quenching (e.g Peng et al. 2010; Ilbert et al. 2013) or the presence of many satellite galaxies in massive halos which cut off the gas supply to the BCG (Aragon-Calvo et al. 2014).

We focus here in particular on comparing our results with the (Cosmo-) OverWhelmingly Large Simulations (OWLS) (Schaye et al. 2010; Le Brun et al. 2014).

Le Brun et al. (2014) present results from these simulations in terms of K-band luminosity binned by halo mass. They report a very similar trend to the one we observe in our data. In particular, they find a large difference in the luminosity fraction of the BCG when they compare simulations with and without AGN feedback. To compare our results with the Cosmo-OWLS simulation, the r-band results were provided by the Cosmo-OWLS team using the same K-correction and evolution correction we applied to the data (Equation 2.39) for three redshifts snapshots $z = [0.125, 0.25, 0.375]$. When comparing the simulations to the data, we use the results from the snapshots closer to the median redshift of the GAMA groups. We discarded from the simulation all haloes with mass lower than $10^{13}\, h^{-1}\mathrm{M}_{\odot}$, which roughly corresponds to the minimum mass of groups with more than 5 members in the G^3Cv7 catalogue (see section 2.6.4). In this way we try to mimic the selection we applied to the data. Finally, we bin the simulation in the same way we bin the data, using the BCG luminosity fraction as a proxy for the group mass.

Figure 2.15 shows the Cosmo-OWLS results for the run including AGN feedback (solid red line) and for a reference run (REF) without AGN (dashed blue lines). The red area encompasses the 16th and 84th percentile of the mass distribution in each luminosity fraction bin.

For $\mathrm{L_{BCG}/L_{grp}} < 0.2$ the reference run does not contain any groups which on the contrary are clearly present in our group sample. The reason for this is that the gas cooling in the REF simulation is too efficient, leading to BCGs which are always very luminous in comparison to the total luminosity of the group. This evidence alone is sufficient to conclude that the data disfavour a model without AGN feedback. Note that this conclusion is independent of the group mass measurements. Our derived scaling relation between the halo mass and the luminosity fraction of the BCG for $\mathrm{L_{BCG}/L_{grp}} > 0.2$ further supports the above conclusion, being in reasonable agreement with the prediction from the simulation including AGN feedback. A detailed comparison of the trend in Figure 2.15 with simulations would require replicating the GAMA group finder and selection function on the Cosmo-OWLS simulations and is beyond the scope of this paper.

2.6.4 The relation between halo mass and group apparent richness

Finally, we investigate the relation between the total halo mass and the apparent richness of the groups. The groups are binned according to their apparent richness (see Table 2.2), and the average halo mass for each bin is estimated by fitting a halo model to the stacked ESD profile. We show the result in Figure 2.16.

We parametrise the halo mass-richness relation with a power-law, which is fit to the data with the same procedure outlined in the previous sections:

$$\left(\frac{M_{200}}{10^{14}h^{-1}\mathrm{M}_\odot}\right) = (0.43 \pm 0.08)\left(\frac{N_{\rm fof}}{10}\right)^{(1.09\pm0.18)} , \qquad (2.40)$$

and we constrain the average scatter in the halo mass-richness relation to be $\sigma_{\log\langle \mathrm{M}_{200}\rangle} = 0.20$.

As expected, richer groups are also more massive. We caution the reader that this scaling relation is the one most affected by the GAMA selection function. In fact, unlike our treatment of the total group luminosity, we do not correct the apparent richness measurements to account for the faint galaxy members not targeted by GAMA. We compare our results with the GAMA mocks, which have the same selection function as the data, and we generally find good agreement.

We also compare our results with a weak lensing analysis of 130,000 groups and clusters of galaxies in the Sloan Digital Sky Survey (Johnston et al. 2007). The masses were derived from fitting an halo model to the stacked ESD profile in 12 richness bins. The richness was defined as the number of red sequence galaxies with luminosities larger than $0.4\mathrm{L}_{\star}$ within a given projected radius, which is close to R_{200}. In spite of the different richness defintions we find a good agreement with our measurements, both for the amplitude and the slope of the mass-richness relation.

2.7 Conclusions

In this paper, we present the first weak lensing analysis of the mass distribution in the GAMA groups using background sources from the overlapping KiDS survey. The effective overlapping area (accounting for masks) used in this work is 68.5 square degrees and corresponds to the first two data releases of $ugri$ images of the KiDS data (de Jong et al. 2015 and K15).

Our main results are the following:

1. We measure the stacked excess surface density profile of the galaxy groups as a function of their total r-band luminosity, velocity dispersion, fraction of group light in the BCG and apparent richness. Splitting the data into six roughly equal signal-to-noise bins, we derive average halo masses per bin with a typical precision of 0.12 dex. We provide a physical interpretation of the signal using the halo model.

2. We show the importance of modelling the mis-centring of the BCG (used here as tracer of the group centre) with respect to the centre of the group's dark matter halo in order to derive unbiased results, in particular on the halo mass-concentration relation.

3. Our results are consistent with the normalisation of the halo mass-concentration relation proposed by Duffy et al. (2008),when mis-centring is included in the model.

4. We find no evidence of a significant baryonic component in the centre of the groups in excess of the stellar mass of the BCG. However, the

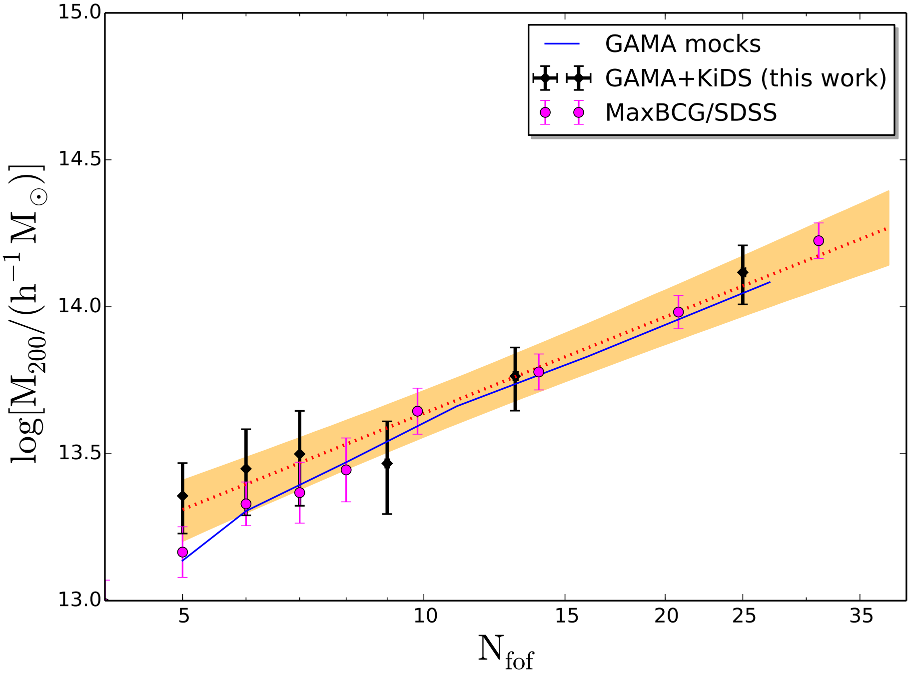

Figure 2.16: Group halo mass as a function of the richness $(N_{\rm fof})$. We use here only groups with at least 5 members brighter than $r_{AB} = 19.8$. The richness of the groups is not corrected to account for the fainter galaxies not targeted by GAMA. The red line shows the best fit power-law relation to the data points. Our estimate of the 1-sigma dispersion around this relation is shown as the orange area. The blue line shows the mass-richness relation derived from the GAMA mocks using the same selection function applied to the data. The magenta points show the result of a weak lensing analysis of 130,000 groups and clusters of galaxies in the Sloan Digital Sky Survey (Johnston et al. 2007).

uncertainty on this result is quite large due to the low signal-to-noise at small scales, which is in turn caused by the difficulties inherent in measuring reliable shapes for blended objects.

5. We obtain clear scaling relations between the halo mass and a number of observable properties of the groups: the group r-band luminosity, the velocity dispersion of the group, its apparent richness and the ratio between the r-band luminosity of the BCG and the total r-band luminosity of the group. The typical scatter in halo mass at fixed observable property is $\sigma_{\log\langle M_{200}\rangle} = 0.2$.
6. We show that our data have the statistical power to discriminate be-

tween models with and without AGN feedback and possibly between different AGN feedback models.

This analysis is part of the first set of weak lensing results using the KiDS data, based on data obtained during the first two years of operation. As the survey continues to cover more sky, both the statistical power and the fidelity of the measurements will grow, further refining these results as well as enabling other analyses of the distribution of dark matter in galaxies, groups and clusters.

Acknowledgements

We would like to thank the anonymous referee for providing useful suggestions to improve the manuscript. We thank Tom Kitching, Joachim Harnois-Deraps, Martin Eriksen and Mario Radovich for providing useful comments to the paper. We are grateful to Matthias Bartelmann for being our external blinder, revealing which of the four catalogues analysed was the true unblinded catalogue at the end of this study. We would like to thank Tamsyn Mcnaught-Roberts for providing the conversion between the halo mass definition used in the GAMA mocks and M_{200}, and Ian McCarthy for providing the data used in Figure 15. We also thank Ludo van Waerbeke for writing the code used to compute the shear additive bias correction used in this work. MV, MC, H.Ho, CS, AC and CH acknowledge support from the European Research Council under FP7 grant number 279396 (MV, MC, CS, H.Ho) and 240185 (AC and CH). BJ acknowledges support by an STFC Ernest Rutherford Fellowship, grant reference ST/J004421/1. EvU acknowledges support from an STFC Ernest Rutherford Research Grant, grant reference ST/L00285X/1. PN acknowledges the support of the Royal Society through the award of a University Research Fellowship, the European Research Council, through receipt of a Starting Grant (DEGAS-259586) and support of the Science and Technology Facilities Council (ST/L00075X/1). RN and EvU acknowledge support from the German Federal Ministry for Economic Affairs and Energy (BMWi) provided via DLR under project no. 50QE1103. H.Hi. is supported by the DFG Emmy Noether grant Hi 1495/2-1. This work is supported by the Netherlands Organisation for Scientific Research (NWO) through grants 614.001.103 (MV) and 614.061.610 (JdJ) and by the Deutsche Forschungsgemeinschaft in the framework of the TR33 'The Dark Universe'. This work is based on data products from observations made with ESO Telescopes at the La Silla Paranal Observatory under programme IDs 177.A-3016, 177.A-3017 and 177.A-3018. GAMA is a joint European-Australasian project based around a spectroscopic campaign using the Anglo-Australian Telescope. The GAMA input catalogue is based on data taken from the Sloan Digital Sky Survey and the UKIRT Infrared Deep Sky Survey. Complementary imaging of the GAMA regions is being obtained by a number of independent survey programs including GALEX MIS, VST KiDS, VISTA VIKING, WISE, Herschel-ATLAS, GMRT and ASKAP providing UV to radio coverage. GAMA is funded by the STFC (UK), the ARC (Australia), the AAO, and the participating institutions. The GAMA website is `http://www.gama-survey.org/`.

Author Contributions: All authors contributed to the development and writing of this paper. The authorship list reflects the lead authors (MV, MC, MB, KK) followed by two alphabetical groups. The first alphabetical group includes those who are key contributors to both the scientific analysis and the data products. The second group covers those who have either made a significant contribution to the data products, or to the scientific analysis.

Appendix A: Alternative definitions of the group centre

We present here the measurements of the stacked ESD profile and the halo model constraints we obtain if we use a different definition of the group centre, compared to the BCG definitions used throughout the paper.

In Figure 2.17 we show the stacked ESD profile for the same 6 luminosity bins used in Section 2.5 but now using the brightest galaxy left after iteratively removing the most distant galaxies from the group centre of light which is labelled as `IterCen` (left panel) and the group centre of light `Cen` (right panel) as the definition for the group centre. When `IterCen` is used, the stacked signal is statistically indistinguishable from the case when `BCG` is used as the group centre. This is not surprising since the two centre definitions differ only for a few percent of the groups.

When `Cen` is used as the group centre, the shape of the stacked ESD profile is very different. The turnover of the signal at scales around 100 h^{-1}kpc is a clear indication of mis-centring between the chosen centre of the halo group and the true minimum of the halo potential well. R11 report that `Cen` is not a good proxy for the halo centre, and hence, this result is not surprising. It is clear in this case that not including the mis-centring parameters in the model would lead to a very poor description of the data.

We do not show the posterior distributions for the halo model parameters corresponding to the case of `Cen`. The degeneracies between the parameters are the same as those found when `BCG` or `IterCen` are used as

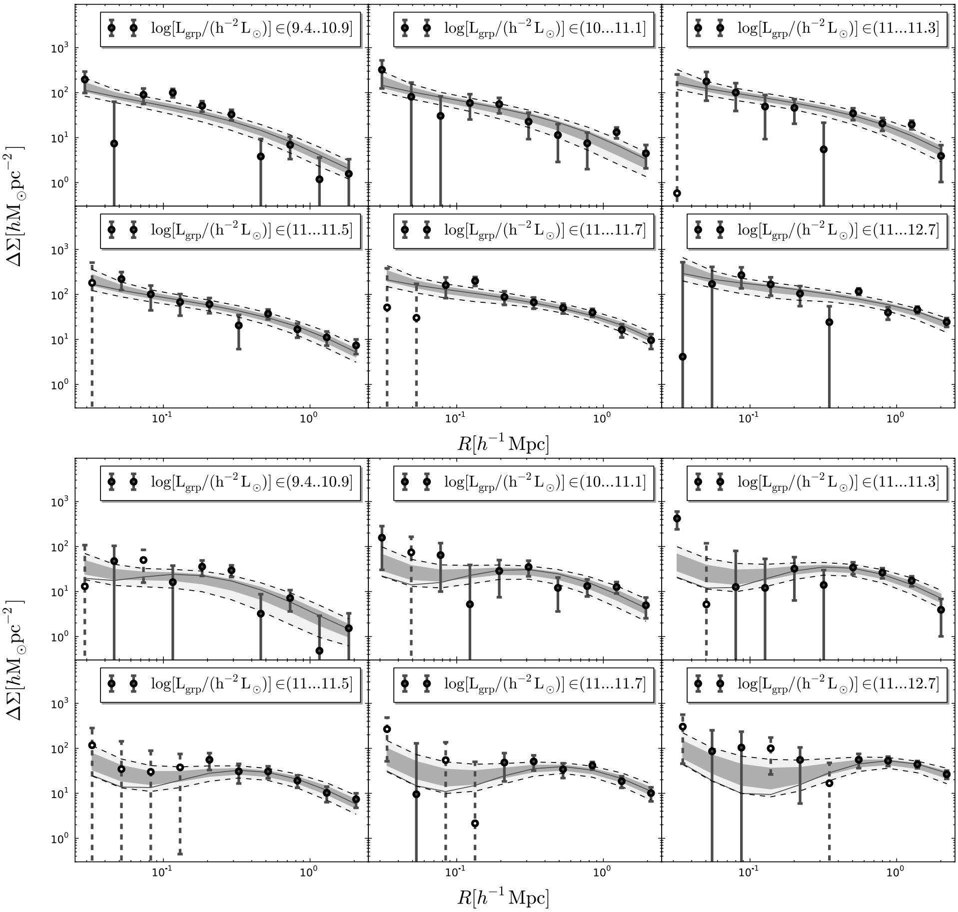

Figure 2.17: Stacked ESD measured around the groups' `IterCen` (**upper panel**) and the groups' centre of light `Cen` (**lower panel**) for 6 group luminosity bins as a function of distance from the group centre. The group luminosity increases from left to right and from top to bottom. The stacking of the signal has been performed considering only groups with $\mathrm{N_{fof}} \geqslant 5$. The error bars on the stacked signal are computed as detailed in section 2.3.4. The grey bands represent the 68 and 95 percentile of the model around the median and the dark lines indicate the best fit model.

proxies for the halo centre. We can derive tight constraints on the probability of mis-centring $\mathrm{p_{off}} \geqslant 0.67$ 2-sigma, and we find that on average the amount of offset of the centre of light with respect to the minimum of the halo potential well is $\mathcal{R}_{\mathrm{off}} = 1.00^{+0.37}_{-0.51}$. We summarise the results in Table 2.3 and 2.4.

The constraints we derive for the halo masses in the 6 luminosity bins and the constraints on $\sigma_{\log\tilde{\mathrm{M}}}$, f_{c}, $\mathrm{A_P}$ are consistent within 1-sigma with the constraints derived using the other two definitions of the halo centre.

These results highlight the importance of a proper model of the mis-centring in the analysis of the lensing signal from groups or clusters of galaxies. Neglecting mis-centring could lead to biases in the derived masses and in the other model parameters, particularly the halo concentration.

3 Galaxy halo mass in the cosmic web environment

Based on: “Dependence of GAMA galaxy halo masses on the cosmic web environment from 100 square degrees of KiDS weak lensing data”
Authors: Margot M. Brouwer, Marcello Cacciato, Andrej Dvornik, Lizzie Eardley, Catherine Heymans, Henk Hoekstra, Konrad Kuijken, Tamsyn McNaught-Roberts, Cristóbal Sifón, Massimo Viola, Mehmet Alpaslan, Maciej Bilicki, Joss Bland-Hawthorn, Sarah Brough, Ami Choi, Simon P. Driver, Thomas Erben, Aniello Grado, Hendrik Hildebrandt, Benne W. Holwerda, Andrew M. Hopkins, Jelte T. A. de Jong, Jochen Liske, John McFarland, Reiko Nakajima, Nicola R. Napolitano, Peder Norberg, John A. Peacock, Mario Radovich, Aaron S. G. Robotham, Peter Schneider, Gert Sikkema, Edo van Uitert, Gijs Verdoes Kleijn
Published in: Monthly Notices of the Royal Astronomical Society, Volume 462, Issue 4, p.4451-4463

Abstract:

Galaxies and their dark matter haloes are part of a complex network of mass structures, collectively called the cosmic web. Using the tidal tensor prescription these structures can be classified into four cosmic environments: voids, sheets, filaments and knots. As the cosmic web may influence the formation and evolution of dark matter haloes and the galaxies they host, we aim to study the effect of these cosmic environments on the average mass of galactic haloes. To this end we measure the galaxy-galaxy lensing profile of 91,195 galaxies, within $0.039 < z < 0.263$, from the spectroscopic Galaxy And Mass Assembly (GAMA) survey, using $\sim 100\,\mathrm{deg}^2$ of overlapping data from the Kilo-Degree Survey (KiDS). In each of the four cosmic environments we model the contributions from group centrals, satellites and neighbouring groups to the stacked galaxy-galaxy lensing profiles. After correcting the lens samples for differences in the stellar mass distribution, we find no dependence of the average halo mass of central galaxies on their cosmic environment. We do find a significant increase in the average contribution of neighbouring groups to the lensing profile in increasingly dense cosmic environments. We show, however, that the observed effect can be entirely attributed to the galaxy density at much smaller scales (within $4\,h^{-1}\mathrm{Mpc}$), which is correlated with the density of the cosmic environments. Within our current uncertainties we find no direct dependence of galaxy halo mass on their cosmic environment.

3.1 Introduction

In the standard ΛCDM cosmological model, with dark energy and cold dark matter, structure formation in our Universe is described as the gravity-induced growth of small perturbations in the matter density field (Peebles and Yu 1970). This field is dominated by Dark Matter (DM) which outweighs the mass in baryons by a factor ~ 5 (Planck XIII 2016). As a consequence, the properties of baryonic structures are expected to be dominated by the underlying DM density field. More specifically, when overdense regions undergo gravitational collapse, they form bound structures referred to as DM haloes (Peebles 1974). Galaxies form in those haloes via the cooling of the gas that falls into the gravitational potential of the DM halo (White and Rees 1978). As a halo grows in mass and size due to smooth accretion and mergers (White and Frenk 1991), so does the galaxy that inhabits it (although the detailed properties of galaxies are also affected by baryon-specific processes, such as star formation and feedback from stars and active galactic nuclei). Due to increased clustering of high-mass haloes and the accretion of halo mass through mergers, the DM halo mass is predicted to depend on the presence of other haloes within a few Mpc range (Bardeen et al. 1986; Cole and Kaiser 1989). The halo abundance at these small scales is henceforth called the *local density* (Budavari et al. 2003).

It is possible that the properties of haloes also depend on the density field on scales much larger than the extent of the local structure, known as the large-scale structure (LSS) of the Universe. The universal LSS, as revealed by simulations of large portions of the Universe (e.g. Springel et al. 2005b; Schaye et al. 2015), manifests itself as an intricate arrangement of matter density distributions: the sheets of DM that separate large underdense voids intersect to form filaments, which again form dense knots wherever they cross. These structures, collectively called the *cosmic web* (Bond et al. 1986), act as a skeleton to large baryonic structures like gas clouds, galaxies, clusters and superclusters. Through the attraction of baryons by DM, large galaxy surveys (e.g. Jones et al. 2009; van Waerbeke et al. 2013; Tempel et al. 2014; Garilli et al. 2014) are able to observe the cosmic DM web reflected in the large-scale distribution of galaxies.

The question arises whether one can establish a correlation between galaxy halo properties and their location in the cosmic web, independently of the effects of the local environment in which the halo resides. Using numerical simulations, Hahn et al. (2009) predicted that the mass of haloes is affected by tidal forces when a large-scale structure resides within 4 virial radii of the halo. According to their simulations these tidal effects can, especially in filaments, suppress halo formation and even extract mass from haloes if they pass the large-scale structure within 1.5 virial radii. On the other hand, they find an increase in the abundance of small haloes near massive structures which, through mergers, can likewise affect halo masses.

The effects of tidal forces on halo formation and mass were also studied by Ludlow and Porciani (2011). Using $\Lambda\mathrm{CDM}$ cosmological simulations they found that, while ~ 70 percent of the DM haloes should collapse at the location of peaks in the local density field with a mass of similar scale, there should exist a small fraction of haloes that arise from smaller density fluctuations. Compared to regular haloes, these 'peakless haloes' should be more strongly affected by tidal forces from neighbouring large-scale structures. However, like Hahn et al. (2009), Ludlow and Porciani (2011) showed that, in the local universe, peakless haloes also reside in denser *local* environments (up to a few Mpc scales).

Eardley et al. (2015), henceforth called E15, wished to observationally probe the effect of the cosmic web on the luminosity function of galaxies. They therefore classified all galaxies into one of four *cosmic environments*: voids, sheets, filaments and knots. Following McNaught-Roberts et al. (2014) they also measured the number density of galaxies within $8\,h^{-1}\mathrm{Mpc}$ radii (*local density*, see Sect. 3.3.2), and found the distribution in local density of galaxies in each cosmic environment. From these local density distributions they concluded that galaxies in denser cosmic environments (e.g. knots) tend to have higher local densities as well. The correlation between large-scale density and the local abundance of haloes complicates observational tests of the predicted tidal effects on galaxy properties. In order to separate the effects of local density from those of the cosmic web, E15 used a 'shuffling' method (see Sect. 3.3.3). By creating four new galaxy samples which retain the local density distribution from the original cosmic environments, but with the galaxies shuffled between the cosmic environments, they erased the information from the cosmic environment classification while retaining the information on local density. By comparing the galaxies in these 'shuffled environments' to those in the true cosmic environments, they were able to eliminate the dependence on the local overdensity of their measurement of the galaxy luminosity function. In this work we use the environment classification from E15, and follow their shuffling method in order to extract the effect on halo mass from the cosmic environment alone, without effects from the local density. As explained in Sect. 3.3.2 we use $4\,h^{-1}\mathrm{Mpc}$ radii to measure the local density, instead of the $8\,h^{-1}\mathrm{Mpc}$ used in E15. This might complicate the comparison of our results with E15, but is necessary due to the different nature of the luminosity function and the halo mass measurement.

The effect of the cosmic web on galaxies was already probed observationally by several groups using different galaxy properties: Alpaslan et al. (2015) measured the effect of the cosmic web on $u - r$ colour, luminosity, metallicity and morphology of galaxies; Darvish et al. (2014) measured the stellar mass, star formation rate (SFR), SFR-mass relation and specific SFR of galaxies in different cosmic environments; and E15 used their method to measure the galaxy luminosity function. In these and similar studies the importance of the DM haloes of galaxies is often stressed, and the possible effect of the cosmic web on the measured galaxy properties is often expected to be a secondary consequence of the effect on the DM halo. Our goal, therefore, is to perform the first direct measurement of the effect of the cosmic web on galaxy halo mass.

To statistically measure the effect of the cosmic environment on the DM halo mass of galaxies we use weak gravitational lensing, currently the only method that provides a direct measure of the mass of a system without any assumptions on its dynamical state. More specifically, we use galaxy-galaxy lensing (see e.g. Brainerd et al. 1996; Hoekstra et al. 2004; Mandelbaum et al. 2006b): the coherent tangential distortion of background galaxy images due to the gravitational deflection of light by the mass of a sample of foreground galaxies and their haloes. To select foreground galaxies we use the spectroscopic Galaxy And Mass Assembly survey (Driver et al. 2011), whereas the images of the background galaxies are taken from the photometric Kilo-Degree Survey (de Jong et al. 2013). This combination of data sets was also employed by the galaxy-galaxy lensing studies of Viola et al. (2015) to measure the masses of galaxy groups, Sifón et al. (2015) to study group satellites, and van Uitert et al. (2016) to measure the stellar-to-halo mass relation. To infer the mass of the haloes associated with the lens galaxies, we employ a simple halo model on the measured galaxy-galaxy lensing signals.

We discuss the lensing methodology and the details of the lens and source samples in Sect. 3.2. The classification of the cosmic environments and the methods used to correct for the differences in the local density and stellar mass distributions of the galaxy samples are discussed in Sect. 3.3. In Sect. 3.4 we present the analysis of the lensing profiles in the cosmic environments and the model fitting procedure used to extract the galaxy halo masses from these density profiles. In Sect. 3.5 we present the resulting masses of DM haloes. Section 3.6 contains the discussion and conclusions.

Throughout the paper we adopt the following cosmological parameters: $\Omega_{\rm m} = 0.315$, $\Omega_{\Lambda} = 0.685$, $\sigma_8 = 0.829$, $n_{\rm s} = 0.9603$ and $\Omega_{\rm b}h^2 = 0.02205$, motivated by Planck XIII (2016). The reduced Hubble constant $h = H_0/(100\,{\rm km/s/Mpc})$ is left free or is substituted with 1 where needed.

3.2 Galaxy-galaxy lensing analysis

The light from distant galaxies is deflected by density fluctuations along the line of sight. As a consequence, the images of distant galaxies are magnified and distorted (sheared). The technique that measures the weak coherent distortion of a population of background galaxies by a foreground density distribution is called *weak gravitational lensing* (WL), or *galaxy-galaxy lensing* (GGL) when it is used to measure the density distribution around foreground galaxies (lenses) using the shear of many background galaxies (sources) (for an overview, see e.g. Bartelmann and Schneider 2001; Schneider et al. 2006). These small shape distortions ($\sim 1\%$ of the intrinsic galaxy ellipticity) can only be measured statistically by azimuthally averaging the shear of a field of sources around individual lenses, and stacking these lens signals for large samples of foreground galaxies, selected according to their observable properties. The measured quantity is the shear component tangential to the line connecting the lens and source galaxy. Combining this quantity for all lens-source pairs of a lens sample results in the average tangential shear $\langle\gamma_{\rm t}\rangle(R)$, which can be related to the Excess Surface Density (ESD) profile $\Delta\Sigma(R)$. This is defined as the surface mass density $\Sigma(R)$ at the projected radial distance R from the lens centre, subtracted from the average density $\bar{\Sigma}(<R)$ within that radius:

$$\langle\gamma_{\rm t}\rangle(R)\Sigma_{\rm crit} = \Delta\Sigma(R) = \bar{\Sigma}(<R) - \Sigma(R)\,. \tag{3.1}$$

Here $\Sigma_{\rm crit}$ is the critical density surface mass density:

$$\Sigma_{\rm crit} = \frac{c^2}{4\pi G}\frac{D(z_{\rm s})}{D(z_{\rm l})\,D(z_{\rm l}, z_{\rm s})}\,, \tag{3.2}$$

which is the inverse of the lensing efficiency: a geometrical factor that determines the strength of the lensing effect, depending on the angular diameter distance from the observer to the lens $D(z_{\rm l})$, to the source $D(z_{\rm s})$, and between the lens and the source $D(z_{\rm l}, z_{\rm s})$. In this equation c denotes the speed of light and G the gravitational constant. Our ESD measurement procedure follows Sect. 3.3 of Viola et al. (2015)[1]

3.2.1 GAMA lens galaxies

The positions of the foreground lenses used for our GGL study are selected from the Sloan Digital Sky Survey (Abazajian et al. 2009, SDSS), and have redshifts measured by the Galaxy And Mass Assembly (hereafter GAMA, Driver et al. 2011) survey, a spectroscopic survey on the Anglo-Australian Telescope with the AAOmega spectrograph. We use the GAMA galaxy catalogue resulting from the three equatorial regions (G09, G12 and G15) of the final GAMA data release (GAMA II, Liske et al. 2015). These equatorial regions span a total of $\sim 180\,\mathrm{deg}^2$ and are 98% complete down to a Petrosian r-band magnitude of $m_\mathrm{r} = 19.8$. This catalogue contains $180,960$ galaxies, of which we use the sample of $\sim 113,000$ galaxies within the redshift range $0.039 < z_\mathrm{l} < 0.263$ (see Sect. 3.3.2) with a high-quality redshift measurement ($nQ \geq 3$) as lenses. Since $\sim 55\%$ of the GAMA area is covered by the Kilo-Degree Survey data that we use for this analysis, $\sim 80\%$ of these galaxies have at least some overlap with the available area (see Sect. 3.2.2), and therefore contribute (in varying degrees) to the lensing signal. This amounts to a total of 91195 galaxies contributing to the lensing signal.

In Sect. 3.3.1 of this paper we make use of the stellar masses of the GAMA galaxies, which are measured by Taylor et al. (2011b) by fitting Bruzual and Charlot (2003) stellar population synthesis models to the *ugriz* observations of the SDSS. The stellar masses are corrected for flux falling outside the automatically selected aperture using the 'flux-scale' parameter (following the procedure discussed in Taylor et al. 2011b). Galaxies without a well-defined stellar mass or fluxscale correction are removed from our sample.

In Sect. 3.4.2 we use the classification of GAMA galaxies into galaxy groups, in order to accurately model the contribution of different galaxies

---

[1] One difference between our procedures is the method that decides which $1\,\mathrm{deg}^2$ KiDS tiles contribute to the ESD profile of every GAMA foreground galaxy. In Viola et al. (2015) the sources within a KiDS tile contributed to the ESD profile of a lens if the projected distance R_lt between the lens and the centre of the tile was smaller then the maximal separation R_max to which the ESD profile was measured: $R_\mathrm{lt} < R_\mathrm{max}$. This method was slightly suboptimal, since not all sources contributed to the lensing signal at larger scales. In this paper the method is optimized to encompass the contribution of all KiDS sources to the ESD profile of each lens. We first calculate the projected radius R_t of the great circle around each $1\,\mathrm{deg}^2$ KiDS tile. The sources within a KiDS tile contribute to the ESD profile of a lens if the radius R_t of the circle is smaller then R_max: $R_\mathrm{t} < R_\mathrm{max}$.

to the GGL signal. We use the classification of galaxies into groups as listed in the 7th GAMA Galaxy Group Catalogue by Robotham et al. (2011). The galaxies in the GAMA II catalogue are classified as either the central or a satellite of their group, using the Friends-of-Friends (FoF) group finding algorithm described in Robotham et al. (2011). The FoF algorithm groups galaxies depending on the distances to each other in both projected and line-of-sight space. The projected and line-of-sight linking lengths are calibrated against mock catalogues. These mocks are also used to test that global properties of groups, such as their total number, are well recovered by the algorithm. The FoF method also finds galaxies that do not belong to any group (non-group galaxies). Note that some non-group galaxies might actually be centrals of groups with satellites that fall below the visible magnitude limit. Conversely, non-group galaxies can erroneously be classified as group members due to projection effects. However, this misidentification is primarily expected to happen at high redshifts, whereas our sample only contains galaxies up to redshift $z_1 = 0.263$. Also note that some galaxies classified as satellites might actually be centrals, and some satellites might be erroneously identified as non-group galaxies. This misidentification is most common for the smallest groups (with less than 5 members). Since we primarily use the group classification to account for the contribution of nearby galaxies to the GGL signal, it is of little consequence whether these galaxies are classified as satellites or neighbouring group centrals since both are accounted for in the model. Furthermore, the GGL analysis of van Uitert et al. (2016) to determine the fraction of satellites in the central galaxy sample, shows that the satellite fraction of GAMA is accurate for galaxies with a stellar mass up to $\sim 10^{11}\mathrm{M}_{\odot}$. For these reasons, it safe to use galaxies with a small number of members in our analysis. The definition of the central galaxy used in this paper is the Brightest Central Galaxy (BCG). In Viola et al. (2015) the BCG is shown to be the most accurate tracer of the centre of a group halo (together with the iteratively selected central galaxy).

3.2.2 KiDS source galaxies

The background sources used to measure the GGL profiles around the lenses are observed with the Kilo-Degree Survey (hereafter KiDS, de Jong et al. 2013), a *ugri* photometric survey on the VLT Survey Telescope (Capaccioli and Schipani 2011) using the OmegaCAM wide-field imager (Kuijken 2011). We use the $109\,\mathrm{deg}^2$ area of the publicly available KiDS-DR1/2 data release (de Jong et al. 2015; Kuijken et al. 2015) that overlaps with the equatorial GAMA areas. With the masks of bright stars and image defects applied, this amounts to a total of 68.5 deg^2 of KiDS area that overlaps with the GAMA survey.

For the measurements of the source ellipticities we use the r-band data, which have a median seeing of $0.7\mathrm{arcsec}$, a mean point spread function (PSF) ellipticity of 0.055 and a rest-frame limiting magnitude of 24.9. The r-band images are first reduced with the THELI pipeline (Erben et al. 2013). The sources are then detected from the stacked images by SEXTRACTOR (Bertin and Arnouts 1996). For each detected source, the Bayesian *lens*fit method (Miller et al. 2013b) measures the ellipticities ϵ_1 and ϵ_2 with respect to the equatorial coordinate frame, together with a weight w_s which is related to the uncertainty on the ellipticity measurements. The corresponding effective number density of sources is $n_\mathrm{eff} \approx \frac{\sigma^2_\mathrm{SN}}{A} \sum_s w_s = 4.48\mathrm{gal}/\mathrm{arcmin}^2$, where A is the area and $\sigma_\mathrm{SN} = 0.255$ the intrinsic ellipticity dispersion (shape noise) (Kuijken et al. 2015).

The photometric redshifts of the sources are derived from all bands, which are first processed and calibrated using the Astro-WISE optical image pipeline (McFarland et al. 2013). The Gaussian Aperture and PSF (GAaP, Kuijken 2008) method measures the matched aperture colours of the sources, corrected for differences in seeing. These are in turn used to determine the photometric redshifts through the Bayesian Photometric Redshift pipeline (BPZ, Benítez 2000 following Hildebrandt et al. 2012). The source redshift probability distribution $p(z)$ is sampled using 70 linearly spaced source redshift bins between $0 < z_\mathrm{s} < 3.5$. The resulting weighted median redshift of all sources is 0.53.

We use the full photometric redshift probability distribution $p(z_\mathrm{s})$ returned by the BPZ to calculate the critical surface density for each lens-source pair:

$$\Sigma^{-1}_\mathrm{crit} = \frac{4\pi G}{c^2} D(z_\mathrm{l}) \int_{z_\mathrm{l}}^{\infty} \frac{D(z_\mathrm{l}, z_\mathrm{s})}{D(z_\mathrm{s})} p(z_\mathrm{s}) \, \mathrm{d}z_\mathrm{s} \,, \tag{3.3}$$

where the integral is over the part of the $p(z_\mathrm{s})$ where the source redshift bins z_s are greater than the redshift z_l of the lens. Only sources with a $p(z)$ peak within $0.005 \leq z_\mathrm{B} < 1.2$, where the summed $p(z)$ posteriors agree well with the spectroscopic redshift distribution (Kuijken et al. 2015), are used for the analysis.

We assign a weight W_ls to each lens-source pair, that incorporates the ellipticity measurement weight w_s (from *lens*fit) which down-weights lens-source pairs that have less reliable shape measurements, as well as the lensing efficiency $\Sigma_{\rm crit}^{-1}$ which down-weights lens-source pairs that are very close or distant in redshift, and are therefore less sensitive to lensing. The total weight is defined as:

$$W_{\rm ls} = w_{\rm s} \Sigma_{\rm crit}^{-2} \,. \tag{3.4}$$

We apply an average multiplicative calibration $1 + K(R)$ to the stacked ESD profile, in order to account for the noise bias in the shape measurement (Melchior and Viola 2012; Heymans et al. 2012). The bias contribution $m_{\rm s}$ of each source is estimated from a *lens*fit analysis of simulated images (Miller et al. 2013b). For every radial bin R we determine the average correction:

$$K(R) = \frac{\sum_{ls} W_{ls} m_s}{\sum_{ls} W_{ls}} \,, \tag{3.5}$$

which has a value of $K(R) \sim 0.1$ for all considered values of R. In addition to an average multiplicative calibration, we apply an additive calibration term $c_{\rm s}$ to each separate ellipticity value. See Kuijken et al. (2015) for more information on these calibrations.

The ESD profile $\Delta\Sigma(R)$ from Eq. (3.1) can be measured by computing the tangential ellipticity $\epsilon_{\rm t}$:

$$\epsilon_{\rm t} = -\epsilon_1 \cos(2\phi) - \epsilon_2 \sin(2\phi) \,, \tag{3.6}$$

where ϕ is the angle between the source and the lens centre. The tangential ellipticity is measured for every lens-source pair in a range of circular bins at radius R with width δR, and the resulting signal is divided by the multiplicative calibration term to arrive at the ESD profile:

$$\Delta\Sigma(R) = \frac{1}{1 + K(R)} \frac{\sum_{ls} W_{ls} \epsilon_{\rm t} \Sigma_{\rm crit}}{\sum_{ls} W_{ls}} \,. \tag{3.7}$$

The uncertainty on the measured ESD profile corresponds to the square root of the diagonal of its analytical covariance matrix. As detailed in Sect. 3.4 of Viola et al. (2015), we compute the analytical covariance of the contributions to the ESD signal from each separate source that contributes to the stacked ESD profile of the lens sample. This covariance is not only computed between each radial bin, but also between the different stacked lens samples. These off-diagonal covariance elements are used within the model fitting procedure (see Sect. 3.4.2). Section 3.4 of Viola et al. (2015) shows that the error bars from the analytical covariance are in agreement with the bootstrap error bars from ~ 100 KiDS tiles, up to projected radius

$R = 2\,h^{-1}\mathrm{Mpc}$. The lensing signal around random points is not consistent with zero beyond this projected radius, due to the patchiness of the survey area. Below $20\,h^{-1}\mathrm{kpc}$ the decreasing number of sources and increasing contamination from foreground galaxy light also result in unreliable measurements. We therefore compute the ESD profile for 10 logarithmically spaced radial bins within $0.2 < R < 2\,h^{-1}\mathrm{Mpc}$.

3.3 Environment classification

3.3.1 Cosmic environments

The goal of this work is to study the mass of galaxy haloes as a function of their location in the cosmic web, henceforth called their *cosmic environment.* In E15 the entire volume of the GAMA survey is classified into four different cosmic environments: voids, sheets, filaments and knots. These environments are identified following the tidal tensor prescription of Hahn et al. (2007), which classifies each Cartesian $R_\mathrm{c} = 3\,h^{-1}\mathrm{Mpc}$ volume element (cell) in the GAMA survey into one of these four cosmic environments, based on the number of gravitationally collapsing dimensions of that cell. A volume element can be collapsing in 0, 1, 2 or 3 dimensions, and is respectively classified as belonging to a void, sheet, filament or knot.

To determine the number of collapsing dimensions of each cell, E15 use the number density of galaxies in the $R_\mathrm{c} = 3\,h^{-1}\mathrm{Mpc}$ Cartesian grid. This discrete density field is smoothed by applying a Gaussian filter with a width σ_s, resulting in the total effective smoothing scale $\sigma^2 = R_\mathrm{c}^2/6 + \sigma_\mathrm{s}^2$. From this smoothed density field E15 derive the gravitational potential, which is used to calculate the tidal tensor of each cell. Since the tidal tensor is a criterion for a cell's gravitational stability, a dimension of a cubic cell is considered to be collapsing if the corresponding real eigenvalue of the tidal tensor lies below a threshold value λ_th. Depending on its number of collapsing dimensions, each cell is allocated a cosmic environment. Correspondingly E15 assign each galaxy in the GAMA catalogue to the environment of the cell it inhabits, allowing us to study these galaxies and their DM haloes as a function of their cosmic environment.

The values of the effective smoothing scale σ_s and the eigenvalue threshold λ_th can be chosen freely in this method, and together determine the number of galaxies that are assigned to each cosmic environment. In order to divide the number of GAMA galaxies as equally as possible among the four cosmic environments, E15 chose $\lambda_\mathrm{th} = 0.4$ and σ_s such that $\sigma =$

Table 3.1: The number, mean redshift, mean stellar mass and satellite fraction of the galaxies in each cosmic environment. Note that only $\sim 80\%$ of these galaxies overlap with the KiDS area, and therefore contribute to the GGL signal. The values of $\langle M_* \rangle$ are displayed in units of $[10^{10}\mathrm{M}_\odot]$.

	N	$\langle z \rangle$	$\langle M_* \rangle$	$f_{\rm sat}$
Void	19742	0.161	2.767	0.146
Sheet	37932	0.169	3.465	0.243
Filament	41753	0.165	3.945	0.363
Knot	13457	0.157	4.354	0.502
Shuffled void	19742	0.160	2.590	0.174
Shuffled sheet	37932	0.165	3.393	0.250
Shuffled filament	41753	0.167	4.048	0.350
Shuffled knot	13457	0.165	4.499	0.484

$4\,h^{-1}\mathrm{Mpc}$, because these values minimized the root-mean-square dispersion between the fraction of galaxies assigned to each of the cosmic environments. This equal division of galaxies was necessary to ensure a sufficiently high Signal-to-Noise (SN) ratio of measurements in each of the four environments. Although we recognize they are not physically motivated, we adopt the same values of $\lambda_{\rm th}$ and σ as E15 for comparison purposes. Furthermore, our analysis likewise benefits from sufficient signal in each cosmic environment, although in our case this does not only depend on the number of lenses but also on the mass of the galaxy haloes. The total number of galaxies in each cosmic environment can be found in Table 3.1. The left panel of Fig. 3.1 gives a visual impression of the spatial distribution of galaxies in the different cosmic environments.

Stellar mass weights

For each of the four cosmic environments, the normalized stellar mass (M_*) distribution of galaxies is slightly different. As shown in Fig. 3.2, galaxies in denser environments tend to have higher stellar masses, and voids tend to have lower-mass galaxies ($\log_{10}(\frac{M_*}{\mathrm{M}_\odot}) < 9.5$) compared to the other cosmic environments. Because there exists a correlation between M_* and halo mass (e.g. Mandelbaum et al. 2006b; Moster et al. 2010; van Uitert et al. 2016), this difference should be corrected for in order to find the unbiased dependence of halo mass on cosmic environment. To this end we assign a stellar mass weight w_* to each lens, which is used to weigh the contribution of that lens to the stacked GGL profile. For 100 linearly spaced bins in

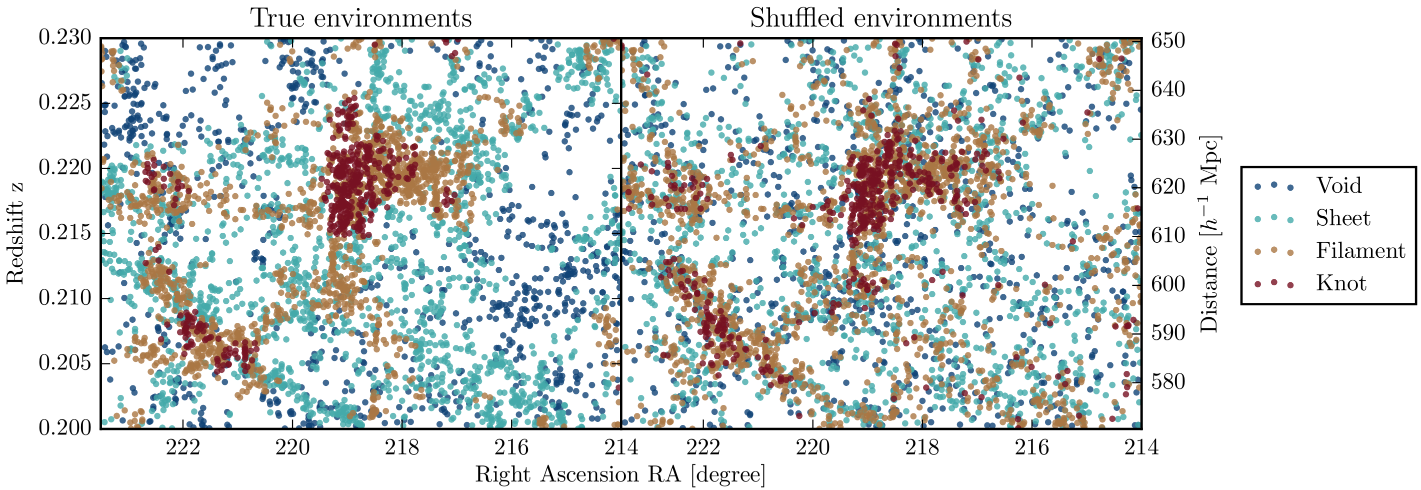

Figure 3.1: The spatial distribution of galaxies, in Right Ascension (x-axis) and redshift (left y-axis) or comoving distance (right y-axis), distinctly shows the cosmic web structure. This figure presents a slice of 5° in Declination (DEC) of a small representative part of the GAMA volume. In the left panel, the colours indicate the classification of galaxies into four cosmic environments: voids (blue), sheets (cyan), filaments (yellow), and knots (red), based on the number of spatial dimensions in which their region is collapsing (E15). In the right panel, the colours represent the corresponding shuffled environments, which only share the local density distribution of the true environments.

$\log_{10}(M_*)$, we count the number of lenses $N(M_*, E)$ in each cosmic environment E. This is compared to the average number of galaxies $\langle N\rangle(M_*)$ in all environments that reside in the corresponding M_* bin, in order to find the stellar mass weight:

$$w_*(M_*, E) = \frac{\langle N\rangle(M_*)}{N(M_*, E)}\,, \tag{3.8}$$

which is assigned to all galaxies in that M_* bin and environment. The stellar mass weight w_* is applied to each galaxy's contribution to the ESD profile through Eq. (3.7), such that it becomes:

$$\Delta\Sigma_*(R) = \frac{1}{1+K_*(R)} \frac{\sum_l w_* \sum_s W_{ls}\epsilon_{\rm t}\Sigma_{\rm crit}}{\sum_l w_* \sum_s W_{ls}}\,. \tag{3.9}$$

where the average multiplicative bias correction from Eq. (3.5) has become:

$$K_*(R) = \frac{\sum_l w_* \sum_s W_{ls} m_s}{\sum_l w_* \sum_s W_{ls}}\,. \tag{3.10}$$

Likewise the lens weight is incorporated into the uncertainty through the calculation of the analytical covariance matrix (see Sect. 3.2.2). In this way, we give higher weights to galaxies with a stellar mass that is under-represented in a specific environment compared to the average of the four environments. However, because the M_*-distributions are similar in our case, there is only a small difference between the stacked ESD profiles with or without the stellar mass weights, and we can use this correction as a reasonable approximation.

3.3.2 Local density

A complicating factor in studying the dependence of halo mass on cosmic environment, is that denser cosmic environments also have a higher average density at smaller (a few Mpc) scales: the *local density*. In order to determine the effects of the cosmic environment independent of local influences, we need to define and measure the local densities of galaxies and correct for them. We measure the local density $\rho_{\rm r}$ following McNaught-Roberts et al. (2014), who define this quantity from the number of tracer galaxies N inside a sphere of co-moving radius r around a galaxy. Following Croton et al. (2005) the tracers used for measuring N belong to a 'volume limited Density Defining Population' (DDP): the sample of galaxies

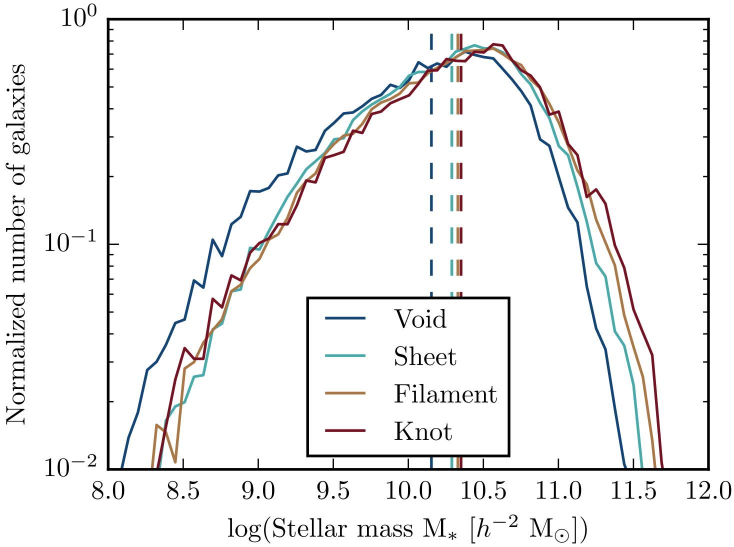

Figure 3.2: The normalized number of galaxies in each cosmic environment as a function of stellar mass M_*. Each vertical dashed lines shows the mean of the M_* distribution. The distributions show that galaxies in denser cosmic environments tend to have slightly higher stellar masses.

that is visible over the entire range in redshift z_l, given a certain cut in r-band absolute magnitude $M_r^h = M_r - 5\log_{10}(h)$ (with the k-correction and luminosity evolution correction applied). McNaught-Roberts et al. (2014) apply a narrow cut in absolute magnitude: $-21.8 < M_r^h < -20.1$, in order to preserve a relatively wide redshift range: $0.039 < z_l < 0.263$. Following this M_r^h and z_l cut, we obtain a DDP containing 44317 GAMA galaxies. We count the number of tracers N_{DDP} in a sphere around GAMA galaxies to determine their local density:

$$\rho_r = \frac{N_{\mathrm{DDP}}}{\frac{4}{3}\pi r^3}\frac{1}{C_v C_z}\,, \tag{3.11}$$

where C_v is the volume correction accounting for the fraction of the sphere lying outside the boundaries of the survey or redshift cut, and C_z accounts for the redshift completeness of the volume (measured using the GAMA masks).

In order to determine the local overdensity δ_r within co-moving radius r around a galaxy, we compare ρ_r to the mean DDP number density $\bar{\rho}$ over the full GAMA volume:

$$\delta_{\mathrm{r}} = \frac{\rho_{\mathrm{r}} - \bar{\rho}}{\bar{\rho}} \,. \tag{3.12}$$

When corrected for redshift completeness using the GAMA masks, the total volume (within the designated redshift range) of the three equatorial GAMA fields is $V_{\mathrm{GAMA}} = 7 \times 10^6 (\,h^{-1}\mathrm{Mpc})^3$, resulting in an effective mean DDP galaxy density of $\bar{\rho} = 6 \times 10^{-3} (\,h^{-1}\mathrm{Mpc})^{-3}$.

Using the DDP we measure the value of δ_4, the overdensity within $r = 4\,h^{-1}\mathrm{Mpc}$, for *all* GAMA galaxies within the redshift range of the DDP (including those outside the absolute magnitude range), amounting to a sample of $\sim\ 113,000$ lenses. We choose spheres with $r\ =\ 4\,h^{-1}\mathrm{Mpc}$ to probe local overdensities at the scale of the correlation length of the LSS (Budavari et al. 2003), which is also the smallest possible scale that still avoids major problems related to scarce tracer galaxies and redshift space distortion on small scales (Croton et al. 2005). For each cosmic environment we find a different distribution in δ_4, as shown in Fig. 3.3. Not surprisingly denser environments (e.g. knots) contain more galaxies with high local overdensity, while sparser environments (e.g. voids) have lower overdensities. Note, however, that there exists a significant overlap between the different overdensity distributions. This overlap allows us to separate the effect of the cosmic environment on the ESD profile from the effect of local overdensity, enabling us to study the direct dependence of the cosmic environment on halo mass. By shuffling galaxies between the cosmic environments while keeping the local overdensity distribution the same, we create so-called shuffled environments.

3.3.3 Shuffled environments

To account for the different local density distributions in each cosmic environment, we follow E15 in creating a set of four *shuffled environments*: galaxy samples that retain the local overdensity distribution of the true cosmic environments, but contain galaxies that are randomly selected from all cosmic environments, effectively erasing the information from the environment classification. By comparing the galaxies in each shuffled environment to those from the corresponding true environment, we are able to eliminate any dependence on the local overdensity, and extract the effects of the cosmic environment alone.

In practice, all galaxies are divided into 100 δ_4 bins. For each true cosmic environment we create a shuffled environment, by assigning the same

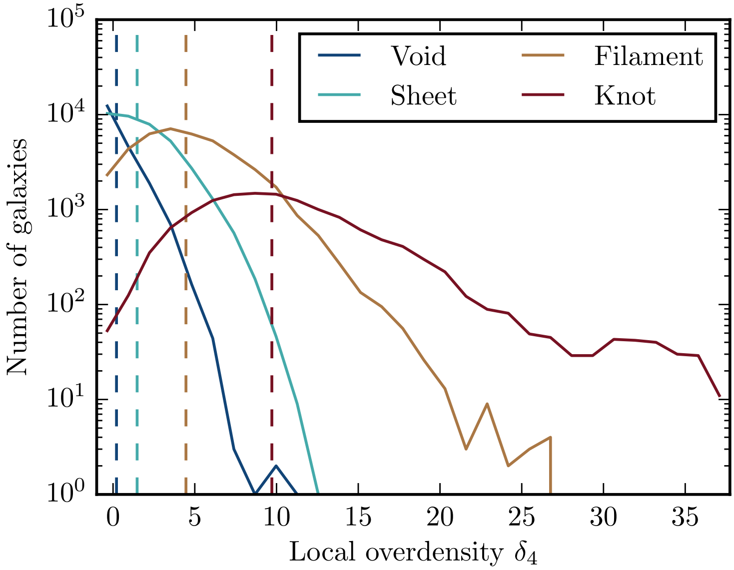

Figure 3.3: The number of galaxies in each environment as a function of local overdensity δ_4 (overdensity within a $4\,h^{-1}\mathrm{Mpc}$ radius). Each vertical dashed line shows the mean of the δ_4 distribution. As expected galaxies in denser cosmic environments tend to have higher local overdensities, although there remains significant overlap between the distributions.

number of galaxies in each δ_4 bin to the corresponding shuffled environment. These galaxies, however, are randomly selected from the full sample, and could therefore be residing in any cosmic environment. Randomly selected galaxies from a high δ_4 bin will be more likely to reside in knots than in voids (due to the correlation between local density and cosmic environment), but every shuffled environment contains a distribution of galaxies from different true environments due to the overlapping δ_4 distributions (see Fig. 3.3). The proportion of galaxies from true cosmic environments residing in each shuffled environment can be seen in Fig. 3.4, which shows that up to half of the galaxies in each shuffled environment originate from the same true cosmic environment. In the right panel of Fig. 3.1 we show the spatial distribution of galaxies in different shuffled environments, which is likewise correlated with the distribution of galaxies in true cosmic environments shown in the left panel. Although the correlation between the true and shuffled environments complicates the detection of a direct effect from cosmic environments, the relationship between cosmic environment and local density cannot be circumvented in another way without significantly

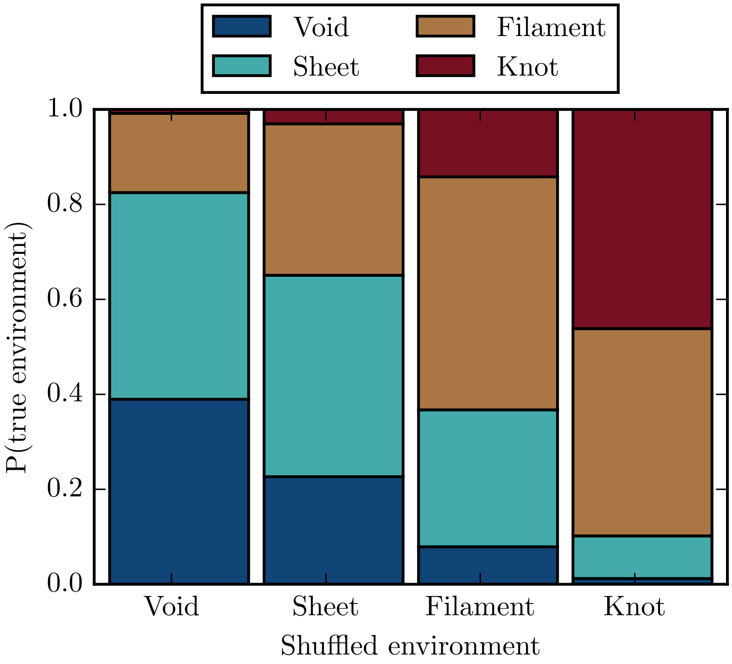

Figure 3.4: The proportion of galaxies from each true cosmic environment that is present in each shuffled environment. As expected a large fraction of galaxies in each shuffled environment originates from the same true environment, although that fraction is < 0.5 for all shuffled environments.

reducing the lens sample. Furthermore, selecting a very different galaxy sample or shuffling method complicates the comparison with the results from E15. We can slightly reduce the proportion of knot galaxies in knots by removing all galaxies with $\delta_4 > 15$ from our sample, but this small effect does not significantly affect our results.

3.4 Analysis of the lensing profiles

3.4.1 Contributions of group samples

To obtain the ESD profile of galaxies in each cosmic environment, we stack the lensing signals of these galaxies as detailed in Sect. 3.2. The interpretation of this stacked ESD profile is complicated by the fact that galaxies, apart from residing in a cosmic environment, may also belong to a galaxy group. We use the 7th GAMA Galaxy Group Catalogue (G^{3}Cv7, Robotham et al. 2011) to identify the group classification of the lenses that contribute to the stacked ESD profile of each cosmic environment. In Fig. 3.5 we show the contribution of different galaxy selections to the total ESD profile of galaxies in the knot environment, where we find the contribution from satellites and neighbouring galaxies to be the largest. We show the signal for central galaxies only, and add the contribution from non-group galaxies, satellite galaxies, or both (all galaxies). The correction for the difference in the stellar mass distribution of the cosmic environments has been applied during the stacking procedure (see Sect. 3.3.1). The GGL profile in knots shows that, after the first radial bin, the ESD is consistent for all lens samples at scales $R < 200\,h^{-1}\mathrm{kpc}$, where the haloes of the stacked galaxies themselves dominate (as opposed to haloes of neighbouring galaxies). Within the first bin we see a hint of the expected difference between central, non-group and satellite galaxy masses (in order of expected mass), although the differences stay within 1σ. However, at $R > 200\,h^{-1}\mathrm{kpc}$ the GGL signal changes significantly with the addition of satellite galaxies to the stack. Where the ESD profiles of lens samples without satellites drop sharply, the profiles of samples with satellites does not, due to the off-set contribution of the satellites' host haloes (also seen in Sifón et al. 2015). These changes in the ESD profile imply that, as the contributions from different group members are added to the stacked signal, we need to model these different components to account for the total lensing signal. This complicates the interpretation of differences between the ESD profiles in the cosmic environments, including halo mass estimates.

Although the sample containing only group centrals is the simplest to model, the low SN ratio of the lensing signal might prohibit the analysis if the SN ratio is too low to even find the expected difference between the four cosmic environments (as measured in e.g. E15), let alone a difference between true and shuffled environments. In order to find whether this is the case, we apply a χ^2 independence test to the ESD profiles $\Delta\Sigma$ in different environments E1 and E2:

$$\chi^2 = \sum_R \frac{(\Delta\Sigma_R^{\mathrm{E1}} - \Delta\Sigma_R^{\mathrm{E2}})^2}{(\sigma_R^{\mathrm{E1}})^2 + (\sigma_R^{\mathrm{E2}})^2}\,, \tag{3.13}$$

where the index R sums over the radial bins, and σ is the uncertainty on $\Delta\Sigma$ calculated from the analytical covariance matrix. We calculate the probability $P(\chi^2)$ to draw the $\Delta\Sigma$ values in question from the same normal distribution, by evaluating the cumulative normal distribution function with

$10 - 1 = 9$ degrees of freedom (based on the 10 radial bins) at χ^2. We consider the difference between the ESD profiles in two cosmic environments to be significant if $P(\chi^2) < 0.05$. Figure 3.6 shows a diagram of the result of the χ^2 independence test for two samples: 'all galaxies' (top) and only 'centrals' (bottom). For the sample of centrals there is no measurable difference between the ESD profiles from any of the environments. For the sample of all galaxies there is also no significant difference between voids and sheets, or between filaments and knots; two combinations that can be considered to be 'adjacent' in density space. However, there is a measurable difference between sheets and filaments which are likewise adjacent. In fact, every comparison that 'crosses' the dotted vertical line between sheets and filaments results in a measurable difference.

In conclusion, this test shows that the difference between the four environments cannot be detected when the stacked ESD profiles contain only the contributions from central galaxies. As a result, we need to add and model the contribution from multiple group members: centrals, satellites and non-group galaxies, in order to measure the average halo mass of galaxies in different cosmic environments.

In this test we can include all or a subset of our 10 radial bins between $20\,h^{-1}\mathrm{kpc} < R < 2000\,h^{-1}\mathrm{kpc}$. We therefore repeat this analysis to test whether the difference between the ESD profiles in the cosmic environments is more significant at small scales (by summing over the five innermost radial bins) or large scales (by summing over the five outermost radial bins). Through this test we found that, when all galaxies contribute to the signal, the difference between the ESD profiles in the four cosmic environments is primarily driven by the large scales, indicating that satellites and neighbouring haloes have a major effect on the ESD profiles.

3.4.2 Surface density model

In order to extract the average halo masses from the ESD profiles, we construct a mathematical description of the main contributions to the ESD profile in terms of the stellar and DM components of different galaxy group members, based on the classification by Robotham et al. (2011) of GAMA galaxies into central, satellite and non-group galaxies. Although they have no (visible) satellites we treat non-group galaxies as centrals of groups, which means the two main components of the model correspond to the mass contribution from 'centrals' (real centrals and non-group galaxies) and satellites, both residing in the main host halo (which corresponds to the halo of the 'central'). Following the prescription of Wright and Brain-

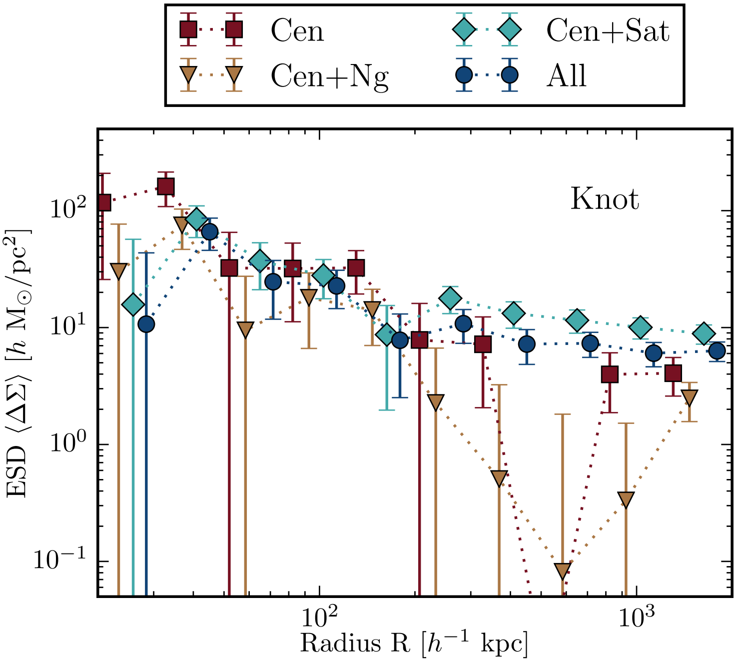

Figure 3.5: The ESD profiles (with 1σ error bars) of GAMA galaxies in the knot environment, stacked according to their group membership and weighted to correct for differences in the stellar mass distribution. The different ESD profiles correspond to four group samples: centrals only (Cen), centrals and non-group (Cen+Ng), centrals and satellites (Cen+Sat), and all galaxies (All: centrals, satellites and non-group). The dotted lines are used to guide the eye between data points of the same group sample.

erd (2000), we model the DM contribution of both centrals and satellites by an NFW profile (Navarro et al. 1995):

$$\rho_{\rm NFW}(r) = \frac{\delta_{\rm c}\rho_{\rm m}(\langle z\rangle)}{(r/r_{\rm s})(1+r/r_{\rm s})^2}\,, \tag{3.14}$$

where $r_{\rm s}$ is the scale radius and $\rho_{\rm m}(\langle z\rangle)$ is the mean density of the Universe, which depends on the mean redshift $\langle z\rangle$ of the lens sample as:

$$\rho_{\rm m} = 3H_0^2(1+\langle z\rangle)^3\Omega_{\rm m}/(8\pi G)\,. \tag{3.15}$$

The dimensionless amplitude is related to the concentration $c = r_{200}/r_{\rm s}$ via:

$$\delta_{\rm c} = \frac{200}{3}\frac{c^3}{\ln(1+c) - c/(1+c)}\,. \tag{3.16}$$

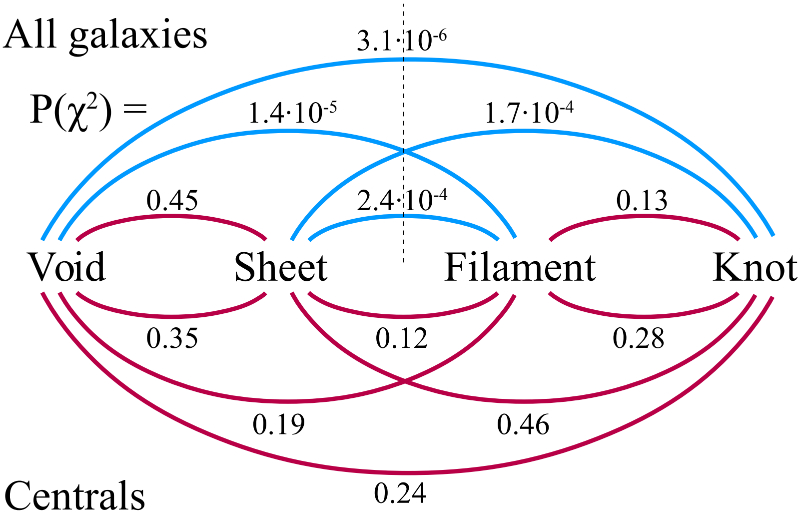

Figure 3.6: The resulting $P(\chi^2)$ values of the χ^2 independence test between the ESD profiles $\Delta\Sigma(R)$ from different cosmic environments, shown for two galaxy samples: all galaxies (top) and centrals only (bottom). When the probability $P(\chi^2)$ to draw the $\Delta\Sigma(R)$ values in question from the same normal distribution is less than 0.05, the line between those environments is coloured blue (independent), otherwise red (dependent). The dotted vertical line emphasises the fact that the difference between two environments is significant when it crosses the border between sheet and filament. This figure shows that the stacked ESD profiles of only centrals do not show any significant difference between cosmic environments, whereas the stacked profiles of all galaxies do.

We include two free parameters in the model: the concentration normalization f_c, which is the normalization of the Duffy et al. (2008) mass-concentration relation[2]

$$c(M_{200}, z) = 10.14 f_\mathrm{c} \left(\frac{M_{200}}{2 \times 10^{12} \mathrm{M}_\odot} \right)^{-0.089} (1+z)^{-1.01} \, , \qquad (3.17)$$

---

[2] We realize that this mass-concentration relation is slightly dated compared to that of e.g. Dutton and Macciò (2014), which is based on the Planck XVI (2014) cosmology. However, we follow the earlier KiDS-GAMA lensing papers (Viola et al. 2015; Sifón et al. 2015; van Uitert et al. 2016), to which our results could then be compared. Furthermore, because of the weak relation of $c(M_{200}, z)$ on M_{200}, and the relatively small z-range of the GAMA galaxies, the final expression for the concentration will be dominated by the normalization parameter f_c, and not by the chosen mass-concentration relation.

and the halo mass M_{200}, which is defined as the virial mass within r_{200} (the radius that encloses a density $\rho(< r_{200}) = 200\rho_{\rm m}(z)$). The virial mass of the halo thus defined is a free parameter for both centrals ($M_{\rm cen}$) and satellite galaxies ($M_{\rm sat}$). In this way, $M_{\rm cen}$ and $M_{\rm sat}$ parametrize the average mass per central/satellite galaxy respectively. The concentration normalization $f_{\rm c}$ is only a free parameter for centrals. Since the satellite contribution to the ESD profile is too small to constrain both $M_{\rm sat}$ and $f_{\rm c}^{\rm sat}$, we fix the latter to 1. Apart from the physical concentration of the halo, $f_{\rm c}$ is affected by mis-centering: the off-set between the (assumed) central galaxy and the actual centre of the DM halo. Because $f_{\rm c}$ mitigates the impact of mis-centering, the measured halo mass is not biased by this effect (as shown by Viola et al. 2015). In addition to the DM halo, we add the contribution of the stellar component, which is modelled as a point mass with $M = \langle M_* \rangle$, the mean stellar mass of the galaxy sample. This component is added to the contribution of both centrals and satellites.

In the case of the satellite contribution to the ESD profile, the DM halo of the host group is modelled by an offset NFW profile. Each stacked satellite adds a host contribution at its respective projected distance $R_{\rm sat}$ to the group central, such that the total host contribution is integrated over the number distribution $n(R_{\rm sat})$ (see Sifón et al. 2015 for a more detailed description). The two ESD components related to satellite galaxies are multiplied by the satellite fraction $f_{\rm sat}$: the fraction of satellites with respect to the total number of galaxies (including satellites, centrals and non-group galaxies). The ESD component due to centrals (real centrals and non-group galaxies) is in turn multiplied by the central fraction ($= 1 - f_{\rm sat}$). The values of the satellite fraction for the (shuffled) cosmic environments are shown in Table 3.1. As expected, the fraction of satellites increases with the density of the cosmic environment.

At scales above $200\,h^{-1}$kpc the neighbouring host haloes add significant contribution to the ESD signal, known as the 2-halo term. This term is modelled by the two-point matter correlation function $\xi(z, r)$ (van den Bosch 2002), which is multiplied by the empirical bias function $b(M)$ (Tinker et al. 2010). As the halo mass M we use the average mass of the central haloes $M_{\rm cen}$. Because we expect that the 2-halo term varies significantly depending on the average density of each cosmic environment, and the correlation function was measured by averaging over all space, we multiply the $\xi(z, r)$ term by a free parameter: the 2-halo amplitude $A_{\rm 2h}$. The final 2-halo contribution becomes:

$$\Delta\Sigma^{\rm 2h}_{\rm cen}(R) = A_{2h}\, b(M_{\rm cen})\, \Delta\Sigma(\xi(R))\,, \tag{3.18}$$

which allows for the flexibility to cover ESD profiles in environments of various densities.

In total, the full model contains four ESD components contributing to the total ESD profile: the central and satellite components ($\Delta\Sigma^{\rm 1h}_{\rm cen}$ and $\Delta\Sigma^{\rm 1h}_{\rm sat}$, modelled by an NFW profile and stellar point mass), the host term corresponding to the satellites ($\Delta\Sigma^{\rm 1h}_{\rm host}$, modelled by an off-set NFW) and the 2-halo term ($\Delta\Sigma^{\rm 2h}_{\rm cen}$, modelled by a scaled matter correlation function):

$$\begin{aligned}\Delta\Sigma(R) = (1 - f_{\rm sat}) \times \Delta\Sigma^{\rm 1h}_{\rm cen}(R|M_{\rm cen}, f_{\rm c}^{\rm cen}) +& \\ f_{\rm sat} \times (\Delta\Sigma^{\rm 1h}_{\rm sat}(R|M_{\rm sat}) + \Delta\Sigma^{\rm 1h}_{\rm host}(R|M_{\rm cen})) +& \\ \Delta\Sigma^{\rm 2h}_{\rm cen}(R|A_{\rm 2h}, M_{\rm cen})\,.&\end{aligned} \tag{3.19}$$

Together, these four components contain four free parameters: the average halo mass of centrals ($M_{\rm cen}$) and satellites ($M_{\rm sat}$), the concentration parameter of centrals ($f_{\rm c}^{\rm cen}$), and the 2-halo amplitude ($A_{\rm 2h}$), as shown inside the brackets of Eq. (3.19) (where, for brevity, fixed parameters are not shown). Each of these parameters is free for all four cosmic environments, such that our model contains a total of 16 free parameters. The priors of all free parameters are shown in Table 3.2, while all fixed values used in the fit can be found in Table 3.1.

This model is fitted to the ESD profiles of the four cosmic environments using the EMCEE sampler (Foreman-Mackey et al. 2013), which ingests our model into a Markov Chain Monte Carlo (MCMC). During the fitting procedure, a number of walkers $N_{\rm walkers}$ is moving through the parameter space for a designated number of steps $N_{\rm steps}$, where the direction of each next step is based on the affine invariance method (Goodman and Weare 2010). Using the Gelman-Rubin convergence diagnostic (Gelman and Rubin 1992), we find that we need $N_{\rm walkers} = 100$ and $N_{\rm steps} = 5000$ for our chain to converge. Of the resulting 500,000 evaluations the first 100,000 are discarded as the burn-in phase, leaving a total of 400,000 evaluations. From these evaluations we estimate the values of the free parameters by taking the median (50th percentile), and their 1σ uncertainties by taking the 16th and 84th percentile. The minimal χ^2 of our chains is 28.0 for true cosmic environments, and 34.2 for shuffled environments. Since the four cosmic environments combined contain $4 \times 10 = 40$ data-points and $4 \times 4 = 16$ free parameters, the number of degrees of freedom (equal to the expected minimum χ^2) is $N_{\rm dof} = 40 - 16 = 24$. Consequently the reduced χ^2 of our chains is $28.0/24 = 1.17$ for true cosmic environments, and $34.2/24 = 1.43$ for shuffled environments. In the Gaussian case the uncertainty on χ^2 is $\sigma_{\chi^2} = \sqrt{2(N_{\rm dof})} = 6.93$ (Gould 2003). This indicates

Table 3.2: Priors and median posterior values (with 16th and 84th percentile error bars) of the free parameters in the model fit: the average mass of central and satellite galaxies (in units of $[10^{12}\mathrm{M}_\odot]$), the central concentration parameter and the 2-halo amplitude, in both true and shuffled cosmic environments.

parameter	$M_{\rm cen}$	$M_{\rm sat}$	$f_{\rm c}^{\rm cen}$	$A_{\rm 2h}$
prior type	flat	flat	Gaussian	flat
prior range	[0.1, 10]	[0.01, 5]	$\mu = 1, \sigma = 0.3$	[0, 20]
voids	$0.75^{+0.31}_{-0.28}$	$2.10^{+1.85}_{-1.41}$	$1.05^{+0.21}_{-0.19}$	$0.93^{+0.72}_{-0.60}$
sheets	$0.74^{+0.63}_{-0.44}$	$1.81^{+2.16}_{-1.40}$	$0.77^{+0.25}_{-0.24}$	$1.50^{+0.79}_{-0.78}$
filaments	$1.43^{+0.86}_{-1.02}$	$0.72^{+2.00}_{-0.54}$	$0.73^{+0.22}_{-0.22}$	$5.22^{+1.18}_{-1.22}$
knots	$0.94^{+1.06}_{-0.63}$	$1.00^{+1.15}_{-0.70}$	$0.95^{+0.22}_{-0.21}$	$10.30^{+2.27}_{-2.25}$
shuffled voids	$0.77^{+0.41}_{-0.33}$	$2.36^{+1.80}_{-1.68}$	$0.87^{+0.20}_{-0.21}$	$1.81^{+0.79}_{-0.78}$
shuffled sheets	$0.48^{+0.48}_{-0.28}$	$2.20^{+1.84}_{-1.64}$	$0.88^{+0.24}_{-0.23}$	$2.77^{+0.70}_{-0.65}$
shuffled filaments	$1.29^{+0.75}_{-0.90}$	$0.72^{+2.01}_{-0.53}$	$0.77^{+0.25}_{-0.25}$	$4.03^{+0.95}_{-0.96}$
shuffled knots	$1.11^{+1.20}_{-0.71}$	$1.81^{+1.51}_{-1.18}$	$0.99^{+0.22}_{-0.21}$	$9.45^{+1.85}_{-1.79}$

that the minimum χ^2 value lies well within 1σ of the expected minimum χ^2 for true environments, and just outside for shuffled environments.

3.5 Results

In order to determine the masses of galaxy haloes as a function of their location in the cosmic web, we measure the average GGL profiles (as detailed in Sect. 3.2) in each of the four cosmic environments (defined in Sect. 3.3.1). These ESD profiles are corrected for the measured increase in stellar mass in increasingly dense cosmic environments (shown in Sect. 3.3.1). By fitting our ESD model (as described in 3.4.2) to these data, we determine the average halo mass of galaxies in each cosmic environment. By applying an identical model to the stacked ESD profiles of galaxies in shuffled cosmic environments (defined in 3.3.3), we can compare their resulting fit parameters. Because the only information from the true cosmic environments that goes into the shuffled environments is that of their local density distribution, any difference between these parameters indicates an effect caused by the cosmic environment alone, i.e. not due to the effects of the local density δ_4. The resulting model fit to the ESD profiles of the four cosmic environments is shown in Fig. 3.7. The resulting values of the free parameters: $M_{\rm cen}$, $M_{\rm sat}$, $f_{\rm c}^{\rm cen}$ and $A_{\rm 2h}$, for both the true and the shuffled environments can be found in Table 3.2 and Fig. 3.8.

In the case of the true cosmic environments, the average halo mass of central galaxies $M_{\rm cen}$ remains constant within the measured uncertainties. Contrary to our expectations, the halo masses of satellites sometimes seem to exceed those of centrals. However, although the median posterior value of $M_{\rm sat}$ can exceed that of $M_{\rm cen}$, the width of the posteriors span almost the whole prior range. We therefore conclude that our model fit is not able to provide any constraints on the satellite mass as a function of environment. When using a flat prior on the concentration of the central halo, we find that the value of $f_{\rm c}^{\rm cen}$ decreases drastically for denser cosmic environments. This is not due to a physical decrease in the concentration of the central halo, as is apparent from the ESD profiles of the galaxy sample containing only centrals. These profiles do not show a significant decrease in the concentration of the central halo in denser cosmic environments (see e.g. the ‘knot’ ESD profile in Fig. 3.5). It is more likely that the increasing signal at larger scales is caused by the increasing number of satellites and neighbouring haloes in denser environments, since the satellite host and 2-halo terms are degenerate with the central concentration. Based on this

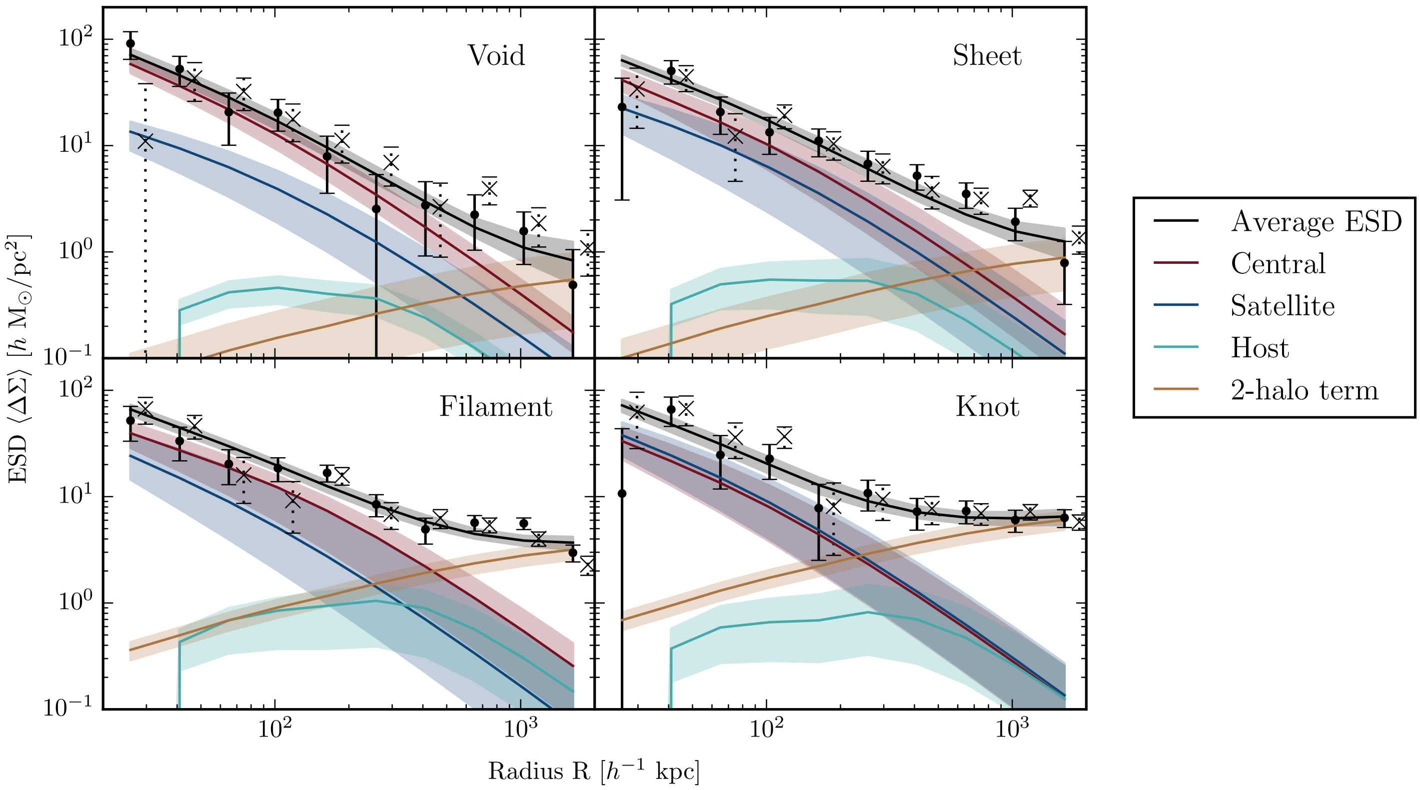

Figure 3.7: The ESD profiles of GAMA galaxies, stacked according to their cosmic environment and weighted to correct for differences in the stellar mass distribution. The four panels represent the different cosmic environments. The dots with 1σ error bars represent the measurement, while the lines with error bands show the median and 16th/84th percentile of different components of the ESD model fit to the ESD measurement. The model consists of a central term (red), a satellite term (blue) with corresponding offset host halo term (cyan), and a 2-halo term (yellow). All these terms combine into the total median profile, shown in black. For comparison, we also show the ESD measurement from the shuffled environments as crosses with dotted 1σ error bars.

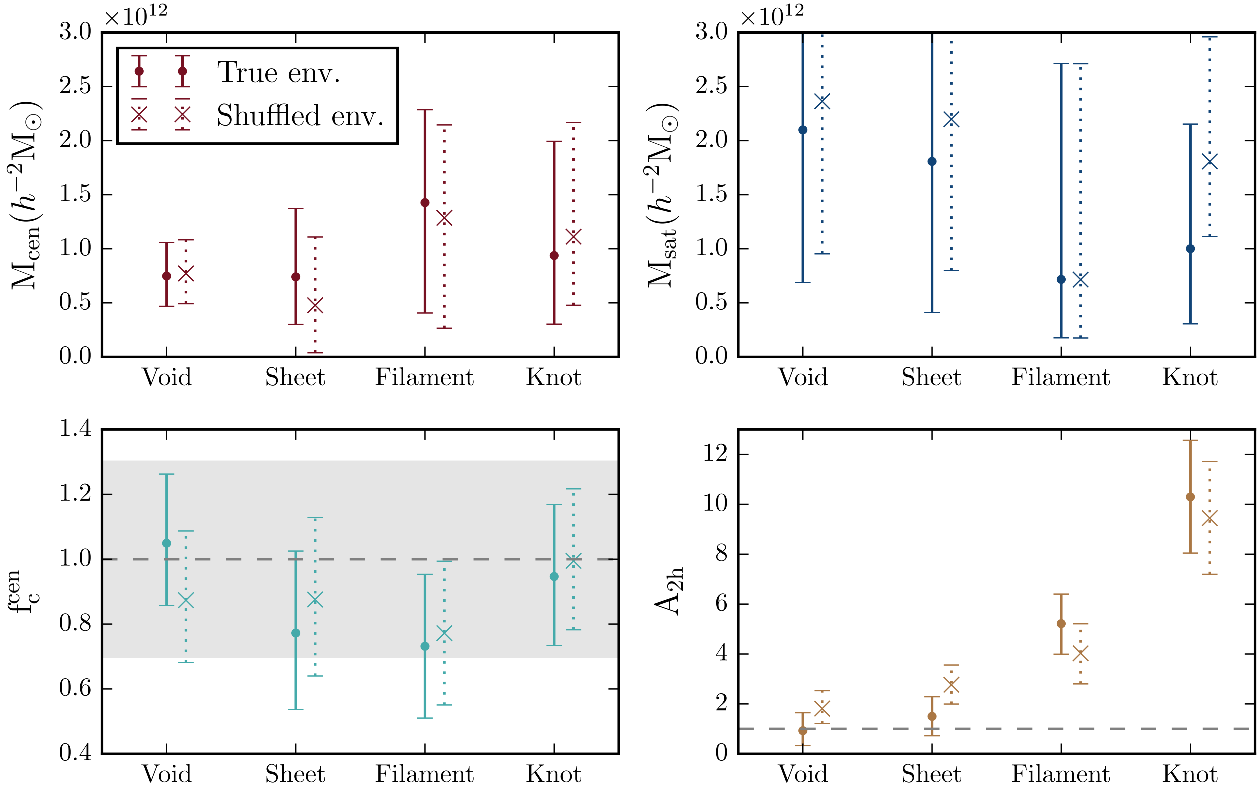

Figure 3.8: The median parameters resulting from the model fit to the ESD profiles in the four cosmic environments, including 16th and 84th percentile error bars. The top panels show (from left to right) the average halo mass of the centrals (red) and satellite galaxies (blue). The bottom left panel shows the concentration parameter f_c of the centrals (cyan), with a band representing the centre μ and dispersion σ of its Gaussian prior. The bottom right panel shows the amplitude of the 2-halo term (yellow), where the dashed line shows the fiducial value. The data points with solid error bars represent the parameters extracted from the ESD profiles of true cosmic environments, while the crosses with dotted error bars represent those from the shuffled environments.

information we use a Gaussian prior with a central value of $\mu = 1$ and a standard deviation of $\sigma = 0.3$, which prevents the decrease of $f_{\mathrm{c}}^{\mathrm{cen}}$. In the resulting fit, the rising signal at larger scales is accounted for by the satellite host and 2-halo terms. As the density of the cosmic environment increases, $A_{2\mathrm{h}}$ increases by a factor ~ 10. This behaviour is expected because, due to the increase in the local density δ_4 for increasingly dense environments (see Fig. 3.3) the contribution of neighbouring haloes to the lensing signal increases.

In Fig. 3.8 we compare the resulting parameter values with those found using shuffled environments, and find that all parameter values are the same within the 1σ error bars. Considering the width of the posterior distributions we conclude that there is no measurable difference between the parameters in true and shuffled cosmic environments, suggesting that the dominant effect on halo mass is that of the local density.

3.6 Discussion and conclusion

We measure the galaxy-galaxy lensing (GGL) signal of 91195 galaxies (within $0.039 < z < 0.263$) from the spectroscopic Galaxy And Mass Assembly (GAMA) survey that overlap with the first $109\,\mathrm{deg}^2$ of photometric data from the Kilo-Degree Survey (KiDS). We use the GGL signal to measure the average halo mass of galaxies in four different cosmic environments: voids, sheets, filaments and knots, classified by Eardley et al. (2015). We create a corresponding set of shuffled environments which retain the distribution in local density (the galaxy overdensity within $4\,h^{-1}\mathrm{Mpc}$) of the true environments, but lose the information bound to the cosmic web environment. By comparing the average halo masses from galaxy samples in true and shuffled cosmic environments, we isolate the effect of the cosmic environments on galaxy halo masses from that of the local density. We extract the average halo masses from the measured Excess Surface Density (ESD) profiles by fitting a simple model consisting of a central, a satellite, an off-set host and a 2-halo contribution to the GGL signal. After correcting for the increase in the stellar mass of galaxies in increasingly dense cosmic environments, we find no difference in the average halo mass of central galaxies in different cosmic environments. Our constraints on the average mass of satellite galaxies are to weak to make any statements. The amplitude of the 2-halo term, however, increases significantly from voids to knots. This increase in the 2-halo contribution to the ESD profile is expected, as the local density (within $4\,h^{-1}\mathrm{Mpc}$) increases with the density of the cosmic environment.

The posterior distributions of the obtained parameters show no significant difference between the haloes in true and shuffled cosmic environments. We can conclude that, within the statistical limits of our survey, the cosmic environment has no measurable effect on galaxy halo mass apart from the effects related to the local density. This null-result is in agreement with the study of Eardley et al. (2015), who found a strong variation in the Luminosity Function (LF) of galaxies in the four cosmic environments, but no significant difference between the LF in true and shuffled cosmic environments, concluding that the measured effect on the LF could be entirely attributed to the difference in local density of the galaxy populations. Using N-body simulations Alonso et al. (2015) studied the dependence of the DM halo mass function on the four cosmic environments. Although they found a strong correlation of the conditional mass function with cosmic environment, they showed that this is caused by the coupling of the cosmic environments to the local density. Using a different classification of GAMA galaxies into cosmic environments (filaments, tendrils and voids), Alpaslan et al. (2015) measured the effect of the cosmic web on energy output, $u - r$ colour, luminosity, metallicity and morphology of galaxies in both cosmic and local environment. In order to remove the effect due to the difference in the stellar mass distributions, they resampled the galaxy population from each cosmic environment. They found that, as long as they apply this correction, the properties of galaxies in different cosmic environments are approximately identical, and concluded that the effects of large-scale structure on galaxy properties are negligible with respect to the effects from stellar mass and local environment. Darvish et al. (2014), who measured the star formation rate (SFR) of galaxies as a function of another cosmic environment classification scheme (fields, filaments, and clusters), found that their observed stellar mass and median SFR, as well as the SFR-mass relation and specific SFR, are mostly independent of environment. They did, however, find a significant increase in the fraction of star forming galaxies in filaments. Although the sub-dominance of the effect of large-scale structure on galaxy properties was foreshadowed by many studies, this is the first direct measurement of the effect of the cosmic web on galaxy halo mass.

Based on our results we conclude that, after correcting for local density and stellar mass, the cosmic environments alone have no measurable effect on DM halo parameters. Even if such an effect exists, future lensing studies would need to reduce the uncertainties on the posteriors found in this study by at least a factor ~ 3. Assuming the same approach is used, these studies would require a KiDS-like photometric lensing survey overlapping with a GAMA-like spectroscopic survey of approximately ten times the size of our current $\sim 100\,\mathrm{deg}^2$ of overlapping data. Of the present-day photometric lensing surveys, the Dark Energy Survey (DES, The Dark Energy Survey Collaboration et al. 2015) currently has $139\,\mathrm{deg}^2$ at its disposal, which is planned to increase to $\sim 5000\,\mathrm{deg}^2$ over the next five years. However, DES currently has no overlap with a spectroscopic survey of the area and completeness of the GAMA survey. The Dark Energy Spectroscopic Instrument (DESI, Levi et al. 2013), which will serve this purpose, is planned to start nominal operation in 2019. Over the next five years KiDS is planning to observe $\sim 1500\,\mathrm{deg}^2$ of the sky (de Jong et al. 2013), overlapping with $\sim 700\,\mathrm{deg}^2$ of spectroscopic data from the Wide Area Vista Extragalactic Survey (WAVES, Driver et al. 2015), nearing the precision needed to find or rule out an effect from the cosmic web on galaxy haloes. Furthermore, we expect that the Euclid mission (Laureijs et al. 2011), with a planned $\sim 15,000\,\mathrm{deg}^2$ of high-quality lensing data, will be able to confirm or negate a possible effect from cosmic environments with very high significance. However, with an estimated launch in 2020 and a nominal mission period of five years, this would take at least five more years to accomplish. Taking all these future missions into consideration we conclude that, using the technique described here, it is unlikely that a direct effect of cosmic environment on halo mass can be measured within the next four to five years.

Acknowledgements

We thank Alexander Mead for useful comments on the manuscript. C. Heymans, M. Viola, M. Cacciato, H.Hoekstra, C. Sifón, A. Choi and C. Heymans acknowledge support from the European Research Council under FP7 grant number 279396 (MV, MC, CS, H.Ho), grant number 240185 (AC and CH) and grant number G47112 (CH). M. Viola acknowledges support from the Netherlands Organisation for Scientific Research (NWO) through grants 614.001.103. H. Hildebrandt is supported by an Emmy Noether grant (No. Hi 1495/2-1) of the Deutsche Forschungsgemeinschaft. R. Nakajima acknowledges support from the German Federal Ministry for Economic Affairs and Energy (BMWi) provided via DLR under project no. 50QE1103. T. M. Roberts and P. Norberg acknowledge support from an European Research Council Starting Grant (DEGAS-259586). This work is supported by the Deutsche Forschungsgemeinschaft in the framework of the TR33 'The

Dark Universe'. G. Verdoes Kleijn acknowledges financial support from the Netherlands Research School for Astronomy (NOVA) and Target. Target is supported by Samenwerkingsverband Noord Nederland, European fund for regional development, Dutch Ministry of economic affairs, Pieken in de Delta, Provinces of Groningen and Drenthe. E. van Uitert acknowledges support from an STFC Ernest Rutherford Research Grant, grant reference ST/L00285X/1.

This research is based on data products from observations made with ESO Telescopes at the La Silla Paranal Observatory under programme IDs 177.A-3016, 177.A-3017 and 177.A-3018, and on data products produced by Target OmegaCEN, INAF-OACN, INAF-OAPD and the KiDS production team, on behalf of the KiDS consortium. OmegaCEN and the KiDS production team acknowledge support by NOVA and NWO-M grants. Members of INAF-OAPD and INAF-OACN also acknowledge the support from the Department of Physics & Astronomy of the University of Padova, and of the Department of Physics of Univ. Federico II (Naples).

GAMA is a joint European-Australasian project based around a spectroscopic campaign using the Anglo-Australian Telescope. The GAMA input catalogue is based on data taken from the Sloan Digital Sky Survey and the UKIRT Infrared Deep Sky Survey. Complementary imaging of the GAMA regions is being obtained by a number of independent survey programs including GALEX MIS, VST KiDS, VISTA VIKING, WISE, Herschel-ATLAS, GMRT and ASKAP providing UV to radio coverage. GAMA is funded by the STFC (UK), the ARC (Australia), the AAO, and the participating institutions. The GAMA website is `www.gama-survey.org`.

This work has made use of PYTHON (`www.python.org`), including the packages NUMPY (`www.numpy.org`), SCIPY (`www.scipy.org`) and IPYTHON (Pérez and Granger 2007). Plots have been produced with MATPLOTLIB (Hunter 2007).

Author contributions: All authors contributed to the development and writing of this paper. The authorship list reflects the lead authors (MB, MC) followed by two alphabetical groups. The first alphabetical group includes those who are key contributors to both the scientific analysis and the data products. The second group covers those who have made a significant contribution either to the data products or to the scientific analysis.

4 Trough Lensing with KiDS, GAMA and MICE

Based on: “A weak lensing study of troughs using the KiDS, GAMA and MICE galaxy catalogues” *(in preparation)*
Authors: Margot M. Brouwer *et al.*

Abstract:

We study projected underdensities in the cosmic galaxy density field called ‘troughs’, and their overdense counterparts which we call ‘ridges’. For their classification we use a bright sample of foreground galaxies from the photometric Kilo-Degree Survey (KiDS), specifically selected for comparison to the spectroscopic Galaxy And Mass Assembly (GAMA). Using an independent sample of KiDS background galaxies, we measure the weak gravitational lensing profiles of the troughs and ridges. We quantify the amplitude A of the lensing signal as a function of their galaxy density percentile P and overdensity δ, and use this to optimally stack the signal, which is detected with a signal to noise of $|S/N| = \{17.1, 14.8, 10.0, 7.6\}$ for troughs with a projected radius $\theta_{\rm A} = \{5, 10, 15, 20\}$ arcmin. We find that the skewness in the galaxy density distribution of troughs/ridges is reflected in the total mass distribution measured by weak lensing. We compare our results by applying the same procedures to a mock galaxy sample from the MICE Grand Challenge lightcone simulation, and find a good agreement between our observations and the simulation. Finally, we select troughs using a volume limited sample of galaxies, divided into two redshift bins between $0.1 < z < 0.3$. For troughs/ridges with comoving projected radius $R_{\rm A} = 1.9\, h_{70}^{-1}{\rm Mpc}$, we find no significant difference between the $A(P)$ and $A(\delta)$ relation of the low and high redshift sample. Using the MICE simulations we predict that trough and ridge evolution could be detected with lensing, using deeper and more accurate lensing surveys.

4.1 Introduction

Over the past two decades, large scale galaxy redshift surveys, such as the 2dF Galaxy Redshift Survey (2dFGRS, Colless et al. 2001) and the Sloan Digital Sky Survey (SDSS, Abazajian et al. 2009) have provided an accurate picture of the distribution of galaxies in the Universe. They show that galaxies form an intricate 'cosmic web' of clusters and filaments, separated by largely empty regions named voids. This distribution is also observed in large scale simulations based on the concordance ΛCDM cosmology, such as the Millennium (Springel et al. 2005b), Illustris (Vogelsberger et al. 2014) and EAGLE (Schaye et al. 2015) projects, which show the gravitational collapse of dark matter (DM) into a web-like structure, establishing the 'skeleton' for baryonic matter which falls into the DM's potential well. Within this framework, the linear growth factor of voids with redshift can be used to constrain the equation of state parameter of dark energy (DE) (Lavaux and Wandelt 2010; Demchenko et al. 2016), which causes the Universe's accelerated expansion. The low density in voids also ensures that they are very clean probes of global cosmological parameters, as their interior is less affected by baryonic physics (Bos et al. 2012). In addition to testing the standard model of cosmology, voids can also be used to detect signatures of modified gravity models, which aim to provide an alternative explanation to the accelerating expansion of the Universe (for reviews, see Jain and Khoury 2010; Clifton et al. 2012). Because these theories should converge to standard general relativity inside the solar system, most implement a screening mechanism that suppresses their '5^{th} force' in high density regions. Simulations based on modified gravity show that low density regions, like voids, are excellent probes for testing these theories (Li et al. 2012; Lam et al. 2015; Zivick et al. 2015).

Studying, detecting, or even defining voids, however, is not a simple matter. There exist numerous void finding algorithms, each one operating with a different void definition (for a comparison study, see e.g. Colberg et al. 2008). Secondly, applying the algorithm of choice to detect voids in observational data requires very accurate redshift measurements of every individual galaxy. Such accuracy is only available through complete spectroscopic surveys, which are far more costly than their photometric counterparts. Finally, the true DM structure of voids can be different than that of the galaxies that trace them, an effect known as 'galaxy bias' (Benson et al. 2000; Tinker et al. 2010). Currently, the only way to study the total mass distribution of voids is through 'gravitational lensing', a statistical method that measures the gravitational deflection (or 'shear' γ) of the light of background galaxies (sources) by foreground mass distributions (lenses). The first detection of the lensing signal from cosmic voids was presented by Melchior et al. (2014), who stacked the gravitational shear around 901 voids detected in SDSS. The depth of their void lensing signal corresponded to the prediction from the analytical model by Krause et al. (2013), who concluded that lensing measurements of medium-sized voids with sufficient precision (i.e. with a signal to noise $S/N \gtrsim 10$) will only be possible with Stage IV surveys such as the Euclid satellite (Laureijs et al. 2011) and the Large Synoptic Survey Telescope (LSST, Dark Energy Science Collaboration 2012). One of the reasons this signal is so difficult to measure, is that the lensing method measures the average density contrast over the entire line-of-sight (LOS). If a dense cluster is located in the same LOS as the void, it can diminish the lensing signal. Another problem of studying voids using their stacked gravitational lensing signal is that this method only measures the average shear as a function of the projected radial distance from the void centre (Hamaus et al. 2014; Nadathur et al. 2015). This means that the detailed detection of void shapes is rendered superfluous, since this information will not be captured. Stacking voids that are not radially symmetric can even diminish the lensing signal. Moreover, the centre and the radius of these non-spherical voids are difficult to define, and choosing the wrong value reduces the lensing signal even further (for an analysis of these effects, see e.g. Cautun et al. 2016).

To circumvent the aforementioned problems, Gruen et al. (2016) (hereafter G16) constructed a definition for projected voids named 'troughs'. These are very simply defined as the most underdense circular regions on the sky, in terms of galaxy number density. Being circular in shape, troughs evade the problem of the centre definition, and are perfectly suited for measuring their stacked shear as a function of radial distance. Because they are defined as *projected* circular regions of low galaxy density, they can also be described in 3D as voids which have the shape of long conical frusta[1] protruding into the sky. Because this definition only includes regions that are underdense over the entire LOS, it automatically excludes LOS's with overdensities massive enough to negate the lensing measurement. Moreover, defining underdensities in projected space alleviates the need for spectroscopic redshifts. Even when projected underdensities are defined in a number of redshift slices, as was done by e.g. Sánchez et al. (2017), photomet-

---

[1] Frusta, the plural form of frustum: the part of a solid, such as a cone or pyramid, between two (usually parallel) cutting planes.

ric redshifts are sufficiently accurate as long as the slices are significantly wider than the redshift uncertainties. In short, the disadvantage of troughs compared to 3D voids is losing the shape information in both projected and redshift space, while their advantage is that they are specifically designed to allow for significant lensing measurements with currently available surveys. Following this new underdensity definition, G16 defined a set of $\sim 110,000$ troughs in the redMaGiC (Rozo et al. 2016) sample of Luminous Red Galaxies (LRGs). Using the Dark Energy Survey (DES, Flaugher et al. 2015) Science Verification Data, they measured the gravitational lensing signal of projected cosmic underdensities with a significance above 10σ, much higher than was ever measured around 3D voids.

The ways in which this new probe can be used for cosmology are still under examination. In the work of G16, they found the trough shear measurements to be in agreement with their theoretical model, which was based on the assumption that galaxies are biased tracers in a Gaussian mass density distribution. Although the lensing profile of their smallest troughs was marginally sensitive to galaxy bias, the trough-galaxy angular correlation function allowed for much stronger constraints. In their more recent paper Gruen et al. (2017) studied the probability distribution function (PDF) of large-scale matter density fluctuations, using the galaxy counts and lensing profiles of under- and overdensities along the LOS, obtained from the DES First Year and SDSS data. Using these troughs and overdensities, they were able to constrain the total matter density $\Omega_{\rm m}$, the power spectrum amplitude σ_8, the galaxy bias, galaxy stochasticity and the skewness of the matter density PDF. Another very promising venue for trough lensing is to test models of modified gravity. Using ray-tracing simulations Higuchi and Shirasaki (2016) found that, while 3D voids could not distinguish between $f(R)$ and ΛCDM even in future ($\sim 1000\,\mathrm{deg}^2$) lensing surveys, the lensing profiles from troughs showed a clear deviation. A recent comparison from Cautun et al. (2017) also found that the shear profiles of projected (2D) underdensities can constrain chameleon $f(R)$ gravity with confidence levels of up to ~ 30 times higher than those of 3D void profiles, using Euclid and LSST. For another type of modified gravity, the normal branch of the Dvali-Gabadadze-Porrati (nDGP) model, Barreira et al. (2017) found that it strenghtened the lensing signal of both projected under- and overdensities. In conclusion, the promise of projected underdensities for cosmology compels the weak lensing community to observationally explore these new probes, especially in preparation for future surveys such as Euclid and LSST.

Our goal is to measure and study the lensing profiles of troughs using the spectroscopic Galaxy And Mass Assembly survey (GAMA, Driver et al. 2011) and photometric Kilo-Degree Survey (KiDS, de Jong et al. 2013), following up on the work by G16. In particular we study troughs as a function of their galaxy number density, and try to find the optimal method of stacking their lensing signal to obtain the highest possible detection significance. We will compare our observed lensing profiles with mock observations devised by the Marenostrum Institut de Ciències de l'Espai (MICE) collaboration: the MICE Galaxy and Halo Light-cone catalogue (Carretero et al. 2015; Hoffmann et al. 2015), based on the MICE Grand Challenge lightcone simulation (MICE-GC, Fosalba et al. 2015b,a; Crocce et al. 2015). G16 also studied the lensing signals of troughs as a function of redshift, by splitting the LRG sample that defined the troughs into two redshift samples. However, they did not account for possible differences between the galaxy samples or trough geometry at different redshifts, nor did they correct for the variation in distance between the troughs and the background sources that measured the lensing signal. As a result, they did not find any signs of *physical* redshift evolution of troughs. By correcting the trough selection method and lensing signal measurement for all known differences between the two redshift samples, we explore the physical evolution of troughs.

Our paper is structured as follows: In Sect. 4.2 we introduce the KiDS and GAMA data used to define the troughs and measure their lensing profiles, and the MICE-GC mock data which we use to interpret our observations. Section 4.3 describes the classification of troughs, and explains the gravitational lensing method in detail. In Sect. 4.4 we show the resulting trough lensing profiles as a function of galaxy density and size, and define our optimal trough stacking method. Our study of troughs as a function of redshift is described in Sect. 4.5. We end with the discussion and conclusion in Sect. 4.6.

Throughout this work we adopt the cosmological parameters used in creating the MICE-GC simulations: $\Omega_{\rm m} = 0.25$, $\Omega_{\Lambda} = 0.75$, and $H_0 = 70\,{\rm km\,s^{-1}Mpc^{-1}}$. We use the following definition for the reduced Hubble constant: $h_{70} \equiv H_0/(70\,{\rm km\,s^{-1}Mpc^{-1}})$.

4.2 Data

We use two samples of foreground galaxies to define the locations of troughs: one sample from the spectroscopic GAMA survey and one from the photometric KiDS survey. Comparing the results obtained from these two samples allows us to test the strength and reliability of trough studies using only photometric data. In Table 4.1 we give a summary of the galaxy selections used to define the troughs. The gravitational lensing signal of these troughs is measured using a sample of KiDS background galaxies. The combination of the KiDS and GAMA datasets and the lensing measurement method, which is used for the observations described in this work, closely resemble those used in earlier KiDS-GAMA galaxy-galaxy lensing (GGL) papers. For more information we recommend reading Sect. 3 of Viola et al. (2015), which discusses the GGL technique in detail, and Dvornik et al. (2017) which makes use of exactly the same versions of the KiDS and GAMA datasets as this work. In order to compare our observational results to predictions from simulations, the same process of selecting troughs and measuring their lensing profiles will be performed using the MICE-GC mock galaxy catalogue. In this section we introduce the KiDS, GAMA and MICE galaxy catalogues, including their role in the trough selection and lensing measurement.

4.2.1 KiDS source galaxies

In order to derive the mass distribution of troughs, we measure their gravitational lensing effect on the images of background galaxies. Observations of these source galaxies are taken from KiDS, a photometric lensing survey in the u, g, r and i bands, performed using the OmegaCAM instrument (Kuijken 2011) mounted on the VLT Survey Telescope (Capaccioli and Schipani 2011). For this work we use the photometric redshift, magnitude, and ellipticity measurements from the third data release (KiDS-DR3, de Jong et al. 2017), which were also used for the KiDS-450 cosmic shear analysis (Hildebrandt et al. 2017). These measurements span $454\,\mathrm{deg}^2$ on the sky, and completely cover the $180\,\mathrm{deg}^2$ equatorial GAMA area.

The galaxy ellipticity measurements are based on the r-band observations, which have superior atmospheric seeing constraints (a maximum of 0.8 arcsec) compared to the other bands (de Jong et al. 2017). The galaxies are located by the SExtractor detection algorithm (Bertin and Arnouts 1996) from the co-added r-band images produced by the Theli pipeline (Erben et al. 2013). The ellipticity of each galaxy is measured using the self-calibrating *lens*fit pipeline (Miller et al. 2007, 2013b; Fenech Conti et al. 2017). Galaxies in areas surrounding bright stars or image defects (such as read-out spikes, diffraction spikes and reflection haloes) are removed, eliminating 14.6% of the original survey area (de Jong et al. 2017).

The photometric redshifts of the sources are measured from co-added

Table 4.1: The names and sizes of the different trough definitions used in this work, including information on the galaxy samples used to select these troughs: the redshift range, the comoving distance range, and the absolute magnitude limits.

Troughs/Galaxies	Trough radius θ_A	Redshift range	Distance ($h_{70}^{-1}\mathrm{Mpc}$)	M_r-limit
Fiducial	$5', 10', 15', 20'$	$0 < z < 0.5$	$0 < D_\mathrm{c} < 1922.5$	< -19.67
Low redshift	$10'\,(1.9\,h_{70}^{-1}\mathrm{Mpc})$	$0.1 < z < 0.198$	$420.0 < D_\mathrm{c} < 813.9$	< -21.0
High redshift	$6.303'\,(1.9\,h_{70}^{-1}\mathrm{Mpc})$	$0.198 < z < 0.3$	$813.9 < D_\mathrm{c} < 1207.7$	< -21.0

$ugri$ images, which were reduced using the Astro-WISE pipeline (McFarland et al. 2013). From the galaxy colours measured by the Gaussian Aperture and PSF pipeline (GAaP Kuijken et al. 2015), the full redshift probability distribution $n(z_{\rm s})$ of the full source population is calculated, using the direct calibration method described in Hildebrandt et al. (2017). We use this full $n(z_{\rm s})$ for our lensing measurements (as described in Sect. 4.5.2), in order to circumvent the bias inherent in individual photometric source redshift estimates.

4.2.2 GAMA foreground galaxies

One of the galaxy samples we use to define the troughs is obtained using the spectroscopic GAMA survey, which was performed with the AAOmega spectrograph mounted on the Anglo-Australian Telescope. The galaxy locations were selected from the Sloan Digital Sky Survey (SDSS, Abazajian et al. 2009). For this study we use the three equatorial regions (G09, G12 and G15) from the GAMA II data release (Liske et al. 2015), which span a total area of $180\,\mathrm{deg}^2$ on the sky, since these areas are completely overlapping with the KiDS survey. GAMA has a redshift completeness of 98.5% down to Petrosian r-band magnitude $m_{\rm r} = 19.8$, resulting in a catalogue containing $180,960$ galaxies with redshift quality $n_{\rm Q} \geq 2$. As recommended, we only use the galaxies with redshift quality $n_{\rm Q} \geq 3$, which amounts to 99.74% of the full catalogue. In order to indicate regions where the survey is less complete, GAMA provides a 'mask' which contains the redshift completeness of galaxies on a $0.001\,\mathrm{deg}$ Cartesian grid. We use this mask to account for incomplete regions during the trough classification.

To mimic the galaxy sample corresponding to resolved haloes in the MICE-GC mock catalogues (see Sect. 4.2.4), we only use galaxies with absolute r-band magnitude $M_{\rm r} < -19.67$. The GAMA restframe $M_{\rm r}$ is determined by fitting Bruzual and Charlot (2003) stellar population synthesis models to the $ugrizZYJHK$ spectral energy distribution of SDSS and VIKING observations (Abazajian et al. 2009; Edge et al. 2013), and corrected for flux falling outside the automatically selected aperture (Taylor et al. 2011b). Together, the $n_{\rm Q}$ and $M_{\rm r}$ cuts result in a sample of 159,519 galaxies (88.15% of the full catalogue), with a redshift range between $0 < z_{\rm G} < 0.5$ and a mean redshift of $\overline{z_{\rm G}} = 0.24$. The projected number density of this sample of GAMA galaxies, together with their completeness mask, will be used to define the troughs as detailed in Sect. 4.3.1.

4.2.3 KiDS foreground selection

Since the currently available area of the KiDS survey is 2.5 times larger than that of the GAMA survey (and will become even larger in the near future) it can be rewarding to perform both the trough selection and lensing measurement using the KiDS galaxies alone, employing the full $454\,\mathrm{deg}^2$ area of the current KiDS-450 dataset. To be able to compare the KiDS troughs to those obtained using GAMA, we select a sample of KiDS galaxies that resembles the GAMA sample as closely as possible. Because GAMA is a magnitude-limited survey ($m_{\mathrm{r,Petro}} < 19.8$), we need to apply the same magnitude cut to the (much deeper) KiDS survey. Since there are no Petrosian r-band magnitudes available for the KiDS galaxies, we use the KiDS magnitudes that have the most similar m_{r}-distribution: the extinction-corrected and zero-point homogenised isophotal r-band magnitudes (de Jong et al. 2017). These magnitude values, however, are systematically higher than the Petrosian magnitudes from GAMA. We therefore match the KiDS and GAMA galaxies using their sky coordinates, and select the magnitude cut based on the completeness of this match. Using $m_{\mathrm{r,iso}} < 20.2$, the completeness of the match is 99.2%. This cut results in a slightly higher number density than that of real GAMA sample, but this small difference does not significantly affect our results which are primarily based on the relative number density (compared to other apertures or the mean density).

In addition, we cut the KiDS galaxies at the maximum redshift of GAMA: $z_{\mathrm{ANN}} < 0.5$. Contrary to the KiDS source redshifts used for the lensing measurement, where we can use the redshift probability distribution of the full population (see Sect. 4.3.2), the application of this cut and the use of KiDS galaxies as lenses requires individual galaxy redshifts. These photometric redshifts are determined using the machine learning method ANNz2 (Sadeh et al. 2016) as described in Sect. 4.3 of de Jong et al. (2017). Following Bilicki et al. (2017) the photo-z's are trained exclusively on spectroscopic redshifts from the equatorial GAMA fields[2]. This is the first work that uses KiDS photometric redshifts through machine learning to estimate the distances of the lenses. Compared to the spectroscopic GAMA redshifts z_{G}, the mean error $\delta z = (z_{\mathrm{ANN}} - z_{\mathrm{G}})/z_{\mathrm{G}}$ on the ANNz2 photometric redshifts is -3.26×10^{-4}, with a standard deviation of 0.036, much smaller than the width of the redshift selections used in this work (see Sect. 4.5.1). Finally, to mimic the galaxy sample corresponding to resolved haloes in the

---

[2] Bilicki et al. (2017) use a slightly different apparent magnitude cut to select the GAMA-like galaxy sample: $m_{\mathrm{r,auto}} < 20.3$. However, since this is an a-posteriori cut it does not influence the determination of the photo-z values.

mock catalogues (see Sect. 4.2.4), we apply the absolute r-band magnitude cut $M_{\rm r} < -19.67$. These absolute magnitudes: $M_{\rm r} = m_{\rm r,iso} - D_{\rm M} + K_{\rm cor}$, are determined using distance moduli $D_{\rm M}$ based on the $z_{\rm ANN}$ redshifts. The K-corrections $K_{\rm cor}$ are calculated from the isophotal g- and i-band magnitudes of the KiDS galaxies, using the empirical relation in Table 4 of Beare et al. (2014).

To remove stars from our galaxy sample, we use a star/galaxy separation method based on the source morphology (described in Sect. 4.4 of de Jong et al. 2015). We also mask galaxies that have been affected by readout and diffraction spikes (flag 1 and 4), by saturation cores and primary haloes of bright stars (flag 2 and 8), or by bad pixels (flag 64) in any band (u, g, r or i). We do not remove galaxies affected by secondary and tertiary stellar haloes (flag 16 and 32) because these do not heavily affect bright galaxies, and we do not apply manual masking (flag 128) because it is not yet performed on the two southern DR3 patches (G23 and GS). For more information on the masking flags, see Sect. 4.5 of de Jong et al. (2015). In addition, we remove galaxies that have an unreliable magnitude measurement in any band, as recommended in App. 3.2 of de Jong et al. (2017). Using this selection, we obtain a sample of 309,021 KiDS galaxies that resemble the GAMA and MICE-GC galaxy populations.

Based on the aforementioned image defects, the KiDS survey provides an automatic mask that flags affected pixels. For simplicity we only use the r-band pixel mask, which has a less than 1% difference with the pixel mask based on all bands. We use this map to account for incomplete regions during the trough classification procedure (see Sect. 4.3.1). In order to save computational time, we create a map that provides the survey completeness on a $0.04\,\rm deg$ Cartesian grid, by calculating the ratio of 'good' pixels (flag 0, 16, 32 and 128) in the square area surrounding each grid point. The grid spacing of the resulting mask is the same as that used for the trough selection, and is chosen such that it is at least two times smaller than the radius of the smallest troughs.

4.2.4 MICE mock galaxies

We wish to apply the same trough detection and analysis to simulated data, in order to compare and interpret our observational results. The MICE-GC N-body simulation presented by Fosalba et al. (2015a) contains $\sim 7 \times 10^{10}$ DM particles in a $(3072\,h_{70}^{-1}{\rm Mpc})^3$ comoving volume, allowing the construction of an all-sky lightcone with a maximum redshift of $z = 1.4$. From this lightcone Crocce et al. (2015) built a halo and galaxy catalogue, using a Halo Occupation Distribution (HOD) and Halo Abundance Matching (HAM) technique. Its large volume and fine spatial resolution make MICE-GC mocks ideally suited for accurate modelling of both large-scale (linear) and small-scale (non-linear) clustering and structure growth. The mock galaxy clustering as a function of luminosity has been constructed to reproduce observations from SDSS (Zehavi et al. 2011) at lower redshifts ($z < 0.25$), and has been validated against the COSMOS catalogue (Ilbert et al. 2009) at higher redshifts ($0.45 < z < 1.1$). The MICE-GC catalogue resolves DM halos down to a mass of $\sim 10^{11}\, h_{70}^{-1}\mathrm{M}_{\odot}$, corresponding to galaxies with an absolute magnitude < -18.9. Since this absolute magnitude includes a cosmology correction such that: $M_{\mathrm{r},\mathrm{MICE}} = M_{\mathrm{r}} - 5\log_{10}(h = 0.7)$, we apply an $M_{\mathrm{r}} < -18.9 - 0.77 = -19.67$ cut to the KiDS and GAMA samples in order to resemble the mock galaxy population.

From the MICE-GC catalogue, which is publicly available through `http://cosmohub.pic.es`, we obtain the sky coordinates, redshifts, comoving distances, absolute magnitudes and SDSS apparent magnitudes of the mock galaxies. In order to create a GAMA-like mock galaxy sample, we limit the MICE redshifts to $z < 0.5$. When considering the choice of magnitude cut, we find that the distribution of the SDSS magnitudes in the MICE catalog is very similar to that of the isophotal KiDS magnitudes. We therefore limit the MICE galaxies to $m_{\mathrm{r}} < 20.2$, and find that indeed the galaxy number density of the GAMA-like KiDS and MICE samples are almost equal (see Fig. 4.1 in Sec. 4.3.1). Like the GAMA galaxies and the GAMA-like KiDS sample, this sample of MICE foreground galaxies is used to define troughs following the classification method described in Sect. 4.3.1.

Each galaxy in the lightcone also carries the lensing shear values γ_1 and γ_2 (with respect to the Cartesian coordinate system) which were calculated from the all-sky weak lensing maps constructed by Fosalba et al. (2015b), following the 'onion shell' method presented in Fosalba et al. (2008). In this approach the DM lightcone is decomposed and projected into concentric spherical shells around the observer, each with a redshift width of $\mathrm{d}z \approx 0.003(1 + z)$. These 2D DM density maps are multiplied by the appropriate lensing weights and combined in order to derive the galaxies' lensing properties. The results agree with the more computationally expensive 'ray-tracing' technique within the Born approximation. We will use these shear values (in the same way we used the ellipticities observed by KiDS) to obtain mock lensing profiles around troughs, following the weak lensing method described in Sect. 4.3.2. To this end we create a MICE background source sample with $0.1 < z < 0.9$ and $m_{\mathrm{r}} > 20$, the same redshift and apparent magnitude cuts as applied to the KiDS background sources (Hildebrandt et al. 2017). Also, in order to resemble the KiDS redshift distribution more closely, we choose to apply an absolute magnitude cut of $M_{\rm r} > -19.3$ on the mock galaxies. Note that any cut on the mock galaxy sample does not affect the shear values (which do not depend on any mock galaxy property) but only the redshift distribution of the sources, which is used in Sect. 4.5.2 to calculate the Excess Surface Density profiles.

Because all quantities in the mock catalogue are exactly known, we do not need to take into account measurement errors into the calculation of the mock lensing signals. However, there do exist differences between measurements from different parts of the sky caused by sample variance, and possibly by underlying large-scale density fluctuations (cosmic variance, Somerville et al. 2004). To obtain an estimate of these uncertainties we use the full MICE-GC public lightcone, which has an area of $90^\circ \times 90^\circ$. We divide this area into 16 patches of $20^\circ \times 20^\circ = 400\,\mathrm{deg}^2$, each spanning approximately the same size as the used KiDS area. One of these patches is used as our fiducial mock galaxy sample. Comparing the results obtained from the fiducial patch with those of the 15 other galaxy samples, provides an estimate of the sample and cosmic variance within the mocks. As MICE has no mask to indicate unreliable survey areas, we create an artificial mask for each $20^\circ \times 20^\circ$ area, which indicates that the patch is 100% complete and is only used to to indicate its borders.

4.3 Data analysis

The two most important aspects of the data analysis are the classification of the troughs, and the subsequent measurement of their gravitational lensing profiles. For the classification we compare using GAMA galaxies to using the GAMA-like KiDS sample (see 4.2.3). For the measurement of the gravitational lensing effect around these troughs, we use the shapes and photometric redshifts of the KiDS background galaxies. In this section we will discuss the trough classification and lensing measurement methods in detail.

4.3.1 Trough classification

Our approach to trough detection is mainly inspired by the method devised by G16. This effectively comprises measuring the projected number density of galaxies within circular apertures on the sky, and finding the apertures with the lowest galaxy density. Following this method, we define a finely spaced Cartesian grid of positions on the sky. Around each sky position x, we count the number of galaxies within a circular aperture of chosen radius $\theta_{\rm A}$. We perform this method for apertures with different projected radii: $\theta_{\rm A} = \{5, 10, 15, 20\}$ arcmin, which allows us to study cosmic structure at different scales. To make sure that no information is lost through under-sampling, we choose a grid spacing of $0.04\,\rm deg$ $(= 2.4\,\rm arcmin)$ which is smaller than $\theta_{\rm A}/2$, even for the smallest aperture size. Although this spacing is much larger than that used by G16 ($0.86\,\rm arcmin$), we still need to cope with the significant overlap between neighbouring troughs. Performing tests with reduced overlap between the circles does not significantly change our results, primarily because the key part of the trough lensing profiles is situated outside the trough radius (such that overlap within the circle is not particularly worse than overlap outside the circle). We account for this overlap by ensuring that: 1) the covariance between the lensing profiles of neighbouring troughs is accounted for in the calculation of the error bars (see Sect. 4.3.2), and 2) the same overlap is embedded in the mock trough selection in the MICE simulations, which we use to interpret our results.

The projected galaxy number density $n_{\rm g}(x, \theta_{\rm A})$ of each aperture is defined as the galaxy count within radial separation $\theta_{\rm A}$ of the sky position x, divided by the unmasked area of the corresponding circle on the sky, determined using the appropriate (KiDS, GAMA or MICE) mask. Each mask provides the survey area completeness on a finely spaced grid, which we average to a $0.04\,\rm deg$ Cartesian grid to save computational time. We measure the total area completeness for the circle around each grid point, and (following G16) exclude those circles that are less than 80% complete from our sample. We verified that this specific choice of completeness threshold does not significantly affect our results.

The histogram in Fig. 4.1 shows the normalized KiDS and MICE galaxy number density distributions (represented by steps and smooth lines respectively) for apertures with different radii $\theta_{\rm A}$. The density roughly follows a log-normal distribution, as was originally modeled by Coles and Jones (1991), but with a slight deviation from the mean density. This effect is larger for circles with a smaller area, which is expected since larger apertures measure the average density over a larger area. The deviation tends more towards higher densities than lower, because the galaxy density can never reach values below 0. This leads to an increasingly skewed density distribution for smaller apertures, which is visible in both observa-

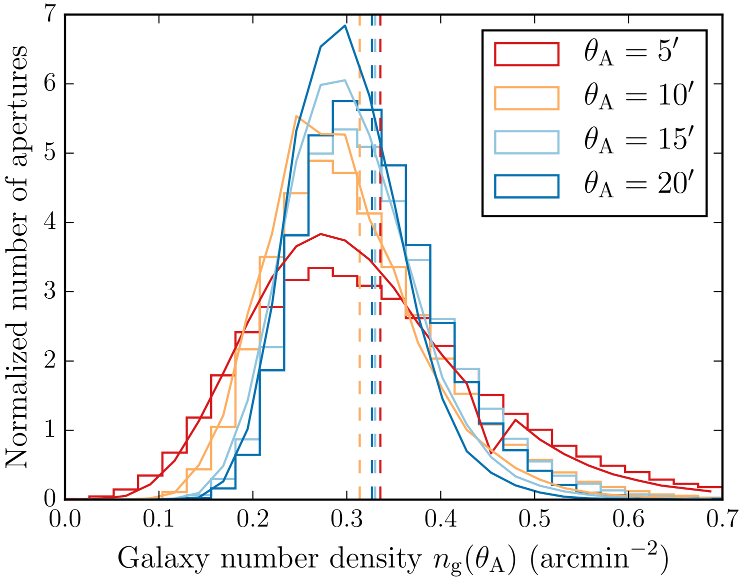

Figure 4.1: This histogram shows the distribution of the normalized number density n_g of the KiDS (steps) and MICE (lines) galaxies used to define the troughs, inside all used apertures (those with an effective area $> 80\%$). The colours designate apertures of different radius θ_A. As expected, the density distribution of circles with a smaller area is more asymmetric, and has a larger deviation from the mean density $\overline{n_g}(\theta_A)$ (dashed lines). The 'troughs' are defined as all underdense apertures (i.e. $n_g < \overline{n_g}(\theta_A)$), while all overdense apertures (i.e. $n_g > \overline{n_g}(\theta_A)$) are called 'ridges'.

tional and mock data. We verified that this skewness is also observed in the density distribution of troughs selected using GAMA galaxies.

Following G16 we determine, for each of these circles, the proportion $P(x, \theta_A)$ of equally sized apertures that have a lower galaxy density than the circle considered. Arranging the apertures in this way means that low-density circles will have a low value of P (down to $P = 0$), while high-density circles will have a high P-value (up to $P = 1$). A circle containing the median density will have $P = 0.5$. In the fiducial definition of G16, all apertures in the lower quintile (20%) of galaxy density (i.e. $P(x, \theta_A) < 0.2$) are called troughs, while apertures in the higher quintile (i.e. $P(x, \theta_A) > 0.8$) are considered overdensities (which we will hereafter call 'ridges').

We will use the terms 'trough' and 'ridges' more generally, based on the overdensity $\delta(x, \theta_A)$ with respect to the mean galaxy number density $\overline{n_g}$ of the total effective area of the survey. The overdensity is defined as:

$$\delta(x, \theta_{\rm A}) = \frac{n_{\rm g}(x, \theta_{\rm A}) - \overline{n_{\rm g}}(\theta_{\rm A})}{\overline{n_{\rm g}}(\theta_{\rm A})} \,. \tag{4.1}$$

In our classification, all underdense apertures (i.e. $\delta(x, \theta_{\rm A}) < 0$) are called troughs, while all overdense apertures are called ridges. This definition does not *a priori* exclude any apertures from our combined sample of troughs and ridges, allowing us to take advantage of all available data. We will further specify sub-samples of troughs and ridges, selected as a function of both P and δ, where necessary throughout the work.

4.3.2 Lensing measurement

In order to measure the projected mass density of the selected troughs and ridges, we use weak gravitational lensing (see Bartelmann and Schneider 2001; Schneider et al. 2006, for a general introduction). This method measures the coherent deflection of light from many background galaxies (sources) by foreground mass distributions (lenses). This gravitational deflection causes a distortion in the observed shapes of the source images of $\sim 1\%$, which can only be measured statistically. This is done by averaging, from many background sources, the projected ellipticity component $\epsilon_{\rm t}$ tangential to the direction towards the centre of the lens, which is equal to the 'tangential shear' $\gamma_{\rm t}$. This quantity is averaged within circular annuli around the center of the lens, to create a shear profile $\gamma_{\rm t}(\theta)$ as a function of the separation angle θ to the lens centre. For each annulus, $\gamma_{\rm t}(\theta)$ is a measure of the density contrast of the foreground mass distribution. In order to obtain a reasonable signal to noise ratio (S/N), the shear measurement around many lenses is 'stacked' to create the average shear profile of a specified lens sample. In this work, the centres of the lenses are the grid points that define our circular troughs and ridges (as defined in Sect. 4.3.1).

The background sources used to measure the lensing effect are the KiDS galaxies described in Sect. 4.2.1. Following Hildebrandt et al. (2017), we only use sources with a best-fit photometric redshift $0.1 < z_{\rm B} < 0.9$. For troughs defined at a specific redshift we only select sources situated beyond the troughs, including a redshift buffer of $\Delta z = 0.2$ (see Sect. 4.5.2). This cut is not applied when troughs are selected over the full redshift range. This can allow sources that reside at similar redshifts as the lenses to be used in the measurement, possibly resulting in a contamination of the lensing signal by sources that are intrinsically aligned with the troughs. However, most low-redshift sources have already been removed by the $m_{\rm r} > 20$

cut (Hildebrandt et al. 2017). Also, the intrinsic alignment effect primarily plays a role in very high density regions, on small ($\lesssim 1\,h_{70}^{-1}\mathrm{Mpc}$) scales. On the large scales probed by the troughs, the effect of intrinsic alignment is at most a few percent, especially since only relatively light (i.e. faint) KiDS galaxies are considered (Heymans et al. 2006b; Blazek et al. 2012). The small effect from intrinsic alignment that remains is also present in the results obtained from the MICE mock catalogue, to which we compare our observations.

The ellipticities of the source galaxies are measured using the self-calibrating *lens*fit pipeline (Miller et al. 2007, 2013b; Fenech Conti et al. 2017). For each galaxy this Bayesian model fitting method also produces the *lens*fit weight w, which is a measure of the precision of the shear estimate it provides. We would like to give more weight to the contribution of sources with a more reliable ellipticity measurement, and therefore incorporate the *lens*fit weight of each source into our combined shear measurement as follows:

$$\overline{\gamma} = \frac{1}{1+\mu} \frac{\sum_{ls} w_s \, \epsilon_{\mathrm{t},ls}}{\sum_s w_s} \,, \tag{4.2}$$

where the sum goes over each lens l and source s, and the factor $1+\mu$ is used to correct for 'multiplicative bias'. Fenech Conti et al. (2017) showed, based on extensive image simulations, that shears are biased at the $1-2\%$ level, and how to correct for this using a multiplicative bias correction m for every ellipticity measurement. Following Dvornik et al. (2017), the value of μ is calculated from the m-corrections in 8 redshift bins (with a width of 0.1) between $0.1 < z_{\mathrm{B}} < 0.9$. The average correction in each bin is defined as follows:

$$\mu = \frac{\sum_s w_s m_s}{\sum_{ls} w_s} \,. \tag{4.3}$$

The required correction is small ($\mu \approx 0.014$) independent of radial distance, and reduces the residual multiplicative bias to $\lesssim 1\%$. The errors on our shear measurement are estimated by the square-root of the diagonal of the analytical covariance matrix, as described in Sect. 3.4 of Viola et al. (2015). The covariance matrix of the lensing signal is based on the contribution of each individual source, and take into account the covariance of sources that contribute to the shear profile of multiple lenses.

In addition to measuring the lensing profile around troughs and ridges, we stack the shear around *all* grid points. This 'random signal' γ_0 does not contain a coherent shear profile, but only systematic effects resulting from the imperfect correction for the PSF anisotropy in combination with the survey edges and masks. In accordance with the real trough measurements, the apertures with an effective area less than 80% of the total circle area are removed (see Sect. 4.3.1). When using the GAMA survey area and masks, the random signal is consistent with 0 within the error bars, up to radius $\theta = 70\,\mathrm{arcmin}$ where it rises to $\gamma_0 \sim 3 \times 10^{-3}$ for all values of θ_A, while the KiDS random signal already starts to deviate at $\theta \approx 20\,\mathrm{arcmin}$ (see Sect. 4.4.1). To correct for this effect at larger scales, we subtract the appropriate γ_0 from all lensing measurements. Given this result, and our grid spacing of $0.04\,\mathrm{deg} = 2.4\,\mathrm{arcmin}$ (see Sect. 4.3.1), we compute our lensing profiles for 20 logarithmically spaced bins within the range $2 < \theta < 100\,\mathrm{arcmin}$.

4.4 Trough shear profiles

After a general classification of the troughs and ridges we define more specific samples, dedicated to obtaining specific observables from their measured lensing profiles. First, we compare the trough shear profiles of the KiDS- vs. GAMA-selected troughs, to decide on the best trough sample. Using these troughs, we measure the shear amplitude of the lensing profiles as a function of their density percentile $P(x, \theta_\mathrm{A})$, for apertures of different sizes θ_A. This allows us to study non-linearities in cosmic structure formation, and to define an optimal way to stack the shear signals of troughs/ridges in order to optimize the S/N.

4.4.1 KiDS vs. GAMA troughs

The very complete and pure sample of GAMA galaxies allows us to define a clean sample of troughs. However, since the currently available area of the KiDS survey is 2.5 times larger than that of the GAMA survey, we also use a set-up that uses the KiDS galaxies to define the troughs. We select both trough samples following the same classification method (see Sect. 4.3.1), using either the real GAMA galaxies (described in Sect. 4.2.2) or the GAMA-like KiDS sample (defined in Sect. 4.2.3) as our trough-defining galaxies. We use the corresponding completeness mask of the KiDS/GAMA survey to remove unreliable troughs (i.e. with an area $< 80\%$ complete).

To correct for systematic effects, the appropriate random shear profile γ_0 (defined in Sect. 4.3.2) is subtracted from the trough lensing profiles. The random signals for KiDS and GAMA are shown in Fig. 4.2. When using the GAMA survey area and mask, γ_0 is consistent with 0 (within 1σ error bars) up to $\theta = 70\,\mathrm{arcmin}$ and slightly positive beyond. When using the

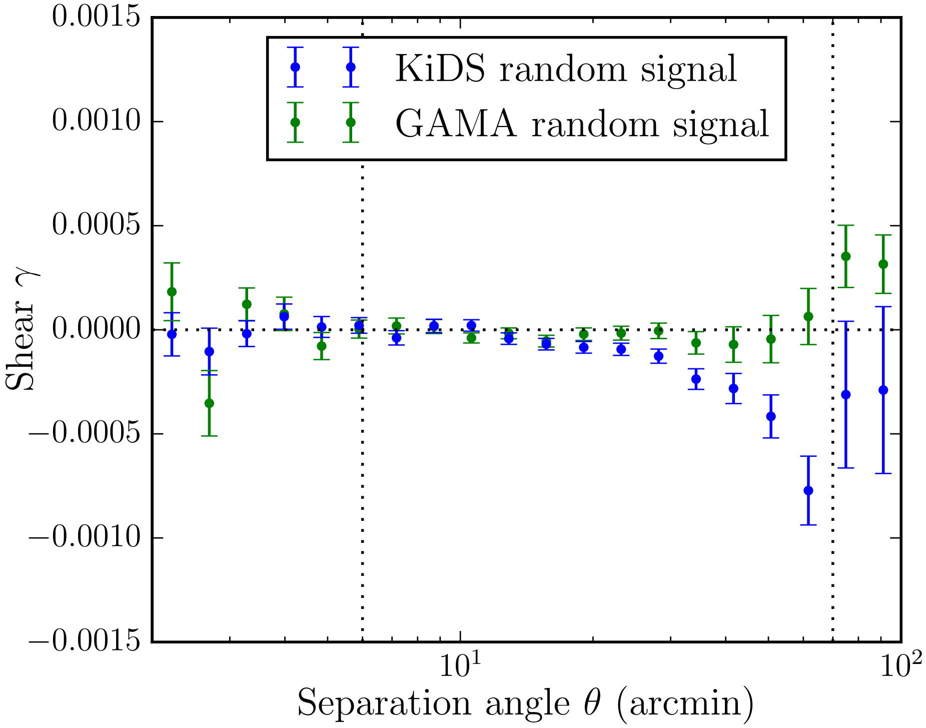

Figure 4.2: The random shear profile γ_0 (including 1σ analytical covariance errors) as a function of separation angle θ, which results from stacking *all* used apertures with an area $> 80\%$ complete. Using the GAMA area and mask, the systematic effects are consistent with 0 up to $\theta = 70\,\mathrm{arcmin}$, while the KiDS random signal already starts to deviate at $\theta \approx 20\,\mathrm{arcmin}$ as a result of the patchy survey area of KiDS outside the GAMA overlap.

KiDS survey area and mask, γ_0 is only consistent with 0 up to $\theta \approx 20\,\mathrm{arcmin}$ and increasingly negative beyond. This difference does not significantly depend on the choice of area completeness threshold, and also occurs when we apply no completeness mask at all. However, when we perform the γ_0 measurement using the KiDS mask on the GAMA area only, the systematic effect is significantly reduced. This shows that the difference between the random signals is primarily caused by the patchy surface of the KiDS-450 dataset beyond the GAMA area (see e.g. Fig. 1 of Hildebrandt et al. 2017).

The main goal of this exercise, however, is to find which galaxy sample provides the best results, i.e. trough lensing profiles with the highest S/N. For this initial test, we use the fiducial trough definition of G16: the apertures with the lowest 20% in density percentile (i.e. $P(\theta_{\mathrm{A}}) < 0.2$).

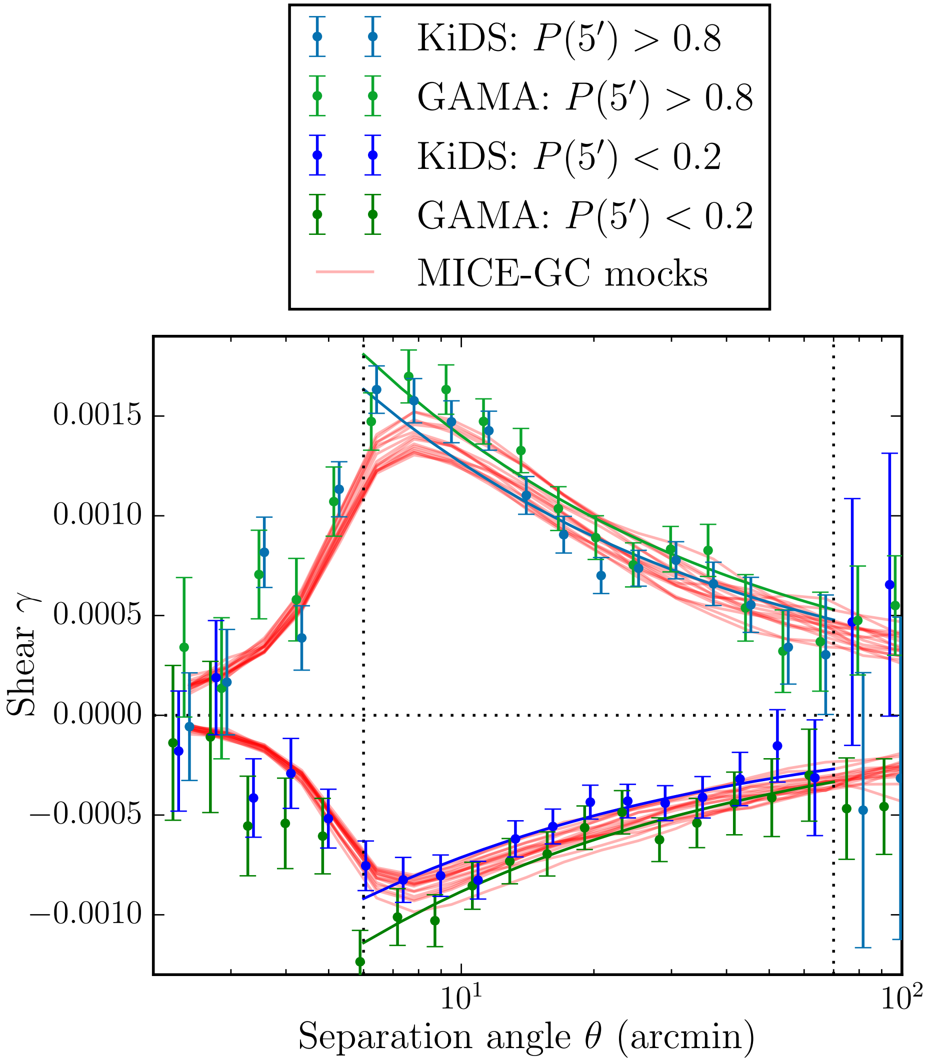

Figure 4.3: The gravitational shear profile $\gamma(\theta)$ (with 1σ errors) resulting from KiDS (blue points) and GAMA (green points) troughs and ridges, including a comparison with the MICE-GC mock troughs from 16 independent patches (red lines). All troughs and ridges have a radius $\theta_\mathrm{A} = 5\,\mathrm{arcmin}$, and are selected following the fiducial G16 definition. A simple $A/\sqrt{\theta}$ function (solid blue/green lines) is used to determine the best-fit amplitude A of the KiDS and GAMA troughs.

In Fig. 4.3 we show the stacked shear profiles $\gamma(\theta)$ of troughs with radius $\theta_{\mathrm{A}} = 5\,\mathrm{arcmin}$, selected using the KiDS or GAMA galaxies. For comparison we also include the trough shear profiles obtained using all 16 patches of the MICE mock catalogue, where the vertical spread in the 16 profiles gives an estimate of the sample and cosmic variance. The GAMA-selected troughs have a slightly deeper shear profile than the KiDS-selected troughs, but within the 1σ analytical covariance errors both profiles agree with the predictions from the MICE-GC simulation. However, when we use the KiDS galaxies to select troughs but restrict the used area to the GAMA equatorial fields, we find that the KiDS trough profiles are of equal depth as those from GAMA. This suggests that, like the systematic effects measured by the randoms, the shallower trough lensing profile is caused by the patchy survey area of KiDS. This patchy area reduces the completeness of the circles, which diminishes the accuracy of the density measurements and results in shallower shear profiles.

The dotted vertical lines indicate the radial separation range: $1.2\,\theta_{\mathrm{A}} < \theta < 70\,\mathrm{arcmin}$, that is sensitive to the shear signal from troughs. The reason for this is that: 1) inside θ_{A} the lensing is not sensitive to the full trough mass (where we leave a 20% buffer outside the trough edge), and 2) the lensing signal is very sensitive to systematic effects outside $\theta = 70\,\mathrm{arcmin}$. Within this radial range, we observe that both the trough and ridge shear signals closely follow a power law. For the positive lensing signal around overdense ridges this is expected, since the lensing profiles around galaxies and clusters can generally be described with the negative power law (with a slope of -0.8) resulting from a Navarro-Frenk-White profile (NFW, Navarro et al. 1996) plus two-halo term (see e.g. Fig. 5 of van Uitert et al. 2011). Fig. 4.3 shows that both the ridges and the troughs follow an approximate power law shape. We can therefore fit a simple power law $\gamma(\theta) = A\,\theta^{\alpha}$ within the specified radial range, to obtain the best-fit amplitude A and index α of the lensing signal. Because we are mainly interested in the amplitude, we fix the value of α with the help of the MICE-GC simulations. By fitting the power law (with both A and α as free parameters) to all 16 fiducial MICE trough lensing signals, we find a mean best-fit index value $\overline{\alpha}$ of -0.45 for troughs and -0.55 for ridges. We therefore choose to fit all trough lensing profiles in this work with the function: $\gamma(\theta) = A/\sqrt{\theta}$. However, we verified that our conclusions do not significantly depend on the specific choice of α, by performing the same analysis with $\alpha = -1$ and finding similar results.

From the best-fit amplitudes thus obtained, we wish to find a measure of the signal to noise ratio S/N in order to select the best troughs. We define the S/N as: $A/\delta A$, where δA is the 1σ error on the best-fit amplitude, based on the full analytical covariance matrix of the shear profile. Using this definition, we find that the GAMA troughs are detected with a significance of $|S/N| = 12.0$, while the KiDS troughs have $|S/N| = 12.3$. So, although the GAMA troughs are slightly deeper, the shear measurements of KiDS compensate for this by having smaller error bars, as expected from the larger survey area. The conclusion of this initial comparison is that, regarding trough lensing studies, the current patchy KiDS area already outperforms the highly complete and contiguous GAMA survey. We will therefore use the KiDS survey to select the troughs and ridges studied within this work, but we verify for each measurement that the same results are obtained using the GAMA galaxies.

4.4.2 Lensing amplitudes

After this initial test, which uses only the deepest (highest) 20% of the troughs (ridges), we wish to study all troughs and ridges as a function of their density percentile $P(\theta_{\rm A})$. Considering apertures of fixed radius $\theta_{\rm A}$ we divide them into 20 samples of increasing percentile value, using a bin width of $\mathrm{d}P = 0.05$. We measure the shear profile $\gamma(\theta)$ (using the method described in Sect. 4.3.2) for the apertures in every percentile bin. Figure 4.4 shows the KiDS and MICE lensing profiles in the 20 percentile bins, for circles with radius $\theta_{\rm A} = 5\,\mathrm{arcmin}$. To each shear measurement we fit the same function, $\gamma(\theta) = A/\sqrt{\theta}$, within the appropriate radial range (see Sect. 4.4.1). As expected the apertures with low P-values correspond to the deepest troughs, resulting in a negative shear signal starting at the trough edge (in this case at $\theta > 5\,\mathrm{arcmin}$). In contrast, the circles with high P-values show a strong positive shear signal beyond the edge of the ridge. It is already apparent that troughs and ridges are not symmetrical, but that the lensing signal is stronger for the highest ridges than for the deepest troughs. This is an indication that the skewness of the galaxy number density distribution (seen in Fig. 4.1) is reflected by the total (baryonic + DM) density distribution. This skewness is not only indicated by most extreme densities, but also by those close to the median. Examining these, we find that the turning point between negative and positive lensing amplitudes is *not* situated at the median density ($P = 0.5$). This can be better appreciated from the left panel of Fig. 4.5, which shows the best-fit A as a function of P for apertures of different radius $\theta_{\rm A}$. For both the KiDS and MICE data the turning point $A = 0$ is not reached at $P = 0.5$, but at $P \approx 0.55 - 0.6$.

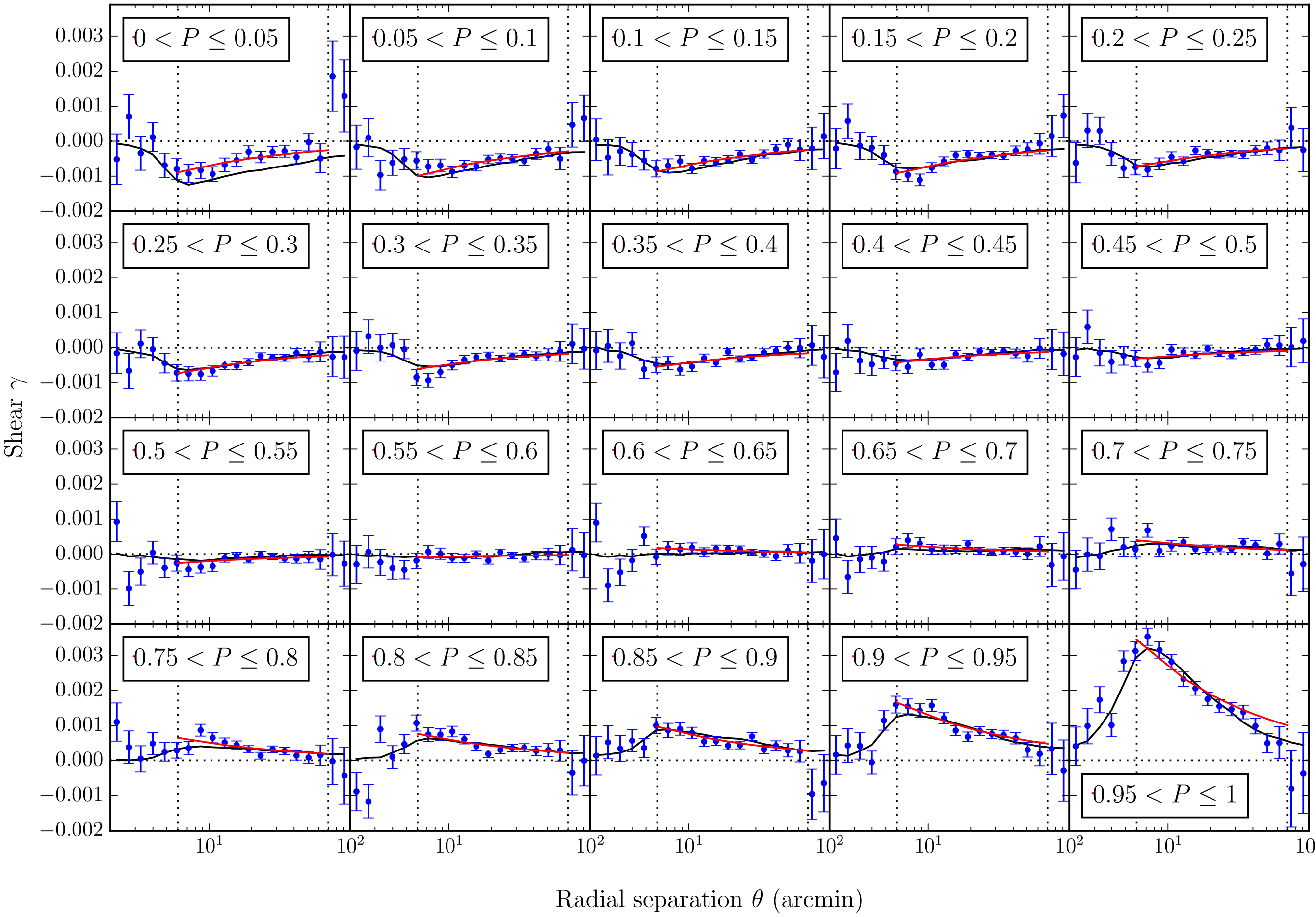

Figure 4.4: Each panel shows the KiDS (blue dots with 1σ errors) and MICE (black line) shear profiles $\gamma(\theta)$, resulting from apertures of size $\theta_{\rm A} = 5\,\mathrm{arcmin}$. The shear profile of these apertures is stacked in 20 bins of increasing density percentile $P(x, \theta_{\rm A} = 5)$. For underdense apertures (troughs) the amplitude A of the lensing signal becomes negative outside the trough radius, while for overdense apertures (ridges) A becomes positive. A simple power law fit: $A/\sqrt{\theta}$ (red line), within the fitting range (dotted vertical lines) is used to obtain A as a function of P.

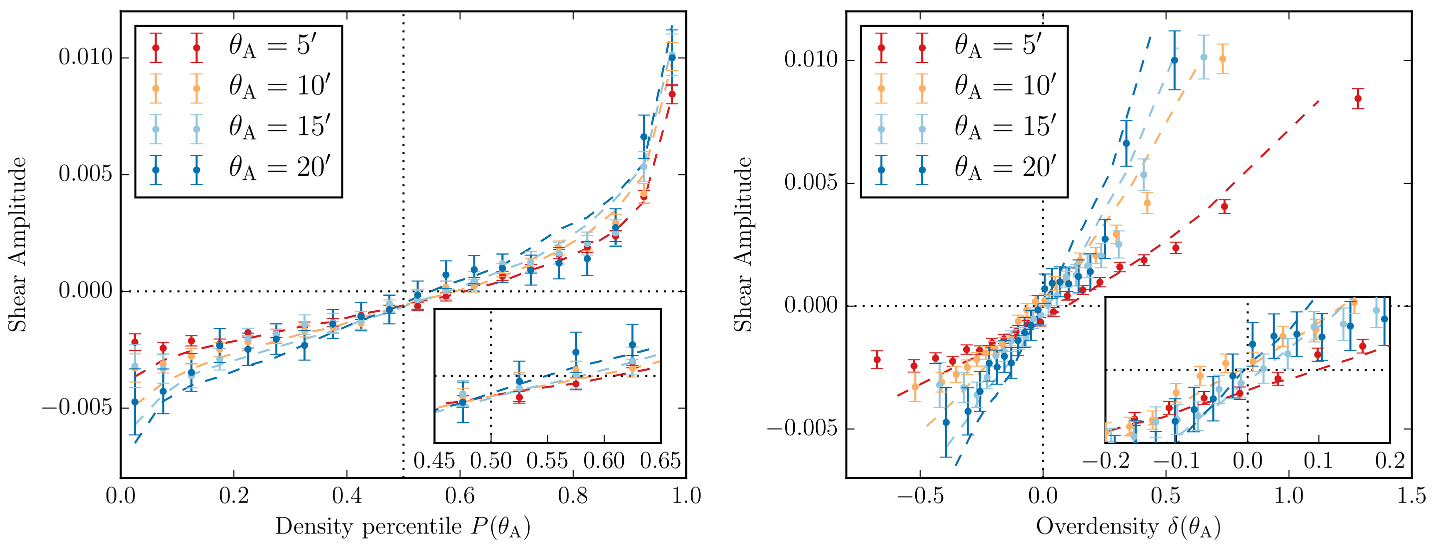

Figure 4.5: The amplitude A of the KiDS (points with 1σ errors) and MICE (dashed lines) shear signals as a function of the density percentile P (left) and overdensity δ (right), for apertures of different angular radius θ_A. The turning point between negative and positive A situated at at the mean density ($\delta = 0$) as is expected when there is only linear galaxy bias, except when $\theta_\mathrm{A} = 5'$. This turning point, however, is not situated at the median density ($P = 0.5$) but at $P \approx 0.55 - 0.6$, which means that the density distribution is skewed. The smallest apertures also reveal the skewness of the density distribution, since their distribution extends to more extreme values of P, δ and A for the ridges than for the troughs, while larger apertures have a more symmetrical $A(\delta)$ distribution.

The right panel of Fig. 4.5 shows A as a function of the overdensity $\delta(\theta_{\mathrm{A}})$, which is defined in Eq. 4.1, for both KiDS and MICE troughs/ridges. The δ-value of each bin is taken to be the mean overdensity $\overline{\delta}(\theta_{\mathrm{A}})$ of all apertures in each percentile bin. For all aperture sizes the $A(\delta)$ relation is approximately linear, with the turning point between negative and positive A situated at the mean density ($\delta = 0$). This is expected when there is only linear galaxy bias, i.e.: there exists a linear relation between galaxies and DM. Only the smallest apertures, $\theta_{\mathrm{A}} = 5\,\mathrm{arcmin}$, seem to show a slight trace of non-linear galaxy bias near the centre, in both the observational and the mock data. This could be explained by the fact that non-linearities in the density field are more prevalent at smaller scales. Furthermore, the discrepancy between the $A(P)$ and $A(\delta)$ relations shows that (like the galaxy number density distribution in Fig. 4.1) the mass distribution measured using lensing is skewed. This asymmetry is caused by the fact that, during cosmic structure formation through clustering, the density of matter is bound to a strict lower limit (a completely empty region) but not to an upper limit. This is also revealed by the asymmetry between the lensing amplitudes at the lowest and highest P and δ. For smaller apertures, the positive amplitudes are significantly larger than the negative amplitudes. This effect is less pronounced for the largest apertures, which have more symmetrical $A(\delta)$ relations. These non-linearities can in principle be used as a statistic to constrain cosmological parameters, analogous to performing shear peak statistics (Dietrich and Hartlap 2010; Liu et al. 2015; Kacprzak et al. 2016).

4.4.3 Optimal trough weighting

Instead of selecting troughs and ridges using a ‘hard cut’ in the percentile $P(x, \theta_{\mathrm{A}})$ of the apertures, one can apply a more sophisticated weighting scheme to stack the shear signals of the apertures. In order to obtain the most significant lensing detection, the optimal weighting should be based on the S/N of the contribution from each trough (or ridge) to the lensing signal (where we define the S/N as $A/\delta A$, see Sect. 4.4.1). The resulting S/N as a function of percentile P is shown in Fig. 4.6. In this relation the peaks at very high and low P are reduced compared to those in the $A(P)$ relation, since very low density troughs (and very high density ridges) tend to cluster at the centres of large voids (or large clusters). This increases the covariance between the lensing signals of the very deep troughs (or high ridges), thereby increasing the error values. Another noteworthy difference is that the smallest apertures have the highest S/N, while they have the smallest amplitude. The reason for this, is that the number of data-points

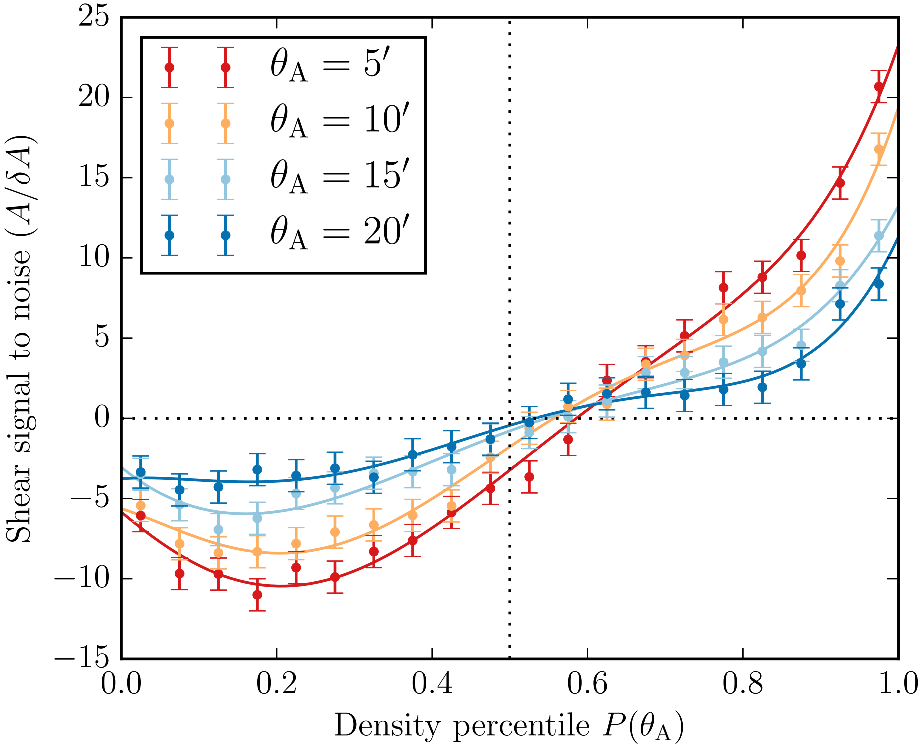

Figure 4.6: The signal to noise ratio, defined as $A/\delta A$, of the KiDS shear profiles as a function of the density percentile P. To obtain the optimal weight to stack the troughs and ridges, we fit a standard $5^{\rm th}$-order polynomial (solid lines) to the measured $A/\delta A$ values (points with 1σ error bars). The resulting weight function $w(P)$ allows us to obtain a (positive) stacking weight $w_{\rm P} = |w(P)|$ for each individual lens.

inside the fitting range ($1.2\,\theta_{\rm A} < \theta < 70\,{\rm arcmin}$) is larger for lower values of $\theta_{\rm A}$. In the end this effect is of no consequence, since only the relative difference in S/N between apertures of the same size are factored into the weighting scheme.

We fit a $5^{\rm th}$-order polynomial to the $A/\delta A$ values in order to find a weight function $w(P)$ that provides a lens weight $w_{\rm P}$ for every individual aperture. We define the weight as the absolute value of this function: $w_{\rm P} = |w(P)|$, in order to obtain a positive weight for both ridges and troughs. Finally, when we compute the combined lensing profile of all troughs or ridges, we use these weights to scale the contribution of each lens to the combined shear signal. The $w_{\rm P}$-value of each lens l is incorporated into

Eq. (4.2), such that it becomes:

$$\overline{\gamma}_{\rm P} = \frac{1}{1+K_{\rm P}} \frac{\sum_l \left(w_{{\rm P},l} \sum_s w_s \epsilon_{\rm t} \right)}{\sum_l \left(w_{{\rm P},l} \sum_s w_s \right)} \, . \tag{4.4}$$

In this way we give higher weights to troughs/ridges that provide a higher S/N, which thus contribute more heavily to the combined shear signal. These same weights are also applied to the average multiplicative bias correction from Eq. (4.3):

$$K_P = \frac{\sum_l \left(w_{{\rm P},l} \sum_s w_s m_s \right)}{\sum_l \left(w_{{\rm P},l} \sum_s w_s \right)} \, . \tag{4.5}$$

Likewise, the lens weight is incorporated into the uncertainty through the calculation of the analytical covariance matrix (see Sect. 4.2.1).

We combine all troughs (ridges) into a single negative (positive) shear signal using the weighting scheme described above. The optimally combined KiDS and MICE lensing profiles are shown in Fig. 4.7, for different aperture sizes $\theta_{\rm A}$. It is clear that the shear signal decreases for troughs/ridges with larger apertures, because the lensing effect is stronger when light passes more closely to the centre of the lens. For the KiDS-selected troughs and ridges, this method results in a $|S/N| = \{17.1, 14.8, 10.0, 7.6\}$ detection of troughs with a size of $\theta_{\rm A} = \{5, 10, 15, 20\}$ arcmin respectively, and a $|S/N| = \{23.6, 19.9, 13.7, 11.0\}$ detection of ridges of the same size. As a comparison, the fiducial stack of troughs with the lowest 20% in density percentile P would result in a $|S/N| = \{12.3, 10.7, 8.4, 5.7\}$ detection trough detection using the same dataset.

To allow for easier visual comparison between the shape of trough and ridge profiles, we include the trough lensing signal with its sign flipped (i.e. $-\gamma_{\rm t}(R)$) in Fig. 4.7. We find that, for all aperture sizes, the shear resulting from ridges is stronger than that from troughs, which again indicates skewness in the total density distribution. Like G16, we observe that the difference between troughs and ridges is slightly increased for the smallest apertures. This can be explained by the fact that non-linearities affect the density field more strongly at smaller scales.

4.5 Redshift evolution

So far we have studied troughs which extend across the entire redshift range of the GAMA galaxies ($0 < z < 0.5$). We can, however, define troughs that

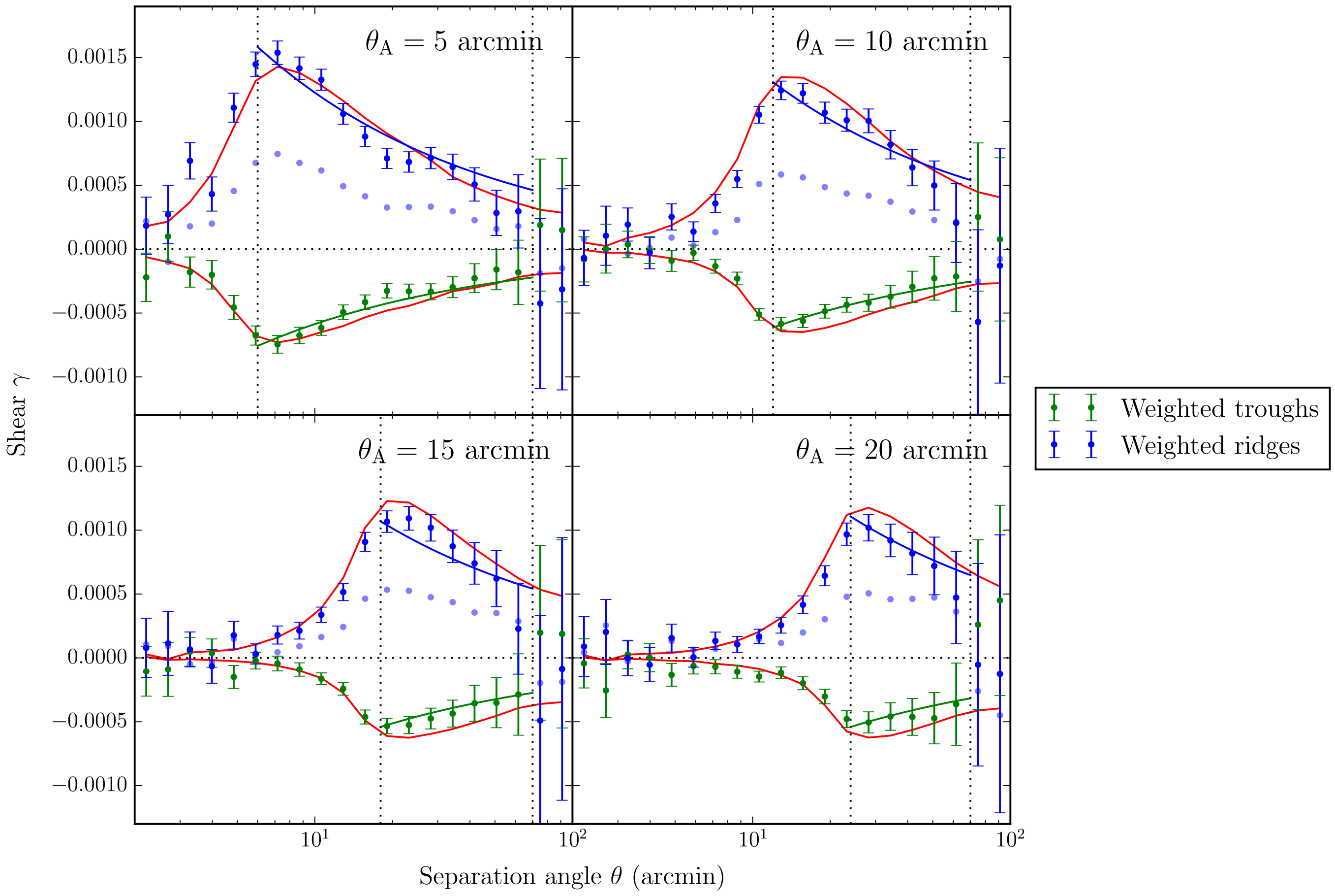

Figure 4.7: The optimally weighted KiDS (dots with 1σ errors) and MICE shear profiles $\gamma(\theta)$ of troughs (green) and ridges (blue), for apertures of increasing radius θ_{A}. The mirror image of each trough profile (light blue dots) is added to allow for a better visual comparison. We fit a simple power law: $A/\sqrt{\theta}$ (blue/green lines), within the fitting range (dotted vertical lines) to obtain the amplitude A of the lensing signals. For all aperture sizes, the shear from overdensities (ridges) is stronger than that of underdensities (troughs). This difference, which signifies non-linearities in the density field, is slightly larger for the smallest apertures.

cover only a part of this range, which allows us to study the evolution of troughs and ridges over cosmic time. In this section we will define the foreground galaxy and trough samples as a function of redshift, and discuss the resulting lensing measurements.

4.5.1 Redshift dependent trough selection

To study the redshift evolution of troughs we create two foreground galaxy samples, a low and a high redshift sample, which are used to select the low and high redshift troughs. These two galaxy samples need to be physically similar to ensure that the trough detection at different redshifts is not subject to bias. One requirement is that the two samples should consist of similar galaxy populations, since different kinds of galaxies might be subject to a varying amount of clustering. Another condition is that the number density of galaxies per comoving volume should be approximately equal for the two samples. In order to meet these two requirements, we define a volume limited sample of galaxies by applying a cut in redshift: $0.1 < z < 0.3$, and in absolute r-band magnitude: $M_{\rm r} < -21.0$. In this volume limited sample, all galaxies visible at the lowest redshift ($z_{\rm min} = 0.1$) are still observable up to the maximum redshift limit ($z_{\rm max} = 0.3$). Figure 4.8 shows the distribution of GAMA galaxies as a function of redshift z and absolute r-band magnitude $M_{\rm r}$, with coloured lines indicating the fiducial and volume limited galaxy samples.

When defining troughs as a function of redshift, we also need to take into account their physical shape. A visualization of the trough geometry is given by Fig. 4.9, which shows a 2D projection of the volumes that define the high and low redshift troughs. Inside these two conical frusta, the projected number density of the low (high) redshift galaxy samples will be measured in order to define the low (high) redshift troughs. The volumes need to be separated at a redshift limit $z_{\rm lim}$, which corresponds to a comoving distance limit $D_{\rm lim}$. In order to obtain a consistent definition of the troughs, $D_{\rm lim}$ is chosen in such a way that the comoving lenghts of the two volumes are equal:

$$L_{\rm low}\left(= D_{\rm lim} - D_{\rm min}\right) = L_{\rm high}\left(= D_{\rm max} - D_{\rm lim}\right) . \tag{4.6}$$

For our chosen redshift range: $0.1 < z < 0.3$, and the corresponding comoving distances (see Table 4.1) we find that $z_{\rm lim} = 0.198$, very close to the 'half-way' redshift of 0.2. Of course $z_{\rm lim}$ depends on our chosen values for the cosmological parameters, but this effect is $\sim 1\%$ at these low redshifts (for reasonable values of the cosmological parameters).

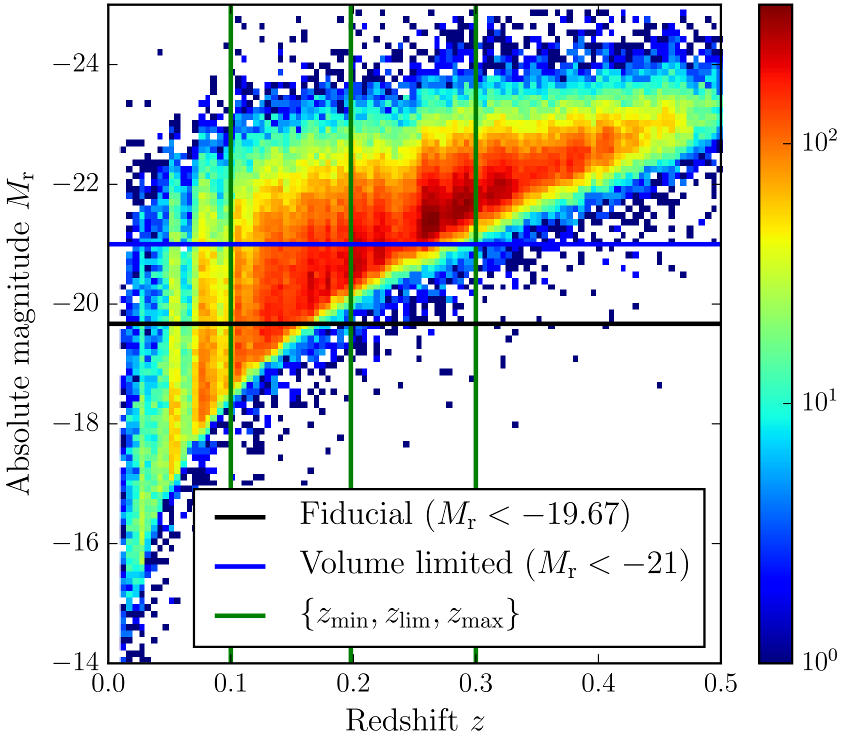

Figure 4.8: The distribution of GAMA galaxies as a function of redshift z (x-axis) and absolute r-band magnitude M_r (y-axis). The black line indicates the minimum M_r of the fiducial galaxy sample, while the blue line indicates the volume limited sample, divided into a high and low redshift sample by the green lines.

In addition to having equal lengths, the cones need to have the same radius. Selecting troughs to have equal physical radii will cause a decrease in the galaxy density at lower redshifts (i.e. later cosmic times), caused by the expansion of the Universe. Therefore, we select low and high redshift troughs that have the same *comoving* radius $R_{\rm low}$ and $R_{\rm high}$, by choosing their opening angles $\theta_{\rm low}$ and $\theta_{\rm high}$ accordingly. Here we define $R_{\rm low}$ ($R_{\rm high}$) as the comoving projected radial distance corresponding to $\theta_{\rm low}$ ($\theta_{\rm high}$) at the mean comoving distance $D_{\rm low}$ ($D_{\rm high}$) of the GAMA galaxies in the low (high) redshift sample[3]. In short:

$$R_{\rm low} \left(= \theta_{\rm low}\, D_{\rm low}\right) = R_{\rm high} \left(= \theta_{\rm high}\, D_{\rm high}\right) , \tag{4.7}$$

---

[3] We use the spectroscopic GAMA redshifts for this calculation, to avoid any possible effects of photo-z scatter.

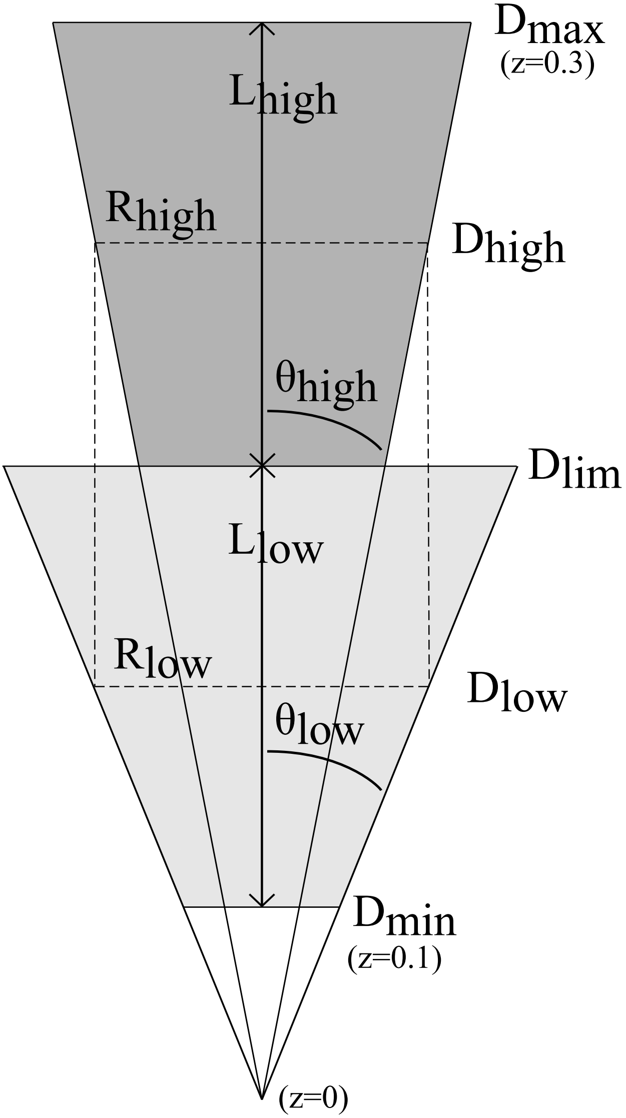

Figure 4.9: A visualization of the trough selection as a function of redshift. The two conical frusta used to define the low redshift troughs (light grey) and the high redshift troughs (dark grey) are divided at the comoving distance limit $D_{\rm lim}$. In order to avoid a biased trough selection, $D_{\rm lim}$ is chosen such that both volumes have the same comoving lenght: $L_{\rm low} = L_{\rm high}$. Moreover, the opening angles $\theta_{\rm low}$ and $\theta_{\rm high}$ of the cones are chosen such that the comoving projected radius $R_{\rm low}$ ($R_{\rm high}$) at the mean comoving distance $D_{\rm low}$ ($D_{\rm high}$) of the low (high) redshift galaxies are the same.

where $\theta_{\rm low}$ is chosen from the fiducial aperture sizes: $\{5, 10, 15, 20\}$ arcmin. We find the mean distances: $D_{\rm low} = 653.5\, h_{70}^{-1}{\rm Mpc}$ and $D_{\rm high} = 1037\, h_{70}^{-1}{\rm Mpc}$, with corresponding high redshift trough radii: $\theta_{\rm high} = \{3.152, 6.303, 9.455, 12.61\}$ arcmin. From these sizes we would like to select the smallest aperture, since this provides the shear signal with the highest S/N (as seen in Sect. 4.4.3). However, we also wish to avoid unreliable density estimates, resulting from the low number of galaxies inside smaller apertures. We therefore select a high redshift aperture size of $\theta_{\rm high} = 6.303\,{\rm arcmin}$, corresponding to $\theta_{\rm low} = 10\,{\rm arcmin}$. This ensures that $\theta_{\rm high}$ is small, but still slightly larger than our smallest fiducial aperture ($\theta_A = 5\,{\rm arcmin}$), which has proved adequate in our results and those of G16. Both opening angles correspond to a comoving projected radial distance $R_{\rm A} = 1.901\, h_{70}^{-1}{\rm Mpc}$ at their respective distances, constituting the comoving sizes of the troughs/ridges. The information on the low and high redshift galaxy samples is summarized in Table 4.1.

4.5.2 Excess surface density measurements

When the lenses have a specified redshift $z_{\rm l}$, the measured shear depends on the distance between the lens, the source and the observer. To correct for this effect, we convert the shear profile $\gamma(\theta)$ to the physical Excess Surface Density (ESD) profile $\Delta\Sigma(R)$ as a function of the physical projected separation R. The ESD is defined as the surface mass density $\Sigma(R)$, subtracted from the mean surface density $\overline{\Sigma}(<R)$ within that radius:

$$\Delta\Sigma(R) = \overline{\Sigma}(<R) - \Sigma(R) = \Sigma_{\rm crit}\gamma_{\rm t}(R)\,. \tag{4.8}$$

The conversion factor between the shear and the physical ESD is the critical surface density $\Sigma_{\rm crit}$, which is inversely proportional to the efficiency of the gravitational lensing effect. It depends on the angular diameter distance from the observer to the lens $D(z_{\rm l})$, to the source $D(z_{\rm s})$, and between the lens and the source $D(z_{\rm l}, z_{\rm s})$, as follows:

$$\Sigma_{\rm crit} = \frac{c^2}{4\pi G}\int_{z_{\rm l}+\Delta z}^{\infty} \frac{D(z_{\rm s})}{D(z_{\rm l})\, D(z_{\rm l}, z_{\rm s})} n(z_{\rm s})\, {\rm d}z_{\rm s}\,. \tag{4.9}$$

Here c denotes the speed of light and G the gravitational constant. As the lens redshifts $z_{\rm l}$ of the low (high) redshift troughs, we use the mean redshift of the low (high) redshift galaxy sample which is used to define the troughs. To estimate the redshifts $z_{\rm s}$ of the sources, we use the redshift probability distribution $n(z_\mathrm{s})$ of the full source population, determined using the direct calibration method described in Hildebrandt et al. (2017). This is done to circumvent the bias inherent in individual photometric source redshift estimates. We determine Σ_crit by integrating over the part of the source redshift probability distribution situated behind the lens ($z_\mathrm{s} > z_\mathrm{l} + \Delta z$) including a redshift buffer $\Delta z = 0.2$, following the method described in Sect. 3.2 (Eq. 9) of Dvornik et al. (2017).

Since lenses with a higher lensing efficiency ($= \Sigma_\mathrm{crit}^{-1}$) produce a stronger shear, we give them more weight in the combined ESD measurement. We incorporate Σ_crit into the total weight:

$$W_\mathrm{ls} = w_\mathrm{s} \left(\Sigma_\mathrm{crit,ls}^{-1} \right)^2 , \tag{4.10}$$

which is used to calculate our combined ESD measurement as follows:

$$\Delta\Sigma = \frac{1}{1+\mu} \frac{\sum_{ls} W_{ls}\, \Sigma_{\mathrm{crit},ls}\, \epsilon_{\mathrm{t},ls}}{\sum_{ls} W_{ls}} . \tag{4.11}$$

The correction for the multiplicative bias is weighted by the same total weight.

The angular separation range $2 < \theta < 100\,\mathrm{arcmin}$, used to measure the shear profiles in Sect. 4.4, corresponds to a physical projected separation of $0.44 < R < 22.24\, h_{70}^{-1}\mathrm{Mpc}$ at the mean angular diameter distance of the fiducial GAMA sample. We therefore measure the ESD profiles of the low/high redshift troughs for 10 logarithmically spaced bins within $0.5 < R < 20\, h_{70}^{-1}\mathrm{Mpc}$. The reason we use only half the number of radial bins, is that dividing the tracer galaxies as function of redshift results in trough profiles with a lower S/N. Although it is customary to use physical distances to measure the ESD profile around galaxies and other bound structures, the trough lensing measurements need to take the expansion of the Universe into account. We therefore translate our physical $\Delta\Sigma(R)$ profiles into the comoving surface density as a function of comoving radius, by dividing each measured $\Delta\Sigma$ by $(1 + z_\mathrm{l})^2$, and multiplying each R with $(1 + z_\mathrm{l})$.

4.5.3 Results

We measure the comoving ESD profiles of the troughs/ridges selected at different redshifts, and apply the same method of amplitude fitting and weighted stacking as discussed in Sect. 4.4.2 and 4.4.3 to both the KiDS and MICE data. The comoving radial fitting range is: $1.2\, R_\mathrm{A} < R < 20\, h_{70}^{-1}\mathrm{Mpc}$,

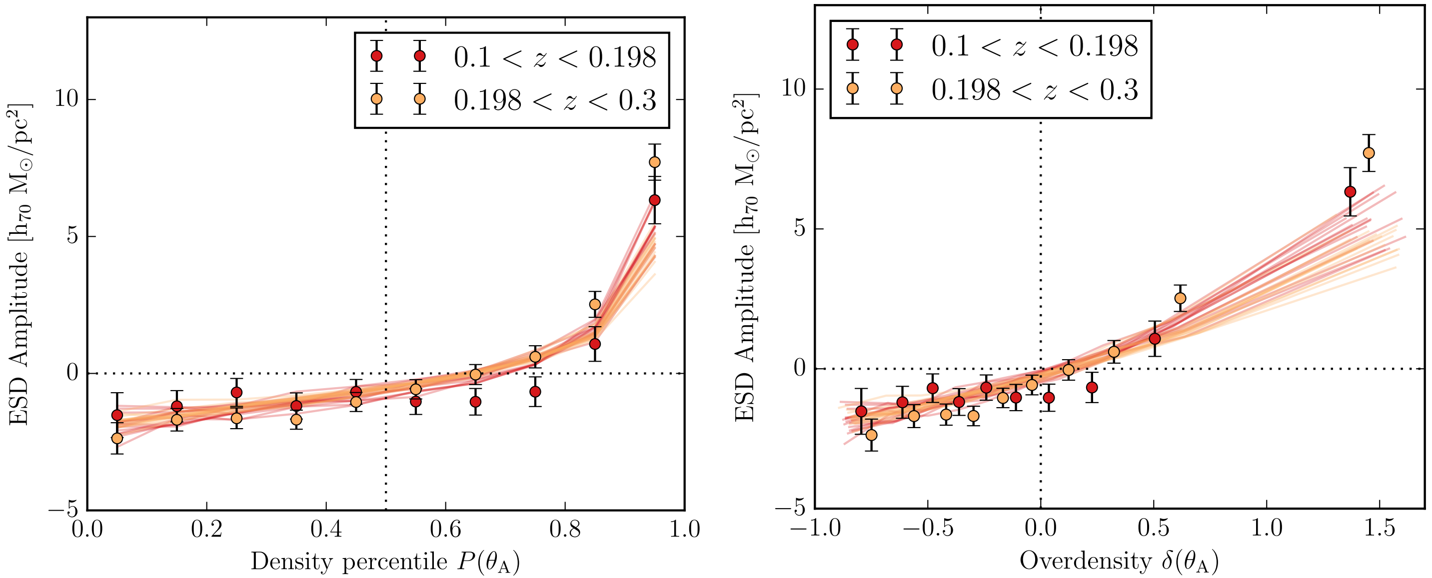

Figure 4.10: The amplitude A of the comoving ESD profiles as a function of the density percentile P (left) and overdensity δ (right), for troughs and ridges selected at two different redshifts. The observed amplitudes from KiDS (points with 1σ errors) are in reasonable agreement with those from 16 independent patches of the MICE mocks (solid lines). For the ridges ($\delta > 0$) in the MICE mocks, the amplitude is slightly higher at low redshifts. This effect, however, is not found in the observations, as we find no significant difference between the observed amplitudes at low and high redshifts.

where the maximum is based on the comoving projected distance corresponding to $\theta < 70\,\mathrm{arcmin}$ (see Sect. 4.4.1) at the mean distance of the fiducial GAMA sample. In the left panel of Fig. 4.10 we again show the best-fit amplitude A (including 1σ error bars derived from the full analytical covariance matrix) as a function of percentile P, this time for the low and high redshift troughs/ridges. For both the high and low redshift sample the shape of the $A(P)$ relation resembles that of the fiducial sample: rising gradually from negative A at low P, crossing the turn-over to positive A at $P \approx 0.6$, and peaking at $P = 1$. The observed relation is in reasonable agreement with the prediction from 16 independent patches of the MICE mocks. To assess whether there is a significant difference between the measurements of the low and high redshift troughs/ridges, we calculate the χ^2 between the amplitude difference and a null result, which is: $\chi^2 = 16.36$. Since the $A(P)$ measurements consist of $N = 10$ data-points (corresponding to a Cumulative Distribution Function with $10 - 1 = 9$ degrees of freedom) this χ^2 corresponds to 1.88σ, which means that there is no significant difference. We verify that this is in agreement with the trough results based on GAMA galaxies.

We again show the same A as a function of the overdensity δ in the right panel of Fig. 4.10. Like for the fiducial troughs, the $A(\delta)$-relation of both troughs samples is approximately linear, and crosses the turn-over point to positive A approximately at the mean density ($\delta \approx 0$) for both KiDS and MICE. Looking more closely at the center of the figure actually shows that both the KiDS and MICE results pass slightly below the origin, like we observed for the fiducial trough amplitudes with $\theta_{\mathrm{A}} = 5\,\mathrm{arcmin}$ (see Sect. 4.4.2). Because the overdensity is a measure of the galaxy number density, this non-linear relation between A and δ would, if the effect were physical, signify a discrepancy between dark and luminous matter known as galaxy bias. Again, there is no significant difference between the observed amplitudes at low and high redshift. For the MICE mocks, however, we can see that the amplitude of the low redshift ridges ($\delta > 0$) is slightly higher than that of the high redshift ridges. This is expected, since the clustering of mass increases the height of ridges at later cosmic times. It is interesting to note that, despite the observed difference in the lensing amplitude, the low and high redshift troughs/ridges span approximately the same galaxy overdensity range: $-0.8 \lesssim \delta \lesssim 1.5$.

4.5.4 Predictions for higher redshifts

The physical interpretation of the mock results in Fig. 4.10 would be that the total density of ridges increases with cosmic time. This is expected, since overdensities in the cosmic structure cluster over cosmic time, forming higher ridges. Since this mass is accreted from more underdense regions, these are expected to form deeper troughs. The latter effect, however, is not observed in the observations or the mocks between $0.1 < z < 0.3$. In order to obtain a more solid interpretation of our results, we study the predictions from the MICE-GC mocks at even higher redshifts. As our galaxy sample we use the same MICE mock galaxies with $M_{\rm r} < -21$, but without a cut in apparent magnitude such that the sample is complete at every redshift. Using this sample we perform the same redshift dependent trough selection as described in Sect. 4.5.1, but instead of dividing galaxies into two redshift bins between $0.1 < z < 0.3$ we divide them into five redshift bins between $0.1 < z < 0.6$. These five redshift slices of equal comoving length have the following redshift limits: $z_{\rm lim} = 0.1, 0.191, 0.286, 0.385, 0.489, 0.6$. As in Sect. 4.5.1 we wish to select the opening angles $\theta_{\rm A}$ corresponding to these redshifts, such that the comoving radii of the apertures are the same and none of the angles is smaller than $5\,{\rm arcmin}$. The chosen opening angles of the troughs, $\theta_{\rm A} = \{20., 12.85, 9.45, 7.44, 6.14\}$, correspond to the same comoving projected separation $R_{\rm A} = 3.712\,h_{70}^{-1}{\rm Mpc}$ at the mean galaxy distance in each redshift bin.

We perform the same measurement of the comoving ESD profiles, and fit the same $A/\sqrt{R}$ function to the results. In the left panel of Fig. 4.11 we again show the best-fit amplitude A of as a function of percentile P, this time for mock troughs/ridges in the five redshift bins. In the highest percentile bin ($0.9 < P < 1$) we can see that the difference that was barely visible in Fig. 4.10 has become a significant trend: as the redshift increases to $z = 0.6$, the ridge amplitude decreases. This trend can be better appreciated in the right panel of Fig. 4.11, which shows the amplitude as a function of overdensity δ: the absolute value of A clearly decreases with redshift for the ridges. This effect is even slightly visible for the troughs where, except for the second redshift bin ($0.191 < z < 0.286$), A continues to increase with z. But while the comoving ESD amplitude range spanned by the troughs/ridges increases with cosmic time, the span of the galaxy overdensity range slightly decreases for the ridges. This apparent increase in the density contrast of the total mass distribution while that of the galaxy distribution decreases, might again signify non-linear galaxy bias. Unfortunately, as seen in Sect. 4.5.3, it is not yet possible to observationally mea-

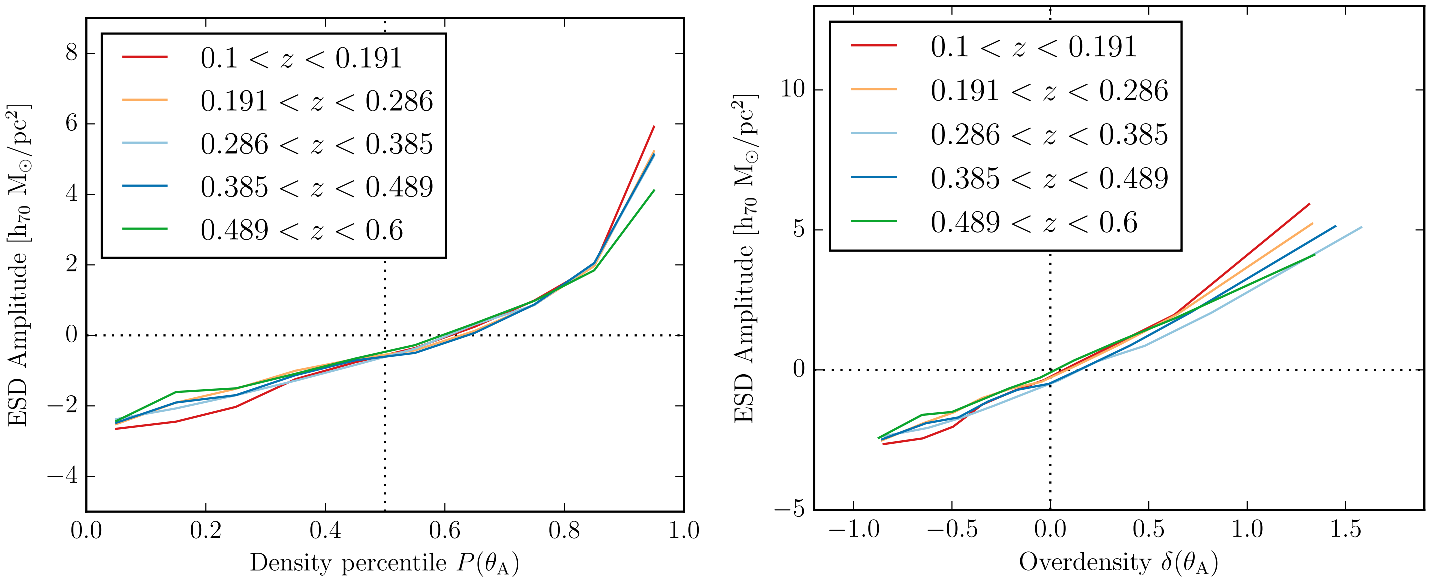

Figure 4.11: The amplitude A of the comoving ESD profiles from MICE mocks as a function of the density percentile P (left) and overdensity δ (right), for troughs and ridges selected at five different redshifts between $0.1 < z < 0.6$. For both troughs and ridges the redshift evolution, that was hinted at by the results at low redshifts, appears to be a continuing trend. Except for the erratic behaviour in the fourth redshift bin, the covered range of A steadily decreases with redshift. This is expected from the clustering of mass with cosmic time, which causes massive ridges to accrete mass from the low density troughs. However, the covered range of δ seems to slightly increase with redshift. If physical, this would signify an increase in the total density contrast with cosmic time, but a decrease in the contrast of the galaxy density distribution.

sure these small effects at high redshifts using the current lensing surveys.

4.6 Discussion and conclusion

We use the Kilo-Degree Survey (KiDS) to perform a weak gravitational lensing study of troughs: circular projected underdensities in the cosmic galaxy density field, following up on the work by Gruen et al. (2016, G16). We define the troughs using two different foreground galaxy samples: 159,519 galaxies from the equatorial fields of the Galaxy and Mass Assembly (GAMA) survey, and a sample of 309,021 KiDS galaxies that is limited to photometric redshift $z_{\mathrm{ANN}} < 0.5$ and apparent magnitude $m_{\mathrm{r}} < 20.2$ in order to mimic the GAMA selection. Both galaxy samples are limited to an absolute magnitude $M_{\mathrm{r}} < -19.67$ in order to mimic the mock galaxy sample from the MICE Grand Challenge (MICE-GC) lightcone simulation, which is used to interpret our results. Following the fiducial trough definition of G16 (apertures with a density percentile $P(\theta_{\mathrm{A}}) < 0.2$), we detect a gravitational lensing signal with a signal to noise of $|S/N| = 12.3$ for the KiDS foreground sample and 12.0 for GAMA. Since the current KiDS area already provides a more significant trough lensing detection than the GAMA survey, we mainly use KiDS for this work (although we confirm all our results using GAMA). As the KiDS survey progresses in the coming years, the available area will become even larger and less irregular. The coming KiDS data release, which aims to make a contiguous area of $900\,\mathrm{deg}^2$ available for lensing studies, will likely reduce the systematic lensing effects found at large scales and increase the detection significance of the trough signal (at most by a factor of $\sim \sqrt{900/180} = 2.24$ compared to GAMA).

In addition to stacking only the most underdense/overdense 20% of the apertures, we study troughs and ridges (overdensities) as a function of their galaxy number density n_{g}. By fitting the simple function $\gamma(\theta) = A/\sqrt{\theta}$ to the lensing signal in bins of increasing n_{g}, we obtain the amplitude A of troughs and ridges as a function of density percentile P and overdensity δ. We discover that the turning point between negative and positive A is situated at $P \approx 0.6$ (and not at the median density $P = 0.5$), while $A(\delta)$ does generally pass through the origin (the mean density $\delta = 0$). This indicates that the non-linearities in the density field caused by structure formation, which are shown by the skewed distribution of n_{g} (see Fig. 4.1), are reflected in the total (baryonic + dark matter) density distribution measured by gravitational lensing. As expected, these non-linearities are more prominent at smaller scales, i.e. for smaller trough radii. This conclusion is supported by mock trough profiles obtained from the MICE-GC lightcone simulation, which show exactly the same trend.

We also use the amplitude A and its 1σ error δA to define the signal to noise (S/N) of the lensing profiles as $A/\delta A$. The S/N as a function of P is used as a weight to optimally stack the shear profiles of all troughs/ridges, in order to obtain the highest possible detection significance. The optimally stacked lensing signals have $|S/N| = \{17.1, 14.8, 10.0, 7.6\}$ for troughs with a size of $\theta_{\rm A} = \{5, 10, 15, 20\}\,{\rm arcmin}$, significantly higher than that of the fiducial trough definition ($|S/N| = \{12.3, 10.7, 8.4, 5.7\}$). Inspecting the optimally stacked trough and ridge profiles shows that the shear profiles of ridges are much stronger than those of troughs, especially for the smallest trough radius. This finding, which is in agreement with the results from the MICE-GC mocks and the observations from G16, again reveals the skewness of the total mass density distribution.

Finally we try to observe physical evolution of the density field, by performing the trough selection in two redshift bins. We create a volume limited sample of foreground galaxies ($z < 0.3$ and $M_{\rm r} < -21$), and split it into a low ($0.1 < z < 0.198$) and high ($1.198 < z < 0.3$) redshift sample of equal comoving length. By adjusting the opening angle $\theta_{\rm high}$ of the high redshift apertures, we ensure that the comoving projected radius of the troughs is identical at both redshifts: $R = 1.901\,h_{70}^{-1}{\rm Mpc}$. The measurement of the Excess Surface Density (ESD) profiles provides the physical surface density distributions of the troughs/ridges, taking into account their distances to the KiDS source galaxies. After converting physical to comoving ESD profiles to correct them for the expansion of the Universe, we do not observe a significant difference between the trough/ridge amplitudes A as a function of P and δ. Applying the same method to 16 independent patches of the MICE-GC mock catalogue provides a reasonable agreement with the observation, although the $A(\delta)$ relation of the mocks reveals a slight decrease in the lensing amplitude of ridges with redshift. This increase in ridge height with cosmic time is expected from the effects of clustering.

The question remains whether this trend continues at higher redshifts, and whether the effects of clustering can also be observed in troughs. We therefore use the MICE mock catalogue to gain more insight into our finding, by extending our measurement to five redshift bins between $0.1 < z < 0.6$. The comoving ESD amplitude of the mock ridges continues to decrease with redshift, indicating that the increasing ridge height with cosmic time is an actual trend. In the mock measurements at high redshifts, we can even find a trace of the corresponding deepening of troughs with cosmic time.

Future efforts using the increasing KiDS area and DES area+depth, or upcoming surveys like Euclid and the LSST, might be able to observationally measure this effect.

Acknowledgements

This research is based on data products from observations made with ESO Telescopes at the La Silla Paranal Observatory under programme IDs 177.A-3016, 177.A-3017 and 177.A-3018, and on data products produced by Target OmegaCEN, INAF-OACN, INAF-OAPD and the KiDS production team, on behalf of the KiDS consortium. OmegaCEN and the KiDS production team acknowledge support by NOVA and NWO-M grants. Members of INAF-OAPD and INAF-OACN also acknowledge the support from the Department of Physics & Astronomy of the University of Padova, and of the Department of Physics of Univ. Federico II (Naples).

GAMA is a joint European-Australasian project based around a spectroscopic campaign using the Anglo-Australian Telescope. The GAMA input catalogue is based on data taken from the Sloan Digital Sky Survey and the UKIRT Infrared Deep Sky Survey. Complementary imaging of the GAMA regions is being obtained by a number of independent survey programs including GALEX MIS, VST KiDS, VISTA VIKING, WISE, Herschel-ATLAS, GMRT and ASKAP providing UV to radio coverage. GAMA is funded by the STFC (UK), the ARC (Australia), the AAO, and the participating institutions. The GAMA website is `www.gama-survey.org`.

This work has made use of PYTHON (`www.python.org`), including the packages NUMPY (`www.numpy.org`), SCIPY (`www.scipy.org`) and IPYTHON (Pérez and Granger 2007). Plots have been produced with MATPLOTLIB (Hunter 2007). The mock shear profiles from MICE are computed using TREECORR (`https://pypi.python.org/pypi/TreeCorr`).

5 Lensing test of Verlinde's Emergent Gravity

Based on: “First test of Verlinde’s theory of Emergent Gravity using Weak Gravitational Lensing measurements”
Authors: Margot M. Brouwer, Manus R. Visser, Andrej Dvornik, Henk Hoekstra, Konrad Kuijken, Edwin A. Valentijn, Maciej Bilicki, Chris Blake, Sarah Brough, Hugo Buddelmeijer, Thomas Erben, Catherine Heymans, Hendrik Hildebrandt, Benne W. Holwerda, Andrew M. Hopkins, Dominik Klaes, Jochen Liske, Jon Loveday, John McFarland, Reiko Nakajima, Cristóbal Sifón, Edward N. Taylor
Published in: Monthly Notices of the Royal Astronomical Society, Volume 466, Issue 3, p.2547-2559

Abstract:
Verlinde (2016) proposed that the observed excess gravity in galaxies and clusters is the consequence of Emergent Gravity (EG). In this theory the standard gravitational laws are modified on galactic and larger scales due to the displacement of dark energy by baryonic matter. EG gives an estimate of the excess gravity (described as an *apparent* dark matter density) in terms of the baryonic mass distribution and the Hubble parameter. In this work we present the first test of EG using weak gravitational lensing, within the regime of validity of the current model. Although there is no direct description of lensing and cosmology in EG yet, we can make a reasonable estimate of the expected lensing signal of low redshift galaxies by assuming a background ΛCDM cosmology. We measure the (apparent) average surface mass density profiles of $33,613$ isolated central galaxies, and compare them to those predicted by EG based on the galaxies' baryonic masses. To this end we employ the $\sim 180\ \mathrm{deg}^2$ overlap of the Kilo-Degree Survey (KiDS) with the spectroscopic Galaxy And Mass Assembly (GAMA) survey. We find that the prediction from EG, despite requiring *no free parameters*, is in good agreement with the observed galaxy-galaxy lensing profiles in four different stellar mass bins. Although this performance is remarkable, this study is only a first step. Further advancements on both the theoretical framework and observational tests of EG are needed before it can be considered a fully developed and solidly tested theory.

5.1 Introduction

In the past decades, astrophysicists have repeatedly found evidence that gravity on galactic and larger scales is in excess of the gravitational potential that can be explained by visible baryonic matter within the framework of General Relativity (GR). The first evidence through the measurements of the dynamics of galaxies in clusters (Zwicky 1937) and the Local Group (Kahn and Woltjer 1959), and through observations of galactic rotation curves (inside the optical disks by Rubin 1983, and far beyond the disks in hydrogen profiles by Bosma 1981) has been confirmed by more recent dynamical observations (Martinsson et al. 2013; Rines et al. 2013). Furthermore, entirely different methods like gravitational lensing (Hoekstra et al. 2004; Mandelbaum 2015; von der Linden et al. 2014; Hoekstra et al. 2015) of galaxies and clusters, Baryon Acoustic Oscillations (BAO's, Eisenstein et al. 2005; Blake et al. 2011) and the cosmic microwave background (CMB, Spergel et al. 2003; Planck XIII 2016) have all acknowledged the necessity of an additional mass component to explain the excess gravity. This interpretation gave rise to the idea of an invisible *dark matter* (DM) component, which now forms an important part of our standard model of cosmology. In our current ΛCDM model the additional mass density (the density parameter $\Omega_{\rm CDM} = 0.266$ found by Planck XIII 2016) consists of cold (non-relativistic) DM particles, while the energy density in the cosmological constant ($\Omega_\Lambda = 0.685$) explains the observed accelerating expansion of the universe. In this paradigm, the spatial structure of the sub-dominant baryonic component (with $\Omega_{\rm b} = 0.049$) broadly follows that of the DM. When a DM halo forms through the gravitational collapse of a small density perturbation (Peebles and Yu 1970) baryonic matter is pulled into the resulting potential well, where it cools to form a galaxy in the centre (White and Rees 1978). In this framework the excess mass around galaxies and clusters, which is measured through dynamics and lensing, has hitherto been interpreted as caused by this DM halo.

In this paper we test the predictions of a different hypothesis concerning the origin of the excess gravitational force: the Verlinde (2017) model of Emergent Gravity (EG). Generally, EG refers to the idea that spacetime and gravity are macroscopic notions that arise from an underlying microscopic description in which these notions have no meaning. Earlier work on the emergence of gravity has indicated that an area law for gravitational entropy is essential to derive Einstein's laws of gravity (Jacobson 1995; Padmanabhan 2010; Verlinde 2011; Faulkner et al. 2014; Jacobson

2016). But due to the presence of positive dark energy in our universe Verlinde (2017) argues that, in addition to the area law, there exists a volume law contribution to the entropy. This new volume law is thought to lead to modifications of the emergent laws of gravity at scales set by the 'Hubble acceleration scale' $a_0 = cH_0$, where c is the speed of light and H_0 the Hubble constant. In particular, Verlinde (2017) claims that the gravitational force emerging in the EG framework exceeds that of GR on galactic and larger scales, similar to the MOND phenomenology (Modified Newtonian Dynamics, Milgrom 1983) that provides a successful description of galactic rotation curves (e.g. McGaugh et al. 2016). This excess gravity can be modelled as a mass distribution of *apparent* DM, which is only determined by the baryonic mass distribution $M_b(r)$ (as a function of the spherical radius r) and the Hubble constant H_0. In a realistic cosmology, the Hubble parameter $H(z)$ is expected to evolve with redshift z. But because EG is only developed for present-day de Sitter space, any predictions on cosmological evolution are beyond the scope of the current theory. The approximation used by Verlinde (2017) is that our universe is entirely dominated by dark energy, which would imply that $H(z)$ indeed resembles a constant. In any case, a viable cosmology should at least reproduce the observed values of $H(z)$ at low redshifts, which is the regime that is studied in this work. Furthermore, at low redshifts the exact specifics of the cosmological evolution have a negligible effect on our measurements. Therefore, to calculate distances from redshifts throughout this work, we can adopt an effective ΛCDM background cosmology with $\Omega_{\rm m} = 0.315$ and $\Omega_{\Lambda} = 0.685$ (Planck XIII 2016), without significantly affecting our results. To calculate the distribution of apparent DM, we use the value of $H_0 = 70\,{\rm km\,s^{-1}Mpc^{-1}}$. Throughout the paper we use the following definition for the reduced Hubble constant: $h \equiv h_{70} = H_0/(70\,{\rm km\,s^{-1}Mpc^{-1}})$.

Because, as mentioned above, EG gives an effective description of GR (with apparent DM as an additional component), we assume that a gravitational potential affects the pathway of photons as it does in the GR framework. This means that the distribution of apparent DM can be observed using the regular gravitational lensing formalism. In this work we test the predictions of EG specifically relating to galaxy-galaxy lensing (GGL): the coherent gravitational distortion of light from a field of background galaxies (sources) by the mass of a foreground galaxy sample (lenses) (see e.g. Fischer et al. 2000; Hoekstra et al. 2004; Mandelbaum et al. 2006b; Velander et al. 2014; van Uitert et al. 2016). Because the prediction of the gravitational potential in EG is currently only valid for static, spherically symmetric and isolated baryonic mass distributions, we need to select our lenses to satisfy these criteria. Furthermore, as mentioned above, the lenses should be at relatively low redshifts since cosmological evolution is not yet implemented in the theory. To find a reliable sample of relatively isolated foreground galaxies at low redshift, we select our lenses from the very complete spectroscopic Galaxy And Mass Assembly survey (GAMA, Driver et al. 2011). In addition, GAMA's stellar mass measurements allow us to test the prediction of EG for four galaxy sub-samples with increasing stellar mass. The background galaxies, used to measure the lensing effect, are observed by the photometric Kilo-Degree Survey (KiDS, de Jong et al. 2013), which was specifically designed with accurate shape measurements in mind.

In Sect. 5.2 of this paper we explain how we select and model our lenses. In Sect. 5.3 we describe the lensing measurements. In Sect. 5.4 we introduce the EG theory and derive its prediction for the lensing signal of our galaxy sample. In Sect. 5.5 we present the measured GGL profiles and our comparison with the predictions from EG and ΛCDM. The discussion and conclusions are described in Sect. 5.6.

5.2 GAMA lens galaxies

The prediction of the gravitational potential in EG that is tested in this work is only valid for static, spherically symmetric and isolated baryonic mass distributions (see Sect. 5.4). Ideally we would like to find a sample of isolated lenses, but since galaxies are clustered we cannot use GAMA to find galaxies that are truly isolated. Instead we use the survey to construct a sample of lenses that dominate their surroundings, and a galaxy sample that allows us to estimate the small contribution arising from their nearby low-mass galaxies (i.e. satellites). The GAMA survey (Driver et al. 2011) is a spectroscopic survey with the AAOmega spectrograph mounted on the Anglo-Australian Telescope. In this study, we use the GAMA II (Liske et al. 2015) observations over three equatorial regions (G09, G12 and G15) that together span $\sim 180\,\mathrm{deg}^2$. Over these regions, the redshifts and properties of 180,960 galaxies[1] are measured. These data have a redshift completeness of 98.5% down to a Petrosian r-band magnitude of $m_\mathrm{r} = 19.8$. This is very useful to accurately determine the positional relation between galaxies, in order to find a suitable lens sample.

---

[1] These are all galaxies with redshift quality $n_\mathrm{Q} \geq 2$. However, the recommended redshift quality of GAMA (that we use in our analysis) is $n_\mathrm{Q} \geq 3$.

5.2.1 Isolated galaxy selection

To select foreground lens galaxies suitable for our study, we consult the 7th GAMA Galaxy Group Catalogue (G3Cv7) which is created by Robotham et al. (2011) using a Friends-of-Friends (FoF) group finding algorithm. In this catalogue, galaxies are classified as either the Brightest Central Galaxy (BCG) or a satellite of a group, depending on their luminosity and their mutual projected and line-of-sight distances. In cases where there are no other galaxies observed within the linking lengths, the galaxy remains 'non-grouped' (i.e., it is not classified as belonging to any group). Mock galaxy catalogues, which were produced using the Millennium DM simulation (Springel et al. 2005b) and populated with galaxies according to the semi-analytical galaxy formation recipe 'GALFORM' (Bower et al. 2006), are used to calibrate these linking lengths and test the resulting group properties.

However, since GAMA is a flux-limited survey, it does not include the satellites of the faintest observed GAMA galaxies when these are fainter than the flux limit. Many fainter galaxies are therefore classified as non-grouped, whereas they are in reality BCGs. This selection effect is illustrated in Fig. 5.1, which shows that the number of non-grouped galaxies rises towards faint magnitudes whereas the number of BCGs peaks well before. The only way to obtain a sample of 'isolated' GAMA galaxies without satellites as bright as f_L times their parents luminosity, would be to select only non-grouped galaxies brighter than $1/f_{\rm L}$ times the flux limit (illustrated in Fig. 5.1 for $f_{\rm L} = 0.1$). Unfortunately such a selection leaves too small a sample for a useful lensing measurement. Moreover, we suspect that in some cases observational limitations may have prevented the detection of satellites in this sample as well. Instead, we use this selection to obtain a reasonable estimate of the satellite distribution around the galaxies in our lens sample. Because the mass of the satellites is approximately spherically distributed around the BCG, and is sub-dominant compared to the BCG's mass, we can still model the lensing signal of this component using the EG theory. How we model the satellite distribution and its effect on the lensing signal is described in Sect. 5.2.2 and Sect. 5.4.3 respectively.

Because centrals are only classified as BCGs if their satellites are detected, whereas non-grouped galaxies are likely centrals with no observed satellites, we adopt the name 'centrals' for the combined sample of BCGs and non-grouped galaxies (i.e. all galaxies which are not satellites). As our lens sample, we select galaxies which dominate their surroundings in three ways: (i) they are centrals, i.e. not classified as satellites in the GAMA group catalogue; (ii) they have stellar masses below $10^{11}\,h_{70}^{-1}{\rm M}_{\odot}$, since we find

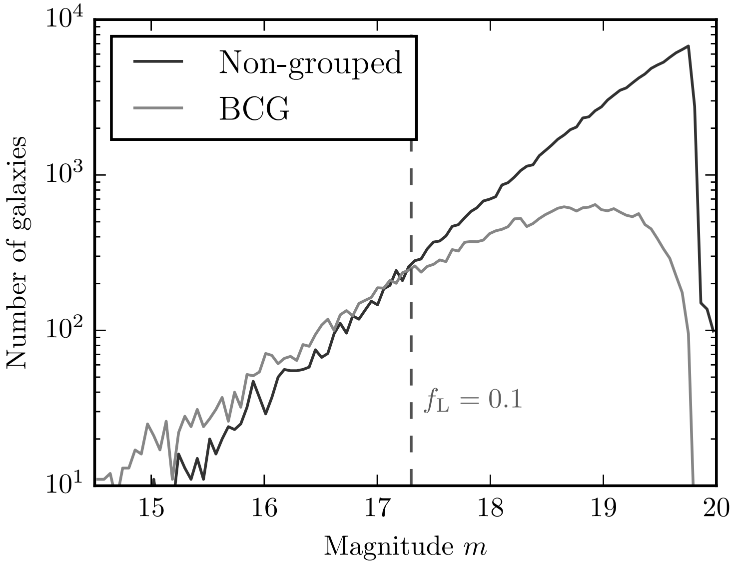

Figure 5.1: The magnitude distribution of non-grouped galaxies (dark grey) and BCGs (light grey). The dashed line indicates the selection that removes galaxies which might have a satellite beyond the visible magnitude limit. These hypothetical satellites have at most a fraction $f_{\rm L} = 0.1$ of the central galaxy luminosity, corresponding to the magnitude limit: $m_{\rm r} < 17.3$. We use this 'nearby' sample to obtain a reliable estimate of the satellite distribution around our centrals.

that galaxies with higher stellar mass have significantly more satellites (see Sect. 5.2.2); and (iii) they are not affected by massive neighbouring groups, i.e. there is no central galaxy within $3\,h_{70}^{-1}{\rm Mpc}$ (which is the maximum radius of our lensing measurement, see Sect. 5.3). This last selection suppresses the contribution of neighbouring centrals (known as the '2-halo term' in the standard DM framework) to our lensing signal, which is visible at scales above $\sim 1\,h_{70}^{-1}{\rm Mpc}$.

Furthermore, we only select galaxies with redshift quality $n_{\rm Q} \geq 3$, in accordance with the standard recommendation by GAMA. After these four cuts (central, no neighbouring centrals, $M_* < 10^{11}\,h_{70}^{-1}{\rm M}_\odot$ and $n_{\rm Q} \geq 3$) our remaining sample of 'isolated centrals' amounts to $33,613$ lenses.

5.2.2 Baryonic mass distribution

Because there exists no DM component in the Verlinde (2017) framework of EG, the gravitational potential originates only from the baryonic mass distribution. Therefore, in order to determine the lensing signal of our galaxies as predicted by EG (see Sect. 5.4), we need to know their baryonic mass distribution. In this work we consider two possible models: the point mass approximation and an extended mass profile. We expect the point mass approximation to be valid, given that (i) the bulk mass of a galaxy is enclosed within the minimum radius of our measurement ($R_{\rm min} = 30\, h_{70}^{-1}{\rm kpc}$), and (ii) our selection criteria ensure that our isolated centrals dominate the total mass distribution within the maximum radius of our measurement ($R_{\rm max} = 3\, h_{70}^{-1}{\rm Mpc}$). If these two assumptions hold, the entire mass distribution of the isolated centrals can be described by a simple point mass. This allows us to analytically calculate the lensing signal predicted by EG, based on only one observable: the galaxies' mass $M_{\rm g}$, which consists of a stellar and a cold gas component. To asses the sensitivity of our interpretation to the mass distribution, we compare the predicted lensing signal of the point mass to that of an extended mass distribution. This more realistic extended mass profile consists of four components: stars, cold gas, hot gas and satellites, which all have an extended density profile. In the following sections we review each component, and make reasonable assumptions regarding their model profiles and corresponding input parameters.

Stars and cold gas

To determine the baryonic masses $M_{\rm g}$ of the GAMA galaxies, we use their stellar masses M_* from version 19 of the stellar mass catalogue, an updated version of the catalogue created by Taylor et al. (2011b). These stellar masses are measured from observations of the Sloan Digital Sky Survey (SDSS, Abazajian et al. 2009) and the VISTA Kilo-Degree Infrared Galaxy survey (VIKING, Edge et al. 2013), by fitting Bruzual and Charlot (2003) stellar population synthesis models to the *ugrizZYJHK* spectral energy distributions (constrained to the rest frame wavelength range 3,000-11,000 Å). We correct M_* for flux falling outside the automatically selected aperture using the 'flux-scale' parameter, following the procedure discussed in Taylor et al. (2011b).

In these models, the stellar mass includes the mass locked up in stellar remnants, but not the gas recycled back into the interstellar medium. Because the mass distribution of gas in our galaxies is not measured, we can only obtain realistic estimates from literature. There are two contributions to consider: cold gas consisting of atomic hydrogen (HI), molecular hydrogen (H_2) and helium, and hot gas consisting of ionized hydrogen and helium. Most surveys find that the mass in cold gas is highly dependent on the galaxies' stellar mass. For low-redshift galaxies ($z < 0.5$) the mass in HI (H_2) ranges from $20-30\%$ ($8-10\%$) of the stellar mass for galaxies with $M_* = 10^{10} \mathrm{M}_\odot$, dropping to $5-10\%$ ($4-5\%$) for galaxies with $M_* = 10^{11} \mathrm{M}_\odot$ (Saintonge et al. 2011; Catinella et al. 2013; Boselli et al. 2014; Morokuma-Matsui and Baba 2015). Therefore, in order to estimate the mass of the cold gas component, we consider a cold gas fraction f_{cold} which depends on the measured M_* of our galaxies. We use the best-fit scaling relation found by Boselli et al. (2014) using the Herschel Reference Survey (Boselli et al. 2010):

$$\log\left(f_{\mathrm{cold}}\right) = \log\left(M_{\mathrm{cold}}/M_*\right) = -0.69 \log(M_*) + 6.63 \,. \tag{5.1}$$

In this relation, the total cold gas mass M_{cold} is defined as the combination of the atomic and molecular hydrogen gas, including an additional 30% contribution of helium: $M_{\mathrm{cold}} = 1.3\left(M_{\mathrm{HI}} + M_{\mathrm{H}_2}\right)$. With a maximum measured radius of ~ 1.5 times the effective radius of the stellar component, the extent of the cold gas distribution is very similar to that of the stars (Pohlen et al. 2010; Crocker et al. 2011; Mentuch Cooper et al. 2012; Davis et al. 2013). We therefore consider the stars and cold gas to form a single galactic mass distribution with:

$$M_{\mathrm{g}} = (M_* + M_{\mathrm{cold}}) = M_*(1 + f_{\mathrm{cold}}) \,. \tag{5.2}$$

For both the point mass and the extended mass profile, we use this galactic mass M_{g} to predict the lensing signal in the EG framework.

In the point mass approximation, the total density distribution of our galaxies consists of a point source with its mass corresponding to the galactic mass M_{g} of the lenses. For the extended mass profile, we use M_{g} as an input parameter for the density profile of the 'stars and cold gas' component. Because starlight traces the mass of this component, we use the Sérsic intensity profile (Sérsic 1963; Sersic 1968) as a reasonable approximation of the density:

$$I_{\mathrm{S}}(r) \propto \rho_{\mathrm{S}}(r) = \rho_{\mathrm{e}} \exp\left\{-b_{\mathrm{n}}\left[\left(\frac{r}{r_{\mathrm{e}}}\right)^{1/n} - 1\right]\right\} \,. \tag{5.3}$$

Here r_{e} is the effective radius, n is the Sérsic index, and b_{n} is defined such that $\Gamma(2n) = 2\gamma(2n, b_{\mathrm{n}})$. The Sérsic parameters were measured for $167,600$ galaxies by Kelvin et al. (2012) on the UKIRT Infrared Deep Sky Survey Large Area Survey images from GAMA and the $ugrizYJHK$ images of SDSS DR7 (where we use the parameter values as measured in the r-band). Of

Table 5.1: For each stellar mass bin, this table shows the number N and mean redshift $\langle z_\mathrm{l} \rangle$ of the galaxy sample. Next to these, it shows the corresponding measured input parameters of the ESD profiles in EG: the mean stellar mass $\langle M_* \rangle$, galactic mass $\langle M_\mathrm{g} \rangle$, effective radius $\langle r_\mathrm{e} \rangle$, Sérsic index $\langle n \rangle$, satellite fraction $\langle f_\mathrm{sat} \rangle$ and satellite radius $\langle r_\mathrm{sat} \rangle$ of the centrals. All masses are displayed in units of $\log_{10}(M / h_{70}^{-1} \mathrm{M}_\odot)$ and all lengths in $h_{70}^{-1}\mathrm{kpc}$.

$M*$-bin	N	$\langle z_\mathrm{l} \rangle$	$\langle M_* \rangle$	$\langle M_\mathrm{g} \rangle$	$\langle r_\mathrm{e} \rangle$	$\langle n \rangle$	$\langle f_\mathrm{sat} \rangle$	$\langle r_\mathrm{sat} \rangle$
$8.5 - 10.5$	14974	0.22	10.18	10.32	3.58	1.66	0.27	140.7
$10.5 - 10.8$	10500	0.29	10.67	10.74	4.64	2.25	0.25	143.9
$10.8 - 10.9$	4076	0.32	10.85	10.91	5.11	2.61	0.29	147.3
$10.9 - 11$	4063	0.33	10.95	11.00	5.56	3.04	0.32	149.0

these galaxies, $69,781$ are contained in our GAMA galaxy catalogue. Although not all galaxies used in this work (the $33,613$ isolated centrals) have Sérsic parameter measurements, we can obtain a realistic estimate of the mean Sérsic parameter values of our chosen galaxy samples. We use r_e and n equal to the mean value of the galaxies for which they are measured within each sample, in order to model the density profile $\rho_\mathrm{S}(r)$ of each full galaxy sample. This profile is multiplied by the effective mass density ρ_e, which is defined such that the mass integrated over the full $\rho_\mathrm{S}(r)$ is equal to the mean galactic mass $\langle M_\mathrm{g} \rangle$ of the lens sample. The mean measured values of the galactic mass and Sérsic parameters for our galaxy samples can be found in Table 5.1.

Hot gas

Hot gas has a more extended density distribution than stars and cold gas, and is generally modelled by the β-profile (e.g. Cavaliere and Fusco-Femiano 1976; Mulchaey 2000):

$$\rho_\mathrm{hot}(r) = \frac{\rho_\mathrm{core}}{\left(1 + (r/r_\mathrm{core})^2\right)^{\frac{3\beta}{2}}} \, , \tag{5.4}$$

which provides a fair description of X-ray observations in clusters and groups of galaxies. In this distribution r_core is the core radius of the hot gas. The outer slope is characterised by β, which for a hydrostatic isothermal sphere corresponds to the ratio of the specific energy in galaxies to that in the hot gas (see e.g. Mulchaey 2000, for a review). Observations of galaxy groups indicate $\beta \sim 0.6$ (Sun et al. 2009). Fedeli (2014) found similar results using the Overwhelmingly Large Simulations (OWLS, Schaye et al. 2010) for the range in stellar masses that we consider here (i.e. with $M_* \sim 10^{10} - 10^{11}\ h_{70}^{-1}\mathrm{M}_\odot$). We therefore adopt $\beta = 0.6$. Moreover, Fedeli (2014) estimate that the mass in hot gas is at most 3 times that in stars. As the X-ray properties from the OWLS model of active galactic nuclei match X-ray observations well (McCarthy et al. 2010) we adopt $M_\mathrm{hot} = 3\langle M_* \rangle$. Fedeli (2014) find that the simulations suggest a small core radius r_core (i.e. even smaller than the transition radius of the stars). This implies that $\rho_\mathrm{hot}(r)$ is effectively described by a single power law. Observations show a range in core radii, but typical values are tens of kpc (e.g. Mulchaey et al. 1996) for galaxy groups. We take $r_\mathrm{c} = r_\mathrm{e}$, which is relatively small in order to give an upper limit; a larger value would reduce the contribution of hot gas, and thus move the extended mass profile closer to the point mass case. We define the amplitude ρ_core of the profile such that the mass integrated over the full $\rho_\mathrm{hot}(r)$ distribution is equal to the total hot gas mass M_hot.

Satellites

As described in 5.2.1 we use our nearby ($m_\mathrm{r} < 17.3$) sample of centrals (BCGs and non-grouped galaxies) to find that most of the non-grouped galaxies in the GAMA catalogue might not be truly isolated, but are likely to have satellites beyond the visible magnitude limit. Fortunately, satellites are a spherically distributed, sub-dominant component of the lens, which means its (apparent) mass distribution can be described within EG. In order to assess the contribution of these satellites to our lensing signal, we first need to model their average baryonic mass distribution. We follow van Uitert et al. (2016) by modelling the density profile of satellites around the central as a double power law[2]:

$$\rho_\mathrm{sat}(r) = \frac{\rho_\mathrm{sat}}{(r/r_\mathrm{sat})(1 + r/r_\mathrm{sat})^2}\,, \tag{5.5}$$

where ρ_sat is the density and r_sat the scale radius of the satellite distribution. The amplitude ρ_sat is chosen such that the mass integrated over the full profile is equal to the mean total mass in satellites $\langle M_*^\mathrm{sat} \rangle$ measured around our nearby sample of centrals. By binning these centrals according to their stellar mass M_*^cen we find that, for centrals within $10^9 < M_*^\mathrm{cen} < 10^{11}\ h_{70}^{-1}\mathrm{M}_\odot$, the total mass in satellites can be approximated by a fraction

---

[2] Although this double power law is mathematically equivalent to the Navarro-Frenk-White profile (Navarro et al. 1995) which describes virialized DM halos, it is in our case not related to any (apparent) DM distribution. It is merely an empirical fit to the measured distribution of satellite galaxies around their central galaxy.

$f_{\rm sat} = \langle M_*^{\rm sat} \rangle / \langle M_*^{\rm cen} \rangle \sim 0.2 - 0.3$. However, for centrals with masses above $10^{11}\, h_{70}^{-1} {\rm M}_\odot$ the satellite mass fraction rapidly rises to $f_{\rm sat} \sim 1$ and higher. For this reason, we choose to limit our lens sample to galaxies below $10^{11}\, h_{70}^{-1} {\rm M}_\odot$. As the value of the scale radius $r_{\rm sat}$, we pick the half-mass radius (the radius which contains half of the total mass) of the satellites around the nearby centrals. The mean measured mass fraction $\langle f_{\rm sat} \rangle$ and half-mass radius $\langle r_{\rm sat} \rangle$ of satellites around centrals in our four M_*-bins can be found in Table 5.1.

5.3 Lensing measurement

According to GR, the gravitational potential of a mass distribution leaves an imprint on the path of travelling photons. As discussed in Sect. 5.1, EG gives an effective description of GR (where the excess gravity from apparent DM detailed in Verlinde 2017 is an additional component). We therefore work under the assumption that a gravitational potential (including that of the predicted apparent DM distribution) has the exact same effect on light rays as in GR. Thus, by measuring the coherent distortion of the images of faraway galaxies (sources), we can reconstruct the projected (apparent) mass distribution (lens) between the background sources and the observer. In the case of GGL, a large sample of foreground galaxies acts as the gravitational lens (for a general introduction, see e.g. Bartelmann and Schneider 2001; Schneider et al. 2006). Because the distortion of the source images is only $\sim 1\%$ of their intrinsic shape, the tangential shear γ_t (which is the source ellipticity tangential to the line connecting the source and the centre of the lens) is averaged for many sources within circular annuli around the lens centre. This measurement provides us with the average shear $\langle \gamma_{\rm t} \rangle (R)$ as a function of projected radial distance R from the lens centres. In GR, this quantity is related to the Excess Surface Density (ESD) profile $\Delta\Sigma(R)$. Using our earlier assumption, we can also use the same methodology to obtain the ESD of the apparent DM in the EG framework. The ESD is defined as the average surface mass density $\langle \Sigma \rangle (< R)$ within R, minus the surface density $\Sigma(R)$ at that radius:

$$\Delta\Sigma(R) = \langle \Sigma \rangle (< R) - \Sigma(R) = \langle \gamma_{\rm t} \rangle (R)\, \Sigma_{\rm crit}\,. \tag{5.6}$$

Here $\Sigma_{\rm crit}$ is the critical surface mass density at the redshift of the lens:

$$\Sigma_{\rm crit} = \frac{c^2}{4\pi G} \frac{D(z_{\rm s})}{D(z_{\rm l})\, D(z_{\rm l}, z_{\rm s})}\,, \tag{5.7}$$

a geometrical factor that is inversely proportional to the strength of the lensing effect. In this equation $D(z_\mathrm{l})$ and $D(z_\mathrm{s})$ are the angular diameter distances to the lens and source respectively, and $D(z_\mathrm{l}, z_\mathrm{s})$ is the distance between the lens and the source.

For a more extensive discussion of the GGL method and the role of the KiDS and GAMA surveys therein, we refer the reader to previous KiDS-GAMA lensing papers: Sifón et al. (2015); van Uitert et al. (2016); Brouwer et al. (2016) and especially Sect. 3 of Viola et al. (2015).

5.3.1 KiDS source galaxies

The background sources used in our GGL measurements are observed by KiDS (de Jong et al. 2013). The KiDS photometric survey uses the OmegaCAM instrument (Kuijken 2011) on the VLT Survey Telescope (Capaccioli and Schipani 2011) which was designed to provide a round and uniform point spread function (PSF) over a square degree field of view, specifically with weak lensing measurements in mind. Of the currently available $454\,\mathrm{deg}^2$ area from the 'KiDS-450' data release (Hildebrandt et al. 2017) we use the $\sim 180\,\mathrm{deg}^2$ area that overlaps with the equatorial GAMA fields (Driver et al. 2011). After masking bright stars and image defects, 79% of our original survey overlap remains (de Jong et al. 2015).

The photometric redshifts of the background sources are determined from $ugri$ photometry as described in Kuijken et al. (2015) and Hildebrandt et al. (2017). Due to the bias inherent in measuring the source redshift probability distribution $p(z_\mathrm{s})$ of each individual source (as was done in the previous KiDS-GAMA studies), we instead employ the source redshift number distribution $n(z_\mathrm{s})$ of the full population of sources. The individual $p(z_\mathrm{s})$ is still measured, but only to find the 'best' redshift z_B at the $p(z_\mathrm{s})$-peak of each source. Following Hildebrandt et al. (2017) we limit the source sample to: $z_\mathrm{B} < 0.9$. We also use z_B in order to select sources which lie sufficiently far behind the lens: $z_\mathrm{B} > z_\mathrm{l} + 0.2$. The $n(z_\mathrm{s})$ is estimated from a spectroscopic redshift sample, which is re-weighted to resemble the photometric properties of the appropriate KiDS galaxies for different lens redshifts (for details, see Sect. 3 of Hildebrandt et al. 2017 and van Uitert et al. 2016). We use the $n(z)$ distribution behind the lens for the calculation of the critical surface density from Eq. (5.7):

$$\Sigma_\mathrm{crit}^{-1} = \frac{4\pi G}{c^2} D(z_\mathrm{l}) \int\limits_{z_\mathrm{l}+0.2}^{\infty} \frac{D(z_\mathrm{l}, z_\mathrm{s})}{D(z_\mathrm{s})} n(z_\mathrm{l}, z_\mathrm{s})\, \mathrm{d}z_\mathrm{s}\,, \tag{5.8}$$

By assuming that the intrinsic ellipticities of the sources are randomly oriented, $\langle\gamma_{\rm t}\rangle$ from Eq. (5.6) can be approximated by the average tangential ellipticity $\langle\epsilon_{\rm t}\rangle$ given by:

$$\epsilon_{\rm t} = -\epsilon_1 \cos(2\phi) - \epsilon_2 \sin(2\phi)\,, \tag{5.9}$$

where ϵ_1 and ϵ_2 are the measured source ellipticity components, and ϕ is the angle of the source relative to the lens centre (both with respect to the equatorial coordinate system). The measurement of the source ellipticities is performed on the r-band data, which is observed under superior observing conditions compared to the other bands (de Jong et al. 2015; Kuijken et al. 2015). The images are reduced by the THELI pipeline (Erben et al. 2013 as described in Hildebrandt et al. 2017). The sources are detected from the reduced images using the SExtractor algorithm (Bertin and Arnouts 1996), whereafter the ellipticities of the source galaxies are measured using the improved self-calibrating *lens*fit code (Miller et al. 2007, 2013b; Fenech Conti et al. 2017). Each shape is assigned a weight $w_{\rm s}$ that reflects the reliability of the ellipticity measurement. We incorporate this *lens*fit weight and the lensing efficiency $\Sigma_{\rm crit}^{-1}$ into the total weight:

$$W_{\rm ls} = w_{\rm s}\Sigma_{\rm crit}^{-2}\,, \tag{5.10}$$

which is applied to each lens-source pair. This factor down-weights the contribution of sources that have less reliable shape measurements, and of lenses with a redshift closer to that of the sources (which makes them less sensitive to the lensing effect).

Inside each radial bin R, the weights and tangential ellipticities of all lens-source pairs are combined according to Eq. (5.6) to arrive at the ESD profile:

$$\Delta\Sigma(R) = \frac{1}{1+K}\frac{\sum_{ls} W_{ls}\epsilon_{\rm t}\Sigma_{{\rm crit},l}}{\sum_{ls} W_{ls}}\,. \tag{5.11}$$

In this equation, K is the average correction of the multiplicative bias m on the *lens*fit shear estimates. The values of m are determined using image simulations (Fenech Conti et al. 2017) for 8 tomographic redshift slices between $0.1 \leq z_{\rm B} < 0.9$ (Dvornik et al., in prep). The average correction is computed for the lens-source pairs in each respective redshift slice as follows:

$$K = \frac{\sum_{ls} W_{ls} m_s}{\sum_{ls} W_{ls}}\,, \tag{5.12}$$

where the mean value of K over the entire source redshift range is -0.014.

We also correct the ESD for systematic effects that arise from the residual shape correlations due to PSF anisotropy. This results in non-vanishing contributions to the ESD signal on large scales and at the survey edges, because the averaging is not done over all azimuthal angles. This spurious signal can be determined by measuring the lensing signal around random points. We use ~ 18 million locations from the GAMA random catalogue, and find that the resulting signal is small (below 10% for scales up to $\sim 1\,h_{70}^{-1}\mathrm{Mpc}$). We subtract the lensing signal around random locations from all measured ESD profiles.

Following previous KiDS-GAMA lensing papers, we measure the ESD profile for 10 logarithmically spaced radial bins within $0.02 < R < 2\,h_{100}^{-1}\mathrm{Mpc}$, where our estimates of the signal and uncertainty are thoroughly tested[3]. However, since we work with the $h \equiv h_{70}$ definition, we use the approximately equivalent $0.03 < R < 3\,h_{70}^{-1}\mathrm{Mpc}$ as our radial distance range. The errors on the ESD values are given by the diagonal of the analytical covariance matrix. Section 3.4 of Viola et al. (2015) includes the computation of the analytical covariance matrix and shows that, up to a projected radius of $R = 2\,h_{100}^{-1}\mathrm{Mpc}$, the square root of the diagonal is in agreement with the error estimate from bootstrapping.

5.4 Lensing signal prediction

According to Verlinde (2017), the gravitational potential $\Phi(r)$ caused by the enclosed baryonic mass distribution $M_{\mathrm{b}}(r)$ exceeds that of GR on galactic and larger scales. In addition to the normal GR contribution of $M_{\mathrm{b}}(r)$ to $\Phi(r)$, there exists an extra gravitational effect. This excess gravity arises due to a volume law contribution to the entropy that is associated with the positive dark energy in our universe. In a universe without matter the total entropy of the dark energy would be maximal, as it would be non-locally distributed over all available space. In our universe, on the other hand, any baryonic mass distribution $M_{\mathrm{b}}(r)$ reduces the entropy content of the universe. This removal of entropy due to matter produces an elastic response of the underlying microscopic system, which can be observed on galactic and larger scales as an additional gravitational force. Although this excess gravity does not originate from an actual DM contribution, it can be effectively described by an *apparent* DM distribution $M_{\mathrm{D}}(r)$.

---

[3] Viola et al. (2015) used the following definition of the reduced Hubble constant: $h \equiv h_{100} = H_0/(100\,\mathrm{km\,s^{-1}Mpc^{-1}})$

5.4.1 The apparent dark matter formula

Verlinde (2017) determines the amount of apparent DM by estimating the elastic energy associated with the entropy displacement caused by $M_{\mathrm{b}}(r)$. This leads to the following relation[4]:

$$\int_0^r \varepsilon_{\mathrm{D}}^2(r')A(r')dr' = V_{M_{\mathrm{b}}}(r)\,, \tag{5.13}$$

where we integrate over a sphere with radius r and area $A(r) = 4\pi r^2$. The strain $\varepsilon_{\mathrm{D}}(r)$ caused by the entropy displacement is given by:

$$\varepsilon_{\mathrm{D}}(r) = \frac{8\pi G}{cH_0}\frac{M_{\mathrm{D}}(r)}{A(r)}\,, \tag{5.14}$$

where c is the speed of light, G the gravitational constant, and H_0 the present-day Hubble constant (which we choose to be $H_0 = 70\,\mathrm{km\,s^{-1}Mpc^{-1}}$). Furthermore, $V_{M_{\mathrm{b}}}(r)$ is the volume that would contain the amount of entropy that is removed by a mass M_{b} inside a sphere of radius r, if that volume were filled with the average entropy density of the universe:

$$V_{M_{\mathrm{b}}}(r) = \frac{8\pi G}{cH_0}\frac{M_{\mathrm{b}}(r)\,r}{3}\,. \tag{5.15}$$

Now inserting the relations (5.14) and (5.15) into (5.13) yields:

$$\int_0^r \frac{GM_{\mathrm{D}}^2(r')}{r'^2}dr' = M_{\mathrm{b}}(r)r\frac{cH_0}{6}\,. \tag{5.16}$$

Finally, by taking the derivative with respect to r on both sides of the equation, one arrives at the following relation:

$$M_{\mathrm{D}}^2(r) = \frac{cH_0r^2}{6G}\frac{d\left(M_{\mathrm{b}}(r)r\right)}{dr}\,. \tag{5.17}$$

This is the apparent DM formula from Verlinde (2017), which translates a baryonic mass distribution into an apparent DM distribution. This apparent DM only plays a role in the regime where the elastic response of the entropy of dark energy S_{DE} takes place: where $V(r) > V_{M_{\mathrm{b}}}(r)$, i.e. $S_{\mathrm{DE}} \propto V(r)$ is large compared to the entropy that is removed by $M_{\mathrm{b}}(r)$

---

[4] Although Verlinde (2017) derives his relations for an arbitrary number of dimensions d, for the derivation in this paper we restrict ourselves to four spacetime dimensions.

within our radius r. By substituting Eq. (5.15) into this condition, we find that this is the case when:

$$r > \sqrt{\frac{2G}{cH_0} M_\mathrm{b}(r)} \,. \tag{5.18}$$

For a lower limit on this radius for our sample, we can consider a point source with a mass of $M = 10^{10}\, h_{70}^{-1} \mathrm{M}_\odot$, close to the average mass $\langle M_\mathrm{g} \rangle$ of galaxies in our lowest stellar mass bin. In this simple case, the regime starts when $r > 2\, h_{70}^{-1}\mathrm{kpc}$. This shows that our observations (which start at $30\, h_{70}^{-1}\mathrm{kpc}$) are well within the EG regime.

However, it is important to keep in mind that this equation does not represent a new fundamental law of gravity, but is merely a macroscopic approximation used to describe an underlying microscopic phenomenon. Therefore, this equation is only valid under the specific set of circumstances that have been assumed for its derivation. In this case, the system considered was a static, spherically symmetric and isolated baryonic mass distribution. With these limitations in mind, we have selected our galaxy sample to meet these criteria as closely as possible (see Sect. 5.2.1).

Finally we note that, in order to test the EG predictions with gravitational lensing, we need to make some assumptions about the used cosmology (as discussed in Sect. 5.1). These concern the geometric factors in the lensing equation (Eq. 5.7), and the evolution of the Hubble constant (which enters in Eq. (5.17) for the apparent DM). We assume that, if EG is to be a viable theory, it should predict an expansion history that agrees with the current supernova data (Riess et al. 1996; Kessler et al. 2009; Betoule et al. 2014), specifically over the redshift range that is relevant for our lensing measurements ($0.2 < z_\mathrm{s} < 0.9$). If this is the case, the angular diameter distance-redshift relation is similar to what is used in ΛCDM. We therefore adopt a ΛCDM background cosmology with $\Omega_\mathrm{m} = 0.315$ and $\Omega_\Lambda = 0.685$, based on the Planck XIII (2016) measurements. Regarding H_0 in Eq. (5.17), we note that a Hubble parameter that changes with redshift is not yet implemented in the EG theory. However, for the lens redshifts considered in this work ($\langle z_\mathrm{l} \rangle \sim 0.2$) the difference resulting from using H_0 or $H(z_\mathrm{l})$ to compute the lensing signal prediction is $\sim 5\%$. This means that, considering the statistical uncertainties in our measurements ($\gtrsim 40\%$, see e.g. Fig. 5.2), our choice to use $H_0 = 70\,\mathrm{km\,s^{-1}Mpc^{-1}}$ instead of an evolving $H(z_\mathrm{l})$ has no significant effect on the results of this work.

From Eq. (5.17) we now need to determine the ESD profile of the apparent DM distribution, in order to compare the predictions from EG to our measured GGL profiles. The next steps toward this $\Delta\Sigma_{\rm EG}(R)$ depend on our assumptions regarding the baryonic mass distribution of our lenses. We compute the lensing signal in EG for two models (which are discussed in Sect. 5.2.2): the point mass approximation and the more realistic extended mass distribution.

5.4.2 Point mass approximation

In this work we measure the ESD profiles of galaxies at projected radial distances $R > 30\,h_{70}^{-1}{\rm kpc}$. If we assume that, beyond this distance, the galaxy is almost entirely enclosed within the radius r, we can approximate the enclosed baryonic mass as a constant: $M_{\rm b}(r) = M_{\rm b}$. Re-writing Eq. (5.17) accordingly yields:

$$M_{\rm D}(r) = \sqrt{\frac{cH_0}{6\,G}}\, r\sqrt{M_{\rm b}} \equiv C_{\rm D}\, r\sqrt{M_{\rm b}}\,, \tag{5.19}$$

where $C_{\rm D}$ is a constant factor determined by c, G and H_0. In order to calculate the resulting $\Delta\Sigma_{\rm D}(R)$ we first need to determine the spherical density distribution $\rho_{\rm D}(r)$. Under the assumption of spherical symmetry, we can use:

$$\rho_{\rm D}(r) = \frac{1}{4\pi r^2}\frac{dM_{\rm D}(r)}{dr} = \frac{C_{\rm D}\sqrt{M_{\rm b}}}{4\pi r^2}\,. \tag{5.20}$$

We calculate the corresponding surface density $\Sigma_{\rm D}(R)$ as a function of projected distance R in the cylindrical coordinate system (R, ϕ, z), where z is the distance along the line-of-sight and $r^2 = R^2 + z^2$, such that:

$$\Sigma_{\rm D}(R) = \int\limits_{-\infty}^{\infty} \rho_{\rm D}(R,z)\,{\rm d}z\,. \tag{5.21}$$

Substituting $\rho_{\rm D}(R,z)$ provides the surface density of the apparent DM distribution associated with our point mass:

$$\Sigma_{\rm D}(R) = \frac{C_{\rm D}\sqrt{M_{\rm b}}}{4\pi}\,2\int\limits_{0}^{\infty}\frac{{\rm d}z}{R^2+z^2} = \frac{C_{\rm D}\sqrt{M_{\rm b}}}{4R}\,. \tag{5.22}$$

We can now use Eq. (5.6) to find the ESD:

$$\Delta\Sigma(R) = \langle\Sigma\rangle(<R) - \Sigma(R) = \frac{2\pi\int_0^R \Sigma(R')R'\,{\rm d}R'}{\pi R^2} - \Sigma(R)\,. \tag{5.23}$$

In the case of our point mass:

$$\Delta\Sigma_{\rm D}(R) = \frac{C_{\rm D}\sqrt{M_{\rm b}}}{2R} - \frac{C_{\rm D}\sqrt{M_{\rm b}}}{4R} = \frac{C_{\rm D}\sqrt{M_{\rm b}}}{4R}\,, \tag{5.24}$$

which happens to be equal to $\Sigma_{\rm D}(R)$ from Eq. (5.22)[5].

Apart from the extra contribution from the apparent DM predicted by EG, we also need to add the standard GR contribution from baryonic matter to the ESD. Under the assumption that the galaxy is a point mass we know that $\Sigma_{\rm b}(R) = 0$ for $R > 0$, and that the integral over $\Sigma_{\rm b}(R)$ must give the total mass $M_{\rm b}$ of the galaxy. Substituting this into Eq. (5.23) gives us:

$$\Delta\Sigma_{\rm b}(R) = \frac{M_{\rm b}}{\pi R^2}\,. \tag{5.25}$$

Ultimately, the total ESD predicted by EG in the point mass approximation is:

$$\Delta\Sigma_{\rm EG}(R) = \Delta\Sigma_{\rm b}(R) + \Delta\Sigma_{\rm D}(R)\,, \tag{5.26}$$

where the contributions are the ESDs of a point source with mass $M_{\rm g}$ of our galaxies, both in GR and EG.

5.4.3 Extended mass distribution

The above derivation only holds under the assumption that our galaxies can be considered point masses. To test whether this is justified, we wish to compare the point mass prediction to a more realistic lens model. This model includes the extended density profile for stars, cold gas, hot gas and satellites as described in Sect. 5.2.2. To determine the ESD profile of the extended galaxy model as predicted by EG, we cannot perform an analytical calculation as we did for the point mass approximation. Instead we need to calculate the apparent DM distribution $M_{\rm D}^{\rm ext}(r)$ and the resulting $\Delta\Sigma_{\rm D}^{\rm ext}(R)$ numerically for the sum of all baryonic components. We start out with the total spherical density distribution $\rho_{\rm b}^{\rm ext}(r)$ of all components:

$$\rho_{\rm b}^{\rm ext}(r) = \rho_{\rm b}^{\rm S}(r) + \rho_{\rm b}^{\rm hot}(r) + \rho_{\rm b}^{\rm sat}(r)\,, \tag{5.27}$$

where the respective contributions are: the Sérsic model for stars and cold gas, the β-profile for hot gas, and the double power law for satellites. We

---

[5] Note that the ESD of the apparent DM distribution: $\Delta\Sigma_{\rm D}(R) \propto \sqrt{H_0 M_{\rm b}}/R \propto \sqrt{h}$, is explicitly dependent on the Hubble constant, which means that an incorrect measured value of H_0 would affect our conclusions.

numerically convert this to the enclosed mass distribution:

$$M_{\rm b}^{\rm ext}(r) = 4\pi \int\limits_0^r \rho_{\rm b}^{\rm ext}(r')r'^2 \, {\rm d}r' \, . \tag{5.28}$$

We rewrite Eq. (5.17) in order to translate $M_{\rm b}^{\rm ext}(r)$ to its corresponding distribution of apparent DM in EG:

$$M_{\rm D}^{\rm ext}(r) = C_{\rm D} r \sqrt{\frac{dM_{\rm b}^{\rm ext}(r)\, r}{dr}} \, , \tag{5.29}$$

which is numerically converted into the apparent DM density distribution $\rho_{\rm D}^{\rm ext}(r)$ by substituting $M_{\rm D}^{\rm ext}(r)$ into Eq. (5.20).

The projected surface density $\Sigma_{\rm D}^{\rm ext}(R)$ from Eq. (5.21) is calculated by computing the value of $\rho_{\rm D}^{\rm ext}(R,z)$ in cylindrical coordinates for 10^3 values of z and integrating over them. The last step towards computing the ESD profile is the subtraction of $\Sigma_{\rm D}^{\rm ext}(R)$ from the average surface density within R, as in Eq. (5.23), where $\langle\Sigma_{\rm D}^{\rm ext}\rangle(<R)$ is calculated by performing the cumulative sum over $2\pi R\, \Sigma_{\rm D}^{\rm ext}(R)$ and dividing the result by its cumulative area. In addition to the lensing signal from apparent DM, we need to include the baryonic ESD profile. We numerically compute $\Delta\Sigma_{\rm b}^{\rm ext}(R)$ from $\rho_{\rm b}^{\rm ext}(r)$ in the same way as we computed $\Delta\Sigma_{\rm D}^{\rm ext}(R)$ from $\rho_{\rm D}^{\rm ext}(r)$. This makes the total ESD predicted by EG for the extended mass distribution:

$$\Delta\Sigma_{\rm EG}^{\rm ext}(R) = \Delta\Sigma_{\rm b}^{\rm ext}(R) + \Delta\Sigma_{\rm D}^{\rm ext}(R) \, . \tag{5.30}$$

When considering the resulting ESD profiles of the extended density models, we must keep in mind that they only represent reasonable estimates which contain uncertainties for two different reasons:

1. The extended baryonic density distribution of each component is approximated using reasonable assumptions on the used model profiles and their corresponding input parameters. These assumptions are based on observations of the galaxies in our sample and of other galaxies, and also on simulations. Although we try to find suitable input parameters corresponding to the measured stellar mass of our galaxy samples, we cannot be certain that our modelled density distributions are completely correct.

2. We cannot model the extended density distribution for each individual GAMA galaxy, but have to assume one average profile per lens

> sample (based on the average stellar mass $\langle M_* \rangle$ of that sample). Translating the extended baryonic mass model to the lensing profile of its corresponding apparent DM distribution (as explained above) is a highly non-linear operation. Therefore, we cannot be certain that the calculated lensing profile of an average density distribution is exactly the same as the lensing profile of all individual galaxies combined, although these would only differ greatly in the unlikely case that there is a large spread in the input parameters of the extended mass profiles within each stellar mass sub-sample.

For these two reasons we cannot use the average profile as a reliable model for the apparent DM lensing signal of our galaxy samples. In the point mass approximation, we do have the measured input parameter (the stellar mass) for each individual galaxy, and we can compute the apparent DM lensing profile for each individual galaxy. However, this approach can only be used when the contribution from hot gas and satellites is small. We therefore compare our estimate of the apparent DM lensing profile of the extended mass distribution to that of the point masses, to assess the error margins in our EG prediction.

The total ESD profile predicted for the extended density distribution, and that of each component[6], is shown in Fig. 5.2. We only show the profiles for the galaxies in our highest stellar mass bin: $10^{10.9} < M_* < 10^{11}\, h_{70}^{-1}\mathrm{M}_\odot$, but since the relations between the mass in hot gas, satellites and their galaxies are approximately linear, the profiles look similar for the other sub-samples. At larger scales, we find that the point mass approximation predicts a lower ESD than the extended mass profile. However, the difference between the $\Delta\Sigma(R)$ predictions of these two models is comparable to the median 1σ uncertainty on the ESD of our sample (which is illustrated by the gray band in Fig. 5.2). We conclude that, given the current statistical uncertainties in the lensing measurements, the point mass approximation is adequate for isolated centrals within the used radial distance range $(0.03 < R < 3\, h_{70}^{-1}\mathrm{Mpc})$.

5.5 Results

We measure the ESD profiles (following Sect. 5.3) of our sample of isolated centrals, divided into four sub-samples of increasing stellar mass. The

---

[6] Note that, due to the non-linear nature of the calculation of the apparent DM distribution, the total ESD profile of the extended mass distribution is not the sum of the components shown in Fig. 5.2.

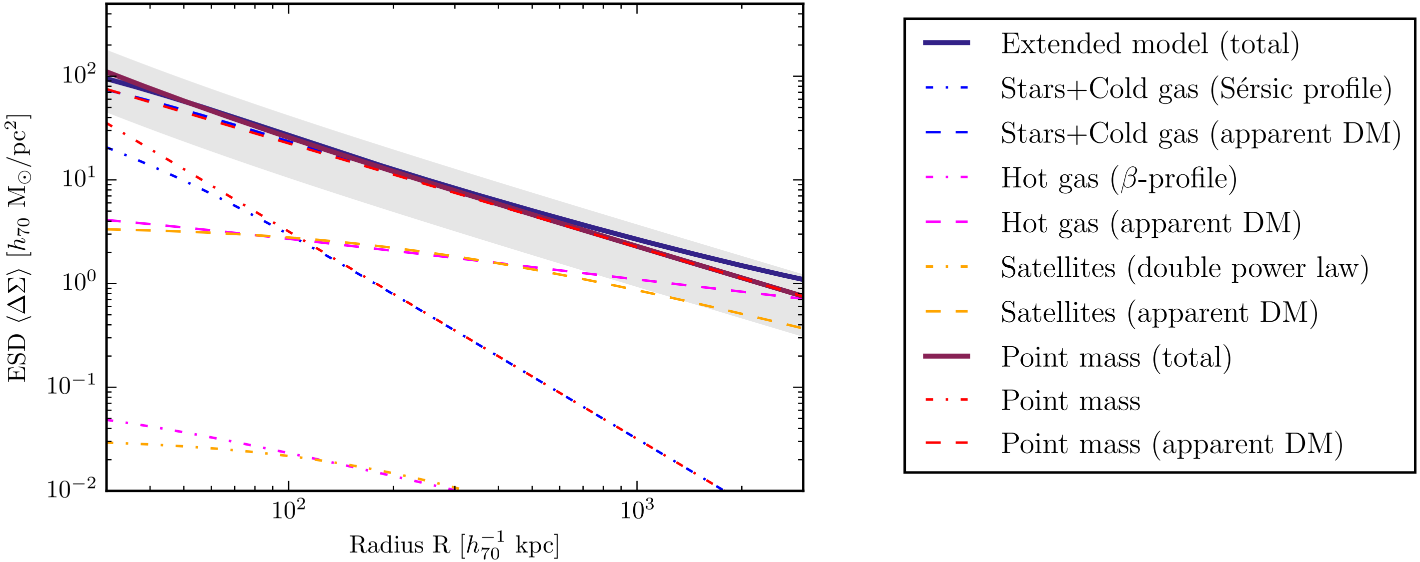

Figure 5.2: The ESD profile predicted by EG for isolated centrals, both in the case of the point mass approximation (dark red, solid) and the extended galaxy model (dark blue, solid). The former consists of a point source with the mass of the stars and cold gas component (red), with the lensing signal evaluated for both the baryonic mass (dash-dotted) and the apparent DM (dashed). The latter consists of a stars and cold gas component modelled by a Sérsic profile (blue), a hot gas component modelled by a β-profile (magenta), and a satellite distribution modelled by a double power law (orange), all with the lensing signal evaluated for both the baryonic mass (dash-dotted) and the apparent DM (dashed). Note that the total ESD of the extended mass distribution is not equal to the sum of its components, due to the non-linear conversion from baryonic mass to apparent DM. All profiles are shown for our highest mass bin ($10^{10.9} < M_* < 10^{11}\ h_{70}^{-1}\mathrm{M}_\odot$), but the difference between the two models is similar for the other galaxy sub-samples. The difference between the ESD predictions of the two models is comparable to the median 1σ uncertainty on our lensing measurements (illustrated by the grey band).

Table 5.2: For each stellar mass bin, this table shows the median values (including 16th and 84th percentile error margins) of the halo mass M_h obtained by the NFW fit, and the 'best' amplitude A_B that minimizes the χ^2 if the EG profile were multiplied by it (for the point mass and extended mass profile). The halo masses are displayed in units of $\log_{10}(M/\,h_{70}^{-1}\mathrm{M}_\odot)$.

$M*$-bin	M_h	A_B	$A_\mathrm{B}^\mathrm{ext}$
$8.5 - 10.5$	$12.15^{+0.10}_{-0.11}$	$1.36^{+0.21}_{-0.21}$	$1.21^{+0.19}_{-0.19}$
$10.5 - 10.8$	$12.45^{+0.10}_{-0.11}$	$1.32^{+0.19}_{-0.19}$	$1.20^{+0.18}_{-0.18}$
$10.8 - 10.9$	$12.43^{+0.17}_{-0.22}$	$1.07^{+0.27}_{-0.27}$	$0.94^{+0.25}_{-0.25}$
$10.9 - 11$	$12.62^{+0.13}_{-0.16}$	$1.33^{+0.25}_{-0.26}$	$1.20^{+0.23}_{-0.24}$

boundaries of the M_*-bins: $\log(M_*/\,h_{70}^{-1}\mathrm{M}_\odot) = [8.5,\ 10.5,\ 10.8,\ 10.9,\ 11.0]$, are chosen to maintain an approximately equal signal-to-noise in each bin. Figure 5.3 shows the measured ESD profiles (with 1σ error bars) of galaxies in the four M_*-bins. Together with these measurements we show the ESD profile predicted by EG, under the assumption that our isolated centrals can be considered point masses at scales within $0.03 < R < 3\,h_{70}^{-1}\mathrm{Mpc}$. The masses M_g of the galaxies in each bin serve as input in Eq. (5.26), which provides the ESD profiles predicted by EG for each individual galaxy. The mean baryonic masses of the galaxies in each M_*-bin can be found in Table 5.1. The ESDs of the galaxies in each sample are averaged to obtain the total $\Delta\Sigma_\mathrm{EG}(R)$. It is important to note that the shown EG profiles do *not contain any free parameters*: both their slope and amplitudes are fixed by the prediction from the EG theory (as stated in Eq. 5.17) and the measured masses M_g of the galaxies in each M_*-bin. Although this is only a first attempt at testing the EG theory using lensing data, we can perform a very simple comparison of this prediction with both the lensing observations and the prediction from the standard ΛCDM model.

5.5.1 Model comparison

In standard GGL studies performed within the ΛCDM framework, the measured ESD profile is modelled by two components: the baryonic mass of the galaxy and its surrounding DM halo. The baryonic component is often modelled as a point source with the mean baryonic mass of the galaxy sample, whereas the DM halo component usually contains several free parameters, such as the mass and concentration of the halo, which are evaluated by fitting a model to the observed ESD profiles. Motivated by N-body simulations, the DM halo is most frequently modelled by the Navarro-Frenk-White density profile (NFW, Navarro et al. 1995), very similar to the double

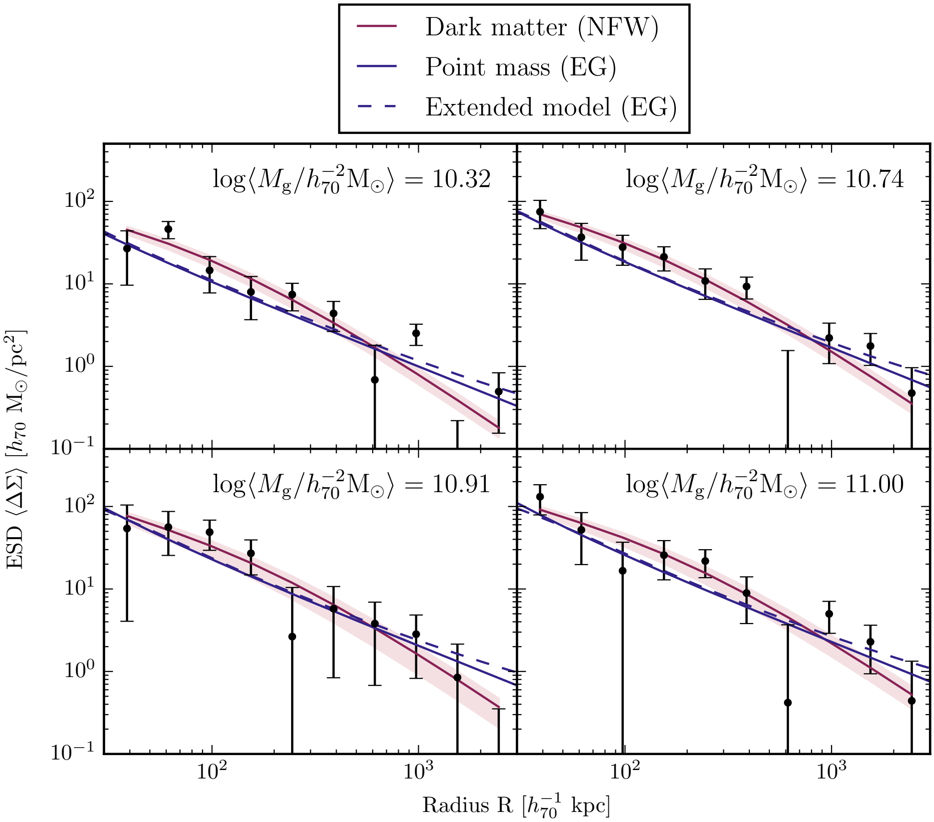

Figure 5.3: The measured ESD profiles of isolated centrals with 1σ error bars (black), compared to those predicted by EG in the point mass approximation (blue) and for the extended mass profile (blue, dashed). Note that *none of these predictions are fitted to the data*: they follow directly from the EG theory by substitution of the baryonic masses M_g of the galaxies in each sample (and, in the case of the extended mass profile, reasonable assumptions for the other baryonic mass distributions). The mean measured galaxy mass is indicated at the top of each panel. For comparison we show the ESD profile of a simple NFW profile as predicted by GR (red), with the DM halo mass M_h fitted as a free parameter in each stellar mass bin.

power law in Eq. (5.5). This profile has two free parameters: the halo mass M_h, which gives the amplitude, and the scale radius r_s, which determines where the slope changes. Following previous GAMA-KiDS lensing papers (see e.g. Sifón et al. 2015; Viola et al. 2015; van Uitert et al. 2016; Brouwer et al. 2016) we define M_h as M_{200}: the virial mass contained within r_{200}, and we define the scale radius in terms of the concentration: $c \equiv r_{200}/r_\mathrm{s}$. In these definitions, r_{200} is the radius that encloses a density of 200 times $\rho_\mathrm{m}(z)$, the average matter density of the universe. Using the Duffy et al. (2008) mass-concentration relation, we can define c in terms of M_h. We translate the resulting density profile, which depends exclusively on the DM halo mass, into the projected ESD distribution following the analytical description of Wright and Brainerd (2000). We combine this NFW model with a point mass that models the baryonic galaxy component (as in Eq. 5.25). Because our lens selection minimizes the contribution from neighbouring centrals (see Sect. 5.2.1), we do not need to add a component that fits the 2-halo term. We fit the NFW model to our measured ESD profiles using the EMCEE sampler (Foreman-Mackey et al. 2013) with 100 walkers performing 1000 steps. The model returns the median posterior values of M_h (including 16th and 84th percentile error margins) displayed in Table 5.2. The best-fit ESD profile of the NFW model (including 16th and 84th percentile bands) is shown in Fig. 5.3.

For both the $\Delta\Sigma_\mathrm{EG}$ predicted by EG (in the point mass approximation) and the simple NFW fit $\Delta\Sigma_\mathrm{NFW}$, we can compare the $\Delta\Sigma_\mathrm{mod}$ of the model with the observed $\Delta\Sigma_\mathrm{obs}$ by calculating the χ^2 value:

$$\chi^2 = (\Delta\Sigma_\mathrm{obs} - \Delta\Sigma_\mathrm{mod})^\top \cdot C^{-1}(\Delta\Sigma_\mathrm{obs} - \Delta\Sigma_\mathrm{mod})\,, \tag{5.31}$$

where C^{-1} is the inverse of the analytical covariance matrix (see Sect. 5.3). From this quantity we can calculate the reduced χ^2 statistic[7]: $\chi^2_\mathrm{red} = \chi^2/N_\mathrm{DOF}$. It depends on the number of degrees of freedom (DOF) of the model: $N_\mathrm{DOF} = N_\mathrm{data} - N_\mathrm{param}$, where N_data is the number of data-points in the measurement and N_param is the number of free parameters. Due to our choice of 10 R-bins and 4 M_*-bins, we use $4 \times 10 = 40$ data-points. In the case of EG there are no free parameters, which means $N^\mathrm{EG}_\mathrm{DOF} = 40$. Our simple NFW model has one free parameter M_h for each M_*-bin, resulting in $N^\mathrm{NFW}_\mathrm{DOF} = 40 - 4 = 36$. The resulting total χ^2_red over the four M_*-bins is $44.82/40 = 1.121$ for EG, and $33.58/36 = 0.933$ for the NFW fit. In other

---

[7] While the reduced χ^2 statistic is shown to be a suboptimal goodness-of-fit estimator (see e.g. Andrae et al. 2010) it is a widely used criterion, and we therefore discuss it here for completeness.

words, both the NFW and EG prediction agree quite well with the measured ESD profile, where the NFW fit has a slightly better $\chi^2_{\rm red}$ value. Since the NFW profile is an empirical description of the surface density of virialized systems, the apparent correspondence of both the NFW fit and the EG prediction with the observed ESD essentially reflects that the predicted EG profile roughly follows that of virialized systems.

A more appropriate way to compare the two models, however, is in the Bayesian framework. We use a very simple Bayesian approach by computing the Bayesian Information Criterion (BIC, Schwarz 1978). This criterion, which is based on the maximum likelihood $\mathcal{L}_{\rm max}$ of the data given a model, penalizes model complexity more strongly than the $\chi^2_{\rm red}$. This model comparison method is closely related to other information criteria such as the Akaike Information Criterion (AIK, Akaike 1973) which have become popular because they only require the likelihood at its maximum value, rather than in the whole parameter space, to perform a model comparison (see e.g. Liddle 2007). This approximation only holds when the posterior distribution is Gaussian and the data points are independent. Calculating the BIC, which is defined as:

$$BIC = -2\ln(\mathcal{L}_{\rm max}) + N_{\rm param}\ln(N_{\rm data})\,, \tag{5.32}$$

allows us to consider the relative evidence of two competing models, where the one with the lowest BIC is preferred. The difference ΔBIC gives the significance of evidence against the higher BIC, ranging from "0 - 2: Not worth more than a bare mention" to ">10: Very strong" (Kass and Raftery 1995). In the Gaussian case, the likelihood can be rewritten as: $-2\ln(\mathcal{L}_{\rm max}) = \chi^2$. Using this method, we find that $BIC_{\rm EG} = 44.82$ and $BIC_{\rm NFW} = 48.33$. This shows that, when the number of free parameters is taken into account, the EG model performs at least as well as the NFW fit. However, in order to really distinguish between these two models, we need to reduce the uncertainties in our measurement, in our lens modelling, and in the assumptions related to EG theory and halo model.

In order to further assess the quality of the EG prediction across the M_*-range, we determine the 'best' amplitude $A_{\rm B}$ and index $n_{\rm B}$: the factors that minimize the χ^2 statistic when we fit:

$$\Delta\Sigma_{\rm EG}(A_{\rm B}, n_{\rm B}, R) = A_{\rm B}\frac{C_{\rm D}\sqrt{M_{\rm b}}}{4}\left(\frac{R}{h_{70}^{-1}{\rm kpc}}\right)^{-n_{\rm B}}\,. \tag{5.33}$$

We find that the slope of the EG prediction is very close to the observed slope of the ESD profiles, with a mean value of $\langle n_{\rm B}\rangle = 1.01^{+0.02}_{-0.03}$. In order to obtain better constraints on $A_{\rm B}$, we set $n_{\rm B} = 1$. The values of $A_{\rm B}$ (with 1σ errors) for the point mass are shown in Table 5.2. We find the amplitude of the point mass prediction to be consistently lower than the measurement. This is expected since the point mass approximation only takes the mass contribution of the central galaxy into account, and not that of extended components like hot gas and satellites (described in Sect. 5.2.2). However, the ESD of the extended profile (which is shown in Fig. 5.3 for comparison) does not completely solve this problem. When we determine the best amplitude for the extended mass distribution by scaling its predicted ESD, we find that the values of $A_{\rm B}^{\rm ext}$ are still larger than 1, but less so than for the point mass (at a level of $\sim 1\sigma$, see Table 5.2). Nevertheless, the comparison of the extended ESD with the measured lensing profile yields a slightly higher reduced χ^2: $45.50/40 = 1.138$. However, accurately predicting the baryonic and apparent DM contribution of the extended density distribution is challenging (see Sect. 5.4.3). Therefore, the extended ESD profile can primarily be used as an indication of the uncertainty in the lens model.

5.6 Conclusion

Using the $\sim 180\,\rm deg^2$ overlap of the KiDS and GAMA surveys, we present the first test of the theory of emergent gravity proposed in Verlinde (2017) using weak gravitational lensing. In this theory, there exists an additional component to the gravitational potential of a baryonic mass, which can be described as an *apparent* DM distribution. Because the prediction of the apparent DM profile as a function of baryonic mass is currently only valid for static, spherically symmetric and isolated mass distributions, we select $33,613$ central galaxies that dominate their surrounding mass distribution, and have no other centrals within the maximum radius of our measurement ($R_{\rm max} = 3\,h_{70}^{-1}{\rm Mpc}$). We model the baryonic matter distribution of our galaxies using two different assumptions for their mass distribution: the point mass approximation and the extended mass profile. In the point mass approximation we assume that the bulk of the galaxy's mass resides within the minimum radius of our measurement ($R_{\rm min} = 30\,h_{70}^{-1}{\rm kpc}$), and model the lens as a point source with the mass of the stars and cold gas of the galaxy. For the extended distribution, we not only model the stars and cold gas component as a Sérsic profile, but also try to make reasonable estimates of the extended hot gas and satellite distributions. We compute the lensing profiles of both models and find that, given the current statistical uncertainties in our lensing measurements, both models give an adequate description of isolated centrals. In this regime (where the mass distribution can be approximated by a point mass) the lensing profile of apparent DM in EG is the same as that of the excess gravity in MOND[8], for the specific value $a_0 = cH_0/6$.

When computing the observed and predicted ESD profiles, we need to make several assumptions concerning the EG theory. The first is that, because EG gives an effective description of GR in empty space, the effect of the gravitational potential on light rays remains unchanged. This allows us to use the regular gravitational lensing formalism to measure the ESD profiles of apparent DM in EG. Our second assumption involves the used background cosmology. Because EG is only developed for present-day de Sitter space, we need to assume that the evolution of cosmological distances is approximately equal to that in ΛCDM, with the cosmological parameters as measured by Planck XIII (2016). For the relatively low redshifts used in this work ($0.2 < z_\mathrm{s} < 0.9$), this is a reasonable assumption. The third assumption is the value of H_0 that we use to calculate the apparent DM profile from the baryonic mass distribution. In an evolving universe, the Hubble parameter $H(z)$ is expected to change as a function of the redshift z. This evolution is not yet implemented in EG. Instead it uses the approximation that we live in a dark energy dominated universe, where $H(z)$ resembles a constant. We follow Verlinde (2017) by assuming a constant value, in our case: $H_0 = 70\,\mathrm{km\,s^{-1}Mpc^{-1}}$, which is reasonable at a mean lens redshift of $\langle z_\mathrm{l} \rangle \sim 0.2$. However, in order to obtain a more accurate prediction for the cosmology and the lensing signal in the EG framework, all these issues need to be resolved in the future.

Using the mentioned assumptions, we measure the ESD profiles of isolated centrals in four different stellar mass bins, and compare these with the ESD profiles predicted by EG. They exhibit a remarkable agreement, especially considering that the predictions contain *no free parameters*: both the slope and the amplitudes within the four M_*-bins are completely fixed by the EG theory and the measured baryonic masses M_g of the galaxies. In order to perform a very simple comparison with ΛCDM, we fit the ESD profile of a simple NFW distribution (combined with a baryonic point mass) to the measured lensing profiles. This NFW model contains one free parameter, the halo mass M_h, for each stellar mass bin. We compare the reduced

---

[8] After this paper was accepted for publication, it was pointed out to us that Milgrom (2013) showed that galaxy-galaxy lensing measurements from the Canada-France-Hawaii Telescope Legacy Survey (performed by Brimioulle et al. 2013) are consistent with predictions from relativistic extensions of MOND up to a radius of $140\,h_{72}^{-1}\mathrm{kpc}$ (note added in proof).

χ^2 of the NFW fit (which has 4 free parameters in total) with that of the prediction from EG (which has no free parameters). Although the NFW fit has fewer degrees of freedom (which slightly penalizes $\chi^2_{\rm red}$) the reduced χ^2 of this model is slightly lower than that of EG, where $\chi^2_{\rm red,NFW} = 0.933$ and $\chi^2_{\rm red,EG} = 1.121$ in the point mass approximation. For both theories, the value of the reduced χ^2 is well within reasonable limits, especially considering the very simple implementation of both models. The fact that our observed density profiles resemble both NFW profiles and the prediction from EG, suggests that this theory predicts a phenomenology very similar to a virialized DM halo. Using the Bayesian Information Criterion, we find that $BIC_{\rm EG} = 44.82$ and $BIC_{\rm NFW} = 48.33$. These BIC values imply that, taking the number of data points and free parameters into account, the EG prediction describes our data at least as well as the NFW fit. However, a thorough and fair comparison between ΛCDM and EG would require a more sophisticated implementation of both theories, and a full Bayesian analysis which properly takes the free parameters and priors of the NFW model into account. Nonetheless, given that the model uncertainties are also addressed, future data should be able to distinguish between the two theories.

We propose that this analysis should not only be carried out for this specific case, but on multiple scales and using a variety of different probes. From comparing the predictions of EG to observations of isolated centrals, we need to expand our studies to the scales of larger galaxy groups, clusters, and eventually to cosmological scales: the cosmic web, BAO's and the CMB power spectrum. Furthermore, there are various challenges for EG, especially concerning observations of dynamical systems such as the Bullet Cluster (Randall et al. 2008) where the dominant mass component appears to be separate from the dominant baryonic component. There is also ongoing research to assess whether there exists an increasing mass-to-light ratio for galaxies of later type (Martinsson et al. 2013), which might challenge EG if confirmed. We conclude that, although this first result is quite remarkable, it is only a first step. There is still a long way to go, for both the theoretical groundwork and observational tests, before EG can be considered a fully developed and solidly tested theory. In this first GGL study, however, EG appears to be a good parameter-free description of our observations.

Acknowledgements

M. Brouwer and M. Visser would like to thank Erik Verlinde for helpful clarifications and discussions regarding his emergent gravity theory. We also thank the anonymous referee for the useful comments, that helped to improve this paper.

The work of M. Visser was supported by the ERC Advanced Grant 268088-EMERGRAV, and is part of the Delta ITP consortium, a program of the NWO. M. Bilicki, H. Hoekstra and C. Sifón acknowledge support from the European Research Council under FP7 grant number 279396. K. Kuijken is supported by the Alexander von Humboldt Foundation. M. Bilicki acknowledges support from the Netherlands Organisation for Scientific Research (NWO) through grant number 614.001.103. H. Hildebrandt is supported by an Emmy Noether grant (No. Hi 1495/2-1) of the Deutsche Forschungsgemeinschaft. R. Nakajima acknowledges support from the German Federal Ministry for Economic Affairs and Energy (BMWi) provided via DLR under project no. 50QE1103. Dominik Klaes is supported by the Deutsche Forschungsgemeinschaft in the framework of the TR33 'The Dark Universe'.

This research is based on data products from observations made with ESO Telescopes at the La Silla Paranal Observatory under programme IDs 177.A-3016, 177.A-3017 and 177.A-3018, and on data products produced by Target OmegaCEN, INAF-OACN, INAF-OAPD and the KiDS production team, on behalf of the KiDS consortium. OmegaCEN and the KiDS production team acknowledge support by NOVA and NWO-M grants. Members of INAF-OAPD and INAF-OACN also acknowledge the support from the Department of Physics & Astronomy of the University of Padova, and of the Department of Physics of Univ. Federico II (Naples).

GAMA is a joint European-Australasian project based around a spectroscopic campaign using the Anglo-Australian Telescope. The GAMA input catalogue is based on data taken from the Sloan Digital Sky Survey and the UKIRT Infrared Deep Sky Survey. Complementary imaging of the GAMA regions is being obtained by a number of independent survey programs including GALEX MIS, VST KiDS, VISTA VIKING, WISE, Herschel-ATLAS, GMRT and ASKAP providing UV to radio coverage. GAMA is funded by the STFC (UK), the ARC (Australia), the AAO, and the participating institutions. The GAMA website is `www.gama-survey.org`.

This work has made use of PYTHON (`www.python.org`), including the packages NUMPY (`www.numpy.org`), SCIPY (`www.scipy.org`) and IPYTHON (Pérez and Granger 2007). Plots have been produced with MATPLOTLIB (Hunter

2007).

Author contributions: All authors contributed to the development and writing of this paper. The authorship list is given in three groups: the lead authors (M. Brouwer & M. Visser), followed by two alphabetical groups. The first alphabetical group includes those who are key contributors to both the scientific analysis and the data products. The second group covers those who have either made a significant contribution to the data products, or to the scientific analysis.

6 | Nederlandse samenvatting

"Dit kosmische mysterie van immense proporties, dat ooit op de rand van de oplossing leek, is alleen maar dieper geworden, en verbijstert astronomen en astrofysici nu meer dan ooit. De crux ... is dat het overgrote deel van de massa van het heelal lijkt te ontbreken."

Hiermee beschrijft New York Times journalist William Broad in weinig woorden een van de grootste problemen in de moderne kosmologie. In de loop van de afgelopen tachtig jaar hebben astronomen steeds meer bewijzen gevonden voor een heelal waarin alle materie die we kennen – sterren, planeten, gas, stof, en zelfs exotische objecten zoals zwarte gaten en neutrino's – slechts 20% van alle massa verklaart. De overige 80% bestaat volgens de meeste astronomen uit een onbekend en onzichtbaar soort deeltje dat 'donkere materie' genoemd wordt. Deze mysterieuze substantie straalt geen licht uit en absorbeert het ook niet; het heeft er eigenlijk geen enkele invloed op. Kortom, de op licht gebaseerde waarnemingen waar de astronomie van alle tijden van afhankelijk is (van de oude Babyloniërs tot de modernste ruimte-telescopen) zullen ons bij dit probleem niet helpen. Sterker nog, voor zover de huidige waarnemingen hebben kunnen vaststellen, heeft donkere materie op bijna geen enkele manier wisselwerking met onze normale, zichtbare materie. Dit maakt het ongelofelijk moeilijk om donkere materie te onderzoeken. Maar, als donkere materie zo onzichtbaar is, hoe weten we dan dat ze bestaat? En als die materie bijna niets doet, hoe wordt er dan onderzoek naar gedaan?

6.1 Het donkere universum

Donkere materie is eigenlijk niet één keer, maar meerdere keren op verschillende manieren ontdekt, wat astrofysici steeds sterker van dit probleem heeft overtuigd. Al deze ontdekkingen hangen echter met één concept samen: de zwaartekracht. De zwaartekracht is, voor zover we weten, de enige manier waarop donkere materie met zichtbare materie wisselwerkt, en dit is ook de manier waarop astronomen zulke materie hebben ontdekt. De wetten van de zwaartekracht zijn namelijk al in 1687 beschreven door Isaac Newton, en in 1915 verbeterd door Albert Einstein. Door middel van deze zwaartekrachtwetten kunnen fysici precies uitrekenen hoeveel kracht twee massa's op elkaar uitoefenen, en welke bewegingen daarop moet volgen. Zo hebben astrofysici door het bestuderen van de beweging van zichtbare materie, zoals sterren en gas, kunnen ontdekken dat er meer massa moet zijn dan we kunnen zien.

Eén van de eersten die het bestaan van onzichtbare massa opmerkte was de Nederlandse astronoom Jan Hendrik Oort. In 1932 bestudeerde hij de bewegingen van naburige sterren, en concludeerde dat de massa in ons deel van de Melkweg groter moet zijn dan die van waargenomen sterren en gas. Zijn berekeningen bleken echter onvoldoende bewijs. De eerste die overweldigend bewijs voor de realiteit van het probleem van de donkere materie verzamelde, was de Amerikaanse astronome Vera Rubin. Tussen 1960 en 1970 observeerde ze met haar collega Kent Ford de rotatiekrommen van tientallen sterrenstelsels. In een rotatiekromme wordt de rotatiesnelheid van de sterren rond het centrum van het sterrenstelsel uitgezet tegen hun afstand tot het centrum. Als je weet wat de massa van de sterren en het gas in het sterrenstelsel is, kun je de vorm van deze rotatiekromme voorspellen door middel van Newtons zwaartekrachtwetten. De verwachting was dat de massa, en dus de rotatiesnelheid van het sterrenstelsel, zou afnemen met de afstand tot het centrum. Tot haar verbazing observeerde Vera Rubin echter dat de rotatiesnelheid niet daalde, maar gelijk bleef of zelfs bleef stijgen.

Het is niet verwonderlijk dat Vera's ontdekking in eerste instantie sceptisch werd ontvangen. Haar waarnemingen bevestigden echter wel een vermoeden dat twee grootheden uit de astronomie al eerder had uitgesproken. In 1933, een jaar na het onderzoek van Oort, merkte ook de Zwitser Fritz Zwicky, tijdens zijn onderzoek naar clusters van melkwegstelsels, dat de stelsels aan de rand van het Coma-cluster te snel bewogen om door de zwaartekracht van de zichtbare materie bij elkaar gehouden te worden. Het cluster moest hiervoor zo'n 400 keer zwaarder zijn dan op grond van het zichtbare gas en de sterrenstelsels werd berekend. Frits Zwicky noemde deze missende massa zelfs als eerste 'Dunkele Materie'. Vera Rubin stond dus al snel niet alleen: van alle kanten bleek dat er iets niet in de haak was.

Voor zover we nu weten, kunnen al deze waarnemingen kortweg twee dingen betekenen:

1. Als de totale massa van objecten veel groter is dan kan worden afgeleid uit zichtbare materie, moet er een onzichtbare massa-component zijn die ervoor zorgt dat zowel afzonderlijke sterrenstelsels als clusters zo snel kunnen roteren zonder uit elkaar te vliegen. Deze massa wordt donkere materie genoemd.

2. De zwaartekrachtwetten van Newton en Einstein werken op de kosmische schaal niet hetzelfde als op kleine schaal, zoals op aarde en binnen ons zonnestelsel. Er moet een aanpassing op de huidige zwaartekrachttheorie komen, ook wel "geModificeerde Newtoniaanse Dynamica" (MoND) genoemd.

In beide kampen werken grote groepen astrofysici al jaren aan een definitieve verklaring van het probleem van de donkere materie, maar tot de dag van vandaag is de strijd nog altijd niet beslecht. Hoe kom je er nu achter welke van deze twee opties de missende massa het beste verklaart? En als donkere materie echt bestaat, hoe vind je het dan?

6.2 Buigende ruimte-tijd

Het probleem van zoeken naar donkere materie is dat het onzichtbaar is: volgens de huidige theorieën straalt het geen licht uit en absorbeert het dat ook niet; het heeft er eigenlijk geen enkele invloed op. Sterker nog: donkere materie heeft, voor zover we weten, geen enkele wisselwerking met normale materie, behalve door middel van de zwaartekracht. Omdat donkere materie, indien het bestaat, in ieder geval zwaartekracht uitoefent (en dus massa heeft), kunnen we er meer over te weten te komen door deze onzichtbare massa in kaart brengen. De methode hiervoor is al in 1915 door Albert Einstein voorspeld in zijn algemene relativiteitstheorie. In deze theorie zijn ruimte en tijd niet statisch en strikt gescheiden, maar een vierdimensionaal geheel (de ruimte-tijd) dat kan inkrimpen, uitrekken en buigen. Volgens Einstein is zwaartekracht niets anders dan kromming van de ruimte-tijd. Elke massa vervormt de ruimte-tijd, en kan daardoor het pad

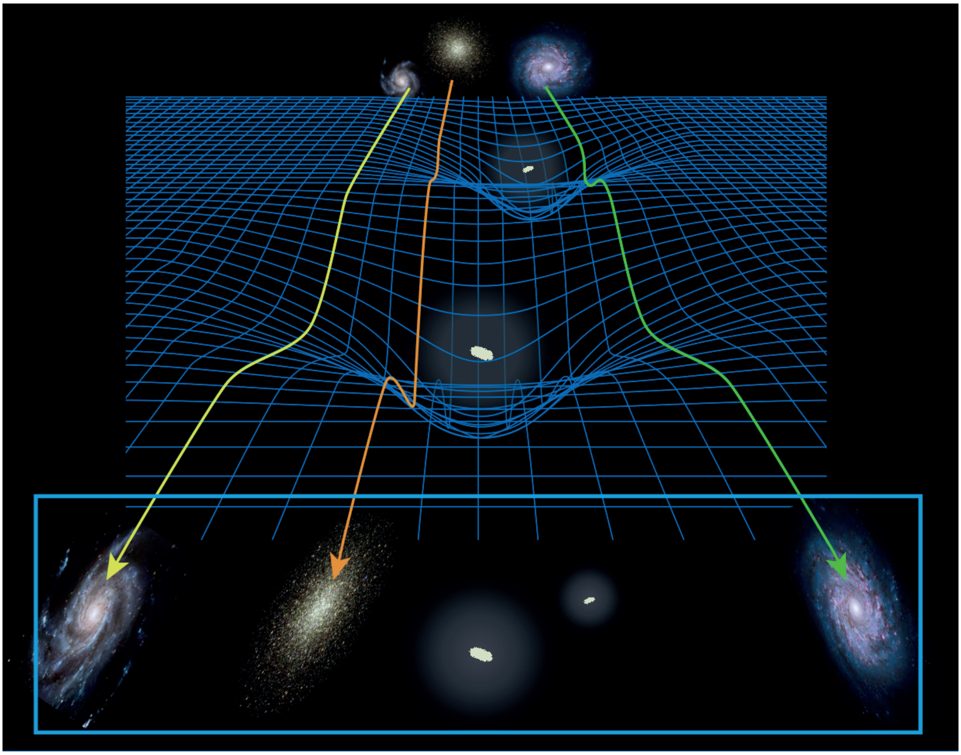

Figuur 6.1: De kromming van de ruimte door de zwaartekracht rondom voorgrond-sterrenstelsels buigt het licht van achtergrond-sterrenstelsels dat door deze ruimte reist. Door de vervorming van de achtergrond-sterrenstelsels waar te nemen met een telescoop, kan de verdeling van zwaartekracht rondom de voorgrond-sterrenstelsels worden gereconstrueerd. Credit: APS/Alan Stonebraker; galaxy images from STScI/AURA, NASA, ESA, and the Hubble Heritage Team.

van een andere massa veranderen of zelfs van een lichtstraal buigen. Dit effect is voor het eerst waargenomen door de Britste astronoom Arthur Eddington in 1919. Hij reisde met een telescoop en fotografische platen naar West-Afrika, om daar tijdens de zonsverduistering de sterren die rondom de zon lijken te staan waar te nemen. Doordat de zwaartekracht van de zon de ruimte-tijd kromt, waren de lichtstralen van deze sterren gebogen en leken ze verder van de rand zon te staan dan in werkelijkheid. Dit effect heet de “lenswerking van zwaartekracht”, omdat de zwaartekracht het licht net als een lens afbuigt. Eddington bewees met zijn waarneming dat Einsteins zwaartekrachttheorie de juiste was, waardoor Einstein in één klap beroemd werd.

Deze lenswerking is dus een unieke manier om de verdeling van zwaartekracht rondom astronomische objecten te meten. In dit proefschrift gebruiken we de lenswerking van zwaartekracht om de verdeling van donkere materie (of "extra zwaartekracht") te meten rondom sterrenstelsels en grotere structuren. Dit gebeurt als volgt: stel dat we met onze telescoop in de richting van twee sterrenstelsels kijken. Op afbeelding 6.1 zijn deze sterrenstelsels te zien als gele vlekjes, met daaromheen de gekromde blauwe lijnen, die de ruimte weergeven. Ver achter deze sterrenstelsels staan een paar achtergrond-sterrenstelsels. Het licht van de achtergrond-sterrenstelsels reist door de gekromde ruimte. Hierdoor zien we deze sterrenstelsels vervormd door onze telescoop. De vervorming van de achtergrond-sterrenstelsels geeft dus aan waar de zwaartekracht zich bevindt. Omdat de lenswerking van zwaartekracht erg zwak is, zijn er niet één of twee, maar duizenden voorgrond-sterrenstelsels (met miljoenen achtergrond-sterrenstelsels) nodig om dit effect nauwkeurig te meten. De voorgrond-sterrenstelsels die bestudeerd worden in dit werk zijn waargenomen met de Galaxy And Mass Assembly (GAMA) survey, een samenwerkingsverband dat met de Anglo-Australian Telescope (AAT) zeer nauwkeurig de afstand en eigenschappen van tienduizenden sterrenstelsels heeft bepaald. De vervorming van de achtergrond-sterrenstelsels is zeer nauwkeurig waargenomen met de Kilo-Degree Survey (KiDS). Deze survey, die speciaal ontworpen is om de lenswerking van zwaartekracht waar te nemen, wordt uitgevoerd met de Very Large Survey Telescope (VST). Deze telescoop staat op de 2,6 kilometer hoge berg Cerro Paranal in Chili (te zien op afbeelding 6.2).

6.3 Dit proefschrift

In dit proefschrift meten we met KiDS de lenswerking van zwaartekracht rondom sterrenstelsels die zijn waargenomen met GAMA. Op deze manier kunnen we de verdeling van donkere materie (de extra zwaartekracht) vergelijken met de verdeling van zichbare materie (de sterrenstelsels). Dit kan ons meer inzicht geven in het gedrag van donkere materie, wat ons aanwijzingen kan geven over wat het mogelijk zou kunnen zijn.

In **Hoofdstuk 2** van dit proefschrift bestuderen we de donkere materie rond groepen van sterrenstelsels (met 5 leden of meer). Groepen vertegenwoordigen de meest voorkomende omgeving waarin sterrenstelsels zich bevinden, wat ze belangrijke studie-objecten maakt. We verdelen de ~ 1400 groepen in verschillende categorieën op basis van hun waargenomen eigenschappen, en meten de gemiddelde massa van de donkere materie-wolk

Figuur 6.2: Het Paranal-observatorium in Chili. De Very Large Survey Telescope, waarmee de lenswerking van zwaartekracht wordt waargenomen, staat op de grote berg vooraan, net achter de vier telescopen van de Very Large Telescope. Credit: J.L. Dauvergne & G. Hüdepohl (`atacamaphoto.com`)/ESO

(die 'halo' wordt genoemd) rond de groepen in elke categorie. Zo kunnen we de massa van de halo meten als functie van o.a. de helderheid, de rotatiesnelheid, en het aantal leden van de groepen. Door onze waarnemingen te vergelijken met de Cosmo-OverWhelmingly Large Simulations (Cosmo-OWLS), kunnen we bepalen dat sterrenstelsels en hun halo's sterk worden beïnvloed door de actieve kernen van sterrenstelsels, zogenaamde "Active Galactic Nuclei" (AGN), waardoor simulaties die deze niet in rekening nemen onrealistische voorspellingen geven.

In **Hoofdstuk 3** vragen we ons af of de donkere materie-halo's rond sterrenstelsels worden beïnvloed door de grootschalige omgeving van de sterrenstelsels. Deze omgeving bestaat uit het zogenaamde "kosmische web", een groot netwerk van structuren die bestaan uit donkere materie, sterrenstelsels en gas. Afhankelijk van het aantal dimensies waarin deze structuren zich uitstrekken worden ze gedefinieerd als: Voids (3-dimensionale leegtes), Sheets (2-dimensionale platen), Filaments (1-dimensionale filamenten) en Knots (0-dimensionale knopen). We verdelen de GAMA-sterrenstelsels in 4 categorieën op basis van de kosmische omgeving waarin ze wonen, en meten de gemiddelde massa van hun donkere materie-halo's. We corrigeren deze massa voor de zichtbare massa's van de sterrenstelsels (gebaseerd op het licht van sterren en gas) en de invloed van de lokale omgeving (dichtbijzijnde sterrenstelsels), en richten ons puur op de invloed van de kosmische omgeving. Wanneer we deze correcties toepassen vinden we geen afhankelijkheid van de halo-massa met betrekking tot de kosmische omgeving.

In **Hoofdstuk 4** bestuderen we de structuur van het kosmische web zelf, door het meten van de lenswerking van de zwaartekracht van 'troughs' (langwerpige leegtes of 'troggen') en 'ridges' (langwerpige verdichtigen of 'ruggen'). Dit zijn cirkelvormige gebieden aan de hemel die minder (in het geval van de troughs) of meer (ridges) sterrenstelsels bevatten dan gemiddeld. Door de kracht van de lenswerking rondom troughs en ridges te meten als functie van hun sterrenstelsel-dichtheid, kunnen we de connectie tussen hun normale (lichtgevende) massa en hun donkere massa bestuderen. Door de troughs en ridges te scheiden as functie van hun afstand in de ruimte (wat door de beperkte snelheid van het licht gelijk staat aan een afstand in de tijd) proberen we hun ontwikkeling door de tijd te bepalen. Op de relatief kleine afstanden die we momenteel tot onze beschikking hebben kunnen we geen significante evolutie van deze structuren vinden. Echter, met behulp van simulaties kunnen we voorspellen dat deze evolutie gemeten zou kunnen worden met toekomstige nauwkeurigere telescopen, die sterrenstelsels op grotere afstanden kunnen waarnemen.

In **Hoofdstuk 5** beschrijven we de eerste test van Erik Verlinde's nieuwe theorie van Emergente Zwaartekracht door middel van de lenswerking van zwaartekracht. Deze theorie probeert een alternatieve verklaring te geven voor de extra zwaartekracht die momenteel aan donkere materie wordt toegeschreven. De voorspellingen van de theorie zijn nog beperkt toepasbaar: alleen op bolsymmetrische, statische en geïsoleerde massaverdelingen. Daarom hebben we de 33,613 GAMA-sterrenstelsels die we voor deze test hebben gebruikt nauwkeurig geselecteerd. Met behulp van de zichtbare massa's van deze sterrenstelsels kunnen we de voorspelde zwaartekrachtverdeling van Verlindes theorie bepalen, en daarmee de voorspelde lenswerking van de zwaartekracht. Hierbij moeten we aannemen dat Emergente Zwaartekracht het licht precies zo afbuigt als in Einsteins algemene relativiteitstheorie, en het omgevende heelal zich op ongeveer dezelfde manier blijft gedragen. Deze voorspelling lijkt veel op die van MoND in het geval van een puntmassa, maar wijkt af voor grotere massaverdelingen. We vergelijking Verlindes voorspelling met de door ons gemeten zwaartekrachtsverdeling rond sterrenstelsels van vier verschillende massa's. Onze conclusie is dat de Emergente Zwaartekrachttheorie de waarnemingen even goed voorspelt als het donkere materie-model. In dit laatste model zijn echter vier vrije parameters nodig voor het bepalen van de vier verschillende massa's van de halo's rond de sterrenstelsels, terwijl Verlindes voorspelling direct voortvloeit uit de gemeten zichtbare massa's van de sterrenstelsels. Hoewel dit een interessant eerste resultaat is, zijn er nog zeer veel waarnemingen die niet door Emergente Zwaartekracht kunnen worden verklaard. Zowel de theoretische achtergrond als de observationele tests van deze theorie zullen daarom sterk moeten worden uitgebreid voordat het kan worden beschouwd als een alternatieve verklaring voor donkere materie.

Deze samenvatting is gebaseerd op:

- *Donkere materie (1): Een duistere ontdekking*, Margot Brouwer (`http://www.quantumuniverse.nl/donkere-materie-1-een-duistere-ontdekking`)
- *Donkere Materie (2): Strijd tussen de sterren*, Margot Brouwer (`http://www.quantumuniverse.nl/donkere-materie-2-strijd-tussen-de-sterren`)
- *Een eerste test van de theorie van Erik Verlinde*, Margot Brouwer & Manus Visser (`http://www.quantumuniverse.nl/een-eerste-test-van-de-theorie-van-erik-verlinde`)

Bibliography

K. N. Abazajian, J. K. Adelman-McCarthy, M. A. Agüeros, et al. *ApJS*, 182:543-558, June 2009. doi: 10.1088/0067-0049/182/2/543.

A. Aguirre, J. Schaye, and E. Quataert. *ApJ*, 561:550–558, Nov. 2001. doi: 10.1086/323376.

H. Akaike. *Biometrika*, 60(2):255–265, 1973. doi: 10.1093/biomet/60.2.255. URL `http://biomet.oxfordjournals.org/content/60/2/255.abstract`.

D. Alonso, E. Eardley, and J. A. Peacock. *MNRAS*, 447:2683–2695, Mar. 2015. doi: 10.1093/mnras/stu2632.

M. Alpaslan, S. Driver, A. S. G. Robotham, et al. *MNRAS*, 451:3249–3268, Aug. 2015. doi: 10.1093/mnras/stv1176.

R. A. Alpher, H. Bethe, and G. Gamow. *Physical Review*, 73:803–804, Apr. 1948. doi: 10.1103/PhysRev.73.803.

R. Andrae, T. Schulze-Hartung, and P. Melchior. *ArXiv e-prints*, Dec. 2010.

M. A. Aragon-Calvo, M. C. Neyrinck, and J. Silk. *ArXiv e-prints*, Dec. 2014.

I. K. Baldry, A. S. G. Robotham, D. T. Hill, et al. *MNRAS*, 404:86–100, May 2010. doi: 10.1111/j.1365-2966.2010.16282.x.

I. K. Baldry, M. Alpaslan, A. E. Bauer, et al. *MNRAS*, 441:2440–2451, July 2014. doi: 10.1093/mnras/stu727.

J. M. Bardeen, J. R. Bond, N. Kaiser, et al. *ApJ*, 304:15–61, May 1986. doi: 10.1086/164143.

A. Barreira, S. Bose, B. Li, and C. Llinares. *J. Cosmology Astropart. Phys.*, 2:031, Feb. 2017. doi: 10.1088/1475-7516/2017/02/031.

M. Bartelmann and P. Schneider. *Phys. Rep.*, 340:291–472, Jan. 2001.

R. Beare, M. J. I. Brown, and K. Pimbblet. *ApJ*, 797:104, Dec. 2014. doi: 10.1088/0004-637X/797/2/104.

P. S. Behroozi, C. Conroy, and R. H. Wechsler. *ApJ*, 717:379–403, July 2010. doi: 10.1088/0004-637X/717/1/379.

P. S. Behroozi, R. H. Wechsler, and C. Conroy. *ApJ*, 762:L31, Jan. 2013. doi: 10.1088/2041-8205/762/2/L31.

J. D. Bekenstein. *Phys. Rev. D*, 70(8):083509, Oct. 2004. doi: 10.1103/PhysRevD.70.083509.

N. Benítez. *ApJ*, 536:571–583, June 2000. doi: 10.1086/308947.

A. J. Benson, S. Cole, C. S. Frenk, et al. *MNRAS*, 311:793–808, Feb. 2000. doi: 10.1046/j.1365-8711.2000.03101.x.

A. A. Berlind, J. Frieman, D. H. Weinberg, et al. *ApJS*, 167:1–25, Nov. 2006. doi: 10.1086/508170.

E. Bertin and S. Arnouts. *A&AS*, 117:393–404, June 1996. doi: 10.1051/aas:1996164.

M. Betoule, R. Kessler, J. Guy, et al. *A&A*, 568:A22, Aug. 2014. doi: 10.1051/0004-6361/201423413.

M. Bilicki, H. Hoekstra, V. Amaro, C. Blake, M. J. I. Brown, S. Cavuoti, J. T. A. de Jong, H. Hildebrandt, C. Wolf, A. Amon, M. Brescia, S. Brough, M. V. Costa-Duarte, T. Erben, K. Glazebrook, A. Grado, C. Heymans, T. Jarrett, S. Joudaki, K. Kuijken, G. Longo, N. Napolitano, D. Parkinson, C. Vellucci, G. A. Verdoes Kleijn, and L. Wang. *ArXiv e-prints*, Sept. 2017.

C. Blake, T. Davis, G. B. Poole, et al. *MNRAS*, 415:2892–2909, Aug. 2011. doi: 10.1111/j.1365-2966.2011.19077.x.

J. Blazek, R. Mandelbaum, U. Seljak, et al. *J. Cosmology Astropart. Phys.*, 5:041, May 2012. doi: 10.1088/1475-7516/2012/05/041.

G. R. Blumenthal, S. M. Faber, J. R. Primack, and M. J. Rees. *Nature*, 311:517–525, Oct. 1984. doi: 10.1038/311517a0.

J. R. Bond, B. J. Carr, and C. J. Hogan. *ApJ*, 306:428–450, July 1986. doi: 10.1086/164355.

C. M. Booth and J. Schaye. *Scientific Reports*, art. 1738, May 2013. doi: 10.1038/srep01738.

E. G. P. Bos, R. van de Weygaert, K. Dolag, et al. *MNRAS*, 426:440–461, Oct. 2012. doi: 10.1111/j.1365-2966.2012.21478.x.

F. C. van den Bosch. *MNRAS*, 331:98–110, Mar. 2002. doi: 10.1046/j.1365-8711.2002.05171.x.

F. C. van den Bosch, X. Yang, H. J. Mo, et al. *MNRAS*, 376:841–860, Apr. 2007. doi: 10.1111/j.1365-2966.2007.11493.x.

F. C. van den Bosch, S. More, M. Cacciato, et al. *MNRAS*, 430:725–746, Apr. 2013. doi: 10.1093/mnras/sts006.

A. Boselli, S. Eales, L. Cortese, et al. *PASP*, 122:261–287, Mar. 2010. doi: 10.1086/651535.

A. Boselli, L. Cortese, M. Boquien, et al. *A&A*, 564:A66, Apr. 2014. doi: 10.1051/0004-6361/201322312.

A. Bosma. *AJ*, 86:1791–1846, Dec. 1981. doi: 10.1086/113062.

R. G. Bower, A. J. Benson, R. Malbon, et al. *MNRAS*, 370:645–655, Aug. 2006. doi: 10.1111/j.1365-2966.2006.10519.x.

T. G. Brainerd, R. D. Blandford, and I. Smail. *ApJ*, 466:623, Aug. 1996. doi: 10.1086/177537.

F. Brimioulle, S. Seitz, M. Lerchster, et al. *MNRAS*, 432:1046–1102, June 2013. doi: 10.1093/mnras/stt525.

S. Brough, D. A. Forbes, V. A. Kilborn, et al. *MNRAS*, 370:1223–1246, Aug. 2006. doi: 10.1111/j.1365-2966.2006.10542.x.

M. M. Brouwer, M. Cacciato, A. Dvornik, et al. *MNRAS*, 462:4451–4463, Nov. 2016. doi: 10.1093/mnras/stw1602.

M. M. Brouwer, M. R. Visser, A. Dvornik, et al. *MNRAS*, 466:2547–2559, Apr. 2017. doi: 10.1093/mnras/stw3192.

G. Bruzual and S. Charlot. *MNRAS*, 344:1000–1028, Oct. 2003. doi: 10.1046/j.1365-8711.2003.06897.x.

T. Budavari, A. J. Connolly, A. S. Szalay, et al. *ApJ*, 595(1):59, 2003.

J. S. Bullock, T. S. Kolatt, Y. Sigad, et al. *MNRAS*, 321:559–575, Mar. 2001. doi: 10.1046/j.1365-8711.2001.04068.x.

R. F. J. van der Burg, A. Muzzin, H. Hoekstra, et al. *A&A*, 561:A79, Jan. 2014. doi: 10.1051/0004-6361/201322771.

M. Cacciato, F. C. van den Bosch, S. More, et al. *MNRAS*, 394:929–946, Apr. 2009. doi: 10.1111/j.1365-2966.2008.14362.x.

M. Cacciato, F. C. van den Bosch, S. More, et al. *MNRAS*, 430:767–786, Apr. 2013. doi: 10.1093/mnras/sts525.

D. Calzetti, L. Armus, R. C. Bohlin, et al. *ApJ*, 533:682–695, Apr. 2000. doi: 10.1086/308692.

M. Capaccioli and P. Schipani. *The Messenger*, 146:2–7, Dec. 2011.

R. G. Carlberg, H. K. C. Yee, S. L. Morris, et al. *ApJ*, 552:427–444, May 2001. doi: 10.1086/320555.

J. Carretero, F. J. Castander, E. Gaztañaga, et al. *MNRAS*, 447:646–670, Feb. 2015. doi: 10.1093/mnras/stu2402.

B. Catinella, D. Schiminovich, L. Cortese, et al. *MNRAS*, 436:34–70, Nov. 2013. doi: 10.1093/mnras/stt1417.

M. Cautun, Y.-C. Cai, and C. S. Frenk. *MNRAS*, 457:2540–2553, Apr. 2016. doi: 10.1093/mnras/stw154.

M. Cautun, E. Paillas, Y.-C. Cai, S. Bose, J. Armijo, B. Li, and N. Padilla. *ArXiv e-prints*, Oct. 2017.

A. Cavaliere and R. Fusco-Femiano. *A&A*, 49:137–144, May 1976.

G. Chabrier. *PASP*, 115:763–795, July 2003. doi: 10.1086/376392.

C. Chang, M. Jarvis, B. Jain, et al. *MNRAS*, 434:2121–2135, Sept. 2013. doi: 10.1093/mnras/stt1156.

A. Choi, J. A. Tyson, C. B. Morrison, et al. *ApJ*, 759:101, Nov. 2012. doi: 10.1088/0004-637X/759/2/101.

T. Clifton, P. G. Ferreira, A. Padilla, et al. *Phys. Rep.*, 513:1–189, Mar. 2012. doi: 10.1016/j.physrep.2012.01.001.

D. Clowe, M. Bradač, A. H. Gonzalez, et al. *ApJ*, 648:L109–L113, Sept. 2006. doi: 10.1086/508162.

J. M. Colberg, F. Pearce, C. Foster, et al. *MNRAS*, 387:933–944, June 2008. doi: 10.1111/j.1365-2966.2008.13307.x.

S. Cole and N. Kaiser. *MNRAS*, 237:1127–1146, Apr. 1989. doi: 10.1093/mnras/237.4.1127.

P. Coles and B. Jones. *MNRAS*, 248:1–13, Jan. 1991. doi: 10.1093/mnras/248.1.1.

M. Colless, G. Dalton, S. Maddox, et al. *MNRAS*, 328:1039–1063, Dec. 2001. doi: 10.1046/j.1365-8711.2001.04902.x.

A. Cooray and R. Sheth. *Phys. Rep.*, 372:1–129, Dec. 2002. doi: 10.1016/S0370-1573(02)00276-4.

J. Coupon, S. Arnouts, L. van Waerbeke, et al. *MNRAS*, 449:1352–1379, May 2015. doi: 10.1093/mnras/stv276.

B. C. Coutinho, S. Hong, K. Albrecht, et al. *ArXiv e-prints*, Apr. 2016.

M. Crocce, F. J. Castander, E. Gaztañaga, et al. *MNRAS*, 453:1513–1530, Oct. 2015. doi: 10.1093/mnras/stv1708.

A. F. Crocker, M. Bureau, L. M. Young, et al. *MNRAS*, 410:1197–1222, Jan. 2011. doi: 10.1111/j.1365-2966.2010.17537.x.

D. J. Croton, G. R. Farrar, P. Norberg, et al. *MNRAS*, 356(3):1155–1167, 2005.

M. P. van Daalen, J. Schaye, C. M. Booth, et al. *MNRAS*, 415:3649–3665, Aug. 2011. doi: 10.1111/j.1365-2966.2011.18981.x.

Dark Energy Science Collaboration. *ArXiv e-prints*, Nov. 2012.

B. Darvish, D. Sobral, B. Mobasher, et al. *ApJ*, 796:51, Nov. 2014. doi: 10.1088/0004-637X/796/1/51.

T. A. Davis, K. Alatalo, M. Bureau, et al. *MNRAS*, 429:534–555, Feb. 2013. doi: 10.1093/mnras/sts353.

A. Dekel and J. Silk. *ApJ*, 303:39–55, Apr. 1986. doi: 10.1086/164050.

V. Demchenko, Y.-C. Cai, C. Heymans, and J. A. Peacock. *MNRAS*, 463:512–519, Nov. 2016. doi: 10.1093/mnras/stw2030.

J. P. Dietrich and J. Hartlap. *MNRAS*, 402:1049–1058, Feb. 2010. doi: 10.1111/j.1365-2966.2009.15948.x.

S. P. Driver, D. T. Hill, L. S. Kelvin, et al. *MNRAS*, 413:971–995, May 2011. doi: 10.1111/j.1365-2966.2010.18188.x.

S. P. Driver, L. J. Davies, M. Meyer, et al. *ArXiv e-prints*, July 2015.

Y. Dubois, R. Gavazzi, S. Peirani, et al. *MNRAS*, 433:3297–3313, Aug. 2013. doi: 10.1093/mnras/stt997.

A. R. Duffy, J. Schaye, S. T. Kay, et al. *MNRAS*, 390:L64–L68, Oct. 2008. doi: 10.1111/j.1745-3933.2008.00537.x.

A. A. Dutton and A. V. Macciò. *MNRAS*, 441:3359–3374, July 2014.

A. Dvornik, M. Cacciato, K. Kuijken, et al. *MNRAS*, 468:3251–3265, July 2017. doi: 10.1093/mnras/stx705.

E. Eardley, J. A. Peacock, T. McNaught-Roberts, et al. *MNRAS*, 448:3665–3678, Apr. 2015. doi: 10.1093/mnras/stv237.

H. J. Eckmiller, D. S. Hudson, and T. H. Reiprich. *A&A*, 535:A105, Nov. 2011. doi: 10.1051/0004-6361/201116734.

A. Edge, W. Sutherland, K. Kuijken, et al. *The Messenger*, 154:32–34, Dec. 2013.

D. J. Eisenstein, I. Zehavi, D. W. Hogg, et al. *ApJ*, 633:560–574, Nov. 2005. doi: 10.1086/466512.

V. R. Eke, J. F. Navarro, and M. Steinmetz. *ApJ*, 554:114–125, June 2001. doi: 10.1086/321345.

V. R. Eke, C. S. Frenk, C. M. Baugh, et al. *MNRAS*, 355:769–784, Dec. 2004. doi: 10.1111/j.1365-2966.2004.08354.x.

T. Erben, H. Hildebrandt, L. Miller, et al. *MNRAS*, 433:2545–2563, Aug. 2013. doi: 10.1093/mnras/stt928.

S. Ettori, V. Ghirardini, D. Eckert, et al. *MNRAS*, 470:L29–L33, Sept. 2017. doi: 10.1093/mnrasl/slx074.

A. E. Evrard, J. Bialek, M. Busha, et al. *ApJ*, 672:122–137, Jan. 2008. doi: 10.1086/521616.

D. Fabjan, S. Borgani, L. Tornatore, et al. *MNRAS*, 401:1670–1690, Jan. 2010. doi: 10.1111/j.1365-2966.2009.15794.x.

T. Faulkner, M. Guica, T. Hartman, et al. *Journal of High Energy Physics*, 3:51, Mar. 2014. doi: 10.1007/JHEP03(2014)051.

C. Fedeli. *J. Cosmology Astropart. Phys.*, 4:028, Apr. 2014. doi: 10.1088/1475-7516/2014/04/028.

I. Fenech Conti, R. Herbonnet, H. Hoekstra, et al. *MNRAS*, 467:1627–1651, May 2017. doi: 10.1093/mnras/stx200.

A. Finoguenov, M. Tanaka, M. Cooper, et al. *ArXiv e-prints*, Jan. 2015.

P. Fischer, T. A. McKay, E. Sheldon, et al. *AJ*, 120:1198–1208, Sept. 2000. doi: 10.1086/301540.

B. Flaugher, H. T. Diehl, K. Honscheid, et al. *AJ*, 150:150, Nov. 2015. doi: 10.1088/0004-6256/150/5/150.

D. Foreman-Mackey, D. W. Hogg, D. Lang, et al. *PASP*, 125:306, Mar. 2013. doi: 10.1086/670067.

P. Fosalba, E. Gaztañaga, F. J. Castander, et al. *MNRAS*, 391:435–446, Nov. 2008. doi: 10.1111/j.1365-2966.2008.13910.x.

P. Fosalba, M. Crocce, E. Gaztañaga, et al. *MNRAS*, 448:2987–3000, Apr. 2015a. doi: 10.1093/mnras/stv138.

P. Fosalba, E. Gaztañaga, F. J. Castander, et al. *MNRAS*, 447:1319–1332, Feb. 2015b. doi: 10.1093/mnras/stu2464.

K. C. Freeman. *ApJ*, 160:811, June 1970. doi: 10.1086/150474.

B. Garilli, L. Guzzo, M. Scodeggio, et al. *A&A*, 562:A23, 2014.

A. Gelman and D. B. Rubin. *Statistical Science*, 7(4):457–472, 11 1992. doi: 10.1214/ss/1177011136. URL `http://dx.doi.org/10.1214/ss/1177011136`.

M. R. George, A. Leauthaud, K. Bundy, et al. *ApJ*, 742:125, Dec. 2011. doi: 10.1088/0004-637X/742/2/125.

M. R. George, A. Leauthaud, K. Bundy, et al. *ApJ*, 757:2, Sept. 2012. doi: 10.1088/0004-637X/757/1/2.

B. F. Gerke, J. A. Newman, M. Davis, et al. *ApJ*, 625:6–22, May 2005. doi: 10.

1086/429579.

C. Giocoli, M. Meneghetti, S. Ettori, et al. *MNRAS*, 426:1558–1573, Oct. 2012. doi: 10.1111/j.1365-2966.2012.21743.x.

J. Goodman and J. Weare. *Communications in Applied Mathematics and Computational Science, Vol. 5, No. 1, p. 65-80, 2010*, 5:65–80, 2010. doi: 10.2140/camcos.2010.5.65.

A. Gould. *ArXiv Astrophysics e-prints*, Oct. 2003.

D. Gruen, O. Friedrich, A. Amara, et al. *MNRAS*, 455:3367–3380, Jan. 2016. doi: 10.1093/mnras/stv2506.

D. Gruen, O. Friedrich, E. Krause, et al. *ArXiv e-prints*, Oct. 2017.

A. H. Guth. *Phys. Rev. D*, 23:347–356, Jan. 1981. doi: 10.1103/PhysRevD.23.347.

O. Hahn, C. Porciani, C. M. Carollo, et al. *MNRAS*, 375(2):489–499, 2007.

O. Hahn, C. Porciani, A. Dekel, et al. *MNRAS*, 398:1742–1756, Oct. 2009. doi: 10.1111/j.1365-2966.2009.15271.x.

N. Hamaus, P. M. Sutter, and B. D. Wandelt. *Physical Review Letters*, 112(25): 251302, June 2014. doi: 10.1103/PhysRevLett.112.251302.

J. Han, V. R. Eke, C. S. Frenk, et al. *ArXiv e-prints*, Apr. 2014.

A. Hees, B. Famaey, and G. Bertone. *Phys. Rev. D*, 95(6):064019, Mar. 2017. doi: 10.1103/PhysRevD.95.064019.

C. Heymans, E. F. Bell, H.-W. Rix, et al. *MNRAS*, 371:L60–L64, Sept. 2006a. doi: 10.1111/j.1745-3933.2006.00208.x.

C. Heymans, M. White, A. Heavens, et al. *MNRAS*, 371:750–760, Sept. 2006b. doi: 10.1111/j.1365-2966.2006.10705.x.

C. Heymans, L. Van Waerbeke, L. Miller, et al. *MNRAS*, 427:146–166, Nov. 2012. doi: 10.1111/j.1365-2966.2012.21952.x.

Y. Higuchi and M. Shirasaki. *MNRAS*, 459:2762–2776, July 2016. doi: 10.1093/mnras/stw814.

H. Hildebrandt, T. Erben, K. Kuijken, et al. *MNRAS*, 421:2355–2367, Apr. 2012. doi: 10.1111/j.1365-2966.2012.20468.x.

H. Hildebrandt, M. Viola, C. Heymans, et al. *MNRAS*, 465:1454–1498, Feb. 2017. doi: 10.1093/mnras/stw2805.

H. Hoekstra. *MNRAS*, 347:1337–1344, Feb. 2004. doi: 10.1111/j.1365-2966.2004.07327.x.

H. Hoekstra, M. Franx, K. Kuijken, et al. *ApJ*, 548:L5–L8, Feb. 2001. doi: 10.1086/318917.

H. Hoekstra, H. K. C. Yee, and M. D. Gladders. *ApJ*, 606:67–77, May 2004.

H. Hoekstra, R. Herbonnet, A. Muzzin, et al. *MNRAS*, 449:685–714, May 2015. doi: 10.1093/mnras/stv275.

K. Hoffmann, J. Bel, E. Gaztañaga, et al. *MNRAS*, 447:1724–1745, Feb. 2015. doi: 10.1093/mnras/stu2492.

M. J. Hudson, B. R. Gillis, J. Coupon, et al. *MNRAS*, 447:298–314, Feb. 2015. doi: 10.1093/mnras/stu2367.

J. D. Hunter. *Computing in Science and Engineering*, 9:90–95, May 2007. doi: 10.1109/MCSE.2007.55.

O. Ilbert, P. Capak, M. Salvato, et al. *ApJ*, 690:1236–1249, Jan. 2009. doi: 10.1088/0004-637X/690/2/1236.

O. Ilbert, H. J. McCracken, O. Le Fèvre, et al. *A&A*, 556:A55, Aug. 2013. doi: 10.1051/0004-6361/201321100.

T. Jacobson. *Physical Review Letters*, 75:1260–1263, Aug. 1995. doi: 10.1103/PhysRevLett.75.1260.

T. Jacobson. *Physical Review Letters*, 116(20):201101, May 2016. doi: 10.1103/PhysRevLett.116.201101.

B. Jain and J. Khoury. *Annals of Physics*, 325:1479–1516, July 2010. doi: 10.1016/j.aop.2010.04.002.

M. J. Jee, H. Hoekstra, A. Mahdavi, et al. *ApJ*, 783:78, Mar. 2014. doi: 10.1088/0004-637X/783/2/78.

L. Jiang, J. C. Helly, S. Cole, et al. *MNRAS*, 440:2115–2135, May 2014. doi: 10.1093/mnras/stu390.

D. E. Johnston, E. S. Sheldon, A. Tasitsiomi, et al. *ApJ*, 656:27–41, Feb. 2007. doi: 10.1086/510060.

D. H. Jones, M. A. Read, W. Saunders, et al. *MNRAS*, 399(2):683–698, 2009.

J. T. A. de Jong, G. A. Verdoes Kleijn, K. H. Kuijken, et al. *Experimental Astronomy*, 35:25–44, Jan. 2013. doi: 10.1007/s10686-012-9306-1.

J. T. A. de Jong, G. A. Verdoes Kleijn, D. R. Boxhoorn, et al. *A&A*, 582:A62, Oct. 2015. doi: 10.1051/0004-6361/201526601.

J. T. A. de Jong, G. A. Verdoes Kleijn, T. Erben, et al. *ArXiv e-prints*, Mar. 2017.

T. Kacprzak, D. Kirk, O. Friedrich, et al. *MNRAS*, 463:3653–3673, Dec. 2016. doi: 10.1093/mnras/stw2070.

F. D. Kahn and L. Woltjer. *ApJ*, 130:705, Nov. 1959. doi: 10.1086/146762.

R. E. Kass and A. E. Raftery. *Journal of the American Statistical Association*, 90(430):773–795, 1995. doi: 10.1080/01621459.1995.10476572. URL `http://amstat.tandfonline.com/doi/abs/10.1080/01621459.1995.10476572`.

L. S. Kelvin, S. P. Driver, A. S. G. Robotham, et al. *MNRAS*, 421:1007–1039, Apr. 2012. doi: 10.1111/j.1365-2966.2012.20355.x.

R. Kessler, A. C. Becker, D. Cinabro, et al. *ApJS*, 185:32–84, Nov. 2009. doi: 10.1088/0067-0049/185/1/32.

K. Kettula, A. Finoguenov, R. Massey, et al. *ApJ*, 778:74, Nov. 2013. doi: 10.1088/0004-637X/778/1/74.

T. D. Kitching, L. Miller, C. E. Heymans, et al. *MNRAS*, 390:149–167, Oct. 2008. doi: 10.1111/j.1365-2966.2008.13628.x.

A. A. Klypin, S. Trujillo-Gomez, and J. Primack. *ApJ*, 740:102, Oct. 2011. doi: 10.1088/0004-637X/740/2/102.

C. Knobel, S. J. Lilly, A. Iovino, et al. *ApJ*, 697:1842–1860, June 2009. doi: 10.1088/0004-637X/697/2/1842.

M. I. N. Kobayashi, A. Leauthaud, S. More, N. Okabe, C. Laigle, J. Rhodes, and T. T. Takeuchi. *ArXiv e-prints*, Feb. 2015.

B. P. Koester, T. A. McKay, J. Annis, et al. *ApJ*, 660:239–255, May 2007. doi: 10.1086/509599.

E. Krause, T.-C. Chang, O. Doré, et al. *ApJ*, 762:L20, Jan. 2013. doi: 10.1088/2041-8205/762/2/L20.

K. Kuijken. *A&A*, 482:1053–1067, May 2008. doi: 10.1051/0004-6361:20066601.

K. Kuijken. *The Messenger*, 146:8–11, Dec. 2011.

K. Kuijken, C. Heymans, H. Hildebrandt, et al. *MNRAS*, 454:3500–3532, Dec. 2015. doi: 10.1093/mnras/stv2140.

T. Y. Lam, J. Clampitt, Y.-C. Cai, et al. *MNRAS*, 450:3319–3330, July 2015. doi: 10.1093/mnras/stv797.

R. Laureijs, J. Amiaux, S. Arduini, et al. *ArXiv e-prints*, Oct. 2011.

G. Lavaux and B. D. Wandelt. *MNRAS*, 403:1392–1408, Apr. 2010. doi: 10.1111/j.1365-2966.2010.16197.x.

A. M. C. Le Brun, I. G. McCarthy, J. Schaye, et al. *MNRAS*, 441:1270–1290, June 2014. doi: 10.1093/mnras/stu608.

A. Leauthaud, R. Massey, J.-P. Kneib, et al. *ApJS*, 172:219–238, Sept. 2007. doi: 10.1086/516598.

A. Leauthaud, A. Finoguenov, J.-P. Kneib, et al. *ApJ*, 709:97–114, Jan. 2010. doi: 10.1088/0004-637X/709/1/97.

A. Leauthaud, M. R. George, P. S. Behroozi, et al. *ApJ*, 746:95, Feb. 2012a. doi: 10.1088/0004-637X/746/1/95.

A. Leauthaud, J. Tinker, K. Bundy, et al. *ApJ*, 744:159, Jan. 2012b. doi: 10.1088/0004-637X/744/2/159.

F. Lelli, S. S. McGaugh, and J. M. Schombert. *MNRAS*, 468:L68–L71, June 2017. doi: 10.1093/mnrasl/slx031.

M. Levi, C. Bebek, T. Beers, et al. *ArXiv e-prints*, Aug. 2013.

B. Li, G.-B. Zhao, and K. Koyama. *MNRAS*, 421:3481–3487, Apr. 2012. doi: 10.1111/j.1365-2966.2012.20573.x.

A. R. Liddle. *MNRAS*, 377:L74–L78, May 2007. doi: 10.1111/j.1745-3933.2007.00306.x.

Y.-T. Lin and J. J. Mohr. *ApJ*, 617:879–895, Dec. 2004. doi: 10.1086/425412.

A. von der Linden, M. T. Allen, D. E. Applegate, et al. *MNRAS*, 439:2–27, Mar. 2014. doi: 10.1093/mnras/stt1945.

J. Liske, I. K. Baldry, S. P. Driver, et al. *MNRAS*, 452:2087–2126, Sept. 2015. doi: 10.1093/mnras/stv1436.

X. Liu, C. Pan, R. Li, et al. *MNRAS*, 450:2888–2902, July 2015. doi: 10.1093/mnras/stv784.

J. Loveday, P. Norberg, I. K. Baldry, et al. *MNRAS*, 420:1239–1262, Feb. 2012. doi: 10.1111/j.1365-2966.2011.20111.x.

J. Loveday, P. Norberg, I. K. Baldry, et al. *ArXiv e-prints*, May 2015.

A. D. Ludlow and C. Porciani. *MNRAS*, 413:1961–1972, May 2011. doi: 10.1111/j.1365-2966.2011.18282.x.

A. V. Macciò, A. A. Dutton, and F. C. van den Bosch. *MNRAS*, 391:1940–1954, Dec. 2008. doi: 10.1111/j.1365-2966.2008.14029.x.

A. Mahdavi, H. Hoekstra, A. Babul, et al. *ApJ*, 767:116, Apr. 2013. doi: 10.1088/0004-637X/767/2/116.

R. Mandelbaum. Galaxy Halo Masses from Weak Gravitational Lensing. In M. Cappellari and S. Courteau, editors, *Galaxy Masses as Constraints of Formation Models*, volume 311 of *IAU Symposium*, pages 86–95, Apr. 2015.

R. Mandelbaum, U. Seljak, R. J. Cool, et al. *MNRAS*, 372:758–776, Oct. 2006a. doi: 10.1111/j.1365-2966.2006.10906.x.

R. Mandelbaum, U. Seljak, G. Kauffmann, et al. *MNRAS*, 368:715–731, May 2006b. doi: 10.1111/j.1365-2966.2006.10156.x.

R. Mandelbaum, U. Seljak, and C. M. Hirata. *Journal of Cosmology and Astro-Particle Physics*, 8:6–+, Aug. 2008. doi: 10.1088/1475-7516/2008/08/006.

T. P. K. Martinsson, M. A. W. Verheijen, K. B. Westfall, et al. *A&A*, 557:A131, Sept. 2013. doi: 10.1051/0004-6361/201321390.

J. C. Mather. *Optical Engineering*, 21:769–774, Aug. 1982. doi: 10.1117/12.7972975.

I. G. McCarthy, J. Schaye, T. J. Ponman, et al. *MNRAS*, 406:822–839, Aug. 2010. doi: 10.1111/j.1365-2966.2010.16750.x.

J. P. McFarland, G. Verdoes-Kleijn, G. Sikkema, et al. *Experimental Astronomy*, 35:45–78, Jan. 2013. doi: 10.1007/s10686-011-9266-x.

S. S. McGaugh, F. Lelli, and J. M. Schombert. *Physical Review Letters*, 117(20):201101, Nov. 2016. doi: 10.1103/PhysRevLett.117.201101.

T. McNaught-Roberts, P. Norberg, C. Baugh, et al. *MNRAS*, 445:2125–2145, Dec. 2014. doi: 10.1093/mnras/stu1886.

P. Melchior and M. Viola. *MNRAS*, 424:2757–2769, Aug. 2012.

P. Melchior, P. M. Sutter, E. S. Sheldon, et al. *MNRAS*, 440:2922–2927, June 2014. doi: 10.1093/mnras/stu456.

E. Mentuch Cooper, C. D. Wilson, K. Foyle, et al. *ApJ*, 755:165, Aug. 2012. doi: 10.1088/0004-637X/755/2/165.

A. I. Merson, C. M. Baugh, J. C. Helly, et al. *MNRAS*, 429:556–578, Feb. 2013. doi: 10.1093/mnras/sts355.

M. Milgrom. *ApJ*, 270:371–389, July 1983. doi: 10.1086/161131.

M. Milgrom. *Physical Review Letters*, 111(4):041105, July 2013. doi: 10.1103/PhysRevLett.111.041105.

L. Miller, T. D. Kitching, C. Heymans, et al. *MNRAS*, 382:315–324, Nov. 2007. doi: 10.1111/j.1365-2966.2007.12363.x.

L. Miller, C. Heymans, T. D. Kitching, et al. *MNRAS*, 429:2858–2880, Mar. 2013a. doi: 10.1093/mnras/sts454.

L. Miller, C. Heymans, T. D. Kitching, et al. *MNRAS*, 429:2858–2880, Mar. 2013b. doi: 10.1093/mnras/sts454.

H. Miyatake, S. More, R. Mandelbaum, et al. *ArXiv e-prints*, Nov. 2013.

S. More, F. C. van den Bosch, and M. Cacciato. *MNRAS*, 392:917–924, Jan. 2009a. doi: 10.1111/j.1365-2966.2008.14114.x.

S. More, F. C. van den Bosch, M. Cacciato, et al. *MNRAS*, 392:801–816, Jan. 2009b. doi: 10.1111/j.1365-2966.2008.14095.x.

S. More, F. C. van den Bosch, M. Cacciato, et al. *MNRAS*, 410:210–226, Jan. 2011. doi: 10.1111/j.1365-2966.2010.17436.x.

S. More, H. Miyatake, R. Mandelbaum, et al. *ArXiv e-prints*, July 2014.

S. More, H. Miyatake, R. Mandelbaum, et al. *ApJ*, 806:2, June 2015. doi: 10.1088/0004-637X/806/1/2.

K. Morokuma-Matsui and J. Baba. *MNRAS*, 454:3792–3804, Dec. 2015. doi: 10.1093/mnras/stv2227.

B. P. Moster, R. S. Somerville, C. Maulbetsch, et al. *ApJ*, 710:903–923, Feb. 2010. doi: 10.1088/0004-637X/710/2/903.

B. P. Moster, T. Naab, and S. D. M. White. *MNRAS*, 428:3121–3138, Feb. 2013. doi: 10.1093/mnras/sts261.

J. S. Mulchaey. *ARA&A*, 38:289–335, 2000. doi: 10.1146/annurev.astro.38.1.289.

J. S. Mulchaey, D. S. Davis, R. F. Mushotzky, et al. *ApJ*, 456:80, Jan. 1996. doi: 10.1086/176629.

E. Munari, A. Biviano, S. Borgani, et al. *MNRAS*, 430:2638–2649, Apr. 2013. doi: 10.1093/mnras/stt049.

S. G. Murray, C. Power, and A. S. G. Robotham. *MNRAS*, 434:L61–L65, July 2013. doi: 10.1093/mnrasl/slt079.

S. Nadathur, S. Hotchkiss, J. M. Diego, I. T. Iliev, S. Gottlöber, W. A. Watson, and G. Yepes. *MNRAS*, 449:3997–4009, June 2015. doi: 10.1093/mnras/stv513.

D. Nagai, A. Vikhlinin, and A. V. Kravtsov. *ApJ*, 655:98–108, Jan. 2007. doi: 10.1086/509868.

J. F. Navarro, C. S. Frenk, and S. D. M. White. *MNRAS*, 275:720–740, Aug. 1995.

J. F. Navarro, C. S. Frenk, and S. D. M. White. *MNRAS*, 275(1):56–66, 1995.

J. F. Navarro, C. S. Frenk, and S. D. M. White. *ApJ*, 462:563, May 1996. doi: 10.1086/177173.

P. Norberg, C. M. Baugh, E. Gaztañaga, et al. *MNRAS*, 396:19–38, June 2009. doi: 10.1111/j.1365-2966.2009.14389.x.

M. Oguri and M. Takada. *Phys. Rev. D*, 83(2):023008, Jan. 2011. doi: 10.1103/PhysRevD.83.023008.

T. Padmanabhan. *Reports on Progress in Physics*, 73(4):046901, Apr. 2010. doi: 10.1088/0034-4885/73/4/046901.

L. C. Parker, M. J. Hudson, R. G. Carlberg, et al. *ApJ*, 634:806–812, Dec. 2005. doi: 10.1086/497117.

R. J. Pearson, T. J. Ponman, P. Norberg, et al. *MNRAS*, 449:3082–3106, May 2015. doi: 10.1093/mnras/stv463.

P. J. E. Peebles. *ApJ*, 189:L51, Apr. 1974. doi: 10.1086/181462.

P. J. E. Peebles and J. T. Yu. *ApJ*, 162:815, Dec. 1970. doi: 10.1086/150713.

Y.-j. Peng, S. J. Lilly, K. Kovač, et al. *ApJ*, 721:193–221, Sept. 2010. doi: 10.1088/0004-637X/721/1/193.

F. Pérez and B. E. Granger. *Computing in Science & Engineering*, 9(3):21–29, 2007.

M. Pettini and D. V. Bowen. *ApJ*, 560:41–48, Oct. 2001. doi: 10.1086/322510.

Planck Collaboration, P. A. R. Ade, N. Aghanim, et al. *ArXiv e-prints*, Mar. 2013.

Planck XIII. *A&A*, 594:A13, Sept. 2016. doi: 10.1051/0004-6361/201525830.

Planck XVI. *A&A*, 571:A16, Nov. 2014. doi: 10.1051/0004-6361/201321591.

M. Pohlen, L. Cortese, M. W. L. Smith, et al. *A&A*, 518:L72, July 2010. doi: 10.1051/0004-6361/201014554.

E. Pointecouteau and J. Silk. *MNRAS*, 364:654–658, Dec. 2005. doi: 10.1111/j.1365-2966.2005.09590.x.

F. Prada, A. A. Klypin, A. J. Cuesta, et al. *MNRAS*, 423:3018–3030, July 2012. doi: 10.1111/j.1365-2966.2012.21007.x.

S. W. Randall, M. Markevitch, D. Clowe, et al. *ApJ*, 679:1173-1180, June 2008. doi: 10.1086/587859.

E. Rasia, S. Ettori, L. Moscardini, et al. *MNRAS*, 369:2013–2024, July 2006. doi: 10.1111/j.1365-2966.2006.10466.x.

J. Rasmussen and T. J. Ponman. *MNRAS*, 399:239–263, Oct. 2009. doi: 10.1111/j.1365-2966.2009.15244.x.

A. Refregier, T. Kacprzak, A. Amara, et al. *MNRAS*, 425:1951–1957, Sept. 2012. doi: 10.1111/j.1365-2966.2012.21483.x.

A. G. Riess, W. H. Press, and R. P. Kirshner. *ApJ*, 473:88, Dec. 1996. doi: 10.1086/178129.

K. Rines, M. J. Geller, A. Diaferio, et al. *ApJ*, 767:15, Apr. 2013. doi: 10.1088/0004-637X/767/1/15.

A. Robotham, S. P. Driver, P. Norberg, et al. *PASA*, 27:76–90, Mar. 2010. doi: 10.1071/AS09053.

A. S. G. Robotham, P. Norberg, S. P. Driver, et al. *MNRAS*, 416:2640–2668, Oct. 2011. doi: 10.1111/j.1365-2966.2011.19217.x.

A. S. G. Robotham, J. Liske, S. P. Driver, et al. *MNRAS*, 431:167–193, May 2013. doi: 10.1093/mnras/stt156.

E. Rozo, E. S. Rykoff, A. Abate, et al. *MNRAS*, 461:1431–1450, Sept. 2016. doi: 10.1093/mnras/stw1281.

V. C. Rubin. *Scientific American*, 248:96–106, June 1983. doi: 10.1038/scientificamerican0683-96.

I. Sadeh, F. B. Abdalla, and O. Lahav. *PASP*, 128(10):104502, Oct. 2016. doi: 10.1088/1538-3873/128/968/104502.

A. Saintonge, G. Kauffmann, C. Kramer, et al. *MNRAS*, 415:32–60, July 2011. doi: 10.1111/j.1365-2966.2011.18677.x.

L. V. Sales, J. F. Navarro, J. Schaye, et al. *MNRAS*, 409:1541–1556, Dec. 2010.

doi: 10.1111/j.1365-2966.2010.17391.x.

C. Sánchez, J. Clampitt, A. Kovacs, et al. *MNRAS*, 465:746–759, Feb. 2017. doi: 10.1093/mnras/stw2745.

R. H. Sanders. *MNRAS*, 342:901–908, July 2003. doi: 10.1046/j.1365-8711.2003.06596.x.

K. Sato. *Physics Letters B*, 99:66–70, Feb. 1981. doi: 10.1016/0370-2693(81)90805-4.

J. Schaye, C. Dalla Vecchia, C. M. Booth, et al. *MNRAS*, 402:1536–1560, Mar. 2010. doi: 10.1111/j.1365-2966.2009.16029.x.

J. Schaye, R. A. Crain, R. G. Bower, et al. *MNRAS*, 446:521–554, Jan. 2015. doi: 10.1093/mnras/stu2058.

P. Schneider, C. Kochanek, and J. Wambsganss. *Gravitational Lensing: Strong, Weak and Micro: Saas-Fee Advanced Course 33*, volume 33. Springer Science & Business Media, 2006.

G. Schwarz. *Annals of Statistics*, 6:461–464, July 1978.

U. Seljak. *MNRAS*, 318:203–213, Oct. 2000. doi: 10.1046/j.1365-8711.2000.03715.x.

E. Semboloni, H. Hoekstra, J. Schaye, et al. *MNRAS*, 417:2020–2035, Nov. 2011. doi: 10.1111/j.1365-2966.2011.19385.x.

E. Semboloni, H. Hoekstra, and J. Schaye. *MNRAS*, 434:148–162, Sept. 2013. doi: 10.1093/mnras/stt1013.

J. L. Sérsic. *Boletin de la Asociacion Argentina de Astronomia La Plata Argentina*, 6:41–+, 1963.

J. L. Sersic. *Atlas de Galaxias Australes*. Observatorio Astronomico, Argentina, 1968.

H. Shan, J.-P. Kneib, R. Li, et al. *ArXiv e-prints*, Feb. 2015.

E. S. Sheldon, D. E. Johnston, J. A. Frieman, et al. *AJ*, 127:2544–2564, May 2004. doi: 10.1086/383293.

E. S. Sheldon, D. E. Johnston, M. Masjedi, et al. *ApJ*, 703:2232–2248, Oct. 2009. doi: 10.1088/0004-637X/703/2/2232.

R. K. Sheth and G. Tormen. *MNRAS*, 308:119–126, Sept. 1999. doi: 10.1046/j.1365-8711.1999.02692.x.

R. K. Sheth, H. J. Mo, and G. Tormen. *MNRAS*, 323:1–12, May 2001. doi: 10.1046/j.1365-8711.2001.04006.x.

C. Sifón, M. Cacciato, H. Hoekstra, et al. *MNRAS*, 454:3938–3951, Dec. 2015. doi: 10.1093/mnras/stv2051.

D. Sijacki, V. Springel, T. Di Matteo, et al. *MNRAS*, 380:877–900, Sept. 2007. doi: 10.1111/j.1365-2966.2007.12153.x.

R. A. Skibba and A. V. Macciò. *MNRAS*, 416:2388–2400, Sept. 2011. doi: 10.1111/j.1365-2966.2011.19218.x.

C. Skordis, D. F. Mota, P. G. Ferreira, et al. *Physical Review Letters*, 96(1):011301, Jan. 2006. doi: 10.1103/PhysRevLett.96.011301.

R. S. Somerville, K. Lee, H. C. Ferguson, et al. *ApJ*, 600:L171–L174, Jan. 2004. doi: 10.1086/378628.

D. N. Spergel, L. Verde, H. V. Peiris, et al. *ApJS*, 148:175–194, Sept. 2003. doi: 10.1086/377226.

D. N. Spergel, R. Flauger, and R. Hložek. *Phys. Rev. D*, 91(2):023518, Jan. 2015. doi: 10.1103/PhysRevD.91.023518.

V. Springel, T. Di Matteo, and L. Hernquist. *MNRAS*, 361:776–794, Aug. 2005a. doi: 10.1111/j.1365-2966.2005.09238.x.

V. Springel, S. D. M. White, A. Jenkins, et al. *Nature*, 435:629–636, June 2005b. doi: 10.1038/nature03597.

M. Sun, G. M. Voit, M. Donahue, et al. *ApJ*, 693:1142–1172, Mar. 2009. doi: 10.1088/0004-637X/693/2/1142.

E. N. Taylor, A. M. Hopkins, I. K. Baldry, et al. *MNRAS*, 418:1587–1620, Dec. 2011a. doi: 10.1111/j.1365-2966.2011.19536.x.

E. N. Taylor, A. M. Hopkins, I. K. Baldry, et al. *MNRAS*, 418:1587–1620, Dec. 2011b. doi: 10.1111/j.1365-2966.2011.19536.x.

E. Tempel, R. S. Stoica, V. J. Martínez, et al. *MNRAS*, 438(4):3465–3482, 2014.

The Dark Energy Survey Collaboration, T. Abbott, F. B. Abdalla, et al. *ArXiv e-prints*, July 2015.

J. Tinker, A. V. Kravtsov, A. Klypin, et al. *ApJ*, 688:709–728, Dec. 2008. doi: 10.1086/591439.

J. L. Tinker, B. E. Robertson, A. V. Kravtsov, et al. *ApJ*, 724:878–886, Dec. 2010. doi: 10.1088/0004-637X/724/2/878.

E. van Uitert, H. Hoekstra, M. Velander, et al. *A&A*, 534:A14, Oct. 2011. doi: 10.1051/0004-6361/201117308.

E. van Uitert, M. Cacciato, H. Hoekstra, et al. *A&A*, 579:A26, July 2015. doi: 10.1051/0004-6361/201525834.

E. van Uitert, M. Cacciato, H. Hoekstra, et al. *MNRAS*, 459:3251–3270, July 2016. doi: 10.1093/mnras/stw747.

A. Vale and J. P. Ostriker. *MNRAS*, 353:189–200, Sept. 2004. doi: 10.1111/j.1365-2966.2004.08059.x.

M. Velander, E. van Uitert, H. Hoekstra, et al. *MNRAS*, 437:2111–2136, Jan. 2014. doi: 10.1093/mnras/stt2013.

E. Verlinde. *Journal of High Energy Physics*, 4:29, Apr. 2011. doi: 10.1007/JHEP04(2011)029.

E. P. Verlinde. *SciPost Phys.*, 2:016, 2017. doi: 10.21468/SciPostPhys.2.3.016. URL `https://scipost.org/10.21468/SciPostPhys.2.3.016`.

M. Viola, T. D. Kitching, and B. Joachimi. *MNRAS*, 439:1909–1932, Apr. 2014. doi: 10.1093/mnras/stu071.

M. Viola, M. Cacciato, M. Brouwer, et al. *Monthly Notices*, 452:3529–3550, Oct. 2015. doi: 10.1093/mnras/stv1447.

M. Vogelsberger, S. Genel, V. Springel, et al. *Nature*, 509:177–182, May 2014. doi: 10.1038/nature13316.

L. van Waerbeke, J. Benjamin, T. Erben, et al. *MNRAS*, 433:3373–3388, Aug. 2013. doi: 10.1093/mnras/stt971.

A. R. Wetzel, J. L. Tinker, C. Conroy, et al. *MNRAS*, 439:2687–2700, Apr. 2014. doi: 10.1093/mnras/stu122.

S. D. M. White and C. S. Frenk. *ApJ*, 379:52–79, Sept. 1991. doi: 10.1086/170483.

S. D. M. White and M. J. Rees. *MNRAS*, 183:341–358, May 1978. doi: 10.1093/mnras/183.3.341.

C. O. Wright and T. G. Brainerd. *ApJ*, 534:34–40, May 2000. doi: 10.1086/308744.

X.-d. Xu, B. Wang, and P. Zhang. *Phys. Rev. D*, 92(8):083505, Oct. 2015. doi: 10.1103/PhysRevD.92.083505.

X. Yang, H. J. Mo, and F. C. van den Bosch. *ApJ*, 695:900–916, Apr. 2009. doi: 10.1088/0004-637X/695/2/900.

H. K. C. Yee, M. J. Sawicki, R. G. Carlberg, et al. *Highlights of Astronomy*, 11:460, 1998.

I. Zehavi, Z. Zheng, D. H. Weinberg, et al. *ApJ*, 736:59, July 2011. doi: 10.1088/0004-637X/736/1/59.

P. Zivick, P. M. Sutter, B. D. Wandelt, et al. *MNRAS*, 451:4215–4222, Aug. 2015. doi: 10.1093/mnras/stv1209.

F. Zwicky. *Helvetica Physica Acta*, 6:110–127, 1933.

F. Zwicky. *ApJ*, 86:217, Oct. 1937. doi: 10.1086/143864.

Curriculum vitae

For reasons I cannot begin to understand, I have been interested in Astronomy for as long as I can remember. I must have been about 8 years old when my father started taking me and my brother and sister for weekly library trips. Every time we went I picked books concerning stars, planets, the Solar System and space travel. What I read at that young age astonished me. For instance, I remember that I was quite shocked to find out that the Sun would die in 5 billion years. Everything that happened in space seemed so much bigger and more significant than our life on this tiny Earth.

I started high school in 2002, at the Hervormd Lyceum Zuid in Amsterdam. My interest in the sciences: physics, mathematics, chemistry and biology, grew thanks to my excellent teachers. I was thrilled when my physics teacher, Dick Hoekzema, offered extra classes on special relativity. He always made an effort to discuss modern physics in class, especially quantum mechanics, and even took my class on a field trip to the Large Hadron Collider at CERN, Geneva. In my fifth year, it was 2007, I was a finalist in the first Dutch Astronomy Olympiad, which took place at the Leiden Observatory. Of course in the final year of high school I couldn't wait to study physics and astronomy. I visited several open days at universities in Amsterdam, where I met prof. Huib Henrichs. He immediately became a good friend, and he arranged that I could visit some of the telescopes on La Palma.

I graduated Cum Laude in 2008, and immediately started my study in Physics and Astronomy at the University of Amsterdam. I was overwhelmed with joy to finally be surrounded by people with similar interests, professors and fellow students who where curious and eager to understand the Universe. It was the first time in my life that I truly felt that this important part of me was nourished and accepted. I especially enjoyed the astronomy and fundamental physics classes like cosmology, quantum physics and special relativity. I wrote my bachelor thesis: “Searching for pulsars with the LOFAR telescope", under supervision of Jason Hessels. During this project I studied the physics behind the pulsar phenomenon, as well as the workings of the LOFAR radio telescope. At the ASTRON headquarter in Dwingeloo I learned how to interact in a highly international and multi-disciplinary scientific community, and analysed LOFAR data resulting in the discovery of two new pulsar candidates.

Immediately afterwards, in 2011, I started my master program at the GRAPPA (Gravitation and Astro-Particle Physics in Amsterdam) Center of Excellence. This brand new institute combines subjects from theoretical physics, particle physics and astrophysics to develop a broader view of fundamental cosmology and the dark universe. My master thesis with Gianfranco Bertone was called: "Indirect dark matter detection with the Fermi Gamma-Ray Telescope." During this project I became familiarized with the state of the art of particle dark matter research, as well as the observation of its annihilation products through the analysis of Fermi Gamma-Ray Telescope data. After finishing my thesis I became the very first graduate of the GRAPPA master programme.

As I wanted to continue my investigation into the dark matter problem through a different method, I applied for a PhD position with prof. Koen Kuijken at the Leiden University. I was thrilled that, out of roughly 200 applicants from around the world, and 30 'finalists', I was chosen for his project on 'galaxy-galaxy lensing'. During this project I used weak gravitational lensing to measure the structure of dark matter, on scales ranging from the dark matter haloes around single galaxies and galaxy groups to the large scale structure of the universe: the cosmic web. The final goal was to obtain a deeper understanding of dark matter: what evidence can we find of its existence, how is it distributed, and how does it behave?

During my research I heard of the new theory of Emergent Gravity by prof. Erik Verlinde, who was still working at my 'alma mater'. According to him, the dark matter that I was studying did not exist. This piqued my interest enough to visit one of his talks, where he first showed his prediction for the distribution of emergent gravity around a massive object. I immediately knew that I could easily test this prediction by measuring the gravitational lensing distribution around galaxies, and started working on this as a 'secret side project'. I didn't know at the time that this would result in a close collaboration with prof. Verlinde and his PhD candidate Manus Visser, and in the publication of the first paper that tested his new theory. I was even more surprised when my paper received both national and international media attention, as I was invited to give talks at events and universities, and to give interviews for TV series, documentaries, radio shows, websites, newspapers and magazines. On the side I was writing articles for popular science magazines and websites. It was all rather overwhelming, but lots of fun.

Fortunately for me I really enjoy popular science presenting and writing. I had already taken theatre lessons when I was in high school, and during my masters I had been an author and editor at Scoop, the magazine of our science student union at the University of Amsterdam. By that time one of my articles, “Habitable planets in our Milky Way”, had already been published on Kennislink (a Dutch popular science website) and was later elected as “The best article in 10 years of Kennislink” in the Astronomy category. In 2015 I was a semi-finalist of the national Famelab science communication competition, and on the side I was the coordinator of the cosmology exhibition during the renovation of the astronomy museum at the Historical Observatory in Leiden. All these experiences greatly helped me in dealing with my ‘emergent fame’, and at least I can claim that I already was a reasonable science popularizer on my own merit!

After my PhD I will start as a Postdoc at the Universities of Amsterdam and Groningen. Under supervision of prof. Erik Verlinde and prof. Edwin Valentijn I will continue studying and observationally testing the theory of Emergent Gravity, and I will become an instructor and dark matter & energy researcher of the new Euclid space telescope. I am very much looking forward to this new phase in my career, and this new phase in my life, as I move to Groningen with my brand new husband Jasper.

List of publications

- “Dark matter halo properties of GAMA galaxy groups from 100 square degrees of KiDS weak lensing data”
  Authors: Massimo Viola, Marcello Cacciato, Margot M. Brouwer, Konrad Kuijken, Henk Hoekstra, Peder Norberg, Aaron S. G. Robotham, Edo van Uitert, Mehmed Alpaslan, Ivan K. Baldry, Ami Choi, Jelte T. A. de Jong, Simon P. Driver, Thomas Erben, Aniello Grado, Alister W. Graham, Catherine Heymans, Hendrik Hildebrandt, Anthony M. Hopkins, Nancy Irisarri, Benjamin Joachimi, Jon Loveday, Lance Miller, Reiko Nakajima, Peter Schneider, Cristóbal Sifón, Gijs Verdoes Kleijn
  Published in: MNRAS, Volume 452, Issue 4, p.3529-3550
  Publication Date: October 2015

- “The masses of satellites in GAMA galaxy groups from 100 square degrees of KiDS weak lensing data”
  Authors: Cristóbal Sifón, Marcello Cacciato, Henk Hoekstra, Margot Brouwer, Edo van Uitert, Massimo Viola, Ivan Baldry, Sarah Brough, Michael J. I. Brown, Ami Choi, Simon P. Driver, Thomas Erben, Aniello Grado, Catherine Heymans, Hendrik Hildebrandt, Benjamin Joachimi, Jelte T. A. de Jong, Konrad Kuijken, John McFarland, Lance Miller, Reiko Nakajima, Nicola Napolitano, Peder Norberg, Aaron S. G. Robotham, Peter Schneider, Gijs Verdoes Kleijn
  Published in: MNRAS, Volume 454, Issue 4, p.3938-3951
  Publication Date: December 2015

- “Gravitational Lensing Analysis of the Kilo Degree Survey”
  Authors: Konrad Kuijken, Catherine Heymans, Hendrik Hildebrandt, Reiko Nakajima, Thomas Erben, Jelte T.A. de Jong, Massimo Viola, Ami Choi, Henk Hoekstra, Lance Miller, Edo van Uitert, Alexandra Amon, Chris Blake, Margot Brouwer, Axel Buddendiek, Ian Fenech

Conti, Martin Eriksen, Aniello Grado, Joachim Harnois-Déraps, Ewout Helmich, Ricardo Herbonnet, Nancy Irisarri, Thomas Kitching, Dominik Klaes, Francesco Labarbera, Nicola Napolitano, Mario Radovich, Peter Schneider, Cristóbal Sifón, Gert Sikkema, Patrick Simon, Alexandru Tudorica, Edwin Valentijn, Gijs Verdoes Kleijn, Ludovic van Waerbeke
Published in: MNRAS, Volume 454, Issue 4, p.3500-3532
Publication Date: December 2015

- "The stellar-to-halo mass relation of GAMA galaxies from 100 square degrees of KiDS weak lensing data"
  Authors: "Edo van Uitert, Marcello Cacciato, Henk Hoekstra, Margot Brouwer, Cristóbal Sifón, Massimo Viola, Ivan Baldry, Joss Bland-Hawthorn, Sarah Brough, M. J. I. Brown, Ami Choi, Simon P. Driver, Thomas Erben, Catherine Heymans, Hendrik Hildebrandt, Benjamin Joachimi, Konrad Kuijken, Jochen Liske, Jon Loveday, John McFarland, Lance Miller, Reiko Nakajima, John Peacock, Mario Radovich, A. S. G. Robotham, Peter Schneider, Gert Sikkema, Edward N. Taylor, Gijs Verdoes Kleijn
  Published in: MNRAS, Volume 459, Issue 3, p.3251-3270
  Publication Date: July 2016

- "Dependence of GAMA galaxy halo masses on the cosmic web environment from 100 square degrees of KiDS weak lensing data"
  Authors: Margot M. Brouwer, Marcello Cacciato, Andrej Dvornik, Lizzie Eardley, Catherine Heymans, Henk Hoekstra, Konrad Kuijken, Tamsyn McNaught-Roberts, Cristóbal Sifón, Massimo Viola, Mehmet Alpaslan, Maciej Bilicki, Joss Bland-Hawthorn, Sarah Brough, Ami Choi, Simon P. Driver, Thomas Erben, Aniello Grado, Hendrik Hildebrandt, Benne W. Holwerda, Andrew M. Hopkins, Jelte T. A. de Jong, Jochen Liske, John McFarland, Reiko Nakajima, Nicola R. Napolitano, Peder Norberg, John A. Peacock, Mario Radovich, Aaron S. G. Robotham, Peter Schneider, Gert Sikkema, Edo van Uitert, Gijs Verdoes Kleijn
  Published in: MNRAS, Volume 462, Issue 4, p.4451-4463
  Publication Date: November 2016

- "First test of Verlinde's theory of Emergent Gravity using Weak Gravitational Lensing measurements"
  Authors: Margot M. Brouwer, Manus R. Visser, Andrej Dvornik, Henk Hoekstra, Konrad Kuijken, Edwin A. Valentijn, Maciej Bilicki,

Chris Blake, Sarah Brough, Hugo Buddelmeijer, Thomas Erben, Catherine Heymans, Hendrik Hildebrandt, Benne W. Holwerda, Andrew M. Hopkins, Dominik Klaes, Jochen Liske, Jon Loveday, John McFarland, Reiko Nakajima, Cristóbal Sifón, Edward N. Taylor
Published in: MNRAS, Volume 466, Issue 3, p.2547-2559
Publication Date: April 2017

- “A KiDS weak lensing analysis of assembly bias in GAMA galaxy groups”
  Authors: Andrej Dvornik, Marcello Cacciato, Konrad Kuijken, Massimo Viola, Henk Hoekstra, Reiko Nakajima, Edo van Uitert, Margot Brouwer, Ami Choi, Thomas Erben, Ian Fenech Conti, Daniel J. Farrow, Ricardo Herbonnet, Catherine Heymans, Hendrik Hildebrandt, Andrew. M. Hopkins, John McFarland, Peder Norberg, Peter Schneider, Cristóbal Sifón, Edwin Valentijn, Lingyu Wang
  Published in: MNRAS, Volume 468, Issue 3, p.3251-3265
  Publication Date: July 2017

Acknowledgements

This is the part where I try my best to thank everyone who has supported me over the four years that I have worked on this thesis, both scientifically and psychologically (and in some cases both). If you are scanning the page to see if you are mentioned and it turns out I have forgotten you, I hereby sincerely apologize and thank you anyway (if only for reading my thesis)!

First off: it is stated on the Sterrewacht Wiki that it is "not customary to acknowledge directly your advisor", since he/she is just "doing his/her job". Nevertheless, I really want to say that Koen was the best supervisor I could have wished for. Whenever I encountered an obstacle, he was available for an illuminating discussion. These always provided me with a new way to attack my problem, and often ended with: "Okay, do it!" (although I would have preferred "Make it so!"). He was there for me when I needed him, and he trusted me when I was progressing on my own. Koen, you trusted me even when others doubted me, you trusted me even when I doubted myself.

I would like to thank all the other people from my weak lensing group for the fruitful discussions during the weekly Monday telecons, the Wednesday group meetings and the Friday borrels: first of all Henk, my co-promoter, and also Marcello, Massimo, Maciej (or Maciek, he seems to use both for added confusion), Marcus, Patricia, Arun, Andrej, Cristóbal, Fabian, Ricardo, Marco, Remco, Hugo, Martin, Christos and Maria Cristina. This also includes the KiDS and GAMA friends from overseas: Catherine, Edo, Alex, Dominik, Thomas, Benjamin, Naomi, Angus, Reiko, Hendrik, Marika, Vasiliy, Joachim, Lance, Benjamin, Harry, Tilman, Shahab, Elisa, Jan Luca, Nicolas, Julian, Ami, Ian, India, Qianli, Mohammadjavad, Patrick, Gijs, Peter, Peder, Tim and Tom. I really enjoyed our Busy Weeks together, sorry you always had to come to Leiden!

One aspect of life at the Sterrewacht I will dearly miss is being a member, and later leader, of the Social Committee. I'm very grateful to Henriette, who is the reason I became both. You were a magnificent leader of the SocCom and you taught me well. Of course a big thank you to our members: Wouter, Jackie, Soumyajit, Maaike, Maria Cristina, Jeb, and especially Chris and Ann-Sofie who are now sharing the SocCom leadership. But most of the work was of course done by the support staff: Debbie, Marjan, and Erik Deul, who have been truly invaluable. And although they might prefer to stay anonymous, I really want to thank all the staff-members who have so graciously agreed to play Sinterklaas while I was at the Sterrewacht: Matt, Evelijn (yes, our female Sinterklaas!), Michiel and Frans. Also a big thank you to Adrian and Michael for playing the piano at our events. Sinterklaas was already my favourite holiday, but you all somehow managed to make it even better!

A few other professors I would like to thank are the confidentiality persons: Jarle, who is the most approachable person I know; Xander, who is of course always ready to help all PhD students; and Elena, who also finds time to lead the diversity committee. I was not at all surprised that you had been elected by the Sterrewachters to help those in need. Also: Marijn, thank you for teaching me almost everything I know about the baryonic part of galaxies and about TA'ing. Marcel, Leindert and Marijke, thank you for TA'ing the Galaxies & Cosmology course with me. It was always a lot of fun to inspire the new students together, and I was really glad to share the heavy load of correcting all that homework!

But most of my time was of course spent with my delightful officemates: Vivianni, Donggang, Merijn and Nancy. You have been my daily companions for years and I will sorely miss you. I'm really grateful for the fact that you were sociable when I wanted to talk, but quiet when I wanted to work! I hope you thought the same of me. Valeria, you were a welcome new addition, and I'm sad I couldn't get to know you better. Hugo and Jelte, we didn't get to spend much time together in our office in Leiden, but now I will haunt you in Groningen! And now my delightful PhD colleagues from the other offices: Jeroen, David, Christian, Eva, Andrew, Nico, Bart, Mason, Sascha, Eleonora, Kirstin, Cameron and Jens. And especially my colleagues in offices 553 and 458 (and some other offices too), where I always went with my cup of tea to talk (and irritate them when they want to work): Lucie, Edwin, Carmen, Tjarda, Sylvia, Noel, Santiago, Allison, Mieke and Ann-Sofie. This still leaves my two paranymphs to thank: Edwin and Yvette. As Yvette so aptly put it: You will be the witnesses at my wedding with Science!

Looking to the past, I would like to thank all the teachers that inspired me on my long journey towards becoming a scientist. There are too many to name them all, but a few I will give a special mention. My high school teachers: Mr. Hoekzema, Mr. Forouzanfar, Mr. Dorstijn, Mrs. Spanjaard and Mr. van der Bij, who inspired me to embark on my scientific journey. My professors at the University of Amsterdam: Huib Henrichs, Jason Hessels and Gianfranco Bertone, who have guided me both as supervisors and as friends, and Sera Markoff and Anna Watts, who have shown me what it means to be a great scientist and a strong woman. I have always looked up to you, and am thankful for such amazing role models. And finally my fellow student Dorine who, as the chief editor of Scoop, inspired me to pursue popular science writing.

As I look to the future, I am very grateful to Edwin Valentijn and Erik Verlinde for allowing me to continue my work in cosmology. Thanks to you I am able to stand at the cradle of the new and exciting theory of Emergent Gravity, and of Euclid: the best cosmology telescope devised by mankind. Working with both of you truly feels like a dream come true. This also goes for you Manus, as we will soon continue our elaborate discussions on the secrets of theoretical physics and observational cosmology. I'm looking forward to learning more from all of you.

Hoewel het schrijven van dit proefschrift het grootste gedeelte van mijn leven opgeslokte, waren er gelukkig ook nog momenten dat ik met mijn Amsterdamse vrienden kon vertoeven. Ik wil graag al mijn vrienden uit Vrijburg en de Kelder bedanken die mij door de jaren heen hebben gesteund, en hebben gezorgd voor gezellige avonden met (meestal) lekker eten: Margriet, Dik, Marja, Japke, Joep, Erik, Jelle, Alex, Ana Ide, Arjen, Arnoud, Bram, Emma D., Simon, Thomas, Willem, Ernst, Marthe, Tibor, Ivan, Harold, Joost, Lennaert, Ilona, Isa, Margot S., Mirjam, Roel, Sanne, Max, Noor, Matthijs, Wilbert en Elmieke. En vooral natuurlijk de Oempa's, de volgende generatie sleutelhouders en onze hoop voor de toekomst: David, Marije, Martijn, Joe, Jim, Tosca, Thomas, Pinky, Hidde, Ezra en Vince. Speciaal wil ik de leden van de lees-/filosofiegroep (of moet ik zeggen 'support group') bedanken die met mij de monumentale taak hebben opgevat om "Gödel, Escher, Bach" van kaft tot kaft te lezen: Timber, Florisca, Simon en Maureen.

Al mijn woensdag- (en later donderdag-) avonden gedurende de afgelopen 10 jaar heb ik doorgebracht in de wereld van Dungeons & Dragons, Pathfinder en Chtulhu met mijn lieve RPG-vrienden: Harold, Ivan, Jimmy, Tom, Robert, James en Phil. Heel erg bedankt voor alle fantastische avonden die we hebben gehad. Woensdag is jarenlang mijn favoriete dag van de week geweest dankzij jullie, en ik hoop dat we Baba Yaga nog gaan bevrijden! Ook heb ik een paar

dierbare vrienden over de grens: Liza, Pelle en Elif. Jullie toekomst is nog onzeker, maar ik hoop ontzettend dat jullie het geluk vinden. Jullie verdienen het zo!

Ik wil mijn fantastische familie bedanken, die me mijn hele leven hebben bijgestaan en liefgehad. Lieve pappa en mamma, jullie hebben dit op elke mogelijke manier mogelijk gemaakt. Jullie zijn tegelijk mijn grootste rolmodellen en mijn grootste fans. Ik ben jullie het meest dankbaar van allemaal, meer dan ik in woorden kan uitdrukken. En lieve Arie en Tineke, ik houd ontzettend veel van jullie. Jullie zijn de beste broer en zus die ik me kan wensen, en we hebben altijd zoveel lol met elkaar. Emma, mijn beste vriendin en getuige, ik zet jou ook hier neer omdat ik je als mijn zus beschouw, en ik me geen leven meer kan voorstellen zonder jou. Opa en Oma, ik ben ontzettend blij dat ik al zo lang van jullie mag genieten, en dat jullie me al die jaren hebben bijgestaan en toegejuigd. Ook mijn lieve schoonfamilie heeft me altijd een warm hart toegedragen. Lieve Marijke, Hans, Carine, Erik Jan en Corina, jullie zijn altijd zo lief voor me en zo begaan met mijn leven. Bij jullie kan ik altijd terecht voor een luisterend oor, een dikke knuffel en een grote bak chocolademousse; daar ben ik ontzettend dankbaar voor.

En natuurlijk als allerlaatste: Jasper, mijn kersverse echtgenoot. Dank je dat je al deze jaren zo goed voor me hebt gezorgd, me gelukkig hebt gemaakt, en dat je nooit iets hebt gezegd over de lange avonden en weekenden dat ik zo druk bezig was dat ik geen tijd had voor jou. Je bent mijn geliefde en beste vriend, mijn privé-chef en bodyguard, mijn dominee, filosoof en psycholoog, mijn wandel-, zang- en danspartner, en nog oneindig veel meer. Nu dit hoofstuk letterlijk en figuurlijk is afgesloten gaan we samen, als man en vrouw, een nieuwe beginnen.